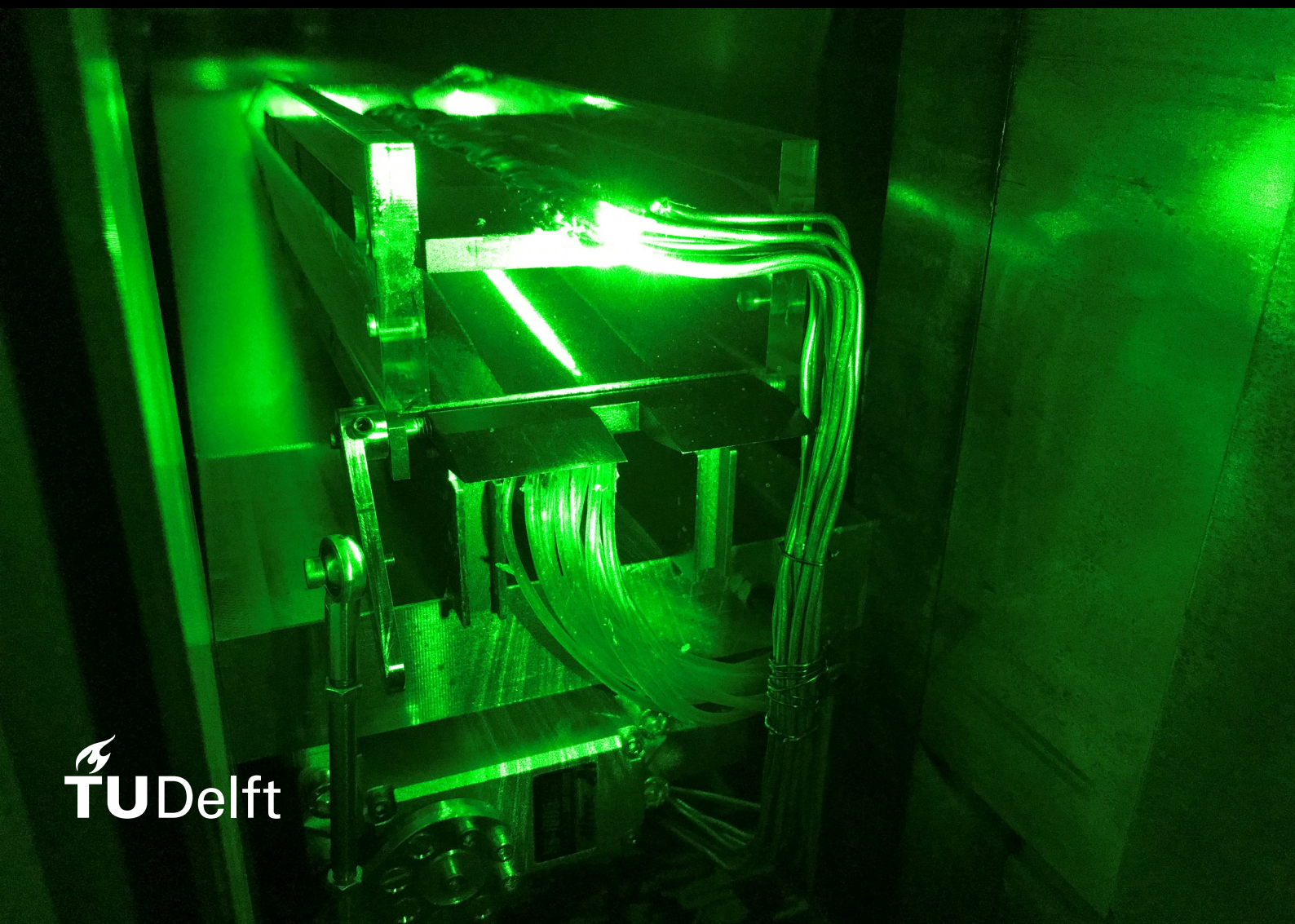


Submerged Supersonic Intakes

An experimental investigation
by means of PIV, Schlieren and
pressure measurements

B.M. Barsom

Department of Aerodynamics
Faculty of Aerospace Engineering



Submerged Supersonic Intakes

An experimental investigation by means of PIV, Schlieren and
pressure measurements

by

B.M. Barsom

In partial fulfillment of the requirements for the degree of
Master of Science in Aerospace Engineering

at Delft University of Technology,

to be defended publicly on August 24th, 2021 at 13:30.

Student number:	4437985	
Thesis committee:	Dr. ir. B. W. van Oudheusden,	TU Delft, committee chair
	Dr. ir. F. F. J. Schrijer,	TU Delft, supervisor
	Ir. R. G. Veraar,	TNO
	Dr. ir. F. Avallone,	TU Delft

This thesis is not confidential

An electronic version of this thesis is available at <http://repository.tudelft.nl/>.

Preface

It took me almost a full year of dedicated work and now I am here, at the brink of closing one chapter of my life and almost ready to start a new one. But before getting there, this last year of my academic venture has been full of hurdles to say the least. It was challenging to overcome all of the difficulties I have encountered, but I am lucky to say that I have had the best supervisors to support me and the best family, friends and peers to cheer me up.

This thesis forms the end result of a laborious research topic and it also marks the end of my time as a student in Delft. Working on this profound project during the pandemic has taught me to be punctual in all my actions, plan far ahead and, most importantly, to work remotely. I will always remember the lessons learned during my thesis project throughout my future endeavors.

Since this effort was done with the help of more than one person, I would like to thank everybody who backed me in finishing this research. I would like to start by sincerely thanking dr. Bas van Oudheusden for his vast knowledge on fluid mechanics and for his advice on how to bridge many obstacles and the same goes for dr. Ferry Schrijer, who continuously guided me on supersonic flow theory, which ultimately shaped the backbone of this report.

I am also very grateful for all technicians that helped me in setting up my experimental systems and overcoming a number of difficulties in the wind tunnel, Dennis Bruikman, Peter Duydam, Frits Donker Duyvis and Nico van Beek. They displayed a very positive attitude towards me and my work and helped me a lot with finding solid solutions to sometimes unpredictable issues. Not to mention the innumerable times in which I requested their assistance in conducting wind tunnel runs, for which I shall always be indebted to them for their help.

I am also indebted to the assistance I got from PhD students Alessandro and Eduardo, who helped me a lot with finding solutions and providing me with useful advice on my PIV setup and how to optimally use the DaVis software.

Also, I will never forget my amazing peers with whom I shared the academic experience in Delft and with whom I have had both professional and funny experiences. They have also helped me in making this last bit of my studies endurable amidst the pandemic.

Finally, I would like to express eternal gratitude towards my father who always fortified me in pursuing all my dreams, my mother who always strengthened me to walk the additional mile and my brother Andro who continuously encouraged me along the way.

After nearly six adventuresome years, my time as a student has come to an end and everybody around me made it an unforgettable experience!

*Bavly Barsom
Delft, May 2021*

Executive Summary

Cruise missiles are becoming more popular and classical rocket engines will not be able to cope with today's performance needs. A lack of oxidizer onboard and insufficient firing range constitute grave dangers to a world filled with adversaries. This marks the rise of ramjet engines as an alternative means of propulsion to satisfy all required performance upgrades of this era. However, storage requirements create another issue, this time with the missile cross-sectional shape. To replace today's missile lateral air intakes, an idea was developed to install intakes that flush with the projectile fuselage surface, which would become known as the supersonic submerged intake.

The intake's performance is assessed by means of its total pressure recovery. This parameter directly relates to one of the paramount factors of missile performance, being the engine thrust. Ramjet thrust performance is regulated by a number of constraints to prevent the missile from operating in hazardous conditions, potentially giving rise to internal shock oscillations and engine surge. Also, the missile drag is another generic parameter for evaluation of the net performance. Intake total drag generally consists of cowl drag, spill-over drag and additive drag. For supersonic missiles, compressible viscous effects dominate the deceleration mechanism of the intake required to bring the flow velocity to an acceptable subsonic engine face velocity. Shock Boundary Layer Interactions do occur inside supersonic intakes, but no viscous phenomenon comes close to the severity of pseudo-shocks. These complicated shock regions control the largest portion of the supersonic intake deceleration scheme and are maliciously known by their swift shock oscillations and lofty flow gradients. Extensive research was conducted to understand the flow mechanics of pseudo-shocks, which consist of a shock train region and, if the conditions permit, a mixing region. Many analytical models were established to estimate the pseudo-shock behavior and to provide a quasi-real approximation on the pressure rise, streamwise length and Mach number distribution of pseudo-shocks.

Supersonic intakes are commonly comprised of three segments: The supersonic diffuser, constant-area duct and the subsonic diffuser. The supersonic diffuser generates a number of oblique shocks to initiate the preliminary deceleration phase of the flow. The constant-area duct serves as the flow station in which the pseudo-shock is encountered. The static pressure increases, and the Mach number and total pressure both decrease over this region. The subsonic diffuser serves as the final deceleration stage and is meant to bring the flow velocity to a proper value at the engine face. Optionally, intakes may be equipped with a boundary layer bleed slot to divert the upstream developed and very polluted boundary layer away to relax the harsh consequences of viscous flow effects.

In general, three operational conditions may be distinguished for supersonic intakes: Supercritical, critical and subcritical condition. In between the first two conditions, a transition region known as the near-supercritical condition is known to exist. When an intake starts, the terminal shock (the pseudo-shock's first shock) is still located deep inside the intake. The pseudo-shock is moved forward by means of increasing the combustion chamber temperature or by increasing the backpressure at the intake's downstream end. A slim presence of the pseudo-shock in the intake's constant duct is known as the supercritical condition. When the pseudo-shock covers roughly half of the constant duct's streamwise area, the intake operates at the near-supercritical condition. After the pseudo-shock reaches the intake throat, which practically coincides with the intake's constant duct entrance, the intake is said to operate in the critical condition which is known to be the most efficient condition in which supersonic intakes can operate since the total pressure recovery becomes maximized. When the terminal shock is pushed out of the intake due to a higher backpressure, the intake enters the subcritical condition. Supersonic intake service requires careful consideration though with the amount of backpressure at the end of the intake. This is determined by the shock oscillations that propagate upstream and the backpressure also dictates their severity. A too high backpressure will result in the pseudo-shock being expelled from the intake constant duct, resulting in erratic shock oscillations frequently referred to as buzz. This may eventually lead to heavy structural damage or loss of the complete missile. To avoid intake unstart situations, precise estimations are required on the intake's contraction ratio and on the total pressure upstream required to properly start the intake, i.e. to appropriately accelerate to supersonic

conditions. Since submerged intakes flush with the missile surface, an expansion corner is introduced to direct the upstream flow inwards.

The experimental campaigns were carried out in the ST-15 blowdown wind tunnel in the High-speed Laboratory at the Faculty of Aerospace Engineering at TU Delft. The submerged supersonic intake model consisted of a cowling on top, a double-shock compression plate on the bottom and two plexiglass sidewalls on each side. This submerged supersonic intake model was connected using two pylons to a support block which had an expansion corner placed upstream to simulate the effect of submerging the flow inside the missile hull. The throttle system handling the mass flow rate consisted of a servo, which upon external command drives a wheel to rotate a butterfly valve. A total of three different butterfly valves were tested using Schlieren imagery and static pressure measurements to ultimately determine which butterfly valve design ensures the most ideal pseudo-shock behavior. This optimal butterfly valve was then used in determining the dynamical flow structure using particle image velocimetry.

Experiments were carried out at a freestream Mach number of 2.0 and a settling chamber pressure of 3.95 bar. A total of three measuring techniques were used to quantify the complete flow mechanics of the submerged intake. Schlieren imagery was used to determine compressible flow features and to quantify any morphological changes of the shock train. The Schlieren imagery campaign involved a classical z-configuration with an optical sensor which acquired images at a rate of 16 frames per second. The static pressure measurements were carried out to reconstruct the pressure profile over the entire intake trajectory. The campaign was conducted using two pressure transducers, each acquiring 500 data points per wind tunnel run at an acquisition rate of 100 Hz. The particle image velocimetry measurements involved quantifying the flow dynamics, mainly the velocity and hence the Mach number, of the entire flow domain. This campaign was executed by taking 300 images per single run, in which two sCMOS camera's were used to capture the entire flow domain at a rate of 10 Hz. The plane of interest used for this campaign was the wall-parallel plane, located along the streamwise direction of the test-section.

The Schlieren and static pressure results clarified that the pseudo-shock inside the duct of a submerged intake behaves just as with generic supersonic intakes. Using the same results, it was confirmed that the diamond valve assured the most ideal operation in the critical condition by safeguarding the terminal shock inside the duct without being expelled outside, minimizing the violent shock oscillations, reaching the highest static pressure and showing the least pressure fluctuations. The PIV results were very powerful in showing the complete dynamical layout of the flow domain. From the PIV results, the Mach number distribution was retrieved and it showed how the Mach number upstream of the pseudo-shock stayed the same for all intake different operating conditions. For the critical condition, it was showed how the Mach number was ultimately decelerated from Mach 1.9 upstream of the pseudo-shock until 1.06 at the end of the duct. Therefore, the flow entered the subsonic diffuser whilst still supersonic. The pseudo-shock was not fully contained in the duct due to insufficient streamwise space, which made part of the pseudo-shock appear in the subsonic diffuser downstream of the duct. Verification with analytical models confirmed that the pseudo-shock in the intake duct was indeed incomplete and would require more space in the duct to enhance the intake performance to a more ideal level. Climatically, the total pressure recovery showed pretty generic behavior in comparison with open literature results. Major differences were attributed to the difference between λ -type normal and χ -type oblique shock trains, owing to the different upstream Mach numbers in front of the pseudo-shocks.

Contents

Executive Summary	iii
List of Figures	vii
List of Tables	xi
Nomenclature	xii
1 Introduction	1
1.1 Prologue	1
1.2 Thesis Goal	3
1.3 Research Objectives & Questions	4
1.4 Scope of this Report	5
2 Air Intake Theoretical Background	6
2.1 Intake Pressure Recovery	6
2.2 Supersonic Air Intake Fundamentals	9
2.2.1 Missile Thrust	9
2.2.2 Thrust coefficient	10
2.2.3 Ramjet Thrust Performance	11
2.2.4 Intake Drag	13
2.3 Supersonic Viscous Flow Effects	14
2.3.1 Shock Wave-Boundary Layer Interactions	15
2.3.2 Pseudo-shock	18
2.4 Supersonic Intake Configuration	29
2.4.1 Supersonic diffuser	29
2.4.2 Constant-area Duct	33
2.4.3 Subsonic Diffuser	34
2.4.4 Boundary Layer Bleed	34
2.5 Supersonic Intake Operation	36
2.5.1 Operating Conditions	36
2.5.2 Limiting Contraction Ratio	38
2.5.3 Shock Oscillations	39
2.6 Submerged Supersonic Intakes	40
3 Experimental Arrangements	42
3.1 Testing Facility	42
3.2 Coordinate system	43
3.3 Experimental Setup	43
3.3.1 Wind Tunnel Setup	43
3.3.2 SSI Model Setup	44
3.3.3 Complete Setup	52
4 Flow Measurement Campaigns	55
4.1 Research Structure	55
4.2 Schlieren imaging	56
4.2.1 Light Propagation Theory	56
4.2.2 Principle of Schlieren measurements	57
4.2.3 Experimental setup	59

4.3	Static pressure measurements	61
4.4	Particle Image Velocimetry	64
4.4.1	Fundamental imaging equations	64
4.4.2	PIV Properties	66
4.4.3	Image processing	72
4.4.4	Experimental setup	78
4.5	Uncertainty analysis	79
4.5.1	Schlieren imagery	79
4.5.2	Static pressure measurements	79
4.5.3	PIV	81
5	Experimental Results	83
5.1	Schlieren & static pressure - Flow analysis	83
5.1.1	Intake flow characteristics	83
5.1.2	Butterfly valve trade-off	84
5.2	Final Results	92
5.3	PIV results	95
5.4	Intake Total Pressure Recovery	105
6	Conclusion	108
7	Future Recommendations	110
7.1	Using alternative flow measurement techniques	110
7.2	Performing measurements using Stereoscopic PIV	110
7.3	Performing measurements with different isolator lengths	110
7.4	Applying flow control techniques regarding SBLI	111
7.5	Applying boundary-layer bleed inside the intake isolator	111
7.6	Designing optimal intake geometry	111
A	Technical drawings of submerged supersonic intake model	112
B	Technical drawings of the throttle system	121
C	Test Matrices	129
D	PIV Results	131
E	Performance study	135

List of Figures

1.1	P-800 Oniks (nose intake), Copyright-free.	2
1.2	MBDA Meteor (lateral intakes), Copyright-free.	2
1.3	Comparison of lateral intakes with submerged intakes.	3
2.1	Process of pressure recovery in an air intake, taken from Seddon and Goldsmith [13].	7
2.2	Relationship between η_f and η_p as a function of the freestream Mach number M_∞ , taken from Goldsmith and Seddon [13].	8
2.3	Schematic of a ramjet engine with labeled flow stages and engine compartments, Copyright-free.	9
2.4	Variation of thrust coefficient with pressure recovery for different Mach numbers, taken from Faget [16].	12
2.5	Variation of thrust coefficient Mach numbers, taken from Faget [16].	12
2.6	Schematic of an internal-compression intake operating with a detached normal shock illustrating the rise of the additive drag, taken from Cronvich and Faro [14].	13
2.7	Intake external drag as a function of the area capture ratio, taken from Cronvich and Faro [14].	14
2.8	Different drag coefficients as a function of the Mach number for an intake designed to operate at $M = 3$, taken from Cronvich and Faro [14].	14
2.9	Schematic drawing of a shock wave boundary layer interaction with boundary layer separation, taken from Sepahi-Younsi et al. [19].	16
2.10	Schematic representation of a shock wave boundary layer interaction in ramp flow, taken from Verma et al. [20].	16
2.11	Proposed variation of separation lengths (along wind tunnel floor centerline) as a function of wind tunnel inverse viscous aspect ratio, taken from Babinsky et al. [25].	17
2.12	Different stages of the forming of a pseudo-shock, taken from Matsuo et al. [28].	19
2.13	Plots of two curves showing the static pressure envelope over the shock train at the wall region and at the centerline in a constant-area duct with a normal shock wave, taken from Matsuo et al. [28].	19
2.14	Illustration of a pseudo-shock with the characteristic supersonic tongue, taken from Weiss et al. [35].	20
2.15	Schlieren photographs of a shock train where from images (a) to (f) the confinement parameter δ/h was gradually increased, taken from Carrol and Dutton [37].	21
2.16	Relationship between centerline flow Mach numbers at the exit of the isolator extension piece and pressure ratios along the entire isolator length for Mach 1.8 and 2.2 flows and for rectangular and round isolators, taken from Lin et al. [42].	22
2.17	Comparison between measurement and prediction from correlations for centerline flow Mach numbers at the exit of the isolator for Mach 1.8 and 2.2 flows and for rectangular and round isolators, taken from Lin et al. [42].	22
2.18	Schematic drawing of successive shock wave in a shock train after the first encounter with the boundary layer, taken from Tamaki et al. [39].	23
2.19	Wall static pressure distributions in a cylindrical duct where a shock train was introduced, taken from Waltrup and Billig [45].	24
2.20	Boundary layer asymmetry at the duct entrance, taken from Wang et al. [50].	25
2.21	Radial static pressure distributions across a shock train, taken from Nagai [52].	25
2.22	Static pressure ratio across pseudo-shock normalized by that across a normal shock wave versus the upstream Mach number, taken from Matsuo et al. [28].	26
2.23	Influence of the wall friction coefficient on the duct pressure rise, taken from Tu and Segal [57].	27
2.24	Non-dimensional pseudo-shock length in constant-area duct versus the Mach number upstream of the shock, taken from Matsuo et al. [28]	28
2.25	Allowed contraction ratios for constant-geometry supersonic diffusers, taken from Kantrowitz [61].	30

2.26	Theoretical performance of five different supersonic diffusers by design Mach number M_d , taken from Kantrowitz [61].	30
2.27	Experimental performance of three different supersonic diffusers with different entrance cone angles τ , design Mach number M_d and contraction ratio C_R , taken from Kantrowitz [61].	31
2.28	Schematic of the different types of supersonic diffusers, taken from Parker [67]	32
2.29	Total pressure recovery as a function of duct and pseudo-shock lengths, taken from Mahoney [69].	33
2.30	Generic supersonic intake including a boundary layer bleed slot, taken from Bauer and Kurth [77]	35
2.31	Total Pressure recovery (TPR) as a function of the mass flow ratio (MFR), taken from Soltani et al. [79]	35
2.32	Ram and flush boundary layer bleed slots, taken from Sepahi-Younsi et al. [19].	36
2.33	Illustration of the different operating conditions of supersonic intakes, taken from Mahoney [69].	37
2.34	Diagram showing the influence of flow criticality on intake performance, taken from Soltani et al. [83].	38
2.35	Kantrowitz diagram along with isentropic and Kantrowitz limits together with empirical relations, taken from Flock and Gülhan [84]	39
2.36	Effect of frequency of back pressure oscillation on shock wave response: a) $\tilde{f}_r = 80Hz$, $\tau = 0.22$ and b) $\tilde{f}_r = 10Hz$, $\tau = 1.76$, taken from Biedron and Adamson Jr. [86]	40
3.1	Schematic of ST-15 supersonic wind tunnel, taken from Flinkerbusch [89].	43
3.2	Exploded view of the wind tunnel setup without the SSI model.	44
3.3	Isometric view of the wind tunnel setup without the SSI model.	44
3.4	Side view of the wind tunnel setup without the SSI model.	44
3.5	Exploded view of the SSI model.	45
3.6	Isometric view of the SSI model.	45
3.7	Side view of the SSI model.	45
3.8	Isometric view of the cowling.	46
3.9	Side view of the cowling.	46
3.10	Isometric view of the double-shock compression plate.	46
3.11	Side view of the double-shock compression plate.	46
3.12	The shallow regions on the backside of the intake parts. Left: cowling, right: double-shock compression plate.	47
3.13	Streamwise location of the cowling pressure ports, measured from the leading edge.	47
3.14	Streamwise location of the cowling pressure ports, measured from the leading edge.	47
3.15	Connection between expansion block - support pylons - SSI model.	48
3.16	Flow path representation of the SSI model with an indication of the different intake regions.	49
3.17	Exploded view of the throttle system of the SSI model.	50
3.18	Isometric view of the expansion block containing the SSI model and the throttle system.	50
3.19	Side view of the expansion block containing the SSI model and the throttle system.	50
3.20	Overview of the three different butterfly valves used, seen from both an isometric view and a side view.	51
3.21	Image of the complete actuation system mounted in the wind tunnel, taken from an isometric view.	52
3.22	Isometric view of the complete test setup.	53
3.23	Side view of the complete test setup (3D CAD).	53
3.24	Side view of the complete test setup (real photograph).	54
3.25	This report's test setup integrated into a modern cruise missile.	54
4.1	Deflection of light rays with Snell's law, Copyright-free	57
4.2	Generic Schlieren system setup in the common z-configuration.	58
4.3	Complete three-dimensional CAD view of this report's Schlieren test setup, seen from the port side of the wind tunnel.	60
4.4	Schematic of the experimental static pressure measurement setup.	61
4.5	Three-dimensional view of the pressure measurement test setup, seen from the starboard side.	63
4.6	Image of the pressure setup from the starboard side of the wind tunnel.	63

4.7	Generic example of the PIV working method and processing sequence, taken from Kumara et al. [94].	64
4.8	Particle atomization level plotted against particle diameter, taken from PivPart45 manual [99].	67
4.9	The PivPart45 particle generator used to inject the seeding particles, taken from the PivPart45 manual [99].	67
4.10	Schematic of the wall-normal laser sheet produced on the compression plate.	68
4.11	Schematic of the mirror probe used during the experiments, taken from Donker Duyvis [100].	69
4.12	Three-dimensional CAD view of the wall-normal laser sheet formation parallel to the x-y plane.	69
4.13	Laser components generating and guiding the laser path for the laser sheet formation, from the starboard side of the wind tunnel.	70
4.14	Left: 3D CAD view of the double camera configuration. Right: Schematic of the FOV of the two 105mm-camera's.	71
4.15	Image of the sCMOS camera setup for the PIV campaign.	71
4.16	Schematic representation of the cross-correlation analysis for PIV, taken from the LaVision Davis product manual [103].	72
4.17	Side view of the SSI model featuring the locations with the highest degree of light reflections, indicated with red circles, during the PIV campaign.	73
4.18	Image 1 of a pair, showing the reflections from the laser sheet.	73
4.19	Image 2 of a pair, showing the reflections from the laser sheet.	73
4.20	Image 1 of a pair, after subtracting the Butterworth high-pass filter.	74
4.21	Image 2 of a pair, after subtracting the Butterworth high-pass filter.	74
4.22	Side view of the SSI model featuring the second PIV setup FOVs with the geometric masks indicated by the blue shaded areas.	74
4.23	The histograms of the residual obtained with the conventional median test (a) and the normalized median test (b) for the grid turbulence data at decreasing turbulence levels. The histograms represent at least 99.7% of the vector data, taken from Westerweel and Scarano [104].	76
4.24	Instantaneous velocimetry result of the u-component of the velocity of the image pair of Figure 4.18 and Figure 4.19.	76
4.25	Statistically averaged velocimetry result of the u-component of the velocity of the entire image set.	77
4.26	Final PIV result following the post-processing phase.	78
4.27	Three-dimensional CAD view of the complete PIV test setup, seen from the port side of the wind tunnel.	78
4.28	Schematic of generic wall tapping with the relevant geometry, taken from Tropea et al. [105].	80
5.1	Schlieren image of the SSI model in critical condition showing the different flow features.	84
5.2	Front (left) and aft (right) limits of the oscillation sequence during the critical condition for the airfoil valve.	85
5.3	Mean Schlieren image of the SSI model in the critical condition for the airfoil valve.	86
5.4	Schlieren image featuring the standard deviation of the SSI model in the critical condition for the airfoil valve.	86
5.5	Front (left) and aft (right) limits of the oscillation sequence during the critical condition for the arc valve.	87
5.6	Mean Schlieren image of the SSI model in the critical condition for the arc valve.	87
5.7	Schlieren image featuring the standard deviation of the SSI model in the critical condition for the arc valve.	87
5.8	Front (left) and aft (right) limits of the oscillation sequence during the critical condition for the diamond valve.	88
5.9	Mean Schlieren image of the SSI model in the critical condition for the diamond valve.	88
5.10	Schlieren image featuring the standard deviation of the SSI model in the critical condition for the diamond valve.	89
5.11	Normalized static pressure results vs. streamwise position for all three butterfly valves at the critical condition.	90
5.12	Zoomed in Schlieren image of the pressure orifice locations during the critical condition.	90
5.13	Zoomed in plot of the first four normalized static pressure results vs. streamwise position for all three butterfly valves at the critical condition.	91

5.14	Zoomed in plot of the last three normalized static pressure results vs. streamwise position for all three butterfly valves at the critical condition.	91
5.15	Plot of the SPR of the three valve designs in the critical condition.	92
5.16	Schlieren image and Static pressure plot of the diamond valve in the supercritical condition.	93
5.17	Reflection of a impulse-type wave from a flat surface, taken from Liepmann et al. [114].	93
5.18	Schlieren image and Static pressure plot of the diamond valve in the nearly supercritical condition.	95
5.19	Schlieren image and Static pressure plot of the diamond valve in the critical condition.	95
5.20	Normalized streamwise velocity field of u/V_∞	97
5.21	Normalized vertical velocity field of v/V_∞	97
5.22	Mach plot.	97
5.23	Mach number standard deviation in the critical condition.	98
5.24	Schlieren image, Mach number by PIV and normalized vertical velocity by PIV plots for the supercritical condition.	99
5.25	Schlieren image, Mach number by PIV and normalized vertical velocity by PIV plots for the near-supercritical condition.	100
5.26	Schlieren image, Mach number by PIV and normalized vertical velocity by PIV plots for the critical condition.	101
5.27	Mach number PIV plot for the critical condition with the black contour representing the sonic line of $M = 1$	102
5.28	Relationship between centerline flow Mach numbers at the exit of the isolator extension piece and pressure ratios along the entire isolator length, including this report's experimental result.	103
5.29	Comparison between measured and predicted Mach number ratios from correlations for centerline flow Mach numbers at the exit of the isolator with this report's experimental result.	103
5.30	Static pressure ratio across pseudo shock normalized by that across a normal shock wave versus the upstream Mach number, including a mean trendline and this report's experimental result.	104
5.31	Non-dimensional pseudo shock length in constant-area duct versus the Mach number upstream of the shock, including this report's experimental result.	105
5.32	TPR across the pseudo-shock.	106
A.1	Submerged supersonic intake support block.	113
A.2	Submerged supersonic intake expansion section.	114
A.3	Intake cowling.	115
A.4	Double-shock compression surface.	116
A.5	Intake sidewall.	117
A.6	Upper sidewall strip.	118
A.7	Lower sidewall strip.	119
A.8	Intake support pylon.	120
B.1	Servo bracket (cable side).	122
B.2	Servo bracket (free side).	123
B.3	Pushrod.	124
B.4	Butterfly valve lever.	125
B.5	Butterfly valve (airfoil shape).	126
B.6	Butterfly valve (arc shape).	127
B.7	Butterfly valve (diamond shape).	128
D.1	PIV vector results for the normalized streamwise velocity, normalized vertical velocity and the Mach number for the supercritical condition.	132
D.2	PIV vector results for the normalized streamwise velocity, normalized vertical velocity and the Mach number for the near-supercritical condition.	133
D.3	PIV vector results for the normalized streamwise velocity, normalized vertical velocity and the Mach number for the critical condition.	134

List of Tables

4.1	Overview of the fixed parameters of this test plan's experimental campaign	56
4.2	Detailed list of equipment used for the Schlieren imagery measurement campaign.	59
4.3	Detailed list of equipment used for the pressure measurement campaign.	62
4.4	Detailed list of equipment used for the PIV measurement campaign.	78
4.5	Table reporting the static pressure uncertainty values.	81
4.6	Table reporting the PIV uncertainty values.	82
C.1	Test matrix for the Schlieren imagery and static pressure campaigns	129
C.2	Test matrix for the PIV campaign	130
E.1	Analytical and experimental performance study of the SSI model	135

Nomenclature

Acronym	Full name
CAD	Computer-Aided Design
CCD	Charge-Coupled Device
CMOS	Complementary Metal Oxide Semiconductor
DEHS	Di-Ethyl-Hexyl-Sebacat
F/A	Fuel-to-Air ratio
FOV	Field Of View
FPS	Frames Per Scan
GNC	Guidance, Navigation & Control
MFR	Mass Flow Ratio
Nd:YAG	Neodymium-doped Yttrium Aluminum Garnet
Nd:YLF	Neodymium-doped Yttrium Lithium Fluoride
OSW	Oblique Shock Wave
PIV	Particle Image Velocimetry
PTU	Programmable Timing Unit
RCS	Radar Cross-Section
SBLI	Shock wave-Boundary Layer Interaction
SPR	Static Pressure Recovery
SRIM	Submerged Ramjet Intake Model
SSI	Submerged Supersonic Intake
TNO	Netherlands Organisation for Applied Scientific Research
TPR	Total Pressure Recovery

Latin	Definition	Unit
A	Cross-sectional area	[m ²]
C_T	Thrust coefficient	[-]
D	Intake drag	[N]
d_{diff}	Particle image diameter due to diffraction effects	[m]
d_{geom}	Particle image diameter viewed with geometrical optics	[m]
d_i	Image distance	[m]
d_{lens}	Camera diaphragm aperture	[m]
d_o	Object distance	[m]
d_p	Particle diameter	[m]
d_τ	Particle image diameter	[m]
F_T	Intake thrust	[N]
f	Focal distance	[m]
$f_\#$	F-stop	[m]
f_{scan}	Static pressure scan rate	[Hz]
\bar{I}	Cross-correlation intensity peak	[-]
l_{FOV}	Field of View size	[m]
l_{pix}	Pixel size	[m]
M	Mach number	[-]

\bar{M}	Magnification factor	[-]
\dot{m}	Mass flow	[kg/s]
N_{pix}	Number of pixels	[-]
n	Refraction index	[-]
P	Total pressure	[bar]
ΔP	Loss of total pressure	[bar]
p	Static pressure	[bar]
q	Dynamic pressure	[bar]
Re	Reynolds number	[-]
S_k	Particle Stokes number	[-]
s_{pix}	Particle average displacement	[m]
s	Light ray path length	[m]
T	Temperature	[K]
t	time	[s]
Δt	Pulse separation time	[s]
δt	Pulse duration time	[s]
u_f	Flow velocity	[m/s]
u_p	Seeding particles velocity	[m/s]
u_s	Particle slip velocity	[m/s]
V	Velocity	[m/s]
x	Streamwise coordinate	[m]
y	Vertical coordinate	[m]
z	Out-of-plane coordinate	[m]
Δz	Laser sheet thickness	[m]
δz	Focal depth	[m]

Greek**Definition****Unit**

γ	Ratio of specific heats	[-]
δ	Boundary layer thickness	[m]
η_{cc}	Combustion efficiency	[-]
η_f	Total pressure recovery at engine face	[-]
η_{fi}	Total pressure recovery at engine face (incompressible)	[-]
η_K	Intake efficiency	[-]
η_{KE}	Engine kinetic efficiency	[-]
η_n	Nozzle efficiency	[-]
η_P	Total pressure recovery at engine face (compressible)	[-]
η_R	Pre-combustion total pressure recovery	[-]
θ	Expansion angle	[rad]
λ	Laser wavelength	[m]
μ	Fluid dynamic viscosity	[kg/(m · s)]
ν	Prandtl-Meyer angle	[rad]
ρ	Fluid density	[kg/m ³]
σ	Standard deviation	[Variable-dependent]
τ_p	Seeding particle response time	[s]
ϕ	Cross-correlation coefficient	[-]
χ	Limiting contraction ratio	[-]

Subscript**Definition**

0	Stagnation conditions
∞	Freestream conditions
1 or c	Intake capture station
2 or f	Engine face station
3	Post-combustion station
e	Engine exit station
pix	Pixel characteristic

1

Introduction

1.1. Prologue

The field of missile warfare has seen tremendous developments in recent years [1]. Investments made by defense contractors rise every year, which eventually lead to the supersonic cruise missiles segment to hold the largest market share as of 2019 [2]. Most of the money involved is allocated to finding optimal solutions for contemporary design challenges for cruise missiles, including greater firing ranges and capabilities to store larger amounts of fuel. The limiting factor to the above specific goals has a common denominator: Oxidizer. Classical rocket motors require sufficient oxidizer to burn fuel. This limits the amount of fuel that can be stored in cruise missiles to make sure enough oxidizer can be stored as well. At the same time, running low on oxidizer will lower the missile's potential firing range. Since ramjet propulsion solves both issues, there is an increasing interest in utilizing ramjet engine technology on supersonic artillery rounds instead of standard rocket engines.

The adoption of ramjets in advanced weaponry, such as cruise missiles, is not a new approach. The use of ramjets can be traced back to WWII. During this global warfare, specific designs were made for ramjet-powered projectiles to be used for artillery combat with a firing range of 350 [km] [3]. Ramjets do not require any stored oxidizer since air is continuously drawn from the ambient atmosphere to burn fuel. This allows missile designs to have less weight, cover larger distances and use the remaining weight for more payload or speed. Since modern cruise missiles have an operational Mach number range between 2 and 4, ramjets form an excellent option for integration into modern cruise missile designs, since the performance of ramjets is optimal within the above Mach number range due to natural compression by the inlet being sufficiently high [4]. However, to ensure that missiles can be stored inside artillery gun barrels and other weapon bays, the missile's form factor is a crucial parameter to indicate whether the missile's shell would fit inside any weapon storage location.

Ramjets operate by compressing the incoming flow using multiple shock waves or compression fans, after which the compressed air is fed into the combustion chamber. From classical aerodynamical considerations, the intake is placed at the nose of the projectile if the weapon system allows it. This is by convention the first choice since this allows the intake to capture the undisturbed freestream flow and it will also reduce the frontal area of the weapon system, resulting in a lower drag profile [5]. However, since many modern missile designs allocate their guidance, navigation and control (GNC) systems at the nose, this location becomes unsuitable for the intake, especially for extended-range missiles. This completely eliminates the possibility of installing the intake in this way. Alternatively, missile designs have their intakes placed at the sides of the missile's fuselage. In [Figure 1.1](#) and [Figure 1.2](#), an example is shown of when the intake is placed at both the nose and laterally next to the fuselage, respectively. Lateral placement of the intakes causes the projectile to be wider, which affects the form factor [6]. This does not only worsen the missile's drag profile (due to an increased cross-sectional area), but this also aggravates the storage possibilities of the missile onboard an aircraft's weapon bay, such as the F-35 Joint Strike Fighter, or inside an artillery barrel. In addition, one has to be aware that the freestream flow's interference with the fuselage also adds to another penalty point for this design choice [7, 8].



Figure 1.1: P-800 Oniks (nose intake),
Copyright-free.



Figure 1.2: MBDA Meteor (lateral intakes),
Copyright-free.

In the wake of advanced weapon system development, the call for including stealth in advanced weaponry keeps getting bigger. A large number of military responsibilities have become airborne and cruise missiles have become an unmissable element of aerial warfare as the demand for high-tech cruise missiles on fighter jets keeps increasing [9]. Therefore, a lack of stealth capabilities for air-launched cruise missiles may lead to security risks for both personnel and hardware. When connecting this back to the aerodynamical explanation of before, this means that placing the missile's intake laterally next to the fuselage does not fit the strategic demands of this era, since the Radar Cross-Section (RCS) of the missile will be way too high in this case. Strategic challenges posed by the appearance of stealth aircraft, like the F-35 Joint Strike Fighter, include designing an armament of stealth cruise missiles [10]. At the same time, the technology of air defense systems has also seen many improvements [11] which encourages defense contractors and arms industries even more to research the viable possibilities of including stealth among the main design criteria of modern cruise missile designs to counter adversary tactics. When combining the different issues discussed above, the following bullet points can be produced:

- The missile nose is an unsuitable location since this location is primarily dedicated to other subsystems, most notably the GNC hardware of the missile.
- The lateral exterior of the missile is an unsuitable location due to the fact that the missile's form factor becomes unavoidably larger, making it difficult to store missiles in artillery barrels or weapon bays.
- The missile intake shall be designed and placed such that the RCS of the overall projectile is kept at a minimum.

To cope with the design issues discussed above, a state-of-the-art design solution is introduced around which the remainder of this report revolves. This solution involves submerging the missile's intake beneath the fuselage. The intake then flushes with the missile's body, which removes the need of placing intakes that laterally protrude from the projectile's exterior fuselage as was shown in Figure 1.2. In Figure 1.3, a comparison is drawn between lateral and submerged intakes. In Figure 1.3, it can be seen that when lateral intakes capture the freestream flow, also the boundary layer is ingested that has developed over the course of the missile hull. This boundary layer is relatively thick and will have harmful effects on the total pressure recovery of the intake, which is a crucial parameter for an optimal combustion process and therefore for the missile's performance. Some missile designs, like the MBDA Meteor shown in Figure 1.2, solve this issue by placing the intakes at an offset from the missile head and by inserting small gaps in between these parts to remove the boundary layer. Consider the submerged intake shown in Figure 1.3. When the freestream flow reaches the intake opening, the flow is turned inwards which consequently generates a Prandtl Meyer expansion fan. This expansion fan increases the Mach number of the flow, which in turn increases the boundary layer thickness. Since the boundary layer's ingestion cannot be prevented, a solution has to be invented to cripple the boundary layer's harmful consequences on the overall missile performance. One way of achieving this is to remove the thick boundary layer by including a bleed slot as shown in the submerged intake of Figure 1.3. This bleed slot diverts the flow containing the boundary layer from the main flow direction. Afterwards, when the flow enters the submerged intake channel, fresh boundary layers are generated on both sides of the intake channel which do not pose as harmful as the boundary layer diverted using the bleed slot. Since the freestream flow passed through an expansion fan, the Mach number has increased which means that the first shock waves of submerged intakes are going to be stronger in comparison to the shock waves of lateral intakes. The latter implies a higher loss in total pressure for submerged intakes, which means that a lower total pressure is found upon entering the combustion chamber.

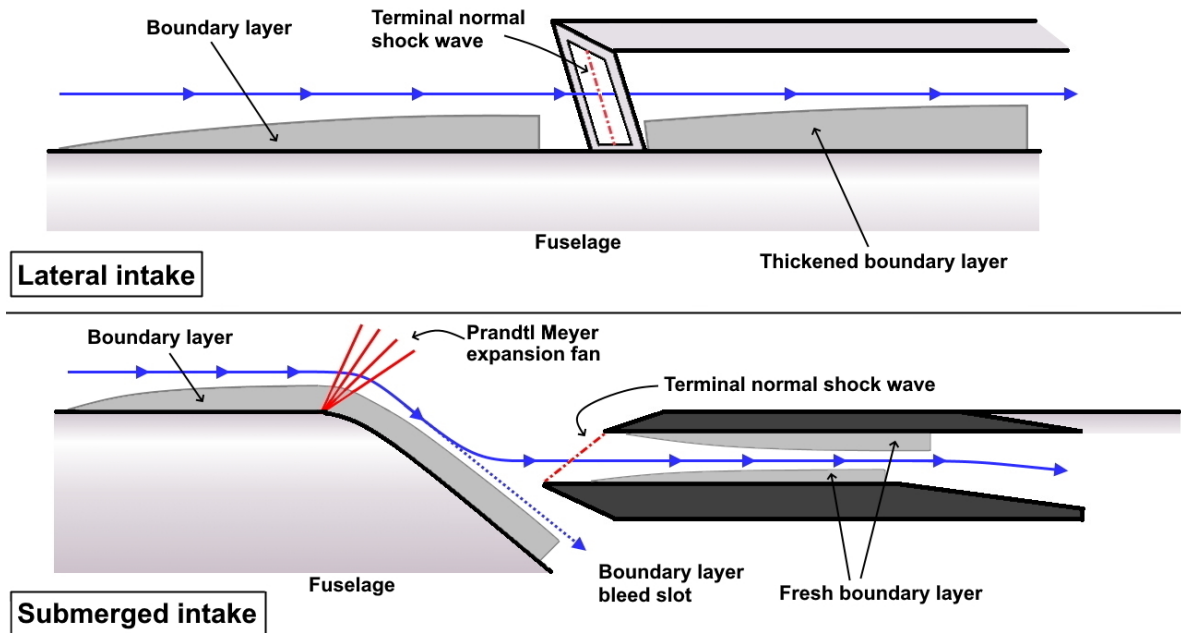


Figure 1.3: Comparison of lateral intakes with submerged intakes.

1.2. Thesis Goal

To gain more insight in the optimal trade-off between the design requirements defined above and the ramjet's performance, experimental analysis is required to verify the theoretical information available on submerged supersonic intakes (SSI) and also to eliminate any confusion on this particular design option from an aerodynamic perspective. A good way to do so is to compare experimental results with a trusted theoretical reference or with other reliable experimental sources. This report aims to apply a method in which a blend of both theoretical and experimental sources are used as a reference. The main theoretical source for SSI was published by Oswatitsch [12], in which an inviscid model was proposed that would form the cornerstone for the future development of SSI. Based on the theory of Oswatitsch, two different research campaigns have been conducted in the past at the request of TNO to investigate the potential advantages of SSI. The first research campaign led to the successful development of the Submerged Ramjet Intake Model (SRIM), which is an analytical computer code which incorporates the possibility of different SSI designs and evaluates how each design would perform from a theoretical perspective. This model was constructed using different validated models that analytically take into account the supersonic flow mechanics inside the intake, including viscous flow effects. Since limited literature is available on SSI at supersonic regimes, and to validate the SRIM, an experimental research campaign was set up to produce the first experimental model for a SSI which would provide empirical results for close comparison with the SRIM. Unfortunately, in this very experimental research campaign the pressure transducers were outdated, resulting in unreliable static pressure readings. Also, due to a lack of velocity measurements inside the intake, the velocity could only be determined using theoretical qualitative methods to first acquire the Mach number in the intake and accordingly the velocity.

Therefore, in light of the results from the previous experimental research campaign, the thesis goal is formulated below.

The objective of this research is to quantify the full flow structure of the Submerged Supersonic Intake model at a Mach 2.0 freestream flow to evaluate the intake performance.

This report will discuss a new research campaign that was initiated to thoroughly investigate the performance of the same experimental model which was used for the last experimental effort. This time however, the research was carried out with state-of-the-art pressure transducers and it included velocimetry measurements. Particular care in this research campaign is given to the influence of viscous flow effects on the submerged intake model performance. Since no decent velocity measurements were made in the previous

research campaign, the particle image velocimetry results of this report contribute to understanding the dynamical flow behavior inside the intake model. This is one of the fundamental outcomes of this report and it is a key milestone along the way in which the question was raised if submerged supersonic intakes will ever become a workable design option for cruise missiles or whether this proposed design will end up in the drawers of history, only to reemerge after decades or generations.

1.3. Research Objectives & Questions

In line with the above breakdown of the problem description, the research goal of this thesis report can be formulated as follows:

To establish an experimental setup that allows for a complete characterization of the aerodynamical effects of viscous flow effects on the overall performance of submerged supersonic intakes and extracting the said information by means of particle image velocimetry, Schlieren images and pressure measurements at Mach 2.0.

With the above research goal in mind, the following research questions and subquestions are established:

1. What information can be gained about the qualitative understanding of viscous flow effects in submerged supersonic intakes at Mach 2.0?
 - (a) What parameters are included in the context of the qualitative understanding of viscous flow effects at Mach 2.0?
 - (b) What information can be gained using particle image velocimetry on the qualitative understanding of viscous flow effects in submerged supersonic intakes at Mach 2.0?
2. What is the most optimal butterfly valve design to obtain proper pseudo-shock occurrences in SSI's at Mach 2.0?
 - (a) What butterfly valve design assures minimal shock oscillations in the submerged intake?
 - (b) What butterfly valve design protects the pseudo-shock from entering the subcritical (unstable) regime?
3. How does the performance of a submerged intake correlate with the results from analytical models?
 - (a) How does the total pressure recovery of a submerged intake correlate with the results from analytical models?
 - (b) How does the Mach-pseudo-shock pressure distribution relation in submerged intakes correlate with the results from analytical models?
 - (c) How does the pseudo-shock pressure ratio in submerged intakes correlate with the results from analytical models?
 - (d) How does the pseudo-shock length in a submerged intake compare with analytical models?

The goal of the first question is to learn more about how viscous flow effects are situated inside submerged intakes. This is done by investigating the realm of qualitative knowledge, especially regarding pseudo-shocks and by exploring the different facets of flow characterization by making use of various measurement techniques to quantify the flow field in which a pseudo-shock is present. The second question serves as a means of trying to find the optimal experimental setup to obtain the closest true-to-nature service conditions for SSI when encountering pseudo-shocks. This is done by investigating different butterfly valve designs to ensure that the wind tunnel flow conditions resemble the ideal service conditions in a more natural fashion. Knowing that the butterfly valve controls the intake's mass flow rate, which is analogous to the intake's supersonic criticality level, and that the critical condition provides the intake with the highest efficiencies, finding the optimal solution to the butterfly valve is a crucial part of this thesis report. Lastly, the final research question is included to complete the research project as a whole, with the main sentiment behind it being the final evaluation of submerged intakes against regular intakes to obtain a margin of judgement on the feasibility of SSI. This is done by comparing the results from the different experimental campaigns on SSI with existing analytical models which were based on generic intakes or geometries to evaluate the discrepancies.

1.4. Scope of this Report

This report is structured in the following manner: [chapter 2](#) takes the reader along the fundamental theory for supersonic intakes, followed by [chapter 3](#) where the complete experimental wind tunnel setup is discussed. Next, [chapter 4](#) covers the theory on flow measurement techniques used in this report and how each campaign is organized. The discussion of the results for all experimental campaigns is reported in [chapter 5](#) which also includes evaluating the performance of SSI. Moreover, the conclusions and recommendations of this thesis report are documented in [chapter 6](#) and [chapter 7](#), respectively.

2

Air Intake Theoretical Background

Before discussing the experimental topics and their outcomes, a firm background on the fundamentals of air intakes has to be established before one can fully comprehend the meaning of the experiments and their results. This chapter forms the paramount building block for the remainder of this document in which an elaborate explanation is provided on the elusive physics that take place in air intakes. Understanding the physics behind intakes will provide more insight into the possibilities and limitations of any intake design in general. Hence, this chapter serves as a point of refreshing our knowledge on the crucial aerodynamics and mechanics that take place in supersonic intakes.

In [section 2.1](#), the basics of intake pressure recovery are discussed. Following, [section 2.2](#) explains the theory of how thrust and drag are related to intake performance. The theory and research on viscous flow effects is dealt with in [section 2.3](#). The generic setup of supersonic intakes is treated next in [section 2.4](#), followed by explanations on proper supersonic intake operation in [section 2.5](#). This chapter is then closed by a brief discussion in [section 2.6](#) on what it takes to submerge the freestream airflow.

2.1. Intake Pressure Recovery

The primary function of intakes is to provide uniform and stable flow, at a proper velocity and pressure, to the engine face, with minimum loss in total pressure. Intakes play a vital role in producing thrust with minimum losses. Proper operation of the combustion process is ensured by incoming air with a sufficient mass flow rate, total pressure and Mach number. In high-speed (supersonic) flight, an intake can be considered to function like a compressor: air is captured at freestream conditions and is converted to a lower Mach number in return for a higher pressure. This is illustrated by [Figure 2.1](#). The static pressure rises from p_∞ at the freestream location to p_f at the engine face. Also, the total pressure drops from P_∞ to P_f . By assuming that the flow at the intake capture station 'c' is uniform, use can be made of the isentropic pressure equation to relate together p_f , P_f and M_f (Mach number at the engine face), which is defined as ([Equation 2.1](#)):

$$\frac{P_f}{p_f} = \left(1 + \frac{\gamma - 1}{2} M_f^2\right)^{\frac{\gamma}{\gamma - 1}} \quad (2.1)$$

where γ is the ratio of specific heats. The efficiency of this pressure recovery process can be defined as ([Equation 2.2](#)):

$$\eta_f = \frac{\text{Work done in compression}}{\text{Kinetic energy available}} \quad (2.2)$$

which for compressible flows becomes ([Equation 2.3](#)):

$$\eta = \frac{\left(\frac{p_f}{p_\infty}\right)^{(\gamma - 1)/\gamma} - 1}{\frac{\gamma - 1}{2} (M_\infty^2 - M_f^2)} \quad (2.3)$$

It is not necessary to know the exact value of M_f as it can be assumed that the compression process is continued isentropically such that P_f will equal p_f , which implies that the M_f term in the denominator of

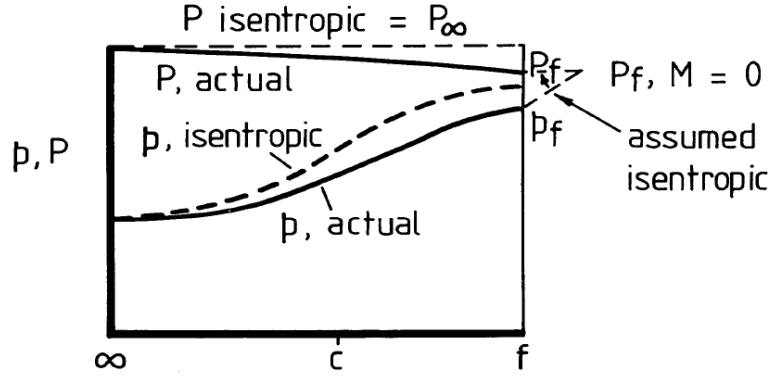


Figure 2.1: Process of pressure recovery in an air intake, taken from Seddon and Goldsmith [13].

Equation Equation 2.3 becomes the kinetic energy initially available. This means that the new equation can be written as (Equation 2.4):

$$\eta_f = \frac{\left(\frac{P_f}{P_\infty}\right)^{(\gamma-1)/\gamma} - 1}{\frac{\gamma-1}{2}(M_\infty^2)} \quad (2.4)$$

which is a function of the total pressure achieved at the engine face and the freestream conditions. For an incompressible process, this equation reduces to (Equation 2.5):

$$\eta_{fi} = \frac{P_f - p_\infty}{q_\infty} \quad (2.5)$$

However, Equation 2.5 only becomes useful for low-speed applications. At higher velocities and particularly for supersonic flows, a better measure for the efficiency can be defined by the ratio of total pressures (Equation 2.6):

$$\eta_P = \frac{P_f}{P_\infty} \quad (2.6)$$

The relationship between the efficiencies found in Equations Equation 2.4 and Equation 2.6 can be related by (Equation 2.7):

$$\left(1 + \frac{\gamma-1}{2}M_\infty^2\right)^{(\gamma-1)/\gamma} \eta_P = 1 + \frac{\gamma-1}{2}M_\infty^2 \eta_f \quad (2.7)$$

This relationship is also illustrated in Figure 2.2. It can be seen that as the freestream Mach number M_∞ tends to zero, the value of η_P approaches unity for all values of η_f . As no real distinction is possible due to this behavior of η_P , it follows that this parameter cannot be used for incompressible flow analysis. Equation 2.5 can therefore be used for incompressible flow analysis, while Equation 2.6 can be used for all other situations. The efficiency as formulated by both equations is commonly known as the pressure recovery of the intake. A lack of efficiency appears as a loss of total pressure with respect to the freestream value. If a loss of total pressure is written as ΔP , the efficiencies can be written as (Equation 2.8):

$$\eta_{fi} = 1 - \frac{\Delta P}{q_\infty} \quad (2.8a)$$

$$\eta_P = 1 - \frac{\Delta P}{P_\infty} \quad (2.8b)$$

In general, loss of total pressure may occur in three possible ways:

- (1) By friction on the walls of the internal duct and on any external surface which is wetted by the flow that enters the duct

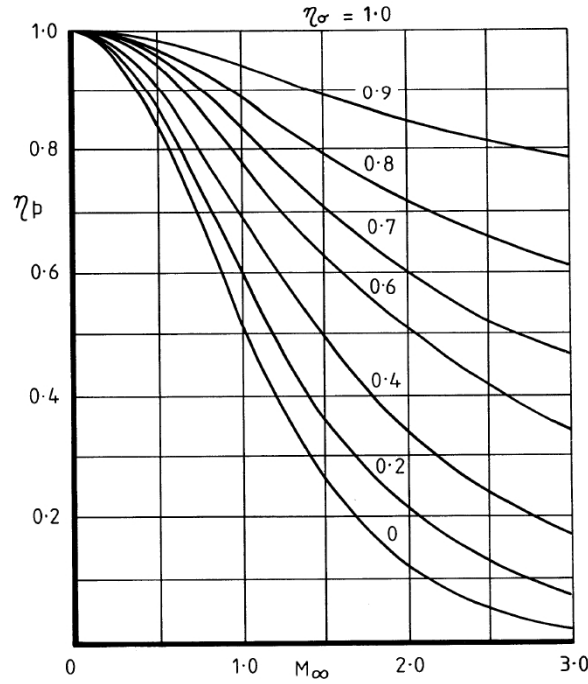


Figure 2.2: Relationship between η_f and η_p as a function of the freestream Mach number M_∞ , taken from Goldsmith and Seddon [13].

- (2) From turbulent mixing, which comes together with flow separation or near-separation
- (3) Through shock waves

Because all of the above causes can be traced back to the dangerous behaviour of the boundary layer, significant care is provided for investigating boundary layer-related problems such as Shock-Boundary Layer Interactions (SBLI), pseudo-shocks and the role of boundary layers in aiding flow separation. Most developments for practical air intakes, including optimizing the pressure recovery, can be associated with gaining new insights on the role of the boundary layer in the intake performance.

According to Cronvich and Faro [14], total pressure loss is composed mainly of the viscous losses and the shock losses, neither of which are amenable to exact calculation. The shock losses may be estimated by knowledge of some of the properties of the shock waves, i.e., whether the shock waves are normal or oblique, the Mach number at which these shocks occur and the streamwise position at which the shocks take place. In actual practice, only the losses through attached bow shocks may be known with any degree of accuracy. The nature of most other shocks is complicated by the interaction of the shock wave and the boundary layer. What is usually considered as a simple normal shock in the throat of an isolator is actually a complex shock system occupying a length many times the equivalent diameter of the intake duct, which is known as the pseudo-shock (more on this in [subsection 2.3.2](#)).

One of the important features of the pressure recovery, which is often ignored when assessing intake performance, is the quality of the flow at the exit, i.e., the pressure (or velocity) distribution over the exit area. This parameter changes significantly during angle-of-attack operation, where large, separated areas may occur in the subsonic ducting. Unevenly distributed mass flow may result in a less efficient combustion process than with a lower but evenly distributed pressure recovery over the pre-combustor region. An often-used measure of the flow quality is the flow distortion D , is given by ([Equation 2.9](#)):

$$D = \frac{P_{0,max} - P_{0,min}}{P_{0,avg}} \quad (2.9)$$

However, the reader should note that the above expression should also be supplemented by a pressure contour plot in order to make it of real value and to create a solid understanding on the flow behavior and performance.

To understand the effect of pressure recovery on the engine thrust, and consequently on the missile performance, it is important to know the characteristics of the engine in question. Loss of total pressure can be related to loss of engine thrust by the relation (Equation 2.10):

$$\frac{\Delta F_T}{F_T} = K \frac{\Delta P}{P_\infty} \quad (2.10)$$

where F_T is the engine thrust, ΔF_T is the loss in engine thrust and K is a factor that depends on the type of engine. In most cases, K is greater than unity and close to 1.5.

2.2. Supersonic Air Intake Fundamentals

After showing how air intakes operate based on fundamental physical principles, proper explanation can be provided on the mechanics of supersonic intakes which will be considered benchmark physics to any submerged supersonic intake design.

2.2.1. Missile Thrust

Since supersonic intakes form the preliminary phase to any high-speed engine, it is considered a good start to first view the thrust equations to find more on the role that intakes play in engine operations. To derive the thrust equations, use will be made of Newton's second and third laws of motion. In the case of air intakes, by using Newton's third law one can reason that when a vehicle is pushed forward, another force must be acting with equal magnitude in the opposite direction. In ramjets, this happens by the mass of air that is captured and accelerated. Deriving the thrust equation using Newton's second law and knowing that in ramjets both mass and velocity are a function of time, the engine thrust can be defined as (Equation 2.11):

$$F_T = \frac{d(mV)}{dt} \quad (2.11)$$

where m denotes the mass of the airflow captured by the engine and V is the velocity of the same airflow, For the time-rate of change of airflow mass, commonly known as the mass flow, one may write that this may be written as (Equation 2.12):

$$\dot{m} = \frac{dm}{dt} \quad (2.12)$$

This means that the new equation for engine thrust can be rewritten to (Equation 2.13):

$$F_T = \dot{m} \frac{dV}{dt} \quad (2.13)$$

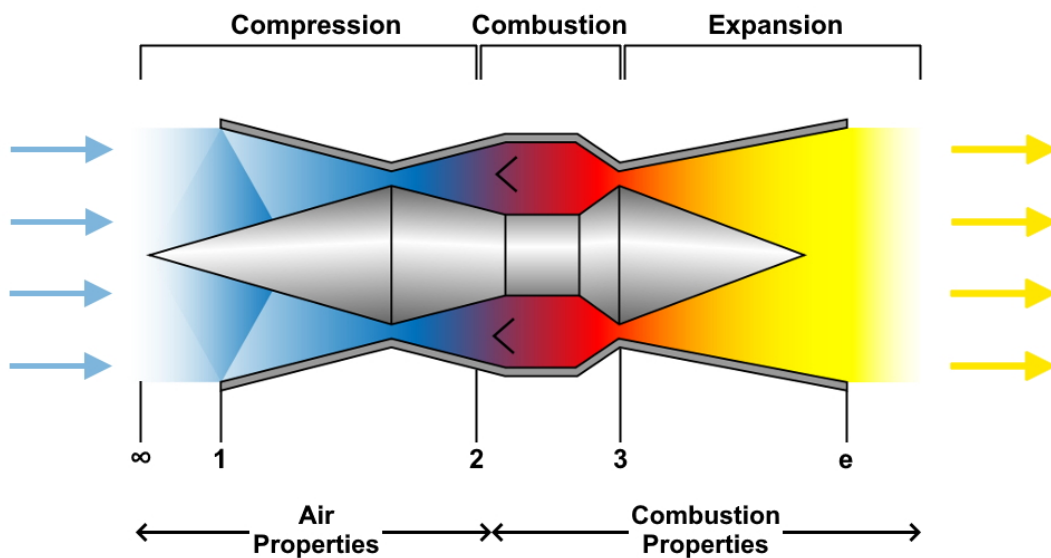


Figure 2.3: Schematic of a ramjet engine with labeled flow stages and engine compartments, Copyright-free.

Using the different stages of a ramjet as illustrated in [Figure 2.3](#) in combination with [Equation 2.13](#), the thrust over a ramjet can be defined as ([Equation 2.14](#)):

$$F_T = \dot{m}_e V_e - \dot{m}_\infty V_\infty \quad (2.14)$$

To account for the net thrust, two things are still missing: the first being that the mass flow at the ramjet exit is equal to the mass flow entering the ramjet at station ' ∞ ' plus the fuel that was added in the combustion chamber. Secondly, the pressure difference at the ramjet's exit also contributes to the net thrust. Therefore, the net engine thrust can be formulated as ([Equation 2.15](#)):

$$F_{T_n} = \underbrace{(\dot{m}_\infty + \dot{m}_{fuel}) V_e}_{\text{Ram drag}} + \underbrace{(p_e - p_\infty) A_e - \dot{m}_\infty V_\infty}_{\text{Gross thrust}} \quad (2.15)$$

where A_e is the nozzle cross-sectional area at the missile exit. In this equation the first term is known as the ram drag and the last two terms are grouped together as the gross thrust. The ram drag is better known as the drag caused by the deceleration of the airflow into the engine. To prevent over- or under-expansion of the jet flow leaving the engine, the pressure difference between engine exit and ambient conditions is kept as low as possible, which implies that the contribution of the pressure -area term to the net thrust is relatively small. This means that achieving a high thrust will require a high mass flow and high pressure recovery. A higher thrust is attained by increasing the velocity difference between the entrance and exit of the engine, which in turn requires a high pressure at the ramjet entrance. A high pressure recovery will also lead to a large velocity increase.

2.2.2. Thrust coefficient

To use the thrust force to compare with other air intakes, this thrust force should first be non-dimensionalized. The equations presented in this report with which thrust can be non-dimensionalized are taken from Wittenberg's vast research on ramjet performance [15]. First, it is assumed that an ideal ramjet is considered in this report's derivation, which implies the following:

- The mass flow of the fuel is relatively small compared to that of the airflow, hence the term \dot{m}_{fuel} is dropped from [Equation 2.15](#)
- The ramjet's exhaust nozzle is assumed to have optimal expansion, meaning that the static pressure in the nozzle equals the ambient pressure ($p_e = p_\infty$). This means that the pressure-area term is dropped from [Equation 2.15](#).

Hence, the final equation for the net thrust can be written as ([Equation 2.16](#)):

$$F_{T_n} = \dot{m}_\infty (V_e - V_\infty) \quad (2.16)$$

Non-dimensionalizing with the dynamic pressure q_∞ and the area of the streamtube at the ramjet's entrance A_∞ , one may rewrite the above to ([Equation 2.17](#)):

$$C_T = \frac{F_{T_n}}{q_\infty A_\infty} = \frac{\dot{m}_\infty (V_e - V_\infty)}{\frac{1}{2} \rho_\infty V_\infty^2 A_\infty} \quad (2.17)$$

The mass flow can also be written as ([Equation 2.18](#)):

$$\dot{m}_\infty = \rho_\infty A_\infty V_\infty \quad (2.18)$$

Knowing the above relation for the mass flow, [Equation 2.17](#) can be rewritten to ([Equation 2.19](#)):

$$C_T = \frac{\dot{m}_\infty (V_e - V_\infty)}{\frac{1}{2} V_\infty \dot{m}_\infty} = 2 \left(\frac{V_e}{V_\infty} - 1 \right) \quad (2.19)$$

The paper by Wittenberg also derives the thrust coefficient in terms of the total kinetic energy and heat input. That particular derivation is omitted here, but can be found in [15]. Doing so, one may write ([Equation 2.20](#)):

$$C_T = 2 \left(\sqrt{\frac{T_{t_3}}{T_{t_\infty}}} \eta_{KE} - 1 \right) \quad (2.20)$$

where the heat input T_{t_3}/T_{t_0} is given in terms of the total temperature ratio of post-combustion chamber conditions to freestream conditions. The kinetic efficiency η_{KE} can be defined as the product of three individual efficiencies and can be written as (Equation 2.21):

$$\eta_{KE} = \eta_{cc}\eta_K\eta_n \quad (2.21)$$

where the efficiencies on the right-hand side can be defined as (Equation 2.22):

$$\eta_R = \frac{p_{t_2}}{p_{t_\infty}} \quad (\text{Pre-combustion total pressure recovery}) \quad (2.22a)$$

$$\eta_K = 1 - \frac{1}{\frac{\gamma-1}{2} M_\infty^2} \left(\frac{1}{\eta_R^{\frac{\gamma-1}{\gamma}}} - 1 \right) \quad (\text{Intake efficiency}) \quad (2.22b)$$

$$\eta_{cc} = 1 - \frac{\left(\frac{p_{t_3}}{p_{t_2}}\right)^{-\frac{\gamma-1}{\gamma}} - 1}{\eta_R^{\frac{\gamma-1}{\gamma}} \left(1 + \frac{\gamma-1}{2} M_\infty^2\right) - 1} \quad (\text{Combustion efficiency}) \quad (2.22c)$$

As can be clearly seen from Equation 2.22b and Equation 2.22c, both the intake and combustion chamber efficiencies are dependent on the freestream Mach number. The combustion chamber efficiency is also dependent on its own total pressure ratio. Since the derivation of this last efficiency did not consider proper thermodynamics, a typical estimate for the total pressure loss in the combustion chamber is roughly $p_{t_3}/p_{t_2} = 0.98$. Also, the exhaust nozzle efficiency η_n , which is beyond the scope of this report, is crucial to remember since this quantity directly influences the thrust coefficient. A typical value for η_n is 0.98.

The only part which has not been discussed yet in Equation 2.19 is the heat input. Estimating this quantity however is not trivial. Therefore, Wittenberg derived the following general form [15] which eliminates the heat input from the comparison (Equation 2.23):

$$\frac{\frac{C_T}{2} + 1}{\sqrt{\frac{T_{t_3}}{T_{t_0}}}} = \sqrt{\eta_{KE}} \quad (2.23)$$

2.2.3. Ramjet Thrust Performance

A typical ramjet performs as is shown in Figure 2.4. This figure features the variation of the thrust coefficient with pressure recovery for several Mach numbers. The work of Faget [16] confirmed the theory discussed in section 2.1, which showed that the pressure recovery declines for increasing Mach numbers. Also, it shows how valuable the pressure recovery is due to the fact that a higher pressure recovery can be translated as a more efficient operation, thus resulting in a higher thrust coefficient value.

In addition, the rich and lean fuel-air ratio (F/A) limits should not be exceeded as shown in Figure 2.5, nor should the ramjet be operated in the region of diffuser "buzz." Shown in this graph are also the lines of constant pressure recovery and the limits of both the pressure recovery and stoichiometric F/A at sea level conditions. General practice has been to accomplish the regulation of fuel rate by some type of F/A meters. However, metering of F/A has many disadvantages. This is because the engine thrust is not a unique function of the F/A. In fact, for a given F/A the thrust will vary with free-stream temperature, pressure, Mach number and combustion efficiency, where the latter varies with the temperature and pressure in the combustion chamber.

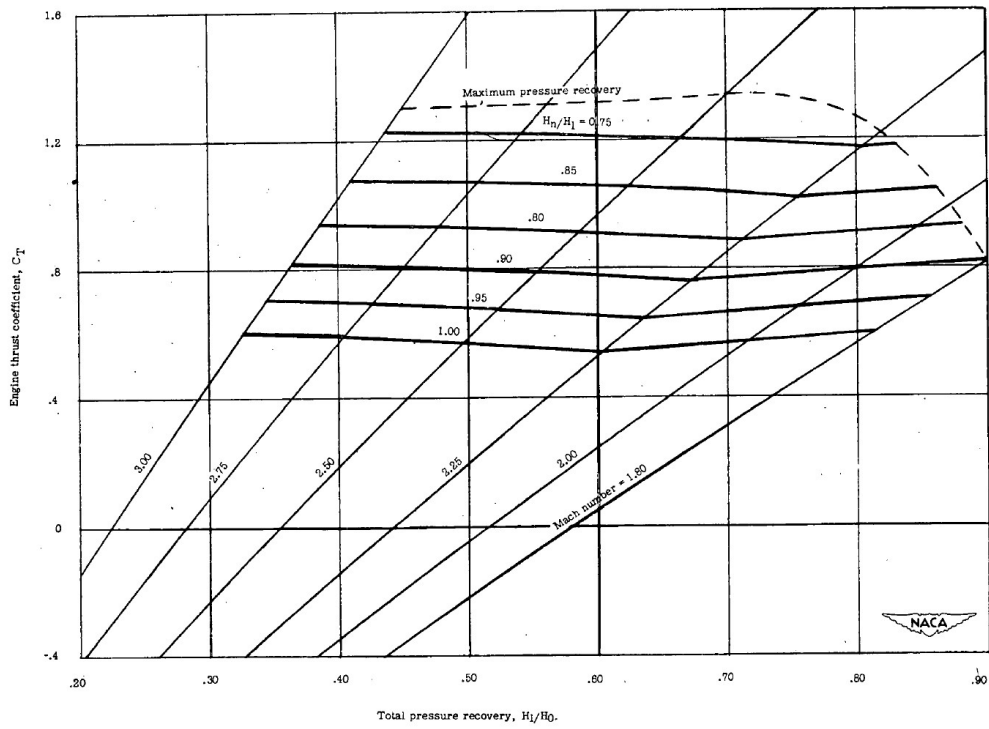


Figure 2.4: Variation of thrust coefficient with pressure recovery for different Mach numbers, taken from Faget [16].

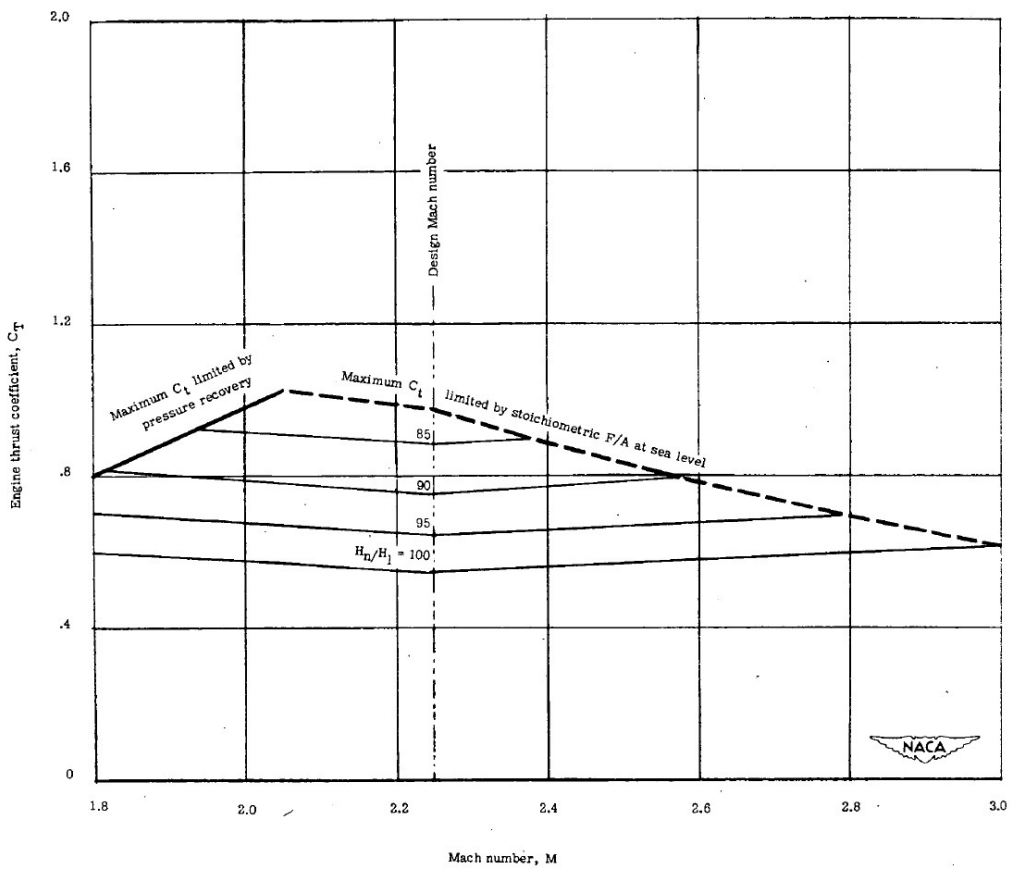


Figure 2.5: Variation of thrust coefficient Mach numbers, taken from Faget [16].

2.2.4. Intake Drag

Like for all aerospace-related applications, the merit of intakes is also assessed by its total drag. The first component of the total drag is that of the cowl itself and is made up of the wave drag and skin-friction drag. The theoretical cowl drag is based on a sharp lip and must be corrected for the presence of a blunt lip where one is used. The change in cowl drag, which is caused due to spill-over at various angles of attack, is usually found experimentally.

Another component of the spill-over drag is known as the additive drag, D_A and is the sum of the pressure forces acting parallel to the axis along the streamlines AB shown in Figure 2.6. When $A_0 = A_1$, meaning when there is no spill-over, there is also no additive drag. The additive drag is usually kept relatively small in the supercritical regime, i.e. for a swallowed shock, by suitable diffuser design, but in the subcritical regime of operation, i.e. for an expelled shock, it rises rapidly with increased spill-over and accounts for a large part of the subcritical drag.

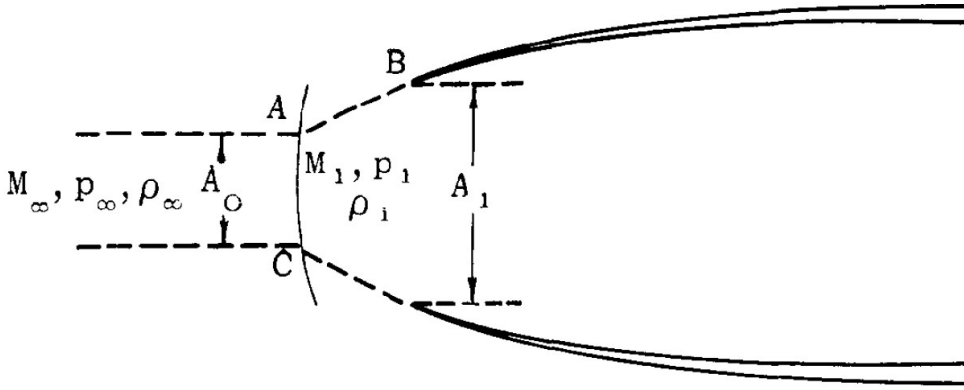


Figure 2.6: Schematic of an internal-compression intake operating with a detached normal shock illustrating the rise of the additive drag, taken from Cronvich and Faro [14].

Application of Newton's second law of motion to the flow shown in Figure 2.6 gives (Equation 2.24):

$$A_0 p_\infty + D_A - A_1 p_1 = \rho_1 A_1 V_1^2 - \rho_0 A_0 V_0^2 \quad (2.24)$$

Since the additive drag will ultimately be combined with the cowl drag, it is necessary that the pressures for both drag components are considered on the same basis, referring to the differences between the measured pressure and the freestream static pressure p_∞ . Using this, Equation 2.24 can be rewritten to (Equation 2.25):

$$D_A = p_\infty A_1 \left[\frac{p_1}{p_\infty} (1 + \gamma M_1^2) - 1 - \gamma \frac{A_0}{A_1} M_\infty^2 \right] \quad (2.25)$$

Assuming that the shock is normal to the freestream direction over the cross section AC, it is possible by means of normal-shock and isentropic-flow tables to calculate D_A from Equation 2.25 in terms of A_0/A_1 , the known freestream conditions and the known value of A_1 . In Figure 2.7, the total external drag is shown at zero angle of attack and at a constant Mach number as a function of the area capture ratio A_0/A_1 . One may remark from this figure how rapidly the additive drag increases with increased spill-over.

In addition, Figure 2.8 shows the typical variation of the drag components for supersonic flow as a function of Mach number for an isolator designed to operate at $M = 3$.

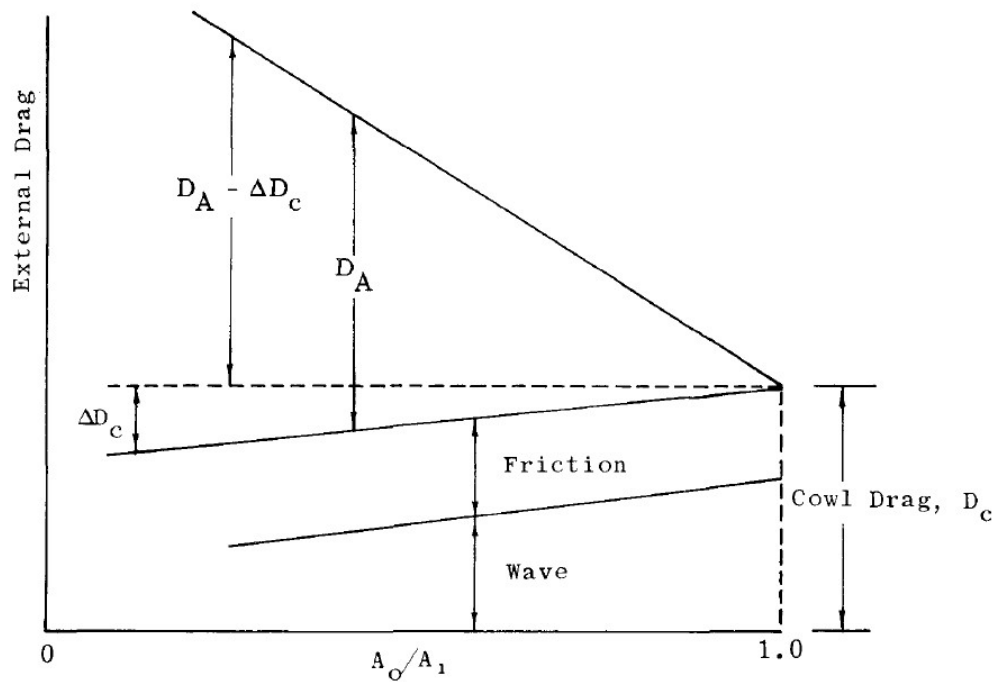


Figure 2.7: Intake external drag as a function of the area capture ratio, taken from Cronvich and Faro [14].

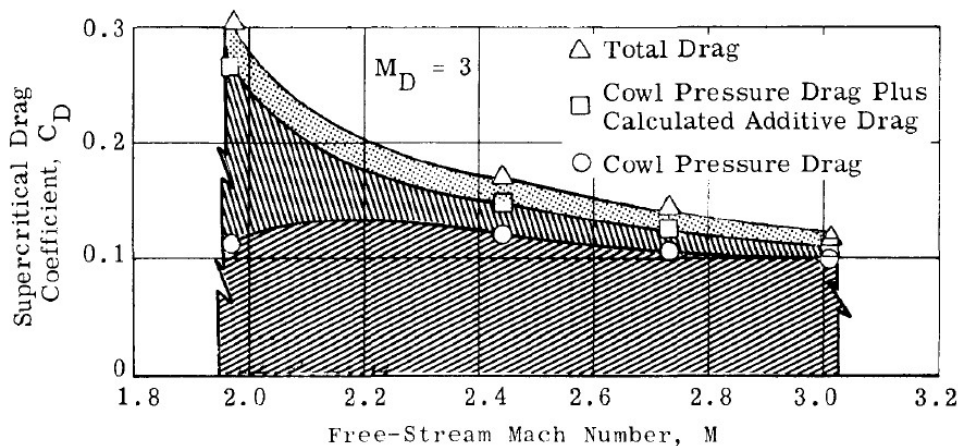


Figure 2.8: Different drag coefficients as a function of the Mach number for an intake designed to operate at $M = 3$, taken from Cronvich and Faro [14].

2.3. Supersonic Viscous Flow Effects

The real challenge every designer has struggled with to maintain sufficient performance over the entire mission envelope for supersonic missiles all comes down to viscous flow-induced shock phenomena. Many difficulties still exist from two closely-related viscous flow phenomena, which are the shock wave-boundary layer interaction (SBLI) and the pseudo-shock, which emanates from the SBLI. Nonetheless, since the 1950s scientists have performed numerous experiments and wind tunnel tests to investigate the essential characteristics of these viscous flow effects and how these could be potentially treated [17]. This also confirms, in light of the goal mentioned at the very start of this report, why a separate section was dedicated to this topic. This section discusses both SBLI in [subsection 2.3.1](#) and pseudo-shocks in [subsection 2.3.2](#). Only pseudo-shocks are discussed in more detail since the obscurity around it makes it more important to get a solid grasp of this topic.

2.3.1. Shock Wave-Boundary Layer Interactions

Supersonic flows are inevitably the seat for shock waves generated by a change in either slope or back pressure. According to Délerly [18], shock waves occur in a variety of applications ranging from early transonic regimes to highly supersonic or even hypersonic conditions. In some cases, shock waves impinge body surfaces on which a boundary layer develops. Here, a complex interaction takes place which always causes strong dissipative and destabilizing effects. Even if the consequences are not extreme, the interaction is generally strong enough to raise amplification of the viscous effects such that the real flow will differ considerably from the perfect fluid model used to define the intake body. It should also be noted that if SBLI are not controlled sufficiently, shock-induced separation may take place in supersonic intakes which usually leads to heavy penalties regarding intake performance, not to mention that there will also be high chances of intake unstart which was confirmed by Dolling [17].

This shows why this phenomenon requires serious attention and why the designer of supersonic intakes has to be fully aware of this aspect to ensure no detrimental effects attain dominance during service to safeguard a secure mission envelope with sufficient performance and minimal losses.

Theory of SBLI The presence of shock waves encompasses the existence of discontinuities and regions of high gradients (which are essentially the shock waves themselves) and the shear layers resulting from the interaction with the developed boundary layer. According to Délerly [18], these high gradients trigger the viscous terms producing entropy, which renders the shocks as a source of high drag:

- Drag caused **directly** by entropy generation in the thickness of the shock. This is known as the *wave drag*
- Drag caused **indirectly** by enhancement of the dissipation in the boundary layers. This is an amplification of the *viscous drag*

This causes the entire flowfield to be altered by means of causing a sudden retardation of the flow, with subsequent thickening and potentially separation of the boundary layer. The severity of this interaction is mainly a function of the upstream Mach number and the Reynolds number related to the boundary layer thickness; more on this later. A classical situation for SBLI is shown in Figure 2.9. Here, one can see an incoming oblique shock wave (OSW) impinging on the boundary layer. The tremendous pressure rise across the OSW will act as an adverse pressure gradient imposed on the boundary layer, causing the boundary layer to separate locally. Due to the fact that subsonic flow cannot create a discontinuous pressure change, the OSW cannot penetrate the subsonic layer of the boundary layer. This subsonic layer is situated beneath the sonic line of the flow (see Figure 2.9). What happens is that the pressure differential between the flow up- and downstream of the shock wave stretches, which increases the thickness of the subsonic layer. Since the high pressure downstream of the shock feeds upstream through the subsonic portion of the boundary layer, the local separation of the boundary layer takes place upstream of the incident shock impingement point. The act of separation of the local flow causes thickening of the subsonic layer. This in turn will cause the flow to be deflected upstream, resulting in the creation of Mach waves. When these smaller waves combine, they form a separation shock that originates slightly upstream of where the OSW impinges the boundary layer. The boundary layer subsequently turns back to the surface and reattaches. At the reattachment point, a reattachment shock is formed by several weaker compression waves that merge together as a result of the boundary layer turning into itself. The points of separation and reattachment are indicated in Figure 2.9 by the letters 'S' and 'R', respectively. Between the boundary layer separation and reattachment points, a Prandtl-Meyer Expansion fan is generated as a result of the boundary layer turning back to the surface. Downstream of the reattachment point the pressure has substantially increased and the boundary layer has become relatively thin. This causes the post-reattachment region to be an area of high aerodynamic heating.

At a ramp as shown in Figure 2.10, the occurrence of a SBLI contains the same mechanics as discussed for flat surfaces. Again the shock wave imposes a pressure differential across the shock wave for flow up- and downstream and the subsonic layer becomes thicker which causes flow deflection and hence creates Mach waves that combine into a shock wave originating in front of the ramp.

The generic SBLI caused by an impinging OSW and the SBLI produced at the ramp are the two most common occurring instances of SBLI in general supersonic intake theory. For more information on the different types of SBLI, the reader is referred to the work of Babinsky et al. [21].

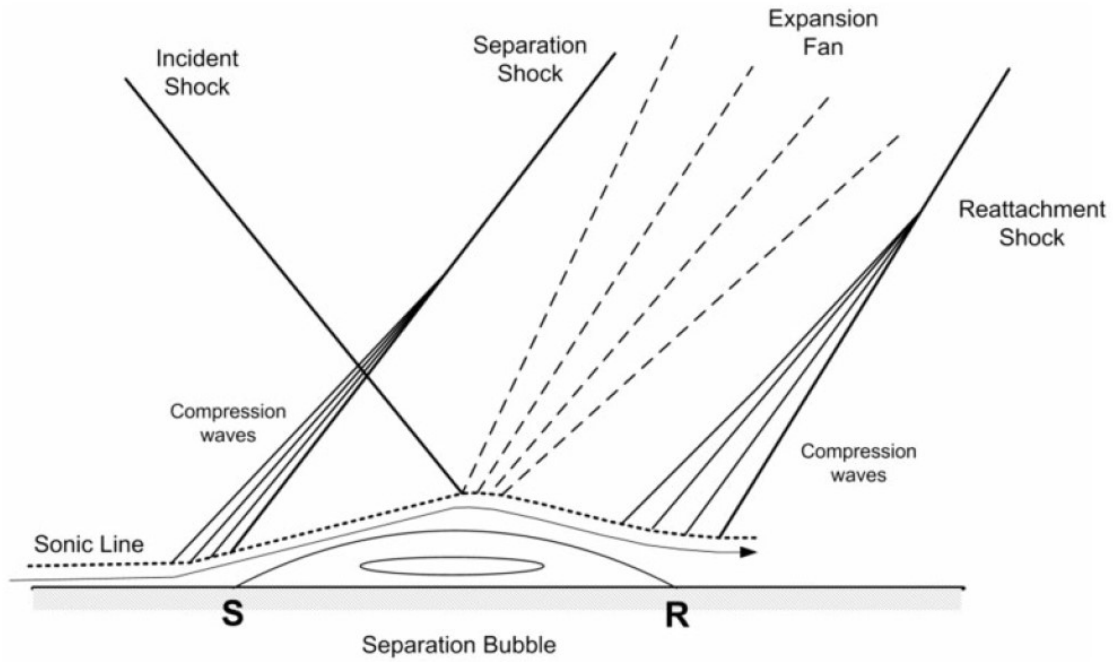


Figure 2.9: Schematic drawing of a shock wave boundary layer interaction with boundary layer separation, taken from Sepahi-Younsi et al. [19].

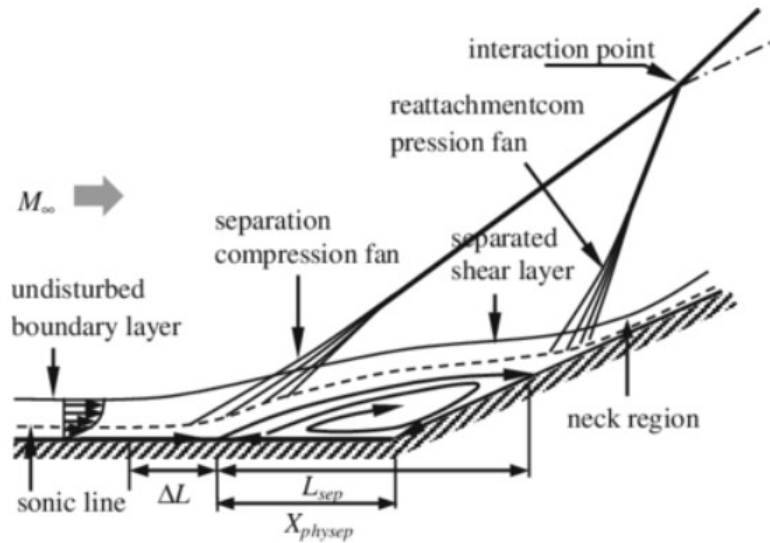


Figure 2.10: Schematic representation of a shock wave boundary layer interaction in ramp flow, taken from Verma et al. [20].

Also, an important note to make is the distinction between the two levels of SBLI, being the weak and strong interaction. The weak interaction will not cause boundary layer separation, while the strong interaction will. For the weak interaction, the flow characteristics can be considered quasi-inviscid, since viscous effects are negligible. For the strong interaction to happen, the point of separation is key to understand the behavior of this interaction, whether it be weak, moderate or strong. Déleroy and Marvin used the Free Interaction Theory [22], which assumes that the flow aspects are independent from the downstream features. Based on this model, an expression was developed by the same gentlemen [23] to determine the limit pressure ratio beyond which boundary layer separation is provoked (Equation 2.26):

$$\frac{p - p_0}{q_0} = \mathcal{F} \left(\frac{x - x_0}{L} \right) \sqrt{2C_f} (M_0^2 - 1)^{1/4} \quad (2.26)$$

where \mathcal{F} is the assumed universal correlation function. For a larger streamwise length x , this function increases. Recalling that the standard definition of the Reynolds number can be written as:

$$Re_x = \frac{\rho V x}{\mu} \quad (2.27)$$

it can be verified that a higher Reynolds number Re_x will consequently cause the limit pressure ratio in Equation 2.26 to increase. This implicitly shows that higher Reynolds numbers (or turbulent flows) are the best candidates for ensuring a larger threshold before separation takes place. However, the antithesis of the Reynolds number in Equation 2.26 is the Mach number. An increase in the Mach number M_0 causes a drop in the limit pressure ratio.

SBLI in Supersonic Intakes To cope with SBLI, one would prefer turbulent boundary layers over laminar ones. This is because turbulent boundary layers are less sensitive to the adverse pressure gradient inside the supersonic intake. Feldmann et al. [24] found that laminar boundary layers on the other hand perform very poor in this perspective and create very large separation bubbles due to the presence of very strong shocks, which increases the chance of flow blockage.

SBLI can be challenging in the sense that the interaction adds negatively to the performance of intakes. This is why it is desired to impair this interaction by various means. One remarkable experiment was conducted by Babinsky et al. [25] to investigate whether the presence and location of corner separations can alter the shape and size of oblique SBLI separation regions. This was achieved by a small amount of suction applied via small slots located on the floor of the working section. To increase the size of any corner separations, rectangular obstacles were placed ahead of the interaction location. The experiments proved that the influence of corner regions reduces with increasing wind tunnel width. With constant wind tunnel size, this is similar to an increase in corner separation. A decrease in corner separation clearly changed the shape of the separated flow in the centre and along the symmetry line of the wind tunnel the separation length was increased considerably. This clarified that if the primary flow experiences a corner shock ahead of the SBLI, the separation would get delayed as a result of the adverse pressure gradient. This final result is shown in Figure 2.11, where it becomes clear that a large wind tunnel inverse viscous aspect ratio will result in the smallest separation distance. The reader can replace in this experiment the wind-tunnel conceptually by the intake, which gives insight into the effect of intake width on the occurrence of SBLI.

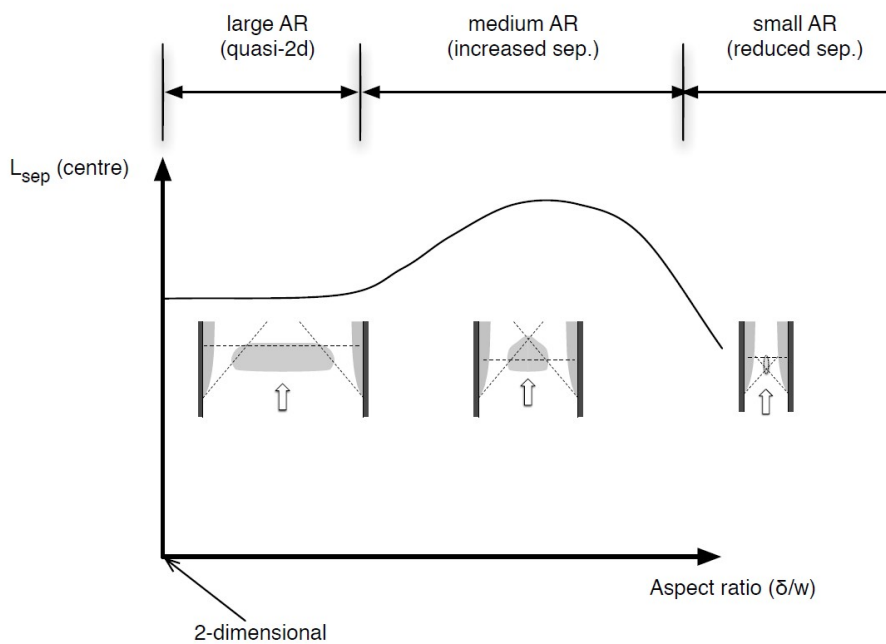


Figure 2.11: Proposed variation of separation lengths (along wind tunnel floor centerline) as a function of wind tunnel inverse viscous aspect ratio, taken from Babinsky et al. [25].

The reader should take note that the control of SBLI is ambiguous, because one can either use control to minimise the effects of shock waves on the boundary layer or to reduce the overall losses caused by the interaction. Therefore, the use of SBLI control never solves the complete problem! One should therefore realize that it becomes crucial, in accordance with the discussion of Kral [26], to conduct a serious design-specific trade-off to learn about what requires optimization in the design to accomplish the design objectives.

In the case of SSI, the knowledge on SBLI will remain of crucial importance and designers might be interested in tweaking with the internal geometry or to add any control options to make a qualitative comparison between the results of these techniques between regular and submerged intakes. For more information on the types and mechanics of SBLI, the reader is referred to the works of Babinsky et al. [17] and Titchener et al. [27].

2.3.2. Pseudo-shock

Since the cradle of supersonic aerodynamics, shock waves have been treated as discontinuities. However, when a shock wave encounters wall surfaces and interacts with the boundary layer on these surfaces, the former statement does not hold anymore. In fact, the shock wave will be characterized by a finite adverse pressure gradient, just as with SBLI. Next to SBLI, another problematic viscous phenomenon in supersonic intakes is the occurrence of pseudo-shocks. Despite decades of research, which was amongst others thoroughly documented by Babinsky [17] and Matsuo [28], pseudo-shocks and their well related shock trains have been poorly understood due to their extremely complex nature and physics. Analogous to SBLI, pseudo-shocks are capable of causing huge losses to intakes, which may even lead to the occurrence of the buzz phenomenon. This is usually the case when a low momentum boundary layer interacts with a stronger shock wave. If no measures are taken, buzz can lead to heavy structural damage or maybe loss of the vehicle. This is why every study on supersonic intake design requires also sufficient attention regarding this phenomenon.

Theory of Pseudo-shocks In many cases of internal supersonic flows, quasi-normal terminal shock waves are formed at a position in the flow passage, as can be seen in Figure 2.12a. This position depends on the pressure imposed up- and downstream, the passage geometry and the wall friction due to viscosity. Crocco [29] stated that in supersonic intakes the deceleration from supersonic to subsonic velocities does not take place through one normal shock wave, but rather through a complex mechanism of shocks following one after the other. This observation was also confirmed by Matsuo et al. [28]. But then what mechanism creates this rather complicated and arduous viscous phenomenon in high-speed intakes?

Consider a supersonic flow moving through a channel. At fairly transonic Mach numbers ($M < 1.2$), the interaction between a shock wave and the boundary layer is so weak that the shock will remain normal to the flow, as can also be seen in Figure 2.12a. This shock wave can be considered a quasi-inviscid normal shock wave and no separation takes place in this case. When the Mach number is increased to about 1.2 or 1.3, the shock wave shape starts to change and gets slightly curved. The interaction between shock wave and boundary layer is still weak, but this time the shock's inclination changes with increasing distance from the walls, as can also be seen in Figure 2.12b. Separation may occur but is not necessarily a must. If it occurs, a strong tendency for reattachment exists. If the Mach number keeps increasing, a normal shock wave with bifurcated ends is observed at the wall. Boundary layer separation starts to become a serious deal from this point onward and there is little to no tendency for reattachment. This is shown in Figure 2.12c. Starting from a Mach number of about 1.5, one or more shock waves are generated as a result of the first normal shock wave with bifurcated ends with the characteristic λ -shape. This becomes clear in Figure 2.12d. As a result of the bifurcated ends of these newly generated shock waves, more and more shock waves keep appearing. The sequence of shock waves in this situation is what is known in today's literature as a shock train [28]. If the Mach number is increased to about $M \sim 1.86$, the λ -shape starts to take on a more χ -shape, which was confirmed by Gnani et al. [30]. According to Heiser and Pratt [31], the approximate Mach number at which the distinction between λ - and χ -shaped shocks becomes the clearest over the entire shock region takes place in the range between Mach 2 and 3.

The flow upstream of a shock train is decelerated and the static pressure increases through the shock train. Behind this shock train, a pressure recovery region is observed. The complete region starting from the first normal shock wave until the end of this pressure recovery region is known as a pseudo-shock.

Extensive research was conducted in the past to learn more about the change in pressure throughout the shock train, observed at the centerline and at the the near wall-region. In Figure 2.13, the result is shown from

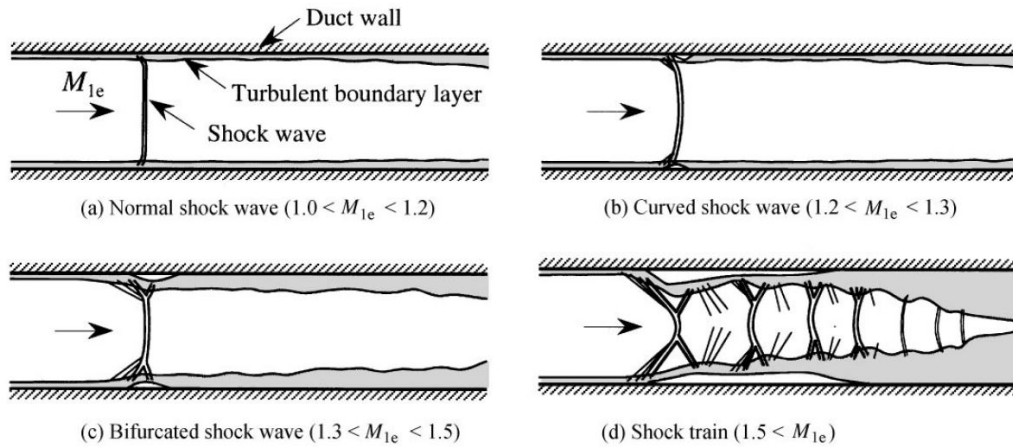


Figure 2.12: Different stages of the forming of a pseudo-shock, taken from Matsuo et al. [28].

the research carried out by Matsuo et al. As becomes clear, the wall pressure increases gradually whereas at the centerline the pressure rises and falls repeatedly due to the presence of successive normal shock waves. After the last normal shock wave, both curves unite and follow the same envelope with the pressure still increasing after this point. Also, it can be observed from Figure 2.13 that the rise in pressure due to the shock train is larger than due to the region behind it, which is known as the mixing region. If at point 'j' the flow becomes fully subsonic, then downstream of this point the pressure should decrease along the duct due to friction effects. However, a shock train is theoretically always followed by the mixing region, where no shock waves are present.

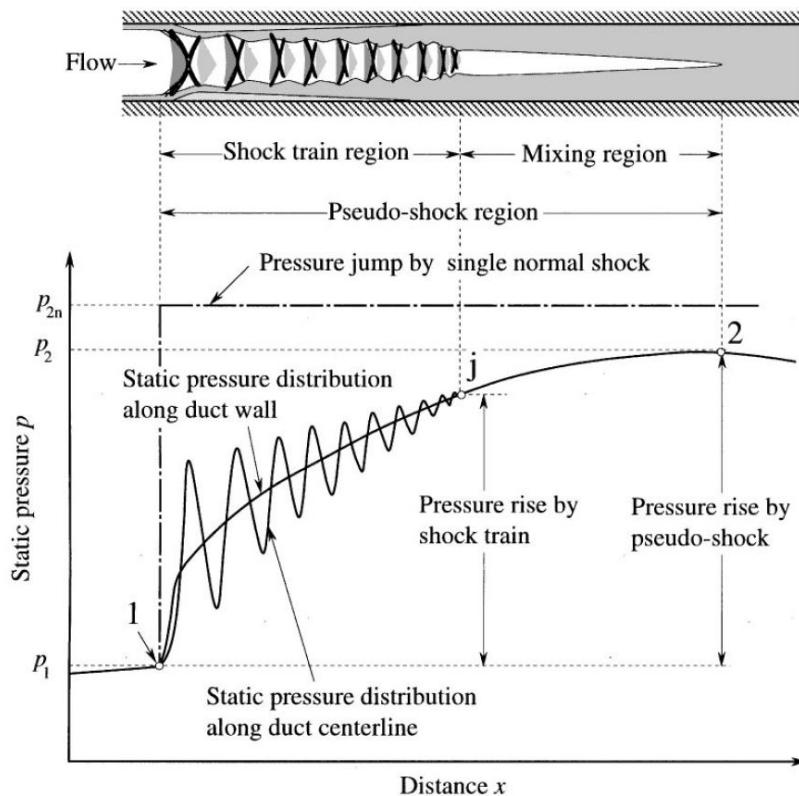


Figure 2.13: Plots of two curves showing the static pressure envelope over the shock train at the wall region and at the centerline in a constant-area duct with a normal shock wave, taken from Matsuo et al. [28].

Instead, this region is characterized by a pressure recovery along the duct length and the pressures at the centerline and at the wall are equal (i.e., a region with an adverse pressure gradient). It is important to note that in practical cases this mixing region only exists if the duct streamwise length is sufficiently large. If not, this mixing region will not occur behind the shock train. This is explained by the fact that a short duct length will cut off the pseudo-shock whilst in the shock train stage, thus preventing the shock train from 'shrinking enough' and generating the mixing region. Another requirement for having a mixing region downstream of the shock train is that the backpressure has to be high enough, which was observed by He et al. [32]. Downstream of this mixing region, the pressure decreases gradually.

A different way of analysing the pseudo-shock was explained by Ostras and Penzin [33], who described the pseudo-shock as a highly complex viscous phenomenon composed of a dissipation layer at the walls and a central, almost isentropic layer at the intake core. Om et al. [34] continues on the latter by adding that the mixing region can be illustrated as a supersonic tongue, consisting of a double-tongue-shaped supersonic flow, which passes through a system of shock waves at the centerline of the channel, bounded by a subsonic outer region. Additional information was provided by Weiss et al. [35], who explained that throughout the shock train region, the flow outside the boundary layer remains supersonic, because only at the center line region, the shocks are strong enough to decelerate the flow below $M = 1$. Weiss et al. also found that in the mixing region, the transition from supersonic to subsonic conditions is a fairly gradual one. This interpretation is schematically shown in Figure 2.14.

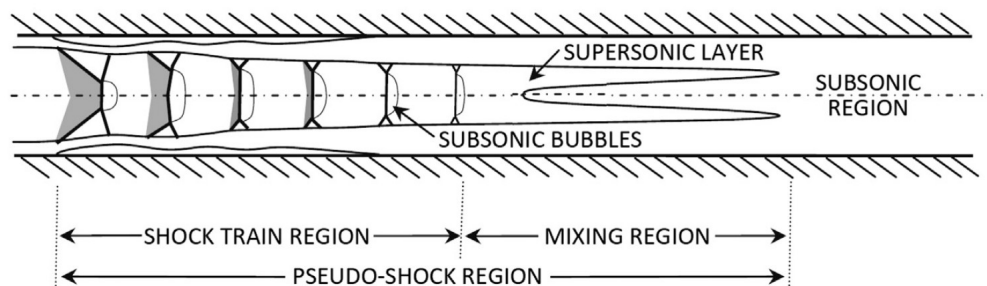


Figure 2.14: Illustration of a pseudo-shock with the characteristic supersonic tongue, taken from Weiss et al. [35].

The reason why this complete viscous incident is called a pseudo-shock stems from the view that this entire envelope, in which shock train and mixing region are considered two combined functions, forms one large and long normal shock wave in a physical way (notably due to the pressure rise). Another point of justification for this name is that the flow starts off supersonic seen in Figure 2.13 in point '1' and ends subsonic as can be seen in point '2' of the same figure. The end of a shock train is not fully subsonic nor supersonic but a mix of sub-supersonic flow with the supersonic portion decelerating the subsonic flow without shock waves. If no boundary layer would be present, the pressure rise would be discontinuous according to a single theoretical normal shock wave and the new pressure after this rise would be a pressure p_{2n} , which is bigger than the actual pressure rise p_2 achieved at the end of a pseudo-shock.

Pseudo-shock Properties Before designing any supersonic intakes, extensive knowledge about the different facets of pseudo-shocks is crucial. First, the shape of the shock train is discussed and its dependence on a variety of parameters is explained. Following, the pseudo-shock Mach number is treated. Next, the static pressure distribution along the pseudo-shock is presented. The static pressure ratio across the pseudo-shock is then briefly addressed and at last some information is provided on the length of pseudo-shocks.

1. Shock train shape The shape of a shock wave in the shock train is determined by the Mach number and boundary layer upstream of the shock train. An interesting parameter for the shock shape is the ratio of the upstream (undisturbed) boundary layer thickness δ against the duct half-height h (or radius for asymmetric geometries). This is known as the flow confinement parameter δ/h . This dependency was first observed by Lustwerk [36], who stated that the shock wave structure changes depending on the variation of this flow confinement parameter. Based on an experiment by Carrol and Dutton [37], where a normal shock wave was generated at a nozzle exit with a shock train lying downstream, it was found that the higher the flow confinement parameter δ/h the more upstream the normal shock is positioned and the larger the distance becomes between two successive shock stations in the shock train. Also, Lin et al. [38] found that as the Mach

number increases, the number of shock waves, the distance between two successive shocks and the length of the shock train all increase too. If the normal shock wave interacts moderately with the boundary layer, then the normal part of this leading shock is still observed in all subsequent shocks as can be seen in Figure 2.15, which depicts Schlieren photographs of the experiments documented in the work of Carroll and Dutton [37]. This is known as a normal shock train. Also, if the Mach number keeps increasing and if the interaction between shock and boundary layer is sufficiently strong, the point of bifurcation at the leading shock moves away from the wall and approaches the duct centerline and thus the shock center. Here, the perpendicularity signature of the shock vanishes and the shock train becomes an oblique shock train. For an oblique shock train, the number of shocks in the shock train and the spacing in between is less sensitive to changes in the flow confinement parameter, which was verified by Carroll and Dutton [37] and Lin et al. [38]. The main difference between a normal and oblique shock train is that for the latter to occur, the Mach number has to be significantly higher, which is around Mach 1.8-2.2 depending on the state of the boundary layer, which was verified by experiments conducted by Tamaki et al. [39] and Ikui et al. [40]. Also, Carroll et al. [41] found that oblique shock trains only occur when the Mach number is high enough and flow confinement is large enough. Since this phenomenon is dependent on the cross-sectional aspect ratio and whether the intake has a circular or rectangular cross-section, no fixed numbers exist as criteria for the occurrence of oblique shock trains.

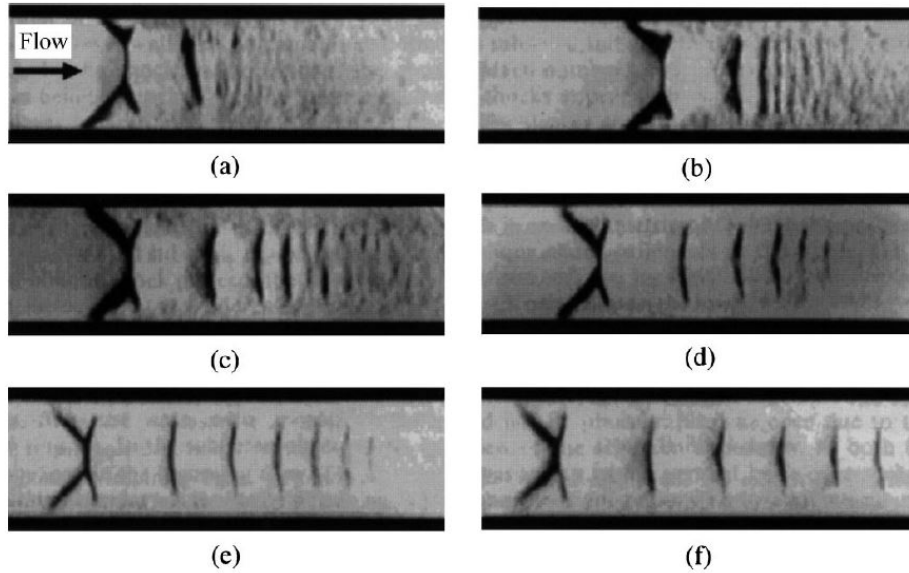


Figure 2.15: Schlieren photographs of a shock train where from images (a) to (f) the confinement parameter δ/h was gradually increased, taken from Carroll and Dutton [37].

2. Shock train Mach number Lin et al. [42] obtained a linear relationship for the centreline Mach number at the duct exit M_{CL} as a function of the pressure ratio over the pseudo-shock wave P_b/P_1 , where the downstream pressure was represented by the backpressure P_b . Although two different correlations were developed for rectangular and circular ducts in Equation 2.28a and Equation 2.28b, respectively, the centreline Mach number linearly decreases with increasing backpressure. Additionally, for a given value of the backpressure, the circular geometry provides higher centreline Mach numbers than for the rectangular geometry. This is also visible in Figure 2.16. The comparison between the predictions made for the Mach number ratio using Equation 2.28a and Equation 2.28b and the actual experimental measurements for the Mach number ratio is shown in Figure 2.17. This clearly illustrates that for different Mach number ratios measured, the correlated Mach number ratio results stay fairly close to the measured Mach number ratio which for different Mach number ratios results in the generation of a linear trendline.

$$\frac{M_{CL}}{M_0} = -1.17M_0^{-2.40} \left(\frac{P_2}{P_1} \right) + 1.78M_0^{-0.64} \quad (2.28a)$$

$$\frac{M_{CL}}{M_0} = -0.94M_0^{-2.20} \left(\frac{P_b}{P_1} \right) + 1.60M_0^{-0.48} \tag{2.28b}$$

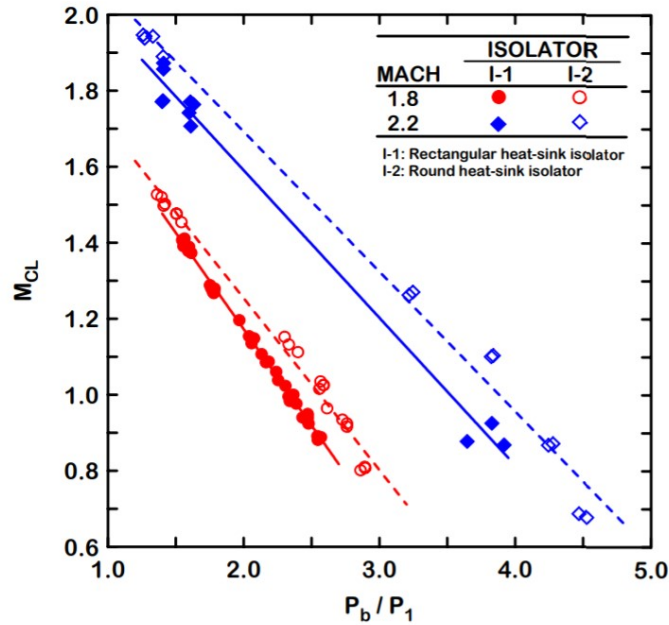


Figure 2.16: Relationship between centerline flow Mach numbers at the exit of the isolator extension piece and pressure ratios along the entire isolator length for Mach 1.8 and 2.2 flows and for rectangular and round isolators, taken from Lin et al. [42].

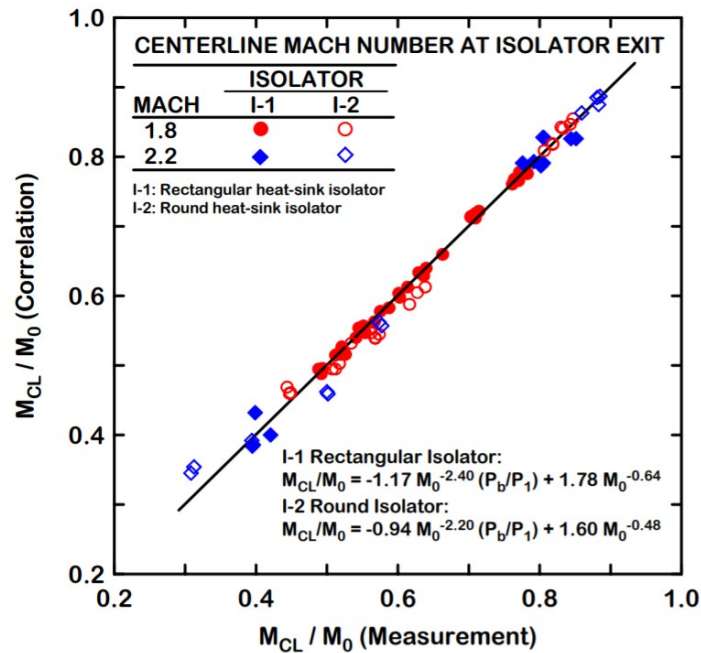


Figure 2.17: Comparison between measurement and prediction from correlations for centerline flow Mach numbers at the exit of the isolator for Mach 1.8 and 2.2 flows and for rectangular and round isolators, taken from Lin et al. [42].

3. Shock train static pressure distribution The reader is now aware of the fact that a pseudo-shock consists of two regions: a shock train and a mixing region. The latter was characterized as a pressure recovery region. But what mechanism allows for the pressure to increase in this mixing region, as observed in [Figure 2.13](#)

between points j and 2 ? According to Om et al. [43], this works as follows: As can be seen in Figure 2.18, the flow outside the boundary layer remains supersonic throughout the entire shock train, while the flow in the core region of the duct experiences continuous transitions from the supersonic to subsonic regimes and back due to the presence of successive shocks and expansion waves. The existence of these expansion waves can be argued based on the fact that in Figure 2.18 every shock locally turns the flow out of itself due to the local bifurcation in every shock, which causes for every single shock wave the flow to successively turn into itself and then out of itself. Crocco also explained that the initial SBLI causes thickening of the boundary layer and the formation of what he describes as a virtual nozzle throat [29]. With the same logic, Gawehn et al. [44] explained that this throat-like geometry is generated between two consequent shocks which results in the duct cross-section getting smaller. Therefore, immediately downstream of the main shock, the flow is accelerated again to supersonic speeds through this virtual nozzle until the next shock recompresses the flow again. At the end of the shock train, the flow is mixed subsonic-supersonic and normal shock waves do not appear anymore. As a result of the shock train, the flow is highly non-uniform and this causes the pressure to increase. When the flow reaches subsonic speeds, friction will cause the flow to accelerate, i.e. the flow becomes a classical Fanno flow. Finally, when the drop in pressure due to the Fanno flow becomes greater than the rise in pressure due to the mixing, this will mark the end of the pseudo-shock where the static pressure has reached a maximum value after which it starts to decrease gently.

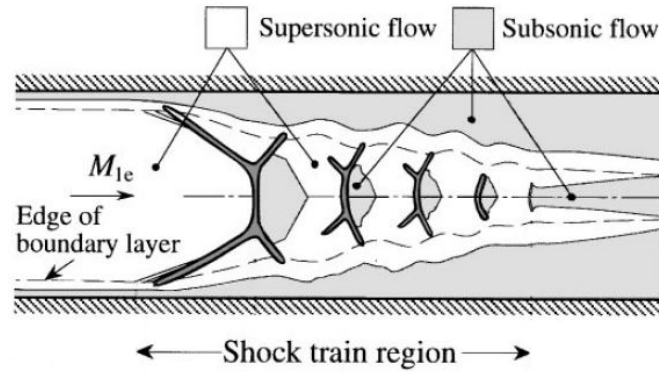


Figure 2.18: Schematic drawing of successive shock wave in a shock train after the first encounter with the boundary layer, taken from Tamaki et al. [39].

When the duct streamwise length is insufficient, the pressure recovery region after the shock train becomes much shorter and the absolute extent by which the pressure rises will also be lesser than the analytical solution for the same flow conditions. To justify this, an experiment was conducted by Waltrup and Billig [45] where compressed air was fed through an asymmetrical nozzle into a constant-area duct where the duct exit was either open to the atmosphere or throttled through a butterfly valve. The results were plotted in Figure 2.19 where the ratio of static pressure over plenum pressure p/p_{op} was plotted against the distance from the duct inlet x .

The static pressure at the duct exit is the external pressure, whether it be atmospheric pressure or the backpressure generated by throttling the butterfly valve. The pressure rise in all curves is caused by the shock train and there is no pressure rise after that. From the results on the pressure distributions, Waltrup and Bellig succeeded in deriving an analytical relationship for the pressure distribution in the shock train as a function of several duct parameters which are documented in their works [45, 46]. This relationship can be expressed as (Equation 2.29):

$$\frac{x(M_1^2 - 1) \text{Re}_\theta^\alpha}{D^{1/2} \theta_1^{1/2}} = 50 \left(\frac{p}{p_1} - 1 \right) + 170 \left(\frac{p}{p_1} - 1 \right)^2 \quad (2.29)$$

where x is the distance downstream from where the pressure rise began, M_1 is the Mach number of the undisturbed upstream flow, θ_1 is the boundary layer momentum thickness for the undisturbed flow, D is the duct diameter, Re_θ is the Reynolds number based on the boundary layer momentum thickness and p/p_1 is the ratio of local wall pressure to the static pressure at the start of the pressure rise. Several experiments con-

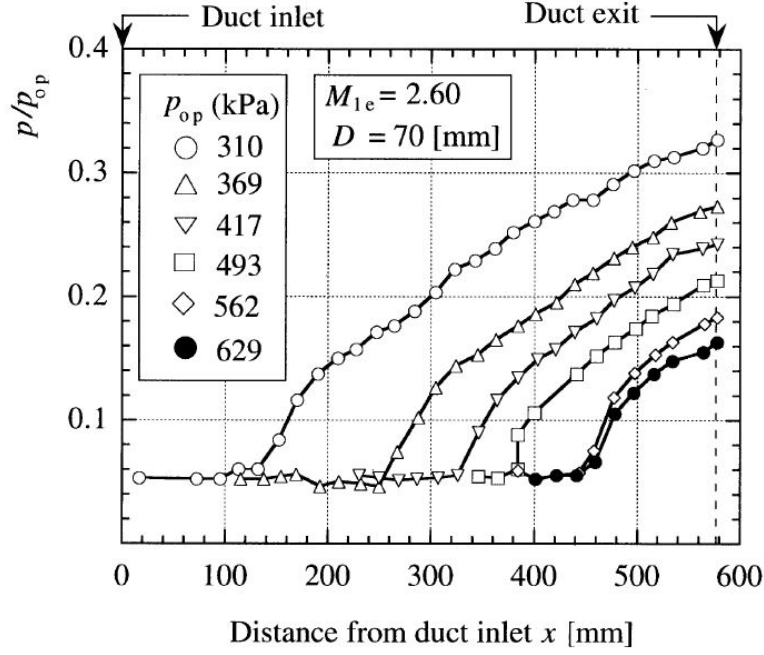


Figure 2.19: Wall static pressure distributions in a cylindrical duct where a shock train was introduced, taken from Waltrup and Billig [45].

ducted at a later stage by Nill and Mattick [47] and Bement et al. [48] confirmed the validity of Equation 2.29. At a later stage, Billig [49] also succeeded in correcting Equation 2.29 for its applicability to rectangular ducts by substituting the duct diameter D with the duct height H . This can be illustrated in Equation 2.30:

$$\frac{x(M_1^2 - 1) Re_\theta^\alpha}{H^{1/2} \theta_1^{1/2}} = 50 \left(\frac{p}{p_1} - 1 \right) + 170 \left(\frac{p}{p_1} - 1 \right)^2 \quad (2.30)$$

Weiss et al. [35] analysed the different shock train models with different pressure levels and Mach numbers up to $M = 2.0$. They concluded that the model developed by Billig [49] in Equation 2.30 accurately represents the pressure gradient for the pseudo-shock in a rectangular duct at low Mach numbers, in particular in the shock train region. However, a better agreement between the measured and predicted values of the shock train length for the Mach number range from 1.33 to 1.85 was obtained by Wang et al. [50] with an additional correction including the degree of flow asymmetry D_θ which is shown in Equation 2.31:

$$\frac{x(M_1^2 - 1) Re_\theta^\alpha}{(1 + D_\theta)^\beta H^{1/2} \theta_1^{1/2}} = 50 \left(\frac{P}{P_1} - 1 \right) + 170 \left(\frac{P}{P_1} - 1 \right)^2 \quad (2.31)$$

where the factor β assumes values based on the actual measurement data. The parameter D_θ is defined as Equation 2.32:

$$D_\theta = \frac{\theta_{max} - \theta_{min}}{\theta_{max}} \times 100 \quad (2.32)$$

with θ_{max} and θ_{min} defined as the boundary layer momentum thickness corresponding to different values of boundary layer thickness at the two walls of the duct, which is also illustrated by Figure 2.20.

It can be observed that when D_θ is zero, the flow is completely symmetric at the duct entrance and Equation 2.31 reduces to Equation 2.30. It was also observed that, for a given pressure ratio, the length of the shock train becomes larger as the asymmetry of the flow grows.

Moreover, the exponent α in Equation 2.29 to Equation 2.31 assumes the value of 1/4 as obtained from a regression analysis of the data compiled by Billig [49]. However, Sridhar et al. [51] found a value of $\alpha = 0.225$ by averaging the values of circular and rectangular ducts.

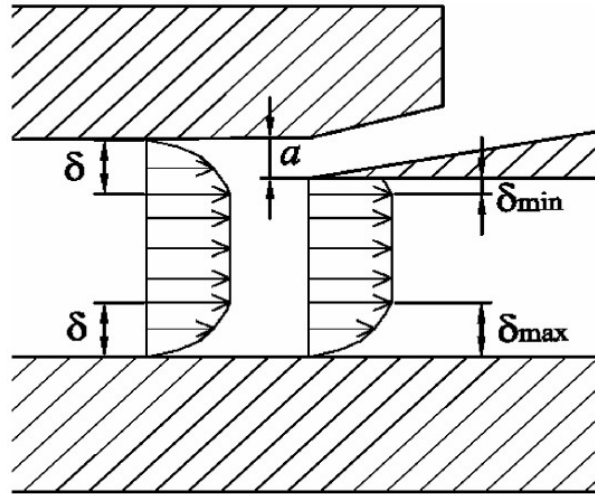


Figure 2.20: Boundary layer asymmetry at the duct entrance, taken from Wang et al. [50].

Also, the radial and circumferential gradients of the flow properties and chemical composition in the mixing region have been hypothesised and confirmed. One of the persons who did so was Nagai [52], who observed that the radial distribution of the total and static pressure across the shock train is subject to complicated changes due to the presence of shock waves and viscous diffusion. This is shown in Figure 2.21.

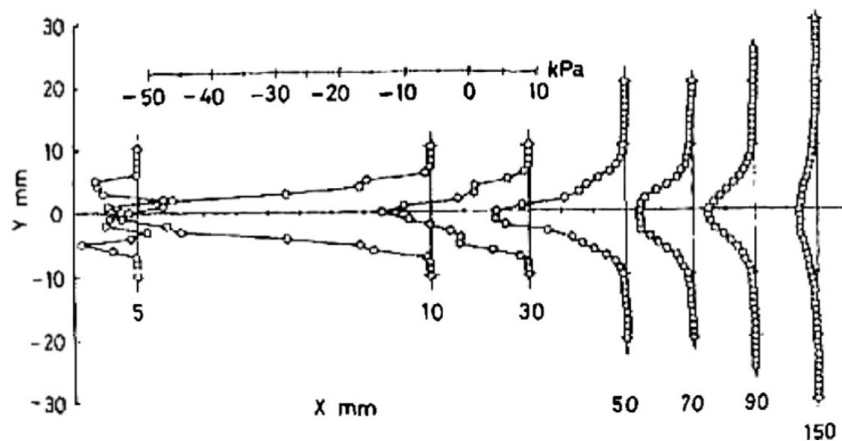


Figure 2.21: Radial static pressure distributions across a shock train, taken from Nagai [52].

4. Shock train pressure ratio Matsuo et al. [28] compiled the data from multiple experiments in which a pseudo-shock appeared in a constant-area duct. Matsuo et al. acquired the data for the ratio of the in turn static pressure ratio across a pseudo-shock to the static pressure ratio of an inviscid normal shock wave $(p_2/p_1)_p/(p_2/p_1)_n$ and this was plotted as a function of the Mach number upstream of the pseudo-shock M_{1e} as shown in Figure 2.22. Here the subscripts p and n refer to the pseudo-shock and inviscid normal shock wave, respectively. As can be clearly concluded from this diagram, the higher the upstream Mach number, the smaller the ratio $(p_2/p_1)_p/(p_2/p_1)_n$ becomes, which implies that the pressure ratio across the pseudo-shock deviates more from the theoretical value of the normal shock wave. The shaded region in between the two drawn curves shows the range of experimental data that was found for the tested Mach numbers. The scattering of the different datasets comes from the fact that the flow confinement effect of the boundary layer differs from one experiment to another. One of the interesting suggestions in the work of Matsuo et al. was to take into account more parameters when discussing this particular experimental problem. Auxiliary parameters can be for example the Reynolds number based on the boundary layer thickness or some of the geometrical variables of the intake duct.

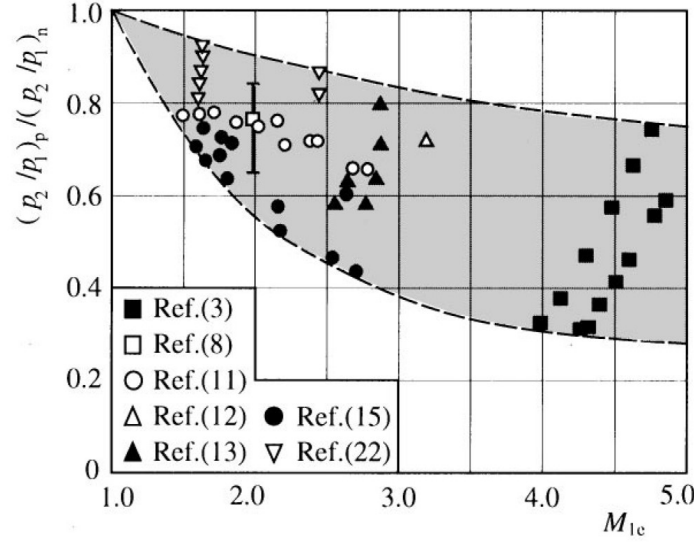


Figure 2.22: Static pressure ratio across pseudo-shock normalized by that across a normal shock wave versus the upstream Mach number, taken from Matsuo et al. [28].

Also, Sun et al. [53] discovered that a more plausible explanation for the trend found in Figure 2.22 is the fact that the boundary layer displacement thickness increases, especially for higher Mach numbers, which in turn causes viscous losses that grow with increasing Mach number.

Neglecting the wall friction and heat transfer inside the pseudo-shock, Nagai and Yaga [54] formulated a relationship shown in Equation 2.33, in which the ratio of the total pressure at the initial and final sections of the pseudo-shock increases as the boundary layer thickness at the initial section increases:

$$\frac{P_2}{P_1} = \frac{\zeta_1 w_1}{1 - \eta_1 w_1^2} \frac{1 - \eta_2 w_2^2}{\zeta_2 w_2} \quad (2.33)$$

where ζ and ξ are the correction factors for the mass flux and energy, respectively, in the integral equations of continuity and conservation of energy.

Matsuo and Miyazato [55] proposed a mass averaging pseudo-shock model to estimate the total pressure recovery. Weiss et al. [35] stated that the total pressure loss across the shock train is well predicted by the mass averaging model by Matsuo and Miyazato. Although a very cumbersome model in its application, this model applies to pseudo-shocks in a constant-area duct with a fully turbulent boundary layer but neglects both friction losses and heat and mass transfer across the wall. In order to account for the incoming boundary layer profile, upstream flow properties are mass averaged by the cross section height. The equations of mass, momentum, energy conservation and the isentropic flow relations are applied to a control volume, which contains the pseudo-shock. By means of this model the flow conditions downstream of the pseudo-shock can be derived solely from the upstream mass averaged flow values, but it is not possible to determine the flow characteristics inside the pseudo-shock. This model, expressed by Equation 2.34, is able to explicitly obtain the flow properties across the pseudo-shock and predicts the static pressure rise and total pressure loss with good accuracy, particularly for high Mach numbers (Equation 2.34):

$$\frac{p_2}{p_1} = \frac{\bar{M}_1}{\sigma_1 M_2} \left[\frac{2 + (\gamma - 1) \bar{M}_1^2}{2 + (\gamma - 1) M_2^2} \right]^{1/2} \quad (2.34)$$

with (Equation 2.35):

$$\sigma = \frac{\bar{\rho} \bar{u} A}{\int \rho u dA} \quad (2.35)$$

Further derivation leads to the expression for the total downstream-upstream pressure ratio of the pseudo-shock, written as (Equation 2.36):

$$\frac{p_{02}}{p_{01}} = \left[\frac{2 + (\gamma - 1)M_2^2}{2 + (\gamma - 1)M_1^2} \right] \frac{p_2}{p_1} \quad (2.36)$$

Another way to inspect the pseudo-shock pressure behavior is by studying the pressure gradient. The only analytical expression which relates the pressure gradient experienced by the flow along a duct in the presence of separated regions and the length required to achieve the full pressure rise was proposed by Ortwerth [56]. This equation was determined from a comprehensive experimental campaign at different Mach numbers, Reynolds numbers and duct geometries, and hence is applicable to a wide range of flow conditions and intake designs (Equation 2.37):

$$\frac{d\left(\frac{P}{P_1}\right)}{dx} = 4K\gamma\left(\frac{P}{P_1}\right)M^2 \quad (2.37)$$

where $4K = 44.5C_{f0}$, in which C_{f0} is the friction coefficient at the location where the flow initially separates. This equation can be used to close the system of differential equations of mass, momentum, and energy in the presence of flow separation to predict the pressure distribution in the entire region of the duct. Equation 2.37 was used by Tu and Segal [57] with two values for the wall friction coefficient, $C_{f0} = 0.01$ and 0.005 , finding a strong dependence of the model accuracy on the selection of the friction coefficient. As Figure 2.23 illustrates, the value of 0.005 underestimates the pressure rise, and even though the 0.01 value initially matches the experimental data, it later gradually diverges.

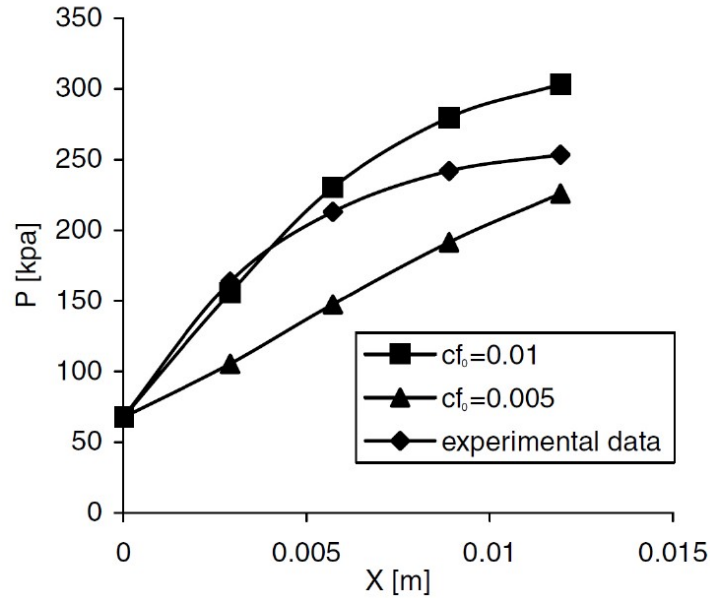


Figure 2.23: Influence of the wall friction coefficient on the duct pressure rise, taken from Tu and Segal [57].

5. pseudo-shock length By definition, the length of a pseudo-shock is defined as the physical distance between the head of the shock train, which technically is the initial terminal shock wave, and the end of the subsequent static pressure recovery region [30]. In other words, this is the physical distance between points 1 and 2 in Figure 2.13, which is the region over which the static pressure has ultimately increased. This definition does not hold anymore for any internal geometries that have additional devices installed such as supersonic diffusers, ejectors and the like, because the flow duct cross-sectional area in the above cases changes from one place to another along the streamwise direction and due to the streamwise gradient the end-point of the pseudo-shock will be difficult to identify. In general, the pseudo-shock length is linearly proportional to both the boundary layer thickness relative to the duct diameter and the Mach number upstream of the shock train, and has been found to vary in the range of 4–15 tube diameters in agreement with the work of Ikui et al. [58].

In Figure 2.24, multiple experimental datasets were compiled and analysed by Matsuo et al. [59] to find the relation of the ratio of length of the pseudo-shock over the duct diameter L_p/D , in literature commonly referred to as the non-dimensional pseudo-shock length, plotted as a function of the Mach number M_{1e} upstream of the terminal shock wave. The solid line represents the result based on the diffusion model for pseudo-shocks derived by Ikui et al. [40]. According to this flow model, the pseudo-shock length can be analytically estimated by the expression (Equation 2.38):

$$\frac{L_p}{D} = \frac{2}{c} \sinh^{-1} \left(\frac{w_1 - w_2}{2w^*} \right) \quad (2.38)$$

where c is an empirical constant equal to 0.114 and w_1, w_2 and w^* are the Crocco numbers at initial and final sections of pseudo-shock and at sonic conditions, respectively. The Crocco number is simply the dimensionless velocity defined as (Equation 2.39):

$$w = \frac{u}{\sqrt{2c_p T_0}} \quad (2.39)$$

where u is the flow velocity, c_p is the specific heat at constant pressure and T_0 is temperature in the wind tunnel settling chamber.

Crocco was among the first to investigate in detail the consequences and the mechanics of pseudo-shocks [29], including their hazy properties. From Figure 2.24, one can derive that if the upstream Mach number keeps increasing, the pseudo-shock length will increase too. However, when the upstream Mach number increases, the growth in pseudo-shock length becomes less steep. If Equation 2.29 would be applied to the pressure distribution of a pseudo-shock and p would be replaced by p_2 at the end of the pseudo-shock, the parameter x in Equation 2.29 would represent the end point of the pressure rise, which in other words indicates the pseudo-shock length L_p . The empirical correlation shows that for a given pressure ratio p_2/p_1 , L_p varies directly with $D^{1/2}\theta_1^{1/2}$ and inversely with $(M_1^2 - 1)Re_\theta^{1/4}$. This shows that the pseudo-shock length is a strong function of the Mach number M and a weak function of both the Reynolds number Re and the duct diameter D .

The same issue of scattered data having very diverse results is found in Figure 2.24, just as with Figure 2.22. Again, this may be due to the differences in the flow confinement parameter. Therefore, it is also recommended here to conduct more experiments where sufficient attention is provided to any additional parameters, such as the Reynolds number or other aerodynamic or geometric variables in this problem.

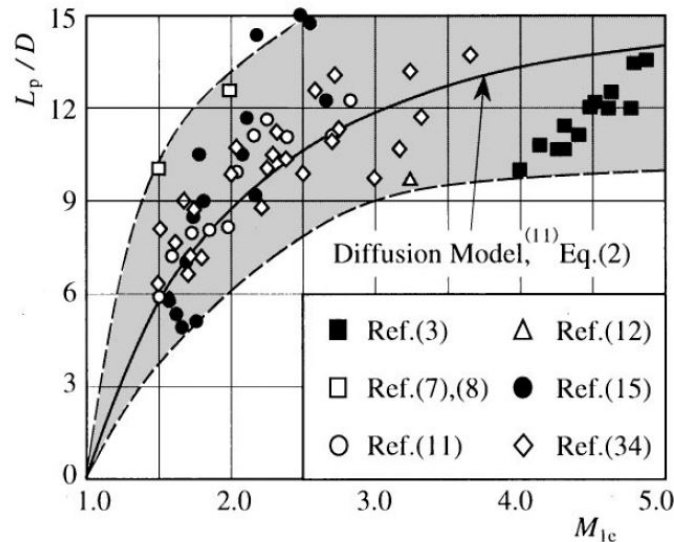


Figure 2.24: Non-dimensional pseudo-shock length in constant-area duct versus the Mach number upstream of the shock, taken from Matsuo et al. [28]

2.4. Supersonic Intake Configuration

The goal of the intake is to capture a high mass flow of air to feed the combustion chamber. After a supersonic intake captures air, the flow is compressed in two to three successive stages, which are the supersonic diffuser, the constant-area duct and the subsonic diffuser. It is common to define the supersonic diffuser and constant-area duct as the stage in which a supersonic stream is decelerated to approximately sonic speed and a subsonic diffuser as the stage in which the kinetic energy in a subsonic stream is completely converted into pressure energy.

The basic design of a highly efficient diffuser for the flow of an ideal non-viscous gas at a constant free-stream Mach number presents relatively few problems. However, viscous forces cannot be ignored since they cause complex shock patterns, shock instabilities, and separated flow in the duct as well as vortex sheets in the spilled flow. Some of these effects may be accounted for by semi-empirical theories but many can be assessed only by experimental means. The wide variations in Mach number that a vehicle experiences in accelerating to a steady flight speed, as well as the variations in angle of attack often required in climb and maneuvers, increase many fold the problems in the design of an optimum intake.

First, the supersonic diffuser (subsection 2.4.1) decelerates the flow to a Mach number which is sufficiently below the freestream value. Second, the flow goes through a constant-area duct (subsection 2.4.2), sometimes also referred to as the isolator in open literature, where a terminal shock decelerates the flow even more, this time to near-sonic or subsonic velocities. Finally, the flow enters a subsonic diffuser (subsection 2.4.3) where the flow velocity is reduced to properly feed the flow into the combustion chamber. Occasionally, bleed systems (subsection 2.4.4) are implemented to enhance intake performance by diverting the thick boundary layer that has developed upstream of the intake.

2.4.1. Supersonic diffuser

Supersonic diffusers form the first stage through which the flow enters the deceleration campaign. According to Dailey [60], supersonic diffusers include two essential criteria: 1) It shall sufficiently decelerate the entering air mass to ensure steady combustion beyond the air intake and 2) it shall compress the air mass adequately before heat addition to realize a good thermal efficiency of the ramjet. The penalty to the first requirement is a reduction in the thrust relative to the engine frontal area. This is countered by an increase in engine cycle efficiency, but the latter gain is usually so small that it is practically of no importance. The second requirement is more difficult: Compressing the incoming air mass well requires a reduction in the area through which the air will pass. Good intake efficiency requires the maximum possible supersonic compression. The latter is realized with the smallest contraction ratio. The contraction ratio is the primary design parameter of a supersonic diffuser, which determines the minimum Mach number at which the supersonic diffuser operates and the amount of compression that the entering air undergoes before it must negotiate the terminal shock. If the contraction ratio of a diffuser is increased, the minimum Mach number at which it operates theoretically increases, as can also be seen in Figure 2.25. From this figure, it becomes clear that the higher the design Mach number, the more the performance becomes less efficient. The reason for obtaining smaller efficiencies at higher Mach numbers is caused predominantly by the presence of stronger shock waves. However, friction effects and turbulent mixing are also considered major causes for smaller efficiencies at higher Mach numbers.

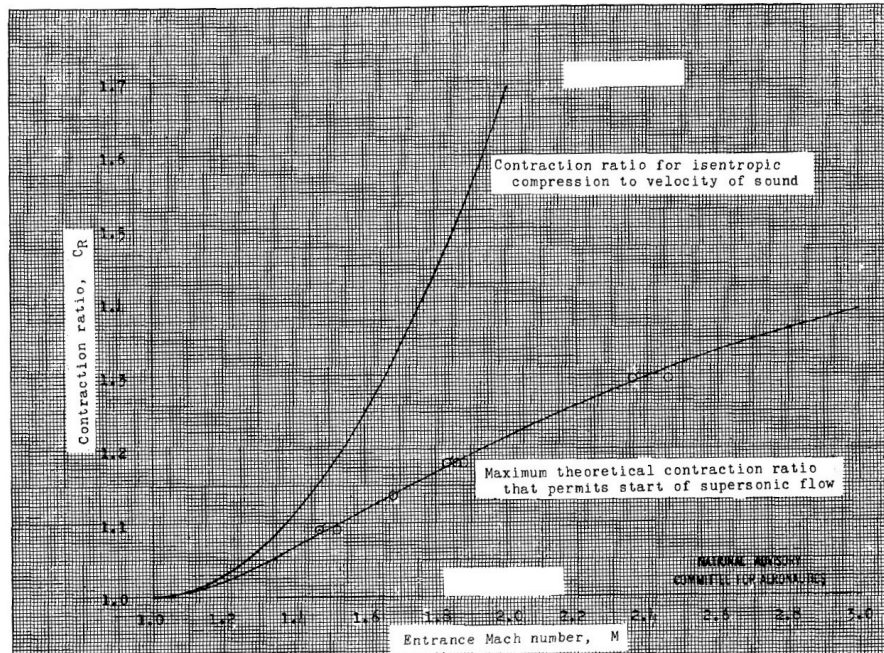


Figure 2.25: Allowed contraction ratios for constant-geometry supersonic diffusers, taken from Kantrowitz [61].

Also, the same research by Kantrowitz [61] investigated the theoretical performance in terms of the pressure recovery of five distinct supersonic diffusers with their maximum contraction ratios corresponding to minimum starting or design Mach numbers. The results are shown in Figure 2.26. From this figure, it becomes clear that the higher the design Mach number, the more the performance becomes less efficient, which is again explained by the presence of stronger viscous flow effects.

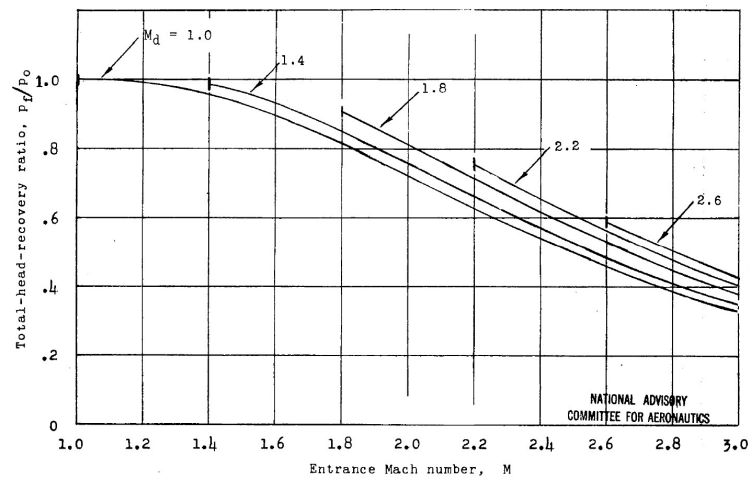


Figure 2.26: Theoretical performance of five different supersonic diffusers by design Mach number M_d , taken from Kantrowitz [61].

Another remarkable aspect of the same research included testing supersonic diffusers at different entrance cone angles. For the current report on submerged intakes, this aspect is crucial since it provides insight into the direct geometrical aspects that may influence the flow entering the immersed intake. The results lead to what is shown in Figure 2.27. As can be clearly deduced, a greater entrance cone angle results in a smaller pressure recovery. This can be explained from the contraction ratio that becomes bigger, which means that the design Mach number also becomes larger, which gives rise to stronger shocks and a less efficient performance.

This result was also justified by Das and Prasad [62], by proving that the performance of supersonic intakes with pressurised exit flow only perform optimal for cowling deflections of the order of 2° . This same

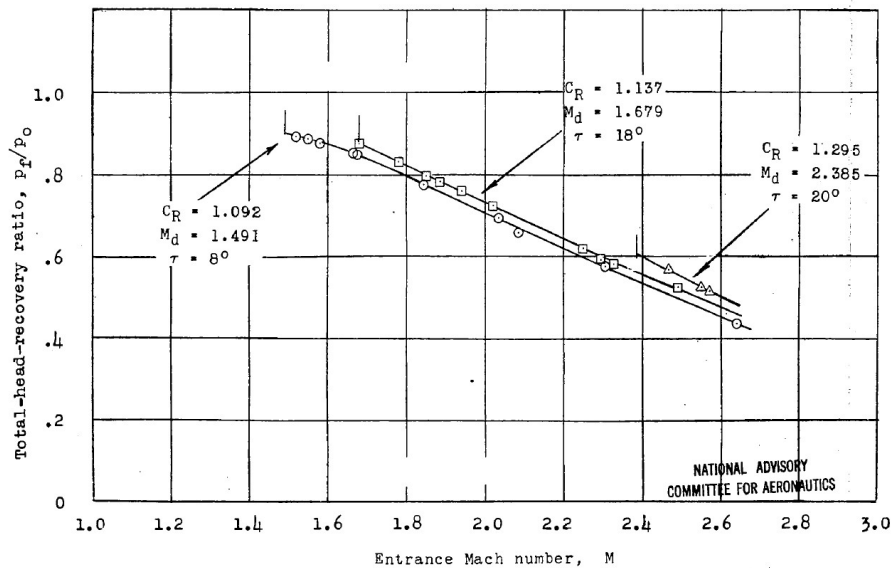


Figure 2.27: Experimental performance of three different supersonic diffusers with different entrance cone angles τ , design Mach number M_d and contraction ratio C_R , taken from Kantrowitz [61].

research also proved that the improvement in performance with a cowling deflection of 2° is comparable to performance with a 2.8% boundary layer bleed. Hence, the cowling deflection can be considered as an alternative to bleed systems.

For fixed geometry diffusers, it is crucial to make use of central bodies or other forms of external compression to overcome the starting problem of the engine. Failing to do so results in the diffuser being so restricted that the intake becomes futile at high Mach numbers. The designer of a supersonic intake should keep in mind that the compression produced by a central body is always followed by a cowling drag contribution. Since both drag and efficiency are directly proportional to the flow deflection, it becomes crucial to optimize the diffuser design in terms of net thrust. Also, Kantrowitz found that as long as the incoming flow is supersonic, the entering mass flow would remain unaffected by events downstream [61].

One of the main aspects in supersonic diffusers is the existence of the supercritical flow behavior, which is the case when the intake flow volume is maximum for a given Mach number. The critical point is then the point of maximum compression efficiency or the point of maximum net-thrust of a ramjet. Operation at the critical point can be achieved through different strategies, including increasing heat addition in the combustion chamber or increasing the back pressure downstream of the inlet. Both methods will cause the shock system to move more upstream towards the intake opening. This ensures that the shock losses in the intake are minimized. Further movement of the shock system beyond the critical point leads to the diffuser entering the subcritical regime, which is a highly unstable region that can lead to structural damage of the missile. The first mention of this phenomenon in literature was done by Oswatitsch in 1942 [12], where he did not discuss the phenomenon in detail but merely observed its occurrence. Pearce [63] compared this phenomenon to power-plant surge, judging from the loud uproar that is heard. From a rational standpoint, it is obviously important to know when this instability might occur, so that operation under these conditions can be avoided. However, this is beyond the scope of this report. For more information on the instabilities of the subcritical regime, the reader is referred to the works of Ferri [64] and Davidson [65].

Generally, three types of supersonic diffusers exist: external, internal and mixed-compression supersonic diffusers. These types are schematically shown in Figure 2.28.

External compression diffusers compress the incoming flow by generating a shock system using one or more ramps. A multitude of ramps is also known as a compression surface. This diffuser is labeled external due to the shock system occurring outside the enclosed intake area. Compression surfaces are usually built to generate the shock system at the lip of the intake cowling. A reason for doing so is to minimize the mass flow losses. The general geometry of supersonic diffusers, as can also be seen in Figure 2.28, is justified by knowing that deceleration of the flow to low supersonic Mach numbers requires the flow to be deflected. To allow the

flow to continue in the intake, this deflection has to be counteracted, which in turn justifies why a supersonic diffuser is followed by a constant-area duct. A more advanced form of a diffuser was proposed by Oswatitsch [12] where the loss of total pressure, or the principle of flow compression by a shock, was minimized.

Internal compression diffusers are characterised by a compression surface and cowl lip that are positioned at the same streamwise position, meaning that the incoming flow is confined at the leading edge of the intake. Hence, the compressive shock system in this phase of the deceleration campaign occurs within an enclosed area. In a number of designs, internal diffusers are symmetrical and no distinction exists between compression surface and cowl lip. An asset of using internal diffusers is the ability to use reflected shock waves to compress the flow, which implies that the intake size relative to the throat area can be minimized knowing that reflected shock waves cancel any flow deflection. A drawback however of these diffusers is their limiting contraction ratio, more commonly known as the Kantrowitz limit [61]. This limits the design of internal diffusers since the flow must accelerate to supersonic conditions upon starting the intake. Another flaw with these diffusers is that the boundary layers are usually thicker in comparison to the boundary layers in external diffusers. A bigger boundary layer will lead to more problems with viscous effects, as was already explained in section 2.3.

Finally, mixed-compression diffusers are constructed by combining both an external and internal diffuser. Theoretically, this diffuser type combines all the favourable effects of external and internal diffusers in one design. Viscous effects are weakened and reflected shock waves will prevent any flow deflection. However, the problem of the limiting contraction ratio still applies to the internal diffuser part of this design. Nonetheless, it was confirmed by Sepahi-Younsi and Feshalami [66] that mixed-compression diffusers perform better in terms of having a smaller drag profile than external compression diffusers, but the penalty appears in the total pressure recovery (TPR), since external compression diffusers outperform mixed-compression diffusers in that regard.

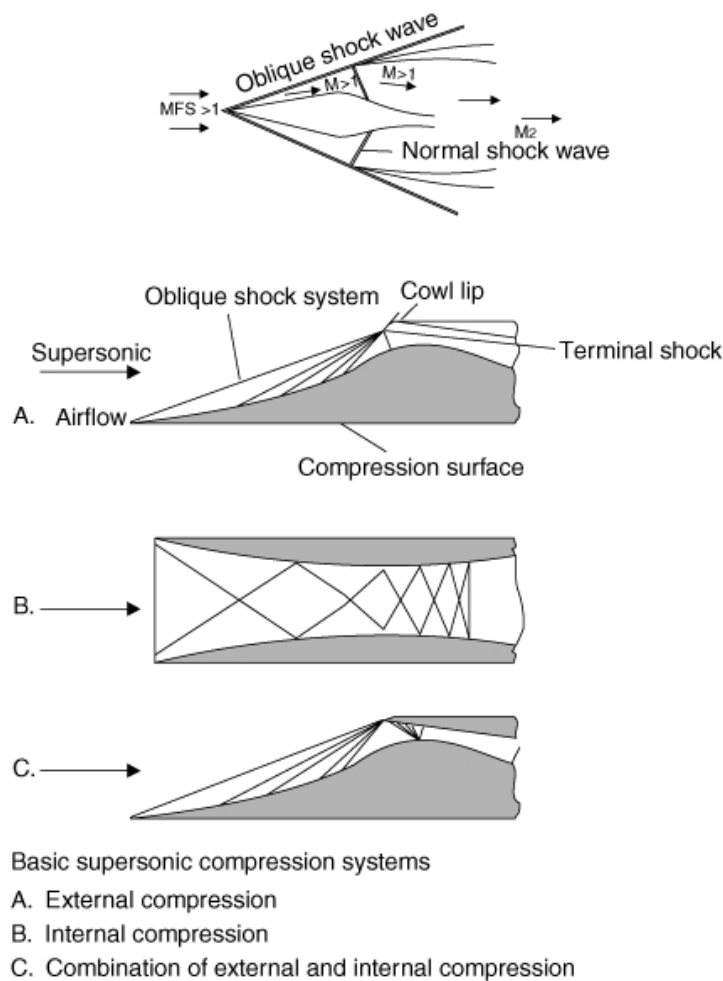


Figure 2.28: Schematic of the different types of supersonic diffusers, taken from Parker [67]

2.4.2. Constant-area Duct

The constant-area duct is the second and main stage in which the flow is decelerated. One of the main reasons of including a constant-area duct in a supersonic intake is to prevent boundary layer separation at the subsonic diffuser entrance. The duct cross-sectional area is often chosen to be rectangular and not circular, owing to the similarities shared between the inviscid and viscous flow cases for rectangular cross-sections, as was shown by Gessner et al. [68]. This makes it easier to make analytical predictions based on inviscid flow theory, which the design team can use to anticipate how the flow is going to behave inside the duct. The work of Gessner et al. also showed that for the same cross-section, clear patterns exist of secondary flows imposed on the primary flow, which stem from the skin friction distributions that are present in the transverse plane of the cross-section.

As a design rule of thumb, the constant-area duct starts where the terminal shock wave starts to capture the imminent pseudo-shock from its earliest stage which is in line with the work of Mahoney [69]. Assuming ideal and inviscid conditions, one normal shock is required to reduce the Mach number to a value smaller than unity. This involves having a minimum area at the duct throat section. However, in reality the boundary layer at significant supersonic Mach numbers will cause the terminal shock to spread, which causes multiple shocks to appear downstream of the terminal one as a result of an initial shock-wave boundary layer interaction, which is the well-known shock train. One of the essential requirements to maximize the deceleration efficiency in the constant-area duct is to have the duct streamwise length equal the pseudo-shock length. An experimental argument for doing so is shown in Figure 2.29. This figure justifies that having the duct physical length becoming equal to the anticipated pseudo-shock length provides the intake with the highest exit pressure, and therefore the highest TPR.

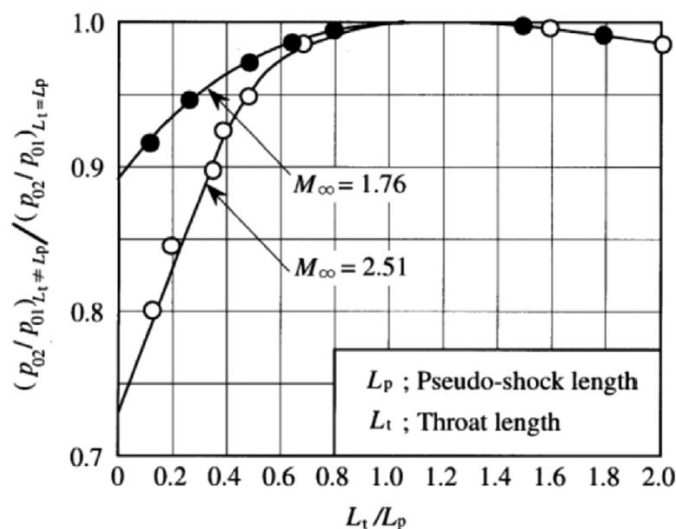


Figure 2.29: Total pressure recovery as a function of duct and pseudo-shock lengths, taken from Mahoney [69].

If this requirement is not met, the shock train is cut off early, resulting in a smaller TPR and therefore a less efficient performance. Another notable requirement for the duct is that its length has to be sufficiently large to prevent intake unstart. However, Billig et al. [70] showed that the duct length should not become too long to avoid adding excessive weight and additional shear losses. According to Neumann et al. [71], the optimal length for constant-area ducts operating between Mach 1.8 and 4.2 lies between 8 and 12 duct diameters. Sullins [72] found that a duct of 10 - 20 duct diameters length is sufficient to generate a shock train that can rise up to 95 % of the theoretical normal shock strength for the same Mach number. However, Emami et al. [73] pointed out that the former findings should never delude the design team from pursuing a duct length that is designed based on a trade-off of all component requirements over the mission envelope.

As was explained in subsection 2.3.2, behind the shock train the flow becomes subsonic. This is an important sign, since the flow should be ideally subsonic before it enters the final deceleration stage, which is the subsonic diffuser. Povinelli and Towne [74] found that in between the constant-area duct and the subsonic diffuser, the boundary layers from both sides of the intake have thickened and may cause high amounts of distortion, strong secondary flows and flow separation. This is one of the reasons why novel supersonic intake designs consider including provisions for bleeding at the side plate and the intermediate corner between

both the constant-area duct and subsonic diffuser. If this is the case, a concession should be made between TPR, distortion, spilling drag and bleed drag [74].

The corner between the duct and subsonic diffuser is regularly the scene of where large-scale separated flow interacts with the pseudo-shock, which is in agreement with the experiment conducted by He et al. [32]. This particular separation behavior is the result of the flow acceleration pattern being asymmetric, since one of the walls is going to accelerate more than the other at the streamwise location of the corner, depending on the slope and other geometrical considerations of the subsonic diffuser. This will cause an increment in flow momentum at the intake nozzle. The larger momentum will then start to cause the downstream boundary layer to firmly resist the downstream accumulative adverse information.

2.4.3. Subsonic Diffuser

The subsonic diffuser is a diverging channel downstream of the constant-area duct where the flow is compressed and decelerated in its final stage before entering the engine. According to Cain [75], the main criterion for a subsonic diffuser is to prevent boundary layer separation from occurring in the adverse pressure gradient and to provide the proper engine face entry velocity. In most designs, the geometry consists of a diverging channel with conical shape, where a cone angle of typically $3-5^\circ$ has proven to be most effective as found by Mahoney [69]. Ran and Mavris [76] observed that in subsonic diffusers, the intake pressure recovery is reduced by about 1–2%. Given the diffuser entry Mach number (the Mach number after the pseudo-shock) and the engine face speed, the geometric factors of the subsonic diffuser are mainly affected by the duct expansion angle. Here the geometric factors include the area ratio of engine face area to entry throat area and the diffuser length.

2.4.4. Boundary Layer Bleed

If an intake ingests a thick boundary layer, the mass flow ratio decreases and the static pressure ratio drops due to less kinetic energy in the flow [13]. Viscous effects can strongly affect the intake performance, especially when the boundary layer interacts with an imminent shock wave which gives rise to a SBLI. This interaction can cause severe degradation of the intake performance and engine thrust loss due to dissipation of the mechanical energy in the boundary layer. Many years of research were dedicated, especially by Dolling [17], to investigating how to circumvent the ruinous nature of the boundary layer. The classical solution is to remove the boundary layer, partially or fully, by means of bleed slots to increase the total pressure recovery and consequently the intake performance. A typical example of how a bleed slot is integrated in a supersonic intake is shown in Figure 2.30. One of the reasons to mitigate the danger of ingesting a thick boundary layer is that thick boundary layers affect the pressure recovery across the viscous flow phenomena in the constant-area ducts, most notably the pseudo-shock which was also investigated by Dolling [17]. Therefore, it becomes key to reduce the boundary layer thickness upstream of this area. A thick boundary is also more prone to flow separation. A grave consequence of boundary layer separation in an intake is that a large blocking effect might take place, which in turn will initiate a well-known intake unstart. After the occurrence of intake unstart and due to a sudden breakdown of the supersonic airflow, the terminal shock inside the duct may start to oscillate back and forth, more commonly defined as the buzz phenomenon. If the buzzing remains present for a while, a violent regime will start to dominate the flow both in- and outside the intake. This in turn may lead to heavy dynamics-induced structural damages to the intake and the missile body as a whole.

The results of Soltani et al. [19] showed that the unstart tolerance, i.e. the disturbance that can be resisted by the intake without unstart, increased as the bleed rate and the bleed hole angle relative to the local surface were increased. This shows that a larger margin of bleed proves to be a productive alternative in countering intake unstart. The effectiveness of the bleed to prevent intake unstart at nonzero angles of attack is significantly linked to the bleed location. As the angle of attack increases, the terminal shock on the leeward moves upstream, and when it crosses the bleed position, flow separation occurs first over the leeward surface and then spreads inside the entire intake which eventually gives rise to intake unstart.

Another research by Soltani et al. [78] showed how different bleed parameters influence the intake performance and what parameters are vital to determine the optimal bleed configuration and location. The results showed that locating the bleed slot upstream of the intake throat section improves intake performance and reduces the amplitude and frequency of the buzz phenomenon. Performance also improved when the bleed slot was located downstream of the intake entrance, i.e. behind the supersonic diffuser. The performance of the intake, measured by the TPR, is higher for aft bleed than with forward bleed when the supersonic diffuser is taken as the streamwise reference point. This result was also supported by Soltani. et al [79] by an exper-

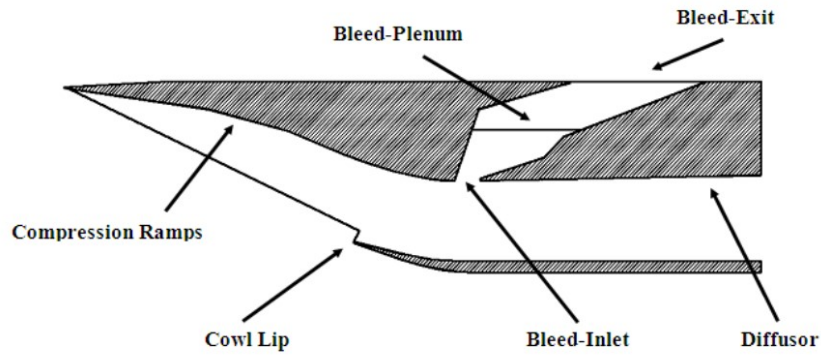


Figure 2.30: Generic supersonic intake including a boundary layer bleed slot, taken from Bauer and Kurth [77]

iment carried out at a design Mach number of $M_\infty = 2.0$ in which the intake performance was evaluated for different bleed parameters. The quantitative results are shown in Figure 2.31, where it becomes rather obvious that a more aft placement of the bleed mechanism enhances the intake performance significantly, even up to the point of encountering the buzz phenomena in the subcritical regime. This is also well anticipated, since downstream of the supersonic diffuser the flow has already passed the diffuser's deceleration phase, i.e. the shock system, and this means that the boundary layer has become thicker. With this in mind, one can imagine that disposing of this thick boundary layer will leave more fruitful results than disposing of a thin boundary layer upstream of the supersonic diffuser.

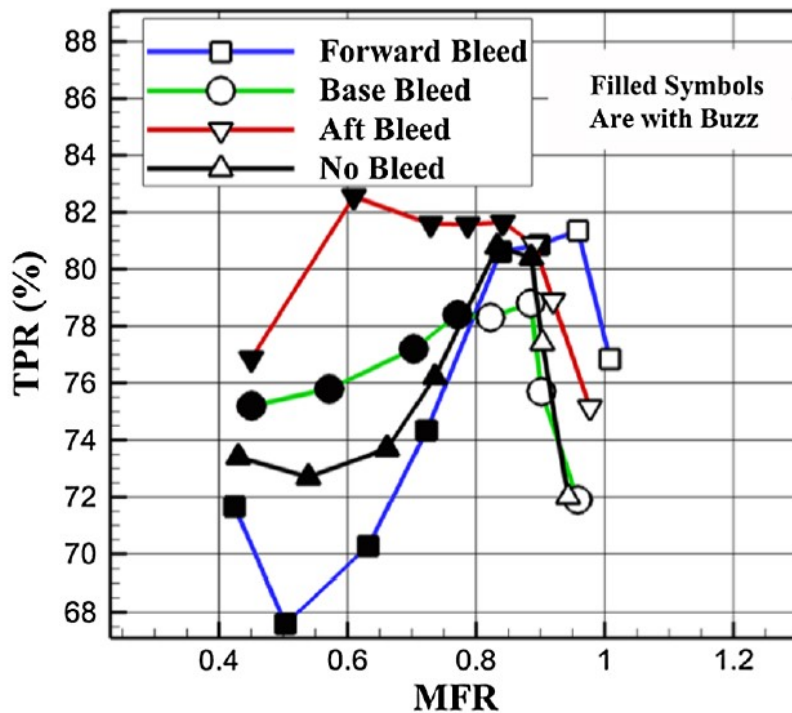


Figure 2.31: Total Pressure recovery (TPR) as a function of the mass flow ratio (MFR), taken from Soltani et al. [79]

Soltani et al. [79] also explained that the increment of the TPR when using boundary layer bleed is caused by the formation of a barrier shock at the bleed entrance. This shock is formed due to flow compression after the flow has turned towards the bleed slot. Since this barrier shock reduces the Mach number of the flow downstream, this means that the strength of the subsequent normal shock waves and total pressure losses in the intake downstream of the bleed slot become less. A decrease of the total pressure losses would then

increase the TPR. Since a more thorough analysis of this barrier shock is beyond the scope of this report, the reader may be referred to the works of Davis et al. [80] and Harloff and Smith [81].

Research by Obery and Cubbison [82] on the effect of boundary bleed also lead to exploring the different bleed slot types. The most well-known types of boundary layer bleed are the ram and flush bleed slots, which are shown in Figure 2.32. According to Sepahi-Younsi et al. [19], ram bleed slots try to isolate the boundary layer from the main airflow by creating a 'sub-channel' inside the main duct. The height of these slots is usually chosen to equal the boundary layer thickness. Flush bleed slots utilize a pressure differential in the bleed channel to completely divert the boundary layer. Achieving the pressure differential is commonly done by placing a flush bleed slot downstream of a shock wave, where the pressure is high. Boundary layer bleed slots can be installed on different positions along an intake. Flush bleed slots can be installed on the compression surface to assure a thin boundary layer and to minimize any interaction with the terminal shock. Bleed slots placed around the start of the intake channel assure intake operation with the thinnest possible boundary layer developing along the intake, which was confirmed by Soltani et al. [79].

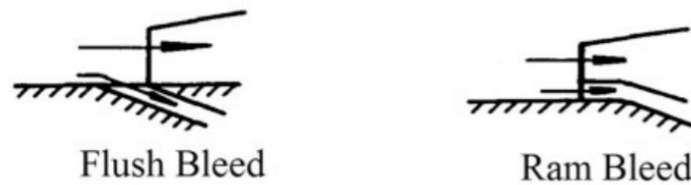


Figure 2.32: Ram and flush boundary layer bleed slots, taken from Sepahi-Younsi et al. [19].

2.5. Supersonic Intake Operation

Supersonic intakes may operate differently, depending on the engine conditions downstream of the intake. The performance in each condition will be dependent on the different aerodynamics which takes place in each of the operating conditions. In subsection 2.5.1, the different supersonic operational conditions for intakes are discussed. Following, the contraction ratio and its related constraints are treated in subsection 2.5.2. Finally, a discussion dedicated to shock oscillations is presented in subsection 2.5.3.

2.5.1. Operating Conditions

A supersonic intake is generally designed to meet certain criteria, such as a design Mach number and a particular backpressure. Designing for a certain Mach number is a clear statement, while designing for a specific backpressure will strongly depend on the pressure in the combustion chamber. The backpressure determines the position of the terminal normal shock wave inside the intake duct. Figure 2.33 shows the different situations that can be experienced by supersonic intakes based on the vehicle Mach number and the terminal shock position, the latter being a direct consequence of the backpressure. The most optimal condition is when a vehicle with supersonic intakes is propelled whilst operating at the critical condition and at the design Mach number, ensuring that the OSW-system is created at the lip of the cowling and that the terminal shock wave is located at the entrance of the intake. An external compression intake is an excellent example of an intake that is designed to have the compression surface generate a shock system at the cowling lip, which ensures that mass flow is maximised and that the airflow is still compressed in an efficient way.

When an intake operates below the design Mach number, the OSW upstream of the intake duct will deflect the streamline that encloses the intake capture area which causes the mass flow to decrease. In addition to the latter, operating below the design Mach number leads to supersonic spillage drag, since the deflected streamlines, which are meant to enter the intake, are forced outside the intake which increases the overall drag profile. When an intake performs above the design Mach number, some of the airflow which entered the duct did not go through the OSW-system and was therefore not compressed before upon entering the intake duct. Since only shock waves can efficiently compress the flow, this non-compressed air will cause losses in the intake performance, especially regarding the pressure recovery. If the flow would have passed through two different shock systems, being the supersonic diffuser OSW-system and the duct terminal shock wave, a shear layer is formed in the intake duct flow that, upon interaction with the boundary layer, may lead to flow separation and subsequently intake unstart or shock oscillations.

If the terminal shock wave is not positioned at the intake entrance, which is equivalent to stating that the in-

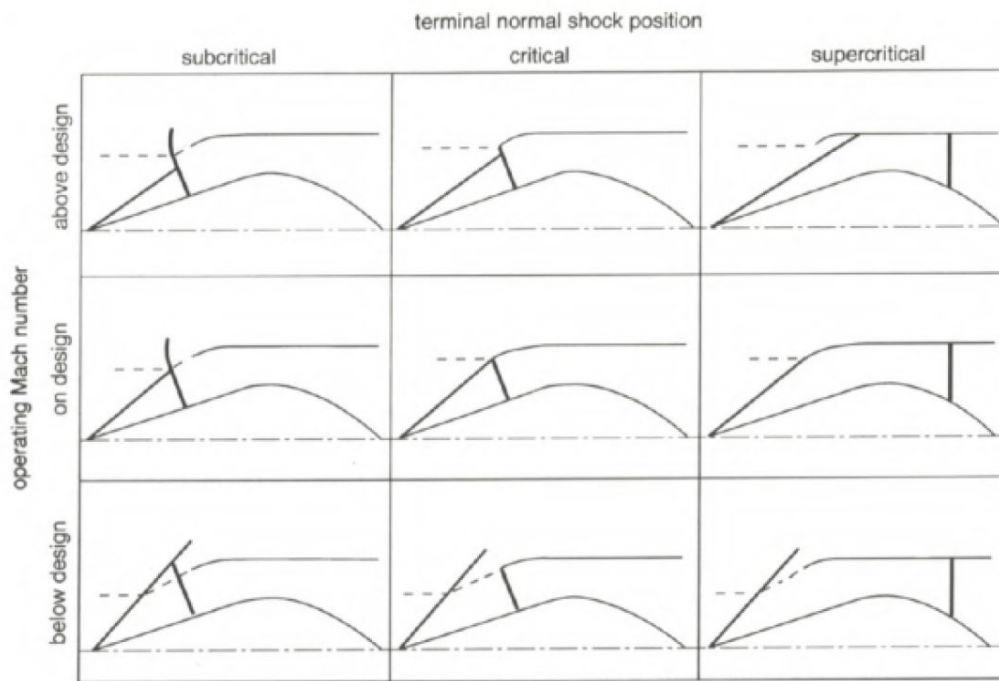


Figure 2.33: Illustration of the different operating conditions of supersonic intakes, taken from Mahoney [69].

take does not operate at the critical condition, the performance may significantly drop just as with operating at Mach numbers different from the design value. At the supercritical condition, which is when the backpressure is lower than the design value, the terminal normal shock wave lies deep downstream in the intake duct. Recalling from [section 2.3](#) that a terminal shock wave at high Mach numbers is followed by a shock train, at supercritical conditions this shock train lies deep downstream in the intake duct. This system of shock waves therefore decelerates the flow at a very late stage, potentially at the intersection between the constant-area duct and subsonic diffuser. Since the flow is theoretically speaking supposed to enter the subsonic diffuser at subsonic speeds, one can imagine that this belated deceleration of the flow will cause problems at the engine face and consequently the vehicle performance due to the flow entering the combustion chamber with an excess velocity. If an intake operates at subcritical conditions, which is when the backpressure becomes higher than the design value, the terminal shock wave gets driven out of the duct and a bow shock is formed in front of the intake entrance. Here, subsonic spillage drag occurs since subsonic flow is spread around the intake which causes additional drag. The highest performance results are found at the critical condition, where the terminal shock wave is tangent to the intake cowling lip. In this condition, the OSW that is formed at the compression surface slightly passes the intake lip, preventing spilled air, and therefore removing any additive drag. However, since the critical condition, due to free stream disturbances and changes in flight Mach number, is almost always unstable, the intake undergoes subcritical or supercritical operation and its parameters vary as a result of shock oscillations.

The different criticality levels for supersonic intakes are visualised in [Figure 2.34](#). In this figure, a graph is shown with the TPR as a function of the Mass Flow Ratio (MFR) given the different flow criticality scenarios. All the results shown in [Figure 2.34](#) hold for the design Mach number.

[Figure 2.34](#) works as follows: When the ramjet engine is started, the flow should accelerate to supersonic conditions, which requires the normal shock to pass the duct. Upon reaching supersonic conditions, the intake operates in the supercritical condition ([Figure 2.34\(a\)](#)). If the backpressure is increased, for example by throttling a butterfly valve downstream of the intake, the terminal shock is pushed upstream until it gets to the throat of the intake's duct. If the intake duct has a significant constant-area region, the intake is considered to operate at the critical condition until when the terminal shock is located at the duct entrance, tangent to the cowling lip ([Figure 2.34\(b\)](#)). The last stable point in between the supercritical and critical conditions, at which the terminal shock is located in the constant-area duct but does not initiate any shock oscillations, is known as the near-supercritical condition. In the critical condition, the TPR is maximized while the MFR has

slightly decreased. When the backpressure is increased even further, the terminal shock is pushed out of the duct and starts to interact with the OSW at the supersonic diffuser, which as mentioned before will generate the shear layer. Here, the flow has reached the subcritical condition (Figure 2.34(c)). Also, as mentioned previously, since the terminal shock will deflect the streamlines away from the intake, the MFR decreases rapidly when the intake goes from critical to subcritical operation. If the backpressure increases beyond this point, the interaction between the oblique and normal shocks gets pushed to even more upstream positions, resulting in the shear layer being ingested by the intake which subsequently leads to a strong decay of the TPR and the occurrence of shock oscillations which give rise to the well-known buzz phenomena. As a last note and in agreement with the explanation of section 2.1, the higher the flight Mach number the more the profile shown in Figure 2.34 is translated downwards.

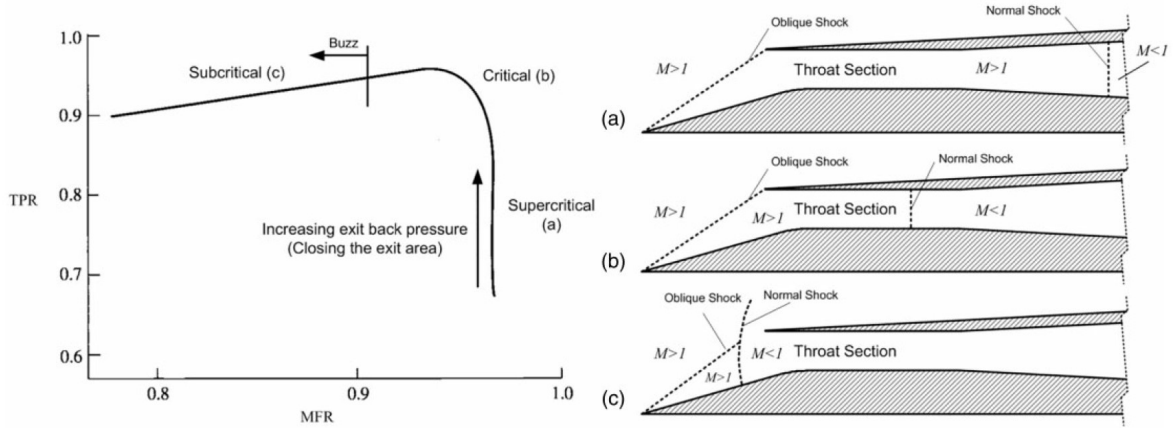


Figure 2.34: Diagram showing the influence of flow criticality on intake performance, taken from Soltani et al. [83].

2.5.2. Limiting Contraction Ratio

To perform optimally, supersonic intakes must 'start', implying that the flow should reach the design conditions. To ensure this, the flow must first accelerate from subsonic to supersonic velocities to enter the supercritical condition as was explained in subsection 2.5.1. Next, the backpressure is increased to make the intake reach the critical condition. The essential part of this procedure is to make sure the intake reaches supersonic speeds in the internal duct, especially for intakes with converging ducts. The only way of ensuring supersonic flow in the internal duct is by generating a terminal shock at or aft of the throat in the internal duct. When an intake is fully choked, a bow shock is formed in front of the converging duct. If the choking is relieved, the bow shock will be swallowed inside the duct and the flow will start to accelerate to supersonic conditions. Based on fundamental aerodynamics, subsonic flows accelerate in converging ducts while supersonic flows decelerate in the same geometry. Knowing this, it may be that the flow reaches sonic speeds before arriving at the duct throat section. In that case, the flow is choked and the terminal shock wave will not move downstream which means that the design conditions will not be met.

The rate at which sonic conditions are reached is determined by the contraction ratio. When speaking of this parameter at the throat section, it is known as the limiting contraction ratio. Because Kantrowitz was the first to derive an expression for the limiting contraction ratio, it may be sometimes referred to as the Kantrowitz ratio in literature. The derivation of this parameter is omitted in this report but can be found in the report by Kantrowitz [61]. The limiting contraction ratio can be written as (Equation 2.40):

$$\chi = \left(\frac{A_{throat}}{A_c} \right)_{lim} = \left(\frac{\gamma - 1}{\gamma + 1} + \frac{2}{(\gamma + 1)M_\infty^2} \right)^{\frac{1}{2}} \times \left(\frac{2\gamma}{\gamma + 1} - \frac{\gamma - 1}{(\gamma + 1)M_\infty^2} \right)^{\frac{1}{\gamma - 1}} \quad (2.40)$$

where A^* is the cross-sectional area at the throat section, A_c is the cross-sectional at the duct entrance, M_∞ is the freestream Mach number and γ is the ratio of specific heats.

In Figure 2.35, the reciprocal of the contraction ratio is shown as a function of the design Mach number. The primary limits of the contraction ratio are the Kantrowitz and isentropic limits. In Figure 2.35,

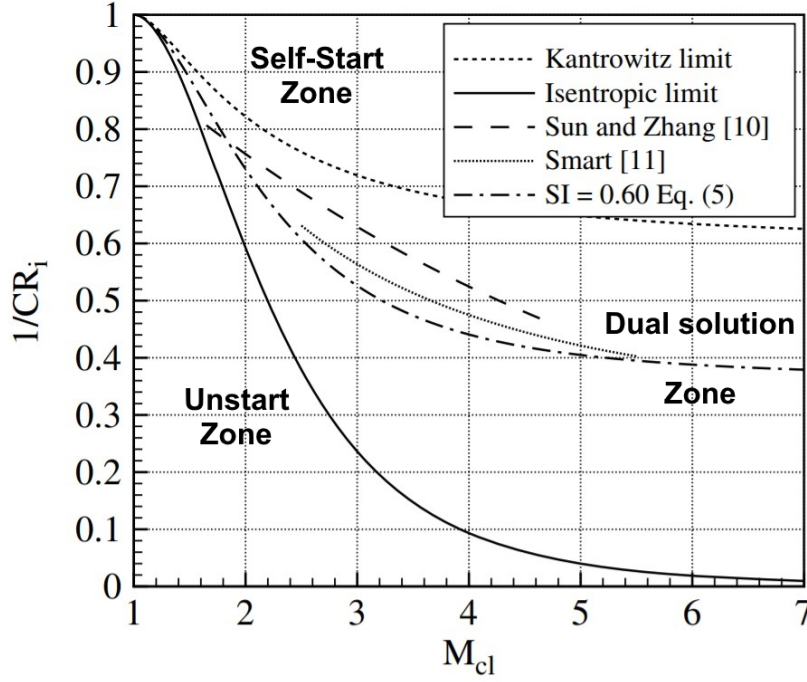


Figure 2.35: Kantrowitz diagram along with isentropic and Kantrowitz limits together with empirical relations, taken from Flock and Gülhan [84]

three regions are bounded by these two limits: first, a region in which intakes cannot work physically of $CR > CR_{isent}$; second, a region in which intakes are self-starting according to the Kantrowitz theory of $CR < CR_{Kant}$; and third, a critical region in between where intakes can work once successfully started. It can be concluded that the two main parameters that influence intake start are 1) the contraction ratio because, for a constant Mach number, intakes with low contraction ratio are more likely to start than geometries with high contraction; and 2) the flight Mach number because, for a constant contraction ratio, intakes are more likely to start when the Mach number is increased, which is known as overspeed and was verified by Timofeev et al. [85]. Note that there is a limit in the contraction ratio for $M \rightarrow \infty$, which imposes a limit on the influence of the Mach number. For air and a ratio of specific heats of $\gamma = 1.4$, this limit is written as (Equation 2.41):

$$\lim_{M \rightarrow \infty} CR_{Kant.} = \left(\frac{\gamma + 1}{\gamma - 1} \right)^{0.5} \left(\frac{\gamma + 1}{2\gamma} \right)^{1/(\gamma-1)} = 1.666 \quad (2.41)$$

Flock and Gülhan [84] reported that other parameters such as the Reynolds number, the total freestream-to-wall temperature ratio and the boundary-layer thickness were found to have minor influences on intake starting.

2.5.3. Shock Oscillations

It is important to stress again that conducting experiments on supersonic intakes requires knowledge on the operational limits. Shock oscillations can be very detrimental to any supersonic intake and knowing how these oscillations are initiated and how these can be stopped is key for any experimental vehicle.

When the backpressure is increased, the terminal normal shock is expelled from the duct and a detached bow shock is generated ahead of the intake entrance. This is known as the forward limit of the oscillation. Because the flow velocity at the intake entrance is now reduced, the bow shock will cause the mass flow at the intake entrance to be smaller than at the exit, due to which the bow shock is swallowed back into the intake. This is the rearward limit of the oscillation. When the mass flow at the intake entrance becomes bigger than at the exit, the intake is filled up and the terminal shock is removed again from the channel and the above cycle is repeated. Biedron and Adamson Jr. [86] investigated the unsteady flow in supersonic intakes caused by the fluttering of the terminal normal shock using asymptotic methods, which also involved inspecting what happens for different values of the characteristic time of the subcritical oscillations \bar{t}_{ch} and the residence time

of the fluid in the intake \bar{t}_{res} . This research lead to the formulation of a unified solution for determining the terminal shock position as a function of mainly the backpressure and the wall shape variations, which in turn is a function of time. Also, it was found that a high frequency of the backpressure oscillations would lead to a more stationary terminal shock in terms of position, while a low frequency would steadily push the terminal shock wave more upstream over time. This is shown in Figure 2.36.

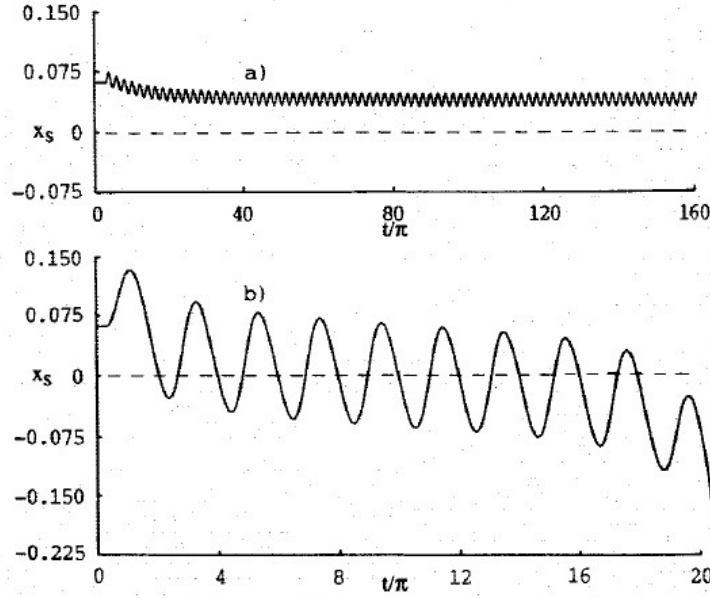


Figure 2.36: Effect of frequency of back pressure oscillation on shock wave response: a) $\bar{f}_r = 80\text{Hz}$, $\tau = 0.22$ and b) $\bar{f}_r = 10\text{Hz}$, $\tau = 1.76$, taken from Biedron and Adamson Jr. [86]

This back and forth motion of the terminal normal shock can be mitigated by lowering the intake's backpressure which is equivalent to throttling down a the ramjet engine or, in case of an experimental assembly, opening the intake's downstream end by relaxing the butterfly valve. Encountering excessive and repetitive shock oscillations, frequently known as buzz, can lead to very dangerous situations which jeopardize the vehicle and, in the case of manned vehicles, also personnel aboard the vehicle. One of the very common cases for the occurrence of buzz is when a thick boundary layer interacts with a strong adverse pressure gradient in the duct. This causes the boundary layer to separate and may lead to flow blockage which subsequently increases the backpressure. The latter will then trigger the oscillating and cyclic motion of the terminal normal shock in the duct. Another case is when a shear layer makes contact with the boundary layer in the internal flow. The criterion in this case is known as the Ferri criterion, named after Ferri and Nucci for their experimental research on this interaction [87]. Upon contact, the shear layer will start to introduce two regions of different flow conditions in the duct, amongst which the low speed region is more prone to cause flow separation. However, when the distance between the shear layer and boundary layer is large enough, the probability of flow separation and therefore the instigation of shock oscillations becomes very low.

2.6. Submerged Supersonic Intakes

To submerge a supersonic intake, the geometry built inside the vehicle's hull should allow for the flow to turn at a specific angle which is known as the expansion angle. This means that the flow is being subjected to supersonic expansion, which increases the flow velocity. Supersonic expansion takes place by the formation of the Prandtl-Meyer expansion fan, which essentially consists of an infinite number of weak Mach waves that isentropically speed up the flow. The Mach number of a flow moving over a convex angle where a Prandtl-Meyer expansion fan is generated can be determined as (Equation 2.42):

$$v(M) = \sqrt{\frac{\gamma+1}{\gamma-1}} \cdot \arctan \sqrt{\frac{\gamma-1}{\gamma+1} (M^2 - 1)} - \arctan \sqrt{M^2 - 1} \quad (2.42)$$

where v is the Prandtl-Mayer angle, M is the Mach number and γ is the ratio of specific heats. Afterwards,

the flow deflection angle is calculated from (Equation 2.43):

$$\theta = \nu(M_2) - \nu(M_1) \quad (2.43)$$

where θ is the expansion angle and $\nu(M_1)$ and $\nu(M_2)$ are the Prandtl-Meyer angles related to the most upstream and most downstream flow conditions in the expansion fan, respectively. Combining Equation 2.42 and Equation 2.43, the flow acceleration around the convex angle can be calculated for any given deflection angle and upstream Mach number. By also knowing the downstream Prandtl-Meyer angle $\nu(M_2)$, the downstream Mach number can also be determined.

3

Experimental Arrangements

This chapter discusses the complete wind tunnel setup in which the presence of a submerged intake was simulated experimentally. In [section 3.1](#), an introduction is provided on the specific wind tunnel in which experiments were conducted. Following, [section 3.2](#) presents this report's coordinate system and [section 3.3](#) reports the complete experimental layout in the wind tunnel's test section.

3.1. Testing Facility

In accordance with both the past experimental campaigns that have been completed with the SSI model and the project goals for this research project, the experimental campaigns documented in the report were carried out in the ST-15 supersonic blow-down wind tunnel, located at the High Speed Aerodynamics Laboratory at the Delft University of Technology. Built in 1959, the wind tunnel became the first supersonic wind-tunnel of the Faculty of Aerospace Engineering of the said university. This blow-down tunnel is driven using dry air, stored in a pressure vessel of 300 m^3 at a pressure of up to 40 [bar] and is powered by a 6000 kW compressor. Upon wind tunnel activation, the air is expanded to the tunnel's settling chamber at the required total pressure which is controlled using a pressure regulator. The wind tunnel allows for multiple nozzle blocks, also referred to as Mach blocks, to be placed inside the test section to simulate different Mach numbers. If two nozzle blocks are used, the test section becomes a convergent-divergent nozzle with rectangular cross-section.

The ST-15 operational testing range includes Mach numbers from 1.5 to 3 with increments of 0.5. The Mach number reached in the tunnel depends on the Mach block installed upstream of the test section. Depending on the run time of the ST-15, between 0.5 and 1.5 [bar] of air is used for every single run. In this report, all experimental campaigns were tested at Mach 2.0. The maximum total pressure is $p_0 = 15\text{ bar}$, but for tests performed at Mach 2.0 the operational total pressure in the settling chamber can only be set in between $p_0 = 2.0\text{ bar}$ and $p_0 = 4.8\text{ bar}$ [88]. The maximum runtime is 20 minutes for a single wind tunnel run. Afterwards, the reservoir vessel has to be pressurized again.

The tunnel's complete test section, including the space occupied by the nozzles and Mach blocks, has a size of $1044 \times 150 \times 350\text{ mm}$, equivalent to nozzle length \times test section width \times test section height. The test section space disregarding the nozzle and Mach blocks, is $150 \times 150 \times 250\text{ mm}$, which corresponds to the test section's length \times width \times height. Comparatively large windows with a diameter of 250 mm on the port and starboard sides of the wind tunnel provide a large field of view for non-intrusive optical measurements, such as Schlieren imagery and Particle Image Velocimetry (PIV). The ST-15 also features two side-mounted doors that can be fully opened to gain access to the test-section for maintenance and/or to change any nozzle blocks if required.

Since the air inside the settling chamber is stagnant, total conditions can be obtained by measuring pressure and temperature at the settling chamber. Upstream of the nozzle, two sheets of wire mesh are placed to weaken the turbulence intensity of the flow. Downstream of the test section, a mechanism is located which allows for placement of traversing probes in three directions. Finally, a diffuser is located at the end of the tunnel to minimize total pressure losses and to allow the wind tunnel to perform at lower pressure ratios. This diffuser is mounted on wheels which allows it to be retractable using a hydraulic system. When the diffuser is closed (i.e. connected to the wind tunnel test-section), minimal access is provided to the downstream

part of the test-section via a hatch that is placed on the diffuser's port side. When the diffuser is retracted, the full downstream part of the test-section can be accessed for inspection and maintenance. In [Figure 3.1](#), a schematic is shown of the wind tunnel with its main components labeled.

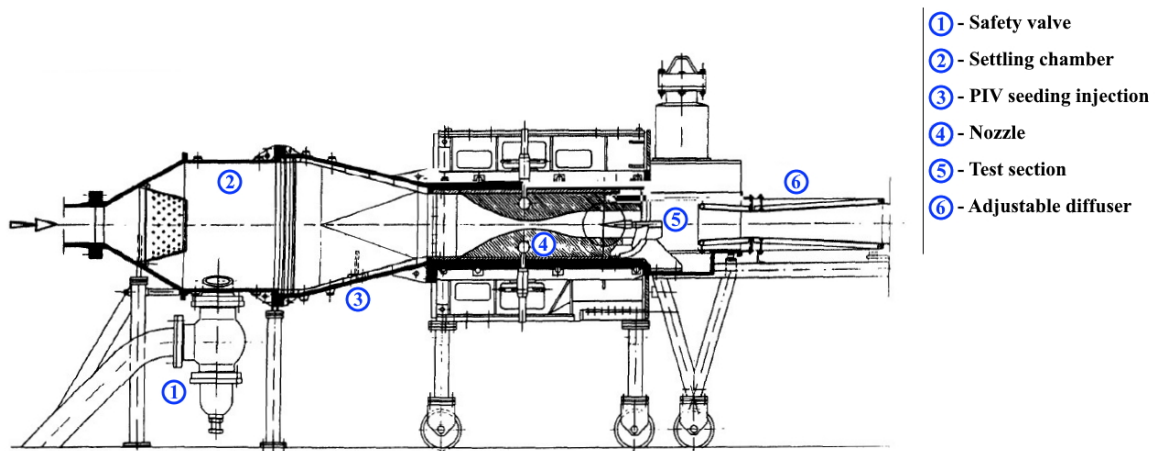


Figure 3.1: Schematic of ST-15 supersonic wind tunnel, taken from Flinkerbusch [89].

3.2. Coordinate system

The frame of reference used in the remainder of this report is a classical right-handed coordinate system, which is defined in the following manner: the x-coordinate corresponds to the flow direction and is defined as positive when facing the downstream direction; the y-direction corresponds to the flow-normal direction, parallel to the gravity force, and is defined as positive when facing upwards (i.e. opposite to gravity); the z-direction is defined as the out-of-plane component and is defined positive when facing the port side of the wind-tunnel. In this way, a right-handed coordinate system is defined for this setup. The origin of this coordinate system is, according to the above three coordinates, located at the leading edge of the compression plate (x-coordinate), along the compression plate main horizontal surface (y-coordinate) and on the out-of-plane center of the compression plate (z-coordinate).

3.3. Experimental Setup

In this section, the complete setup used for the experimental campaigns discussed in this report is explained in full detail. In [subsection 3.3.1](#), the main setup inside the wind tunnel test section is described whereas in [subsection 3.3.2](#), the Submerged Supersonic Intake (SSI) model placed inside the test-section is explained. Also, in [subsection 3.3.3](#) some final images are shown of the test setup as a whole.

3.3.1. Wind Tunnel Setup

Since all experiments documented in this report were meant to be analyzed at Mach 2.0, a Mach 2.0 block was placed at the top of the wind tunnel's test section. Since the SSI is being used to investigate the effect of a submerged intake's effect on the performance of a cruise missile, the lower block was not a Mach block but a green plug nozzle block, belonging to a former PhD-project by Wisse [90], which simulates the missile fuselage ahead of the submerged intake. Finally, an expansion block was placed immediately downstream of the plug nozzle block on the lower side of the tunnel's test section. This expansion block assembly was connected downstream of the plug nozzle block using an auxiliary wind tunnel block. The flow deflection angle from the plug nozzle block over the expansion block was 14° . In [Figure 3.2](#), a 3D CAD view is shown of the different wind tunnel blocks in an exploded view. Also, [Figure 3.3](#) and [Figure 3.4](#) show an isometric view and a side view, respectively of the wind tunnel setup when connected together.

The expansion block is used to simulate a smooth transition for the flow over the plug nozzle block to the flow through the submerged intake. The most downstream horizontal part of the expansion block con-

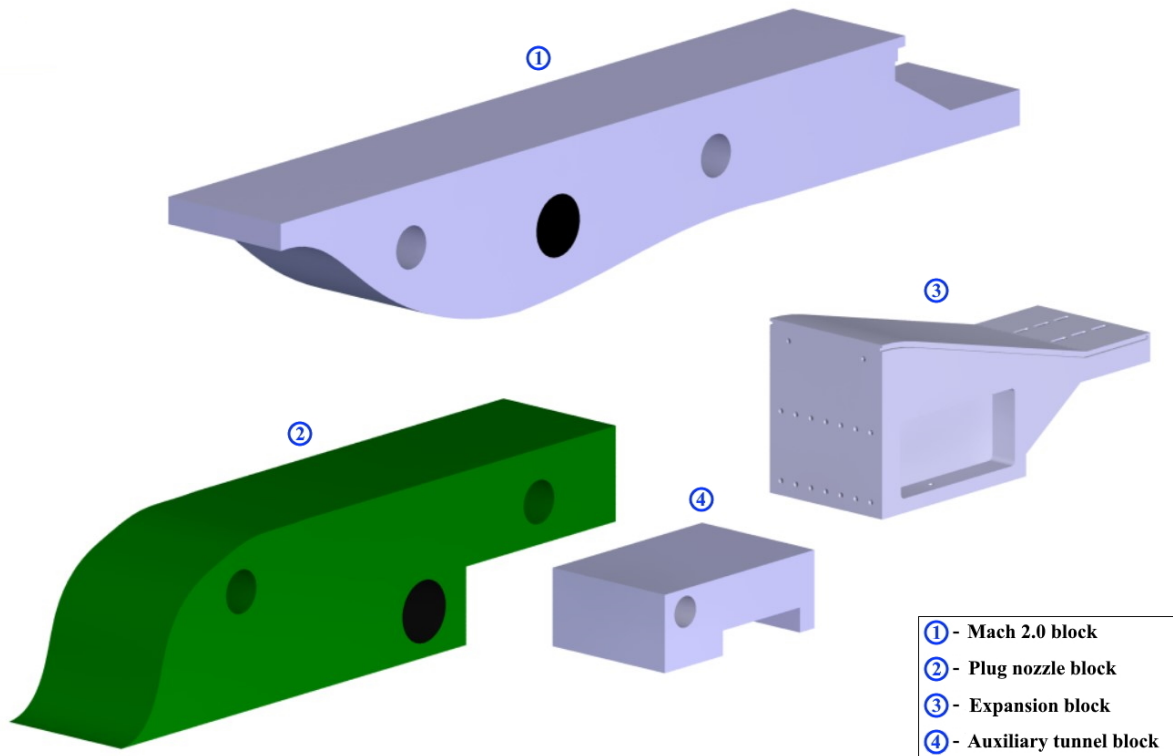


Figure 3.2: Exploded view of the wind tunnel setup without the SSI model.

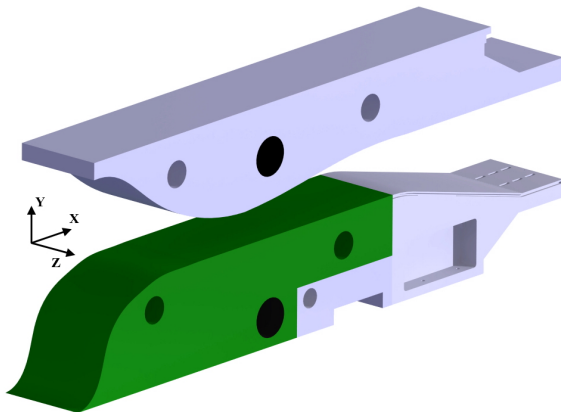


Figure 3.3: Isometric view of the wind tunnel setup without the SSI model.

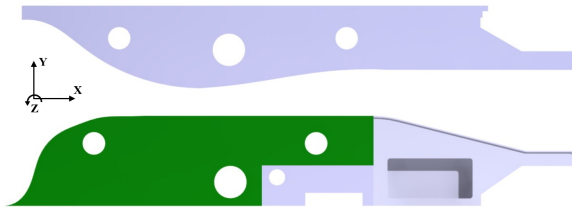


Figure 3.4: Side view of the wind tunnel setup without the SSI model.

tains six cylindrical holes to allow placement of the SSI model using two pylons. The reason why these holes were drilled in a cylindrical fashion stems from the perspective of including performance analysis of the SSI model at different streamwise positions to investigate the effect of boundary bleed underneath the SSI model.

3.3.2. SSI Model Setup

The SSI model consists mainly of four parts that make up the boundaries that confine the flow through the intake. These are the cowling on the top, the compression surface at the bottom and the two plexiglass sidewalls mounted on the sides, adjacent to both cowling and compression surface. The sidewalls are connected to both cowling and compression plate using two sidestrips with drilled out holes at each side. The supersonic diffuser has two compression surfaces, turning the flow twice by an angle of 7° and therefore generating two

oblique shock waves (OSW). The constant-area duct formed by the different parts mentioned above has an area of $6.7 \times 12 \text{ mm}$, which is the channel width \times channel height. This is then followed by the subsonic diffuser, which has a 6° outward deflection on the compression surface. When combined with the straight wall of the cowling on top, the net diffuser divergence becomes 3° . Figure 3.5 shows the different parts that form the SSI model in an exploded view. Moreover, an isometric view and a side view of the SSI model are shown in Figure 3.6 and Figure 3.7, respectively.

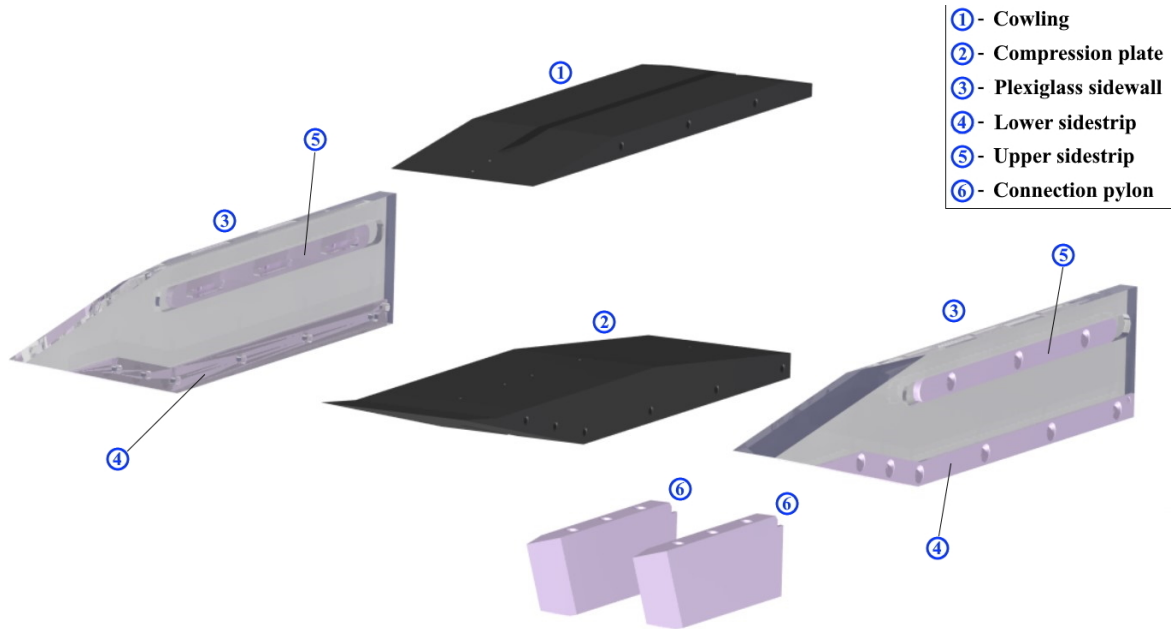


Figure 3.5: Exploded view of the SSI model.



Figure 3.6: Isometric view of the SSI model.

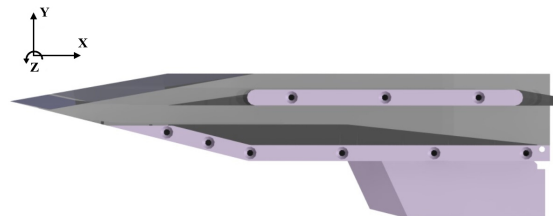


Figure 3.7: Side view of the SSI model.

In the following paragraphs, each of the SSI parts will be discussed in detail.

Cowling The cowling forms the upper boundary of the SSI. An isometric view and a side view of the cowling are shown in Figure 3.8 and Figure 3.9. The cowling streamwise placement in the SSI is an important factor since this will determine the length of the constant-area duct region of the intake. However, an inevitable constraint to the cowling location is that, depending on the Mach number, the OSW from the supersonic diffuser may not enter the duct nor are these allowed to pass the duct by a large margin. This has to do with the optimal operational condition of the intake to perform at the critical condition, which requires the OSW system to touch the cowling leading edge. However, since this only holds in theory, in practice this will not be possible due to the OSW potential reflection at the cowling leading edge. Therefore, the OSW are required to miss the cowling by an infinitesimal distance (see subsection 2.5.1). Even though the above information is of

crucial importance, only one cowling location will be used knowing that the Mach number will not change. Due to sharp edges getting quickly damaged during experiments, the cowling leading edge is not sharp but slightly dulled. The leading edge has a curvature with a diameter of 0.1 mm . Therefore, shock waves formed on the cowling's leading edge may be displaced of it as a result of this imperfection. Consequently, this may affect the quality of the experimental results. The cowling contains 10 pressure ports that were chosen based on the anticipated behavior of the pseudo-shock inside the intake.

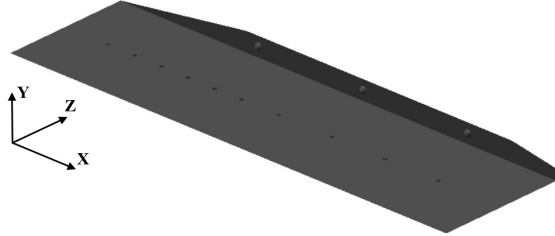


Figure 3.8: Isometric view of the cowling.



Figure 3.9: Side view of the cowling.

Compression surface The compression plate forms the lower boundary of the SSI. Only one compression plate was used during the experimental campaigns, which was a double-shock compression plate. This part fulfills the same purpose as any upstream wedge in generic supersonic intakes, which is to create one or more OSW to initially compress the upstream flow before it enters the enclosed duct. The double-shock compression plate as seen in Figure 3.10 and Figure 3.11 compresses the flow using two OSW, hence the name double-shock. The flow downstream of the expansion corner experiences therefore twice a deflection of 7° .



Figure 3.10: Isometric view of the double-shock compression plate.



Figure 3.11: Side view of the double-shock compression plate.

Similar to what was explained with the cowling, the compression plate's leading edge is not sharp but slightly blunted. The leading edge has a slight curvature with a diameter of 0.1 mm . This will cause any shock waves formed on the compression plate's leading edge to get marginally curved, or in very unfortunate cases even detached. Also, for the double-shock compression plate, the corner between the plate's front lip and horizontal surface, which causes the second OSW, is not sharp but again dulled. Similar to the situation on the leading edge, this will again cause the OSW not to be a perfect shock wave of infinitesimal size. On the contrary, this particular corner will likely experience a fan-like region of isentropic compression waves. The compression plate contains pressure ports just like the cowling. These pressure ports have a diameter of 0.6 mm on the channel side and 3 mm on the back side of the compression plate. Also, the back side is used to place pressure capillaries that lead to the pressure transducers that will read out the wall static pressure inside the duct. The double-shock compression plate has a total of 13 pressure ports. Just as with the cowling, the pressure port locations were chosen based on the presumed behavior of the viscous flow effects inside the duct. To take into account that the backside of both cowling and compression plate will contain pressure capillaries, the backside of both cowling and compression plate contains a shallow region to stash the pressure capillaries. In Figure 3.12, the backside of the cowling and compression plates is shown which contains the shallow region in each of the parts.

After securing the pressure capillaries into the pressure ports located at the shallow backsides of both cowling and compression plate, it was decided to fill these shallow regions with epoxy to prevent the pressure

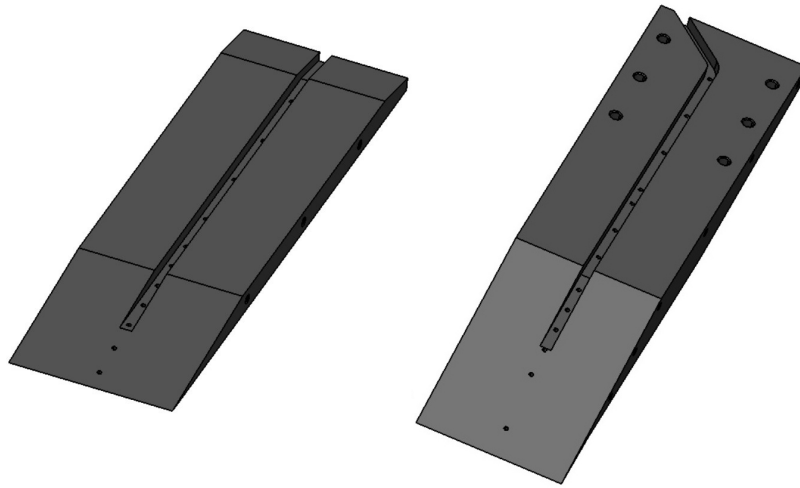


Figure 3.12: The shallow regions on the backside of the intake parts. Left: cowling, right: double-shock compression plate.

capillaries from possibly ejecting from the pressure ports during any wind tunnel runs.

The static pressure port locations are chosen in such a way to capture the flow behavior at the following points of interest:

- Upstream of the constant-area duct to measure the pressure of the compressed flow in the supersonic diffuser.
- Inside the duct, in particular to analyze the pseudo-shock's effect on the the flow.
- Inside the subsonic diffuser, amongst others to verify whether the pressure in the diffuser reaches a plateau (peak pressure) or whether the pressure decreases (indicating that the entire pseudo-shock has taken place in the duct).

In [Figure 3.13](#) and [Figure 3.14](#), the location of the pressure ports on both cowling and compression plate are shown measured from their leading edges, respectively.

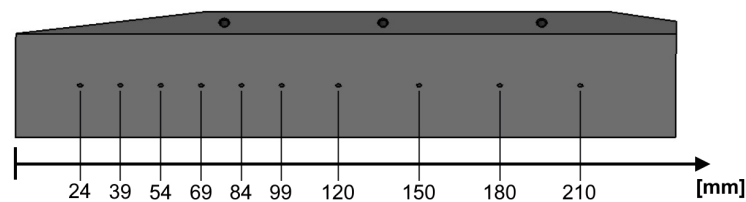


Figure 3.13: Streamwise location of the cowling pressure ports, measured from the leading edge.

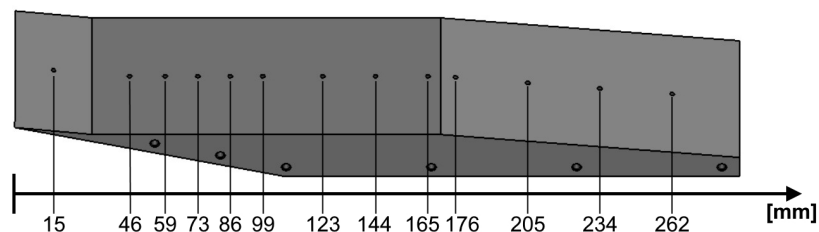


Figure 3.14: Streamwise location of the cowling pressure ports, measured from the leading edge.

Sidewalls The sidewalls, made from plexiglass, are used to hold the cowling and compression plate together. This is done using two sidestrips on each side of the intake to bolster the connection locations. The connection is made using bolts that flush with the surface to minimize flow distortion consequences. Also, using the plexiglass sidewalls is required to enclose the intake's internal channel to represent a quasi-genuine intake environment. To minimize the influence from the sidewalls on the flow, the upstream part of the sidewalls is tapered and the tapered parts are painted matte black to minimize any light distortions that may influence the Schlieren results. Moreover, the reason for the sidewalls being manufactured from plexiglass stems from the idea to have optical access into the intake's interior from outside the wind-tunnel. Also, having the sidewalls transparent in this manner allows for the use of several non-intrusive flow measurement techniques, such as Schlieren imagery and Particle Image Velocimetry. As a last note, it should be mentioned that the sidewalls were manufactured with a larger upper slot than actually required for connecting the cowling to the each sidewall by means of the sidestrips, which is clearly visible in [Figure 3.6](#). The reason for having these extended upper sidestrip slots on the sidewalls is to allow for sufficient fine tuning of the cowling streamwise position to make sure the last OSW from the supersonic diffuser narrowly passes the cowling leading edge, which is a requirement for proper supersonic intake design as discussed in [subsection 2.5.1](#).

Pylons The SSI model is placed on the expansion block, downstream of the expansion corner, using two stainless steel pylons. Since the compression plate has six holes located downstream on its backside, as is also visible from [Figure 3.12](#), six stainless steel hex bolts are fitted through the compression plate and the pylons to connect these together and in turn to connect this assembly to the expansion block through the six connection holes that were milled out of the expansion block. The pylons' connection holes are shown in [Figure 3.15](#). From this figure it also becomes clear that the connection holes on the expansion block are not ordinary holes with one fixed diameter, but rather elongated slots. This was a design choice meant to provide possibilities for adding a degree of freedom along the streamwise axis to the SSI model. In this fashion, the model can shift along a streamwise range of 16 *mm*. Doing so allows for researching the model behavior with different distances to the expansion block, to investigate different boundary layer bleed cases.

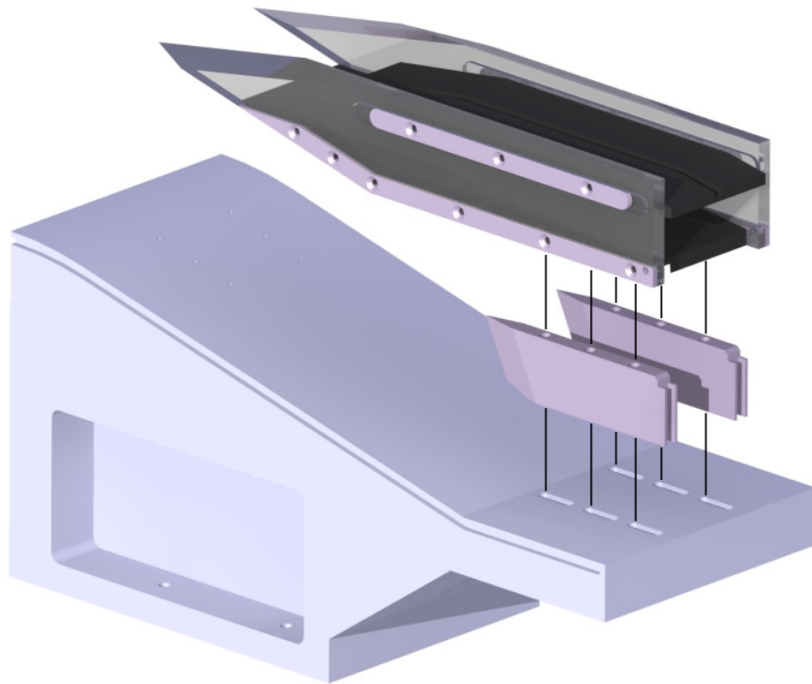


Figure 3.15: Connection between expansion block - support pylons - SSI model.

As a final note, [Figure 3.16](#) shows how the submerged intake is separated in different domains of interest. Also, it shows what the compressible and viscous flow effects are per domain and how each domain contributes to the comprehensive purpose supersonic intakes fulfill. The dotted blue path drawn in [Figure 3.16](#) beneath the blue solid trajectory represents the boundary layer bleed effect.

Domain	Pre-intake region	Supersonic diffuser	Constant-duct	Subsonic diffuser
Flow features	Expansion fan	Oblique shock system	Pseudo-shock	Post pseudo-shock flow
Local purpose	Turning the flow inwards	Initial flow deceleration	Primary flow deceleration mechanism	Final flow deceleration

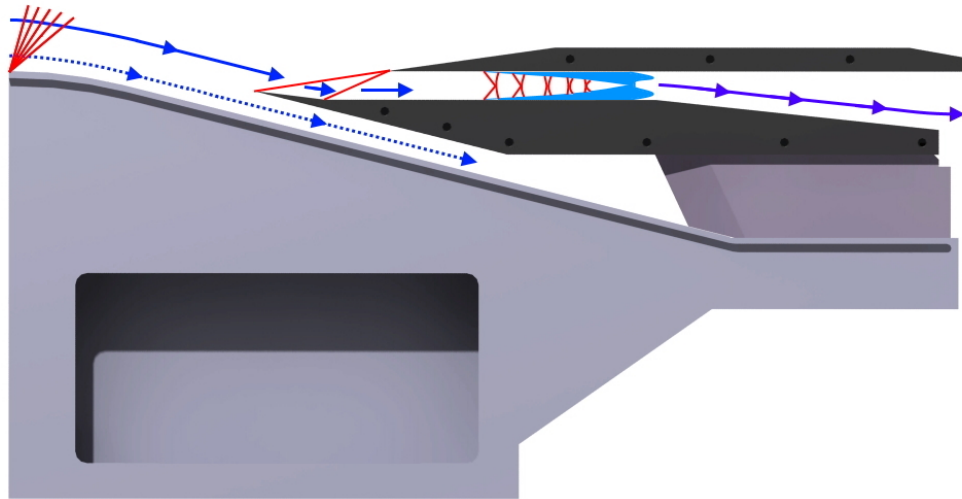


Figure 3.16: Flow path representation of the SSI model with an indication of the different intake regions.

Throttle system At the end of the subsonic diffuser, which also marks the end of the submerged intake, a butterfly valve is located. This valve can be imagined as being the throttle that determines the performance level of the complete projectile. This butterfly valve controls the mass flow captured by the intake and, more importantly, it also controls the supersonic flow condition of the intake. The butterfly valve is controlled using a servo that would rotate this valve upon external control using an arduino control system. The complete actuation system with all different components is shown in [Figure 3.17](#). Also, [Figure 3.18](#) and [Figure 3.19](#) show the complete throttle system while installed on the test setup from both an isometric and a side view, respectively. As a side note, the butterfly valve in the aforementioned figures is shown with a distinct color from reality to make it easier to identify the valve amongst the remainder of the SSI. To make wind-tunnel experiments less insecure, all used butterfly valves were anodized in black since the use of any paint could pollute the wind-tunnel.

The servo is seen attached to the expansion block, on the opposite side of where the SSI model is placed on the same block. To attach the servo firmly, two brackets of different geometry were used to clamp the servo underneath the expansion block. These brackets differ in geometry due to the asymmetry of the servo used for this report's experimental campaigns. One side of the servo contains the cluster of electronic cables and the other side is clean. Next, a pushrod was used of which the length was adjustable based on the required deflection of the butterfly valve. This pushrod is connected between the servo and the butterfly valve lever, which directly operates the butterfly valve itself. Through the port-side plexiglass sidewall of the SSI model, the valve lever is screw-connected to the butterfly valve.

When the flow is minimally blocked by the butterfly valve or not at all, the intake remains in the supercritical condition (i.e. the terminal shock wave is located deep inside the channel). When the valve substantially blocks the flow, the critical condition is reached (i.e. when the terminal shock wave is located at the opening of the internal channel and keeps oscillating back and forth). The upper deflection limit of the butterfly valve corresponds to the position at which the intake's critical condition is achieved. Deflecting the valve beyond this point makes the intake enter subcritical conditions, which creates the well-known buzz phenomenon. To accurately find the best situation in which the intake performs at the critical condition with the least shock oscillations, a total of three different butterfly valve designs were tested.

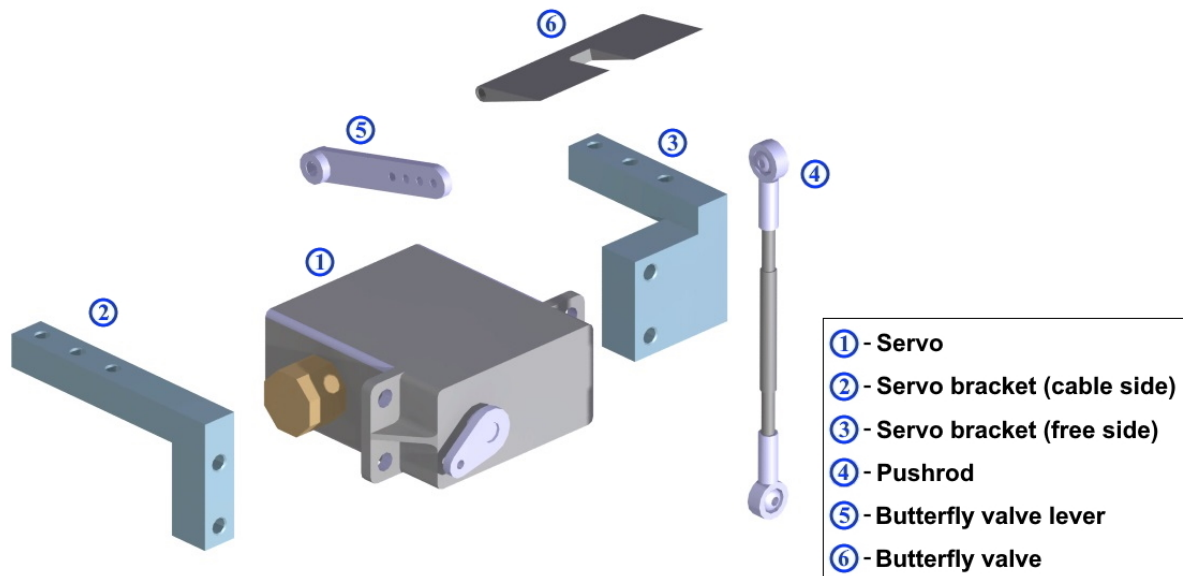


Figure 3.17: Exploded view of the throttle system of the SSI model.

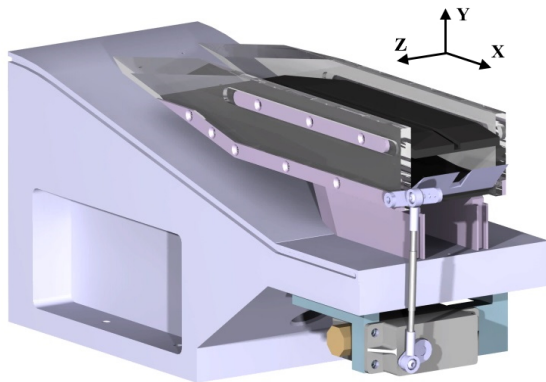


Figure 3.18: Isometric view of the expansion block containing the SSI model and the throttle system.

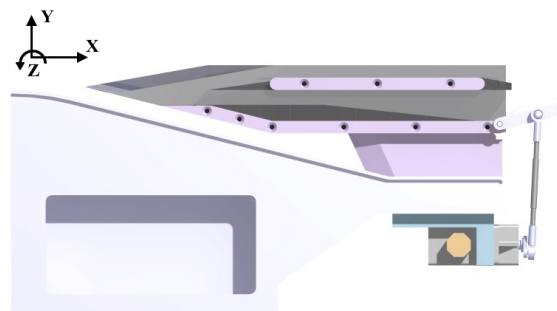


Figure 3.19: Side view of the expansion block containing the SSI model and the throttle system.

These valve designs had the following shapes:

- Airfoil
- Arc
- Diamond

In [Figure 3.20](#), each of these butterfly valve designs is shown in both an isometric view and a side view. As becomes visible from all designs, a $10 \times 19 \text{ mm}$ section was removed from the valve's center. This was done on purpose to allow the PIV laser to enter the test section through this slit for creating the laser sheet required to conduct proper PIV measurements.

The best location for the valve's pivot point is the bottom of the internal channel to avoid any interference with the PIV laser. However, at this location the torque required to rotate the valve was fairly large. This can be traced back to the large force that was required to create this torque. The worst case scenario is when the pressure acting on the butterfly valve is equal to the total pressure, found in the settling chamber of the wind-tunnel, which was 3.95 bar . Assuming that the worst-case scenario is a very rare situation that will certainly not occur on a regular basis, nor will it take place for a long period of time if occurring at all, it was decided

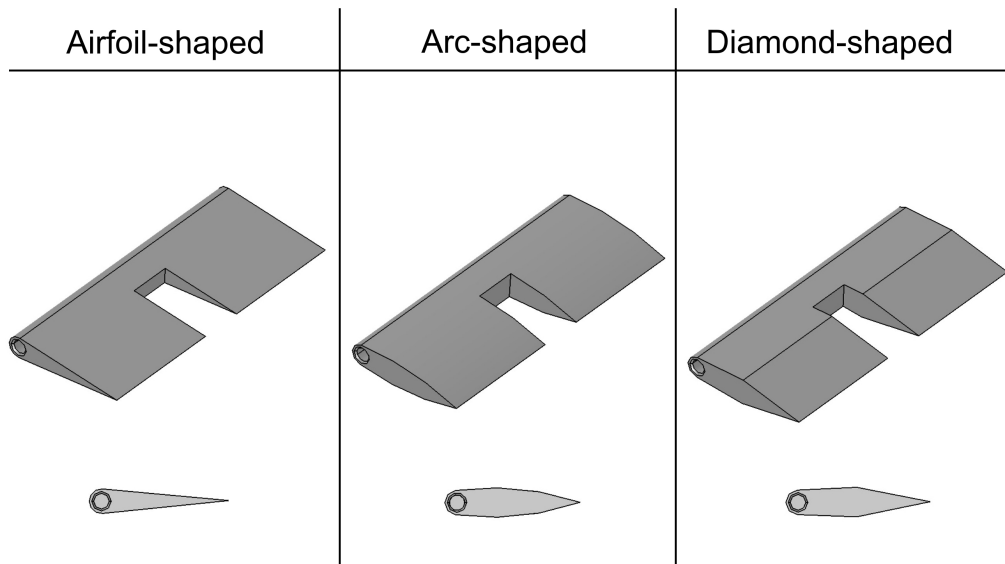


Figure 3.20: Overview of the three different butterfly valves used, seen from both an isometric view and a side view.

to assume a peak pressure that would be equal to half the total pressure in the settling chamber. Taking into account also the maximum allowable size of the valve and the lever distance between servo and butterfly valve, it was found that the required torque would be equal to $75 \text{ kg} \cdot \text{cm}$. Therefore, the actuation system controlling the valve had to include a servo that was powerful enough to move the valve under these high torque requirements. The servo used for this report's project was the Hitec HS-1005SGT. This servo is capable of delivering a torque of $84 \text{ kg} \cdot \text{cm}$ when receiving 11 V from an external power supply and a torque of $110 \text{ kg} \cdot \text{cm}$ when receiving 14.8 V . The power supply used for this report's experiments was a Geti model: GLPS 3005E, capable of providing both constant voltage ($0\text{-}30 \text{ V}$) or constant current ($0\text{-}5 \text{ A}$). For this report's experiments, the only setting used was a constant-voltage of 14.6 V .

As a final note, [Figure 3.21](#) shows an image taken of the complete actuation system when mounted in the wind tunnel setup.



Figure 3.21: Image of the complete actuation system mounted in the wind tunnel, taken from an isometric view.

3.3.3. Complete Setup

Following the explanation on how the test setup is constructed using the large wind tunnel blocks and the SSI model with its different components, the technical drawings of all the test setup parts and throttle system parts can be found in [Appendix A](#) and [Appendix B](#), respectively. In [Figure 3.22](#) and [Figure 3.23](#) the complete test setup is shown in 3D CAD from both an isometric view and a side view. In [Figure 3.24](#), an image is shown taken of the complete setup from a side view while mounted in the wind tunnel.

Also, to provide the reader with a strong impression of how this novel design topic would fit into reality, in [Figure 3.25](#) this report's test setup is shown while integrated into a generic cruise missile.

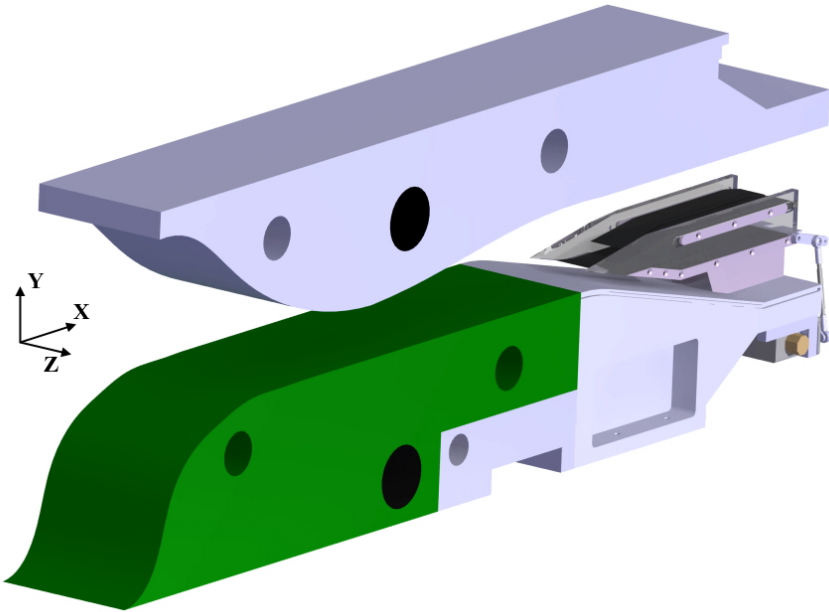


Figure 3.22: Isometric view of the complete test setup.



Figure 3.23: Side view of the complete test setup (3D CAD).

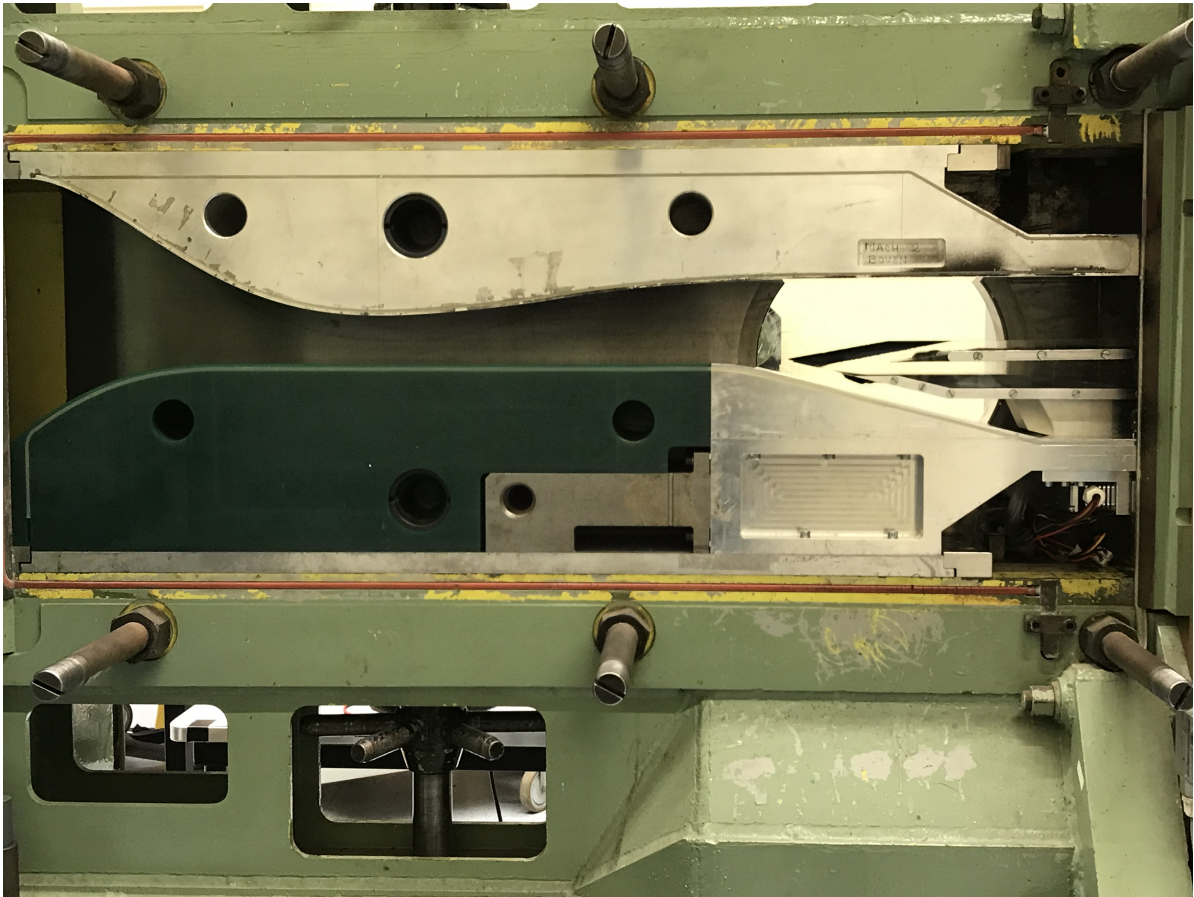


Figure 3.24: Side view of the complete test setup (real photograph).

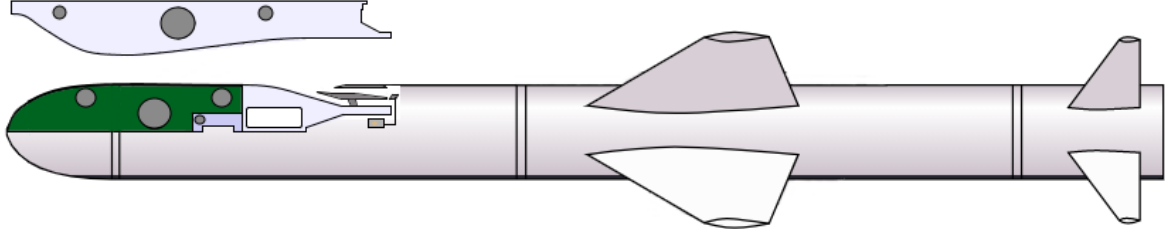


Figure 3.25: This report's test setup integrated into a modern cruise missile.

4

Flow Measurement Campaigns

In this chapter, a detailed outline is provided on the measurement techniques used and on this report's experimental campaigns. In [section 4.1](#), the organizational structure of this report's experiments is described. Following, in [section 4.2](#) to [section 4.4](#), the theory behind and the experimental setups is discussed for the Schlieren imagery, static pressure and Particle Image Velocimetry (PIV) campaigns, respectively. This includes the campaign preparation in terms of how the wind tunnel setups were organized and how the measurements were taken with the different flow measurement techniques. Finally, the uncertainty analysis to this report's measurement campaigns is discussed in [section 4.5](#).

4.1. Research Structure

Due to logistical reasons, two experimental slots had to be booked to finish all measurements which were deemed relevant for this research project. The first campaign revolved around conducting the same measurements that were done by Kwakman [91]. As explained beforehand, that particular campaign only included Schlieren imagery and static pressure measurements. Another reason for repeating this previous experimental effort was that the manufacturing of the parts for this report's throttle system was still pending. The Schlieren images from this first campaign would then serve as a reference to compare the static pressure measurements with. This first campaign as a whole would then eventually serve as a means of 1) getting familiar with testing in the ST-15 wind tunnel and 2) obtaining measurement results that would serve as flow diagnostics for the second and main research slot.

In this second research slot, Schlieren and static pressure measurements were again conducted, this time for the SSI model with the improved throttle system. After completion of that part, planar PIV was used to quantify the flow dynamics. The initial planning for the second testing campaign also included conducting pressure measurements parallel to the PIV measurements. The rationale behind this was to get both the static pressure (from pressure measurements) and the dynamic pressure (from PIV measurements) from every single wind tunnel run. This would then pave the way to determine the total pressure in the intake which is required to determine the total pressure recovery, and consequently the intake performance. However, due to the fact that the laser sheet for the PIV measurements caused considerable reflections at the pressure ports for both cowling and compression plate, it was decided in deliberation with the supervisor to cancel the simultaneous use of both static pressure and PIV measurements. Instead, it was decided to conduct PIV measurements and pressure measurements separately.

The flow conditions at which all experiments documented in this report were conducted are shown in [Table 4.1](#). It should be noted that the net total pressure in the settling chamber consists of both the actual settling chamber pressure in addition to the barometric pressure which was around 1 *bar*. As becomes clear from [Table 4.1](#), experiments were done only at Mach 2.0 since no PIV measurements could be done for any Mach numbers higher than Mach 2.0. This comes from the fact that for higher Mach numbers, the settling chamber pressure would become too high for the seeding particles to adapt well to the flow.

The complete test matrices used for all experimental campaigns are reported in [Appendix C](#). As will become clear from the PIV test matrix, the near-supercritical and critical conditions were tested more often than the supercritical condition. The reason to this is that only one butterfly angle was found to keep the

Parameter	Value	Unit
Freestream Mach number M_∞	2.0	-
Settling chamber pressure P_0	3.95	bar
Settling chamber temperature T_0	279.5	K
Freestream Reynolds nr. Re_∞	5.32e5	-

Table 4.1: Overview of the fixed parameters of this test plan's experimental campaign

intake in the supercritical condition, while two angles were found each at which the intake did operate in the near-supercritical and critical conditions. Although two angles were compatible with each of the near-supercritical and critical conditions, Schlieren imagery and static pressure measurements were only conducted at the steepest of each of the two angles for the aforementioned conditions. In the PIV test matrix, the two angles are indicated as the lower and higher angles. To efficiently make use of the testing facilities, it was decided to test all butterfly valves with the SSI configuration using both Schlieren imagery and static pressure measurements. Afterwards, the valve that provided the most decent results was then selected to be used in the PIV measurements. The criteria for choosing the best butterfly valve are described in [chapter 5](#).

Based on the results from the first testing slot, it was concluded that the effect of boundary bleed was of minor influence on the improvement of the intake's performance. Therefore, in agreement with the supervisor, it was decided to test the SSI model at one streamwise position only, which was chosen to be the most downstream location. This resulted in a boundary layer bleed slot width of 61 mm.

4.2. Schlieren imaging

Schlieren imaging is an optical technique that is used most often to qualitatively investigate flow features that would be impossible to capture with an ordinary camera setup, let alone by the naked eye. Examples of such features are shock waves, expansion waves and the boundary-layer. In this report, the Schlieren imagery measurement technique serves for two main goals:

First, the three butterfly valve designs introduced in [subsection 3.3.2](#) are tested and evaluated using the Schlieren imagery technique to find out which butterfly valve is the most robust option in ensuring stable supersonic flow in the presence of the pseudo-shock. This becomes especially important during the intake critical condition, where the terminal shock is known to make erratic oscillations because of which the pseudo-shock is repeatedly expelled from and swallowed by the intake. Second, during the PIV campaign, it is not possible to inspect the pseudo-shock location due to the fact that the PIV setup is blocking the view of the Schlieren setup. Therefore, it was chosen to carry out three wind tunnel runs for each of the supersonic flow conditions, which are the supercritical, nearly-supercritical and the critical conditions. This was done for all three butterfly valves. After completing all required runs, the arduino-history on the machine running the control software was inspected and the servo-levels corresponding to the different supersonic flow conditions were written down to confirm the reference levels at which the pseudo-shock reached the streamwise locations corresponding to the aforementioned supersonic conditions.

However, before one can speak of the experimental setup or the results of the Schlieren imagery technique, some background knowledge on the working principle of this technique has to be established first. In [subsection 4.2.1](#), the main theory of light propagation is discussed. Following, [subsection 4.2.2](#) explains the working principle of the Schlieren imagery technique. Finally, in [subsection 4.2.3](#) this report's Schlieren setup is presented.

4.2.1. Light Propagation Theory

When an electromagnetic ray crosses the interface between two media, the speed of light changes due to the transition to a new medium of propagation. This new medium has a different density which will cause the light rays to experience angular alterations, which are proportional to the refraction index n . The refraction index can be defined as ([Equation 4.1](#)):

$$n = \frac{C_0}{C} = 1 + K\rho \quad (4.1)$$

This equation states that the refractive index n is defined as the ratio of the speed of light in vacuum (C_0) to the local speed of light (C). A second formulation also states that the refractive index is a function of the

Gladstone-Dale constant K , which is a number that varies according to the composition of the medium, the wavelength of light and the local medium density ρ . For air, the value of K lies in between $K_{air} = 2.24 \cdot 10^{-4}$ and $K_{air} = 2.33 \cdot 10^{-4}$ [m³/kg] when going from infrared to ultraviolet light, respectively. The change of the refractive index is given by Snell's law and can be stated as (Equation 4.2):

$$n_1 \sin(\theta_1) = n_2 \sin(\theta_2) \quad (4.2)$$

Snell's law states that light rays get deflected upon change of the propagation medium. When light rays transition from a less dense medium to a more dense medium, light rays get deflected towards the normal line that runs through both media as shown in Figure 4.1, indicating that the light rays in this case are deflected towards the direction of increasing refractive index. The latter means that the second angle becomes smaller than the first angle, i.e. $\theta_2 < \theta_1$. Since light rays are deflected as a result of a change in density, and thus the refractive index, light rays will also be deflected when passing through compressible flow features with density gradients like shock waves.

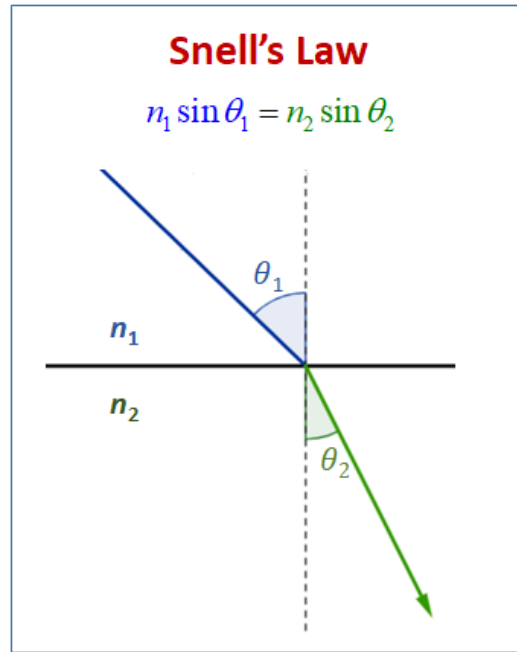


Figure 4.1: Deflection of light rays with Snell's law, Copyright-free

4.2.2. Principle of Schlieren measurements

To understand how a Schlieren image is generated, the ray equation must be introduced which is one of the fundamental equations of optical physics (Equation 4.3):

$$\frac{\partial}{\partial s} \left(n \frac{\partial x}{\partial s} \right) = \nabla n \quad (4.3)$$

where s is the light ray path length, x is the light ray trajectory and ∇n is the spatial gradient of the refractive index. The ray equation states that the variations experienced by light beams depend on the change in local refractive index. Equation 4.3 shows clearly that the light ray trajectory is proportional to the spatial gradient of the refractive index and hence, the density. The latter implies that any light ray will tend to move towards regions of higher density and move away from regions with lower densities (commonly referred to as rarefied flows). If a light ray experiences refraction and the testing domain has a finite width W , the light ray's displacement ϵ_x can be defined as (Equation 4.4):

$$\epsilon_x = \frac{\partial x}{\partial z} = \int_0^W \frac{\partial n}{\partial x} dz = \int_0^W \nabla n dz \stackrel{\text{Gladstone-Dale relation}}{=} \int K \frac{\partial \rho}{\partial x} dz \quad (4.4)$$

For a Schlieren image, the way light is perceived works as follows: Whereas for a shadowgraphy analysis the light is concentrated at the locations with high magnitudes for the second derivative of the density, for Schlieren imagery, a knife-edge filter will be placed at the focal point of the optical sensor to negate part of the light caught to reduce the amount of light perceived by the sensor. This explains why shadowgraphy images are generally more bright than Schlieren images. Assuming the area of the knife-edge filter open to light being a and if d is the additional deflection of the light trajectory, the light intensity caught in the sensor can be defined as (Equation 4.5):

$$\frac{I}{I_0} = \frac{a+d}{a} = 1 + \frac{f\epsilon_y}{a} \quad (4.5)$$

where f is the focal length or the distance between the knife-edge filter and the sensor. Hence, the variation of light intensity ΔI for Schlieren imagery can be written as (Equation 4.6):

$$\frac{\Delta I}{I_0} = \frac{f\epsilon_y}{a} = \frac{f}{a} \int_0^W \frac{\partial n}{\partial y} dz = \frac{f}{a} \int_0^W K \frac{\partial \rho}{\partial y} dz \quad (4.6)$$

Gladstone-Dale relation

This shows that the principle behind Schlieren images revolves around measuring the first derivative of the density through the width of a testing domain, which provides the use of this technique with directional judgement on the regions with high and low densities. Depending on the orientation of the blocked half of the knife-edge filter, high-density phenomena like shocks will appear as either bright or dark. This can be understood in the following way: Consider a shock wave captured in the test section of the Schlieren setup and let the knife-edge filter be placed horizontally to the right of the camera's viewpoint (i.e. on the downstream side). Since the light rays that pass through this shock will be deflected along a new angle according to Snell's law, the light rays will be shielded by the Schlieren knife edge filter and the shock will be shown as a dark line on the image. Regarding the opposite side of this principle, when the density gets lower than the surroundings of the test section, the light rays will get deflected away from the Schlieren knife. This will result in more light being caught locally, which subsequently causes bright lines to appear on the imaging plane. The extent of how much light rays are deflected depends on how much the refractive index changes. A generic Schlieren imagery setup in the classical z-configuration is shown in Figure 4.2.

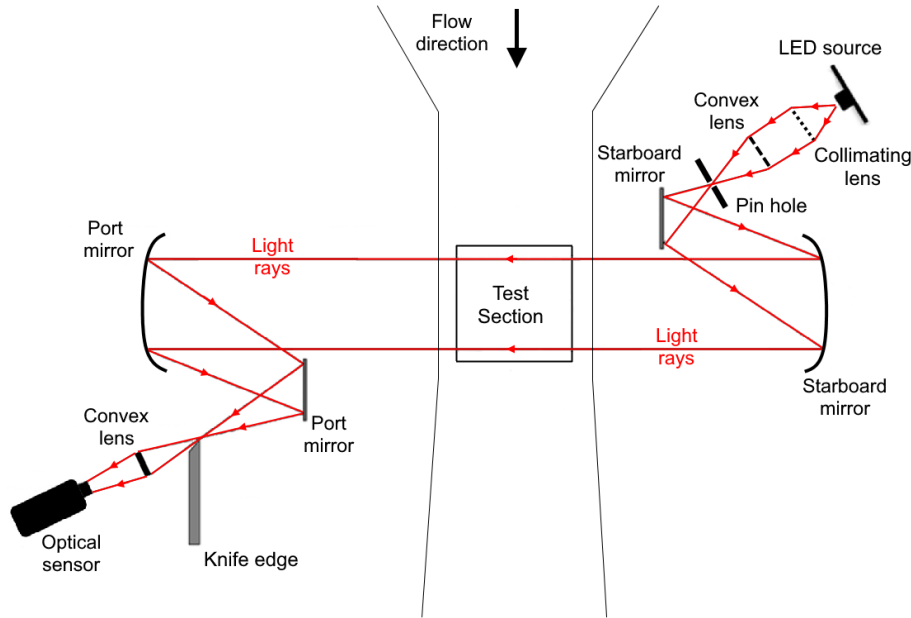


Figure 4.2: Generic Schlieren system setup in the common z-configuration.

4.2.3. Experimental setup

All items required to conduct this report's Schlieren measurements are listed in Table 4.2. The frame rate of the Bobcat camera used for this report's Schlieren measurements was set at 16 FPS. The knife edge filter's dark side was placed at the left-hand side of the optical sensor. Hence, knowing that light rays deflect towards regions with higher densities and that the air moves, from the camera's viewpoint, from left to right, shocks will be imaged as bright lines while expansion waves will be perceived darker. In Figure 4.3, a 3D CAD illustration is shown of the inventory items listed in Table 4.2 placed in the classical z-configuration along with the SSI model.

Item	Quantity	Details
Light source	1x	LED THORLBAS MCWHL1: $\lambda = 405 \text{ nm}$, $P = 1200 \text{ mW}$, THORLABS-LEDD1B controller
Collimating lens	1x	F2.5 lens with $f = 178 \text{ mm}$
Convex lens	2x	Convex lens with $f = 150 \text{ mm}$ Convex lens with $f = 80 \text{ mm}$
Pin hole	1x	Custom-made
Parabolic mirrors	4x	Two mirrors on each side of the test-section
Optical access test-section	2x	Circular Germanium windows with $d = 250 \text{ mm}$
Schlieren knife edge filter	1x	Custom-made
Optical sensor	1x	Imperx B1610M Bobcat CCD

Table 4.2: Detailed list of equipment used for the Schlieren imagery measurement campaign.

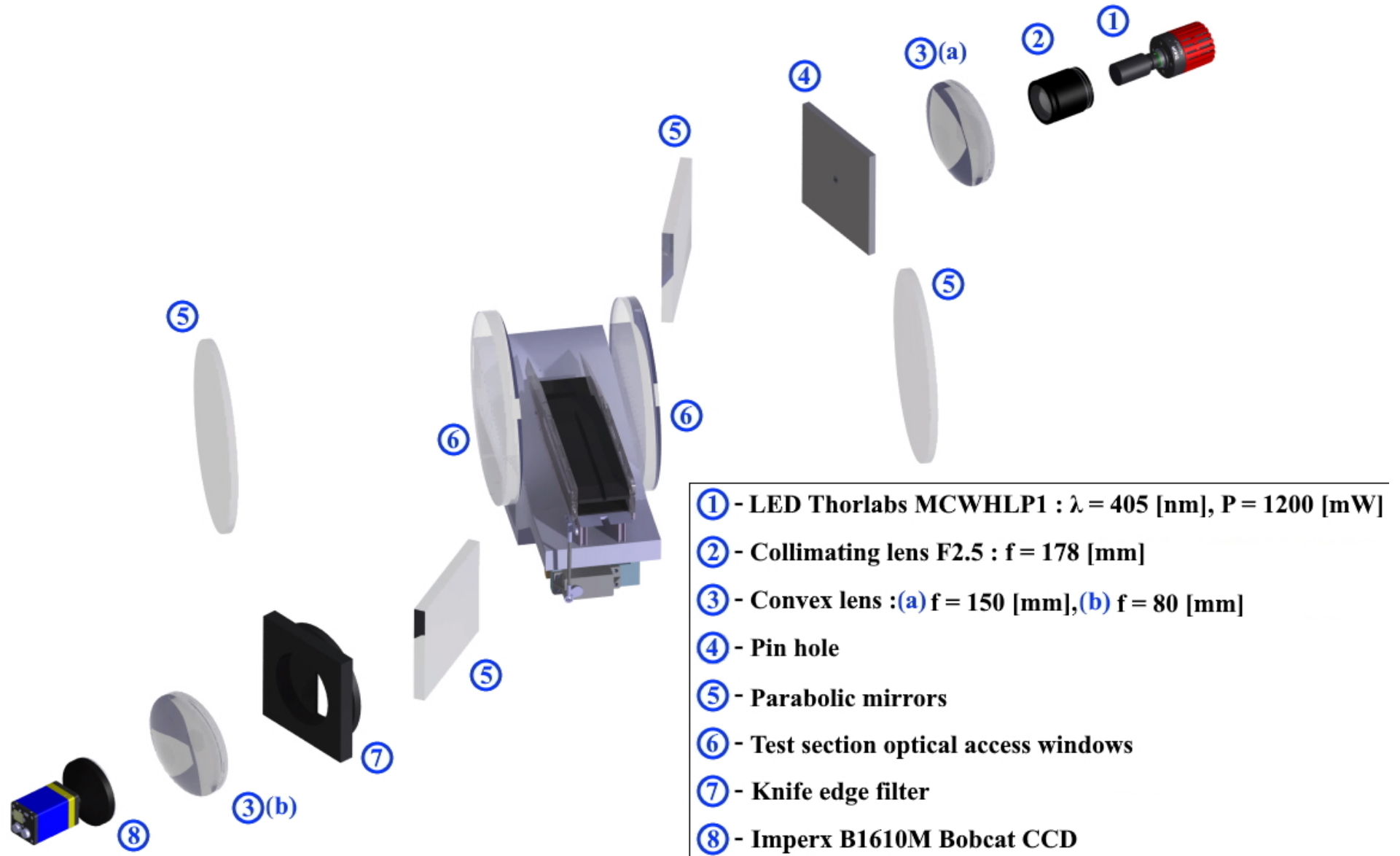


Figure 4.3: Complete three-dimensional CAD view of this report's Schlieren test setup, seen from the port side of the wind tunnel.

4.3. Static pressure measurements

Nowadays, a wide range of different pressure transducers and sensors exist that can aid in recording the local static pressure at specified locations using pressure capillaries that are connected between the locations of interest and the pressure transducer. Most devices do not record the absolute pressure but rather the relative pressure. This is the local pressure excluding the ambient barometric (atmospheric) pressure. Most pressure transducers require an external power supply and a stable connection (usually an Ethernet connection) to a machine that runs the specific utility software which is used to enter commands for calibrations, conducting measurements and storing the data. In Figure 4.4, a schematic is shown of the specific setup used for taking the SSI pressure measurements documented in this report.

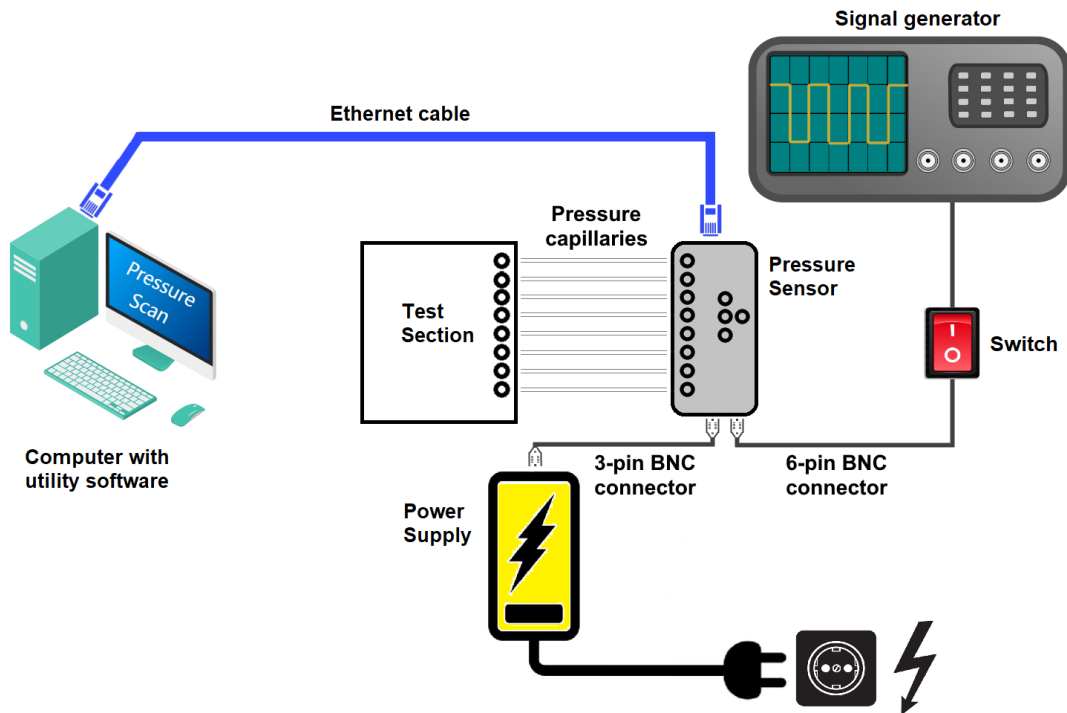


Figure 4.4: Schematic of the experimental static pressure measurement setup.

Flexible pressure capillaries were used to connect the cowling and compression plate pressure ports via the wind tunnel's starboard side swivel to the pressure transducers. In this report's experimental campaigns, the pressure transducers were two Scannivalve DSA3217/16Px sensors, which as the name suggests contain 16 pressure ports. These manometers had a differential pressure limit, excluding the barometric pressure, of 30psid ($\sim 2.0\text{bar}$) and 50psid ($\sim 3.5\text{bar}$). This fits the testing conditions, since the absolute total pressure in the wind tunnel's settling chamber is 3.95bar . Both Scannivalve transducers were able to measure 16 independent pressure readings simultaneously. Apart from the pressure ports of the cowling and compression plates, one additional capillary was connected to the ST-15 settling chamber to also read out the stagnation pressure during each wind tunnel run. The two manometers contained 8 auxiliary ports which can be found next to the pressure ports. These latter ports include control ports, calibration ports and reference ports. None of these additional ports were used during the experimental campaigns. For more information, the reader is referred to the Scannivalve DSA3217 manual [92].

The Scannivalve pressure transducer has a total of three connection ports. The first port, the Ethernet port, was used to connect the manometer to the machine that runs the utility software. The second port, the 3-PIN BNC port, is used to connect each Scannivalve unit to a 24-36 V power source. The external power supply for each Scannivalve device was a PDM1500 power supply that provided the required $28 \pm 8\text{ DC}$ voltage at approximately 8 W . The Scannivalve device's last and optional port, a 6-PIN BNC port, is used to arm external triggering to initiate a scan command by means of a switch. This port was used during this report's experimental campaigns to initiate a simultaneous pressure scan for all pressure transducers. This eliminates the need for manual triggering, which in the case of multiple Scannivalve units may result in inaccurate and

asynchronous results.

The software used to operate the Scannivalve sensors was Scantel V1.23, which is a utility program developed by the Scannivalve company. When operating the Scannivalve sensors during a wind tunnel run, the recorded results included the relative pressure and not the absolute pressure. To obtain the absolute pressure, the local barometric pressure was documented before every wind tunnel run. When adding the local barometric pressure to the Scannivalve results, the absolute pressure was found.

The scan rate at which the static pressure values were captured can be defined as follows (Equation 4.7):

$$f_{scan} = \frac{1}{\text{Period} \cdot 16 \cdot \text{Avg}} \quad (4.7)$$

The total number of frames, or data points, measured during a single run was set at 500. This means that all pressure ports on both cowling and compression plate acquire and save 500 distinct data points per run. The Period is the time interval in between two datapoints, expressed in microseconds. For this measurement campaign, a Period of 125 μs was used. The Avg, or the average, is the number of raw samples acquired before producing a single datapoint, which is the average of the acquired raw samples. An average of 5 was chosen for this report's measurements. This means that during a single frame, 5 raw samples are captured per pressure port and that the final output on a single data point is determined as the mean of these 5 raw samples. Therefore, the scan rate during the entire measurement campaign was set at 100 Hz . With a total of 500 frames per scan captured during each run, the acquisition time during every wind tunnel run lasted for 5 seconds. Note that this does not mean that the wind tunnel run time lasted for 5 seconds, since every wind tunnel run consisted of first successfully starting the intake and then rotating the butterfly valve to the desired position for reaching the favoured operating condition of the flow and only when these steps were realized, the pressure measurement sequence was commenced. Measurements were performed three times per flow condition. Each of these measurement runs was time-averaged to provide a single result per pressure port and the final results per pressure port per flow condition was then determined as the mean of the three individual time-averaged results.

The inventory list of items required to conduct this report's pressure measurements is shown in Table 4.3.

Item	Quantity	Details
Pressure sensor	1x 30 <i>psid</i> 1x 50 <i>psid</i>	Scannivalve DSA 3217/16Px
Pressure capillaries	23x	Flexible tubes with: $d_{outer} = 1.8 \text{ mm}$ $d_{inner} = 1.2 \text{ mm}$
Pressure sensor power supply	2x	PDM 1500
Switch	1x	Hand-pressed mechanical switch
Signal generator	1x	Stanford Research Systems Model DG535
Acquisition machine	1x	Running Scantel V1.23

Table 4.3: Detailed list of equipment used for the pressure measurement campaign.

The setup in the vicinity of the wind tunnel is shown in Figure 4.5. In this figure, the power supply units are shown placed on the ground which was done to make them closer to the power outlets. Additionally, in Figure 4.6 an image is shown of the real setup where the pressure capillaries are shown, how they enter the wind tunnel test section through the starboard-side swivel and how the settling chamber pressure is also measured through a capillary.

Finally, it should be noted that initiating a triggering command was done by connecting a signal generator, which was configured at a specific frequency, to the electrical circuit of the setup. By including a switch in between the scannivalve units and the signal generator, it was possible to initiate a scan-command at will for all pressure transducers at once. The signal generator used for the pressure measurements was a Stanford Research Systems model DG535 and the set frequency was 100 Hz , which is equal to the scan rate of the Scannivalve sensors.

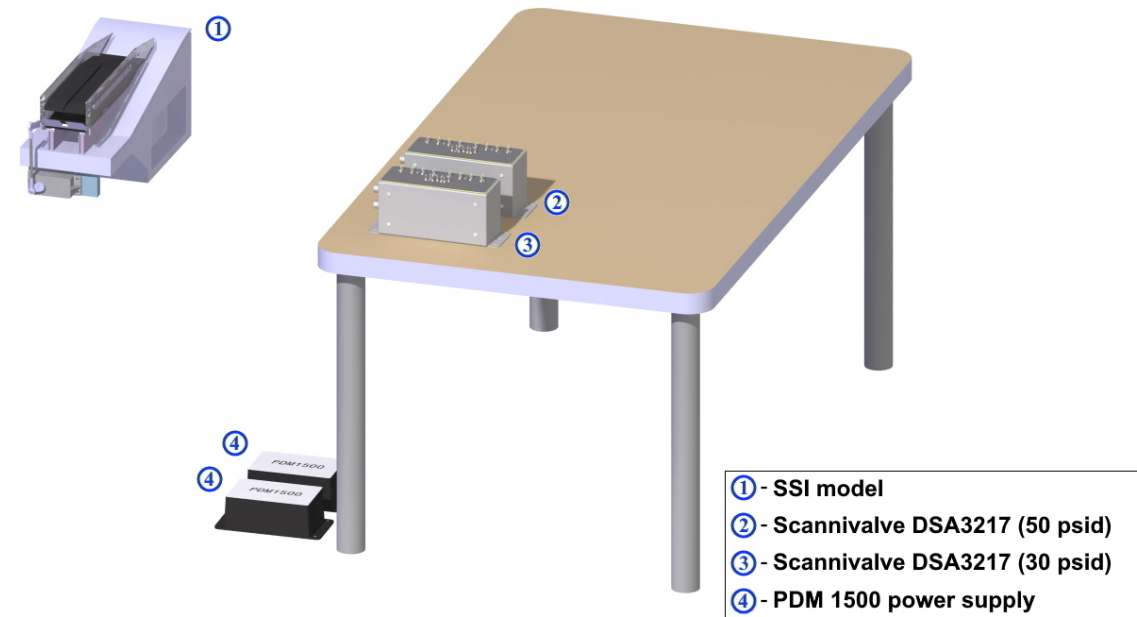


Figure 4.5: Three-dimensional view of the pressure measurement test setup, seen from the starboard side.

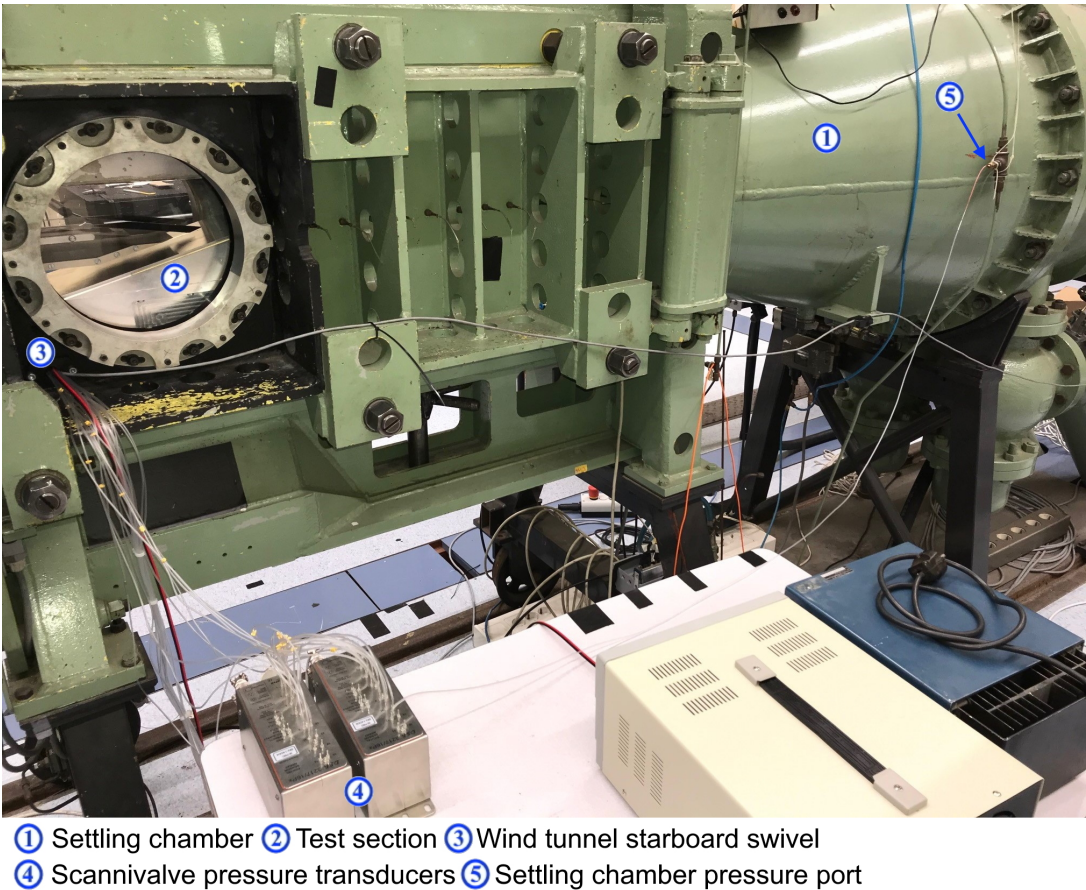


Figure 4.6: Image of the pressure setup from the starboard side of the wind tunnel.

4.4. Particle Image Velocimetry

A relatively recent technique, Particle Image Velocimetry (PIV) has become a state-of-the-art non-intrusive technique to analyze the dynamical flow structure of any fluid mechanics problem, primarily to determine the velocity field. This technique is widely used in a variety of experimental research fields and many professional and academic books have been written on this topic, such as the book of Westerweel [93].

From a basic perspective, PIV involves adding seeding particles to the flow with significant reflective properties. These particles should be small enough as to avoid altering the flow's behavior, but they should also follow the flow accurately. The domain of interest, which is captured within the field of view (FOV), is illuminated with bright laser light to create a firm contrast with the dark surroundings, which is done using one or more optical items; this safeguards the fact that only particles within the FOV will scatter light. As the seeding particles pass the FOV, high-speed digital camera's are used to capture a sequence of images to show the small displacements of the particles per frame. Each pair of successive image frames is separated by a known time-step Δt . To make sure the camera and laser operate simultaneously, it is crucial to also include a synchronizer device that regulates this task. This concludes the experimental part of PIV.

In the data-processing part of PIV, each image pair is equally subdivided into small interrogation windows. A cross-correlation analysis is performed to evaluate the displacement that occurred within one interrogation window over a time-step Δt . The displacement of the average particle within a single interrogation window is then used to determine the velocity at that particular location. This is done using the distance from the window's center to the largest peak on the cross-correlation map. Knowing both the displacement and the time-step, the average velocity field can be determined for the complete FOV. The complete sequence of PIV operations is shown in Figure 4.7.

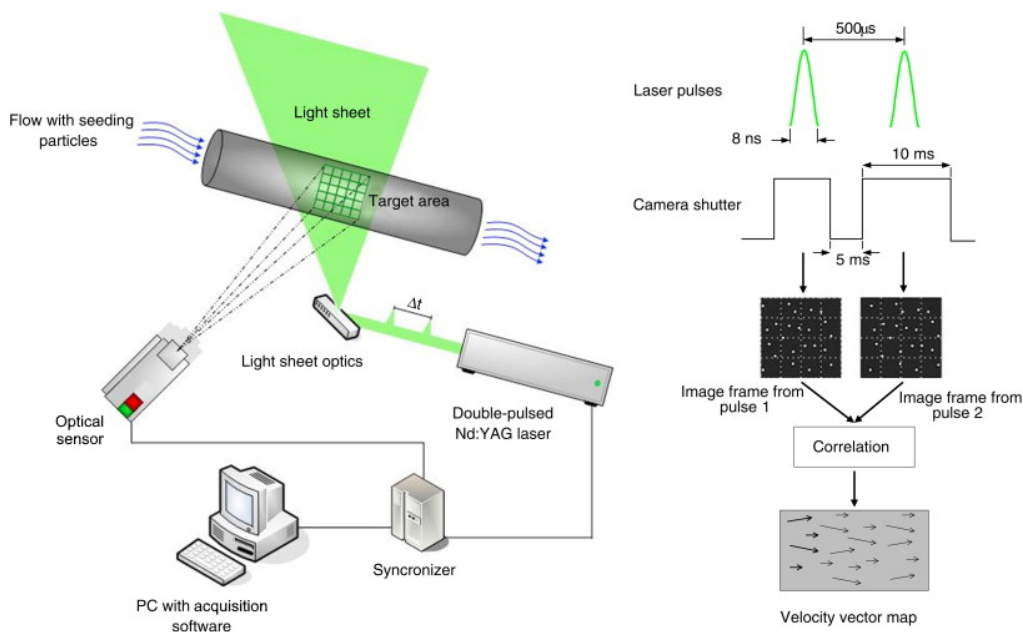


Figure 4.7: Generic example of the PIV working method and processing sequence, taken from Kumara et al. [94].

This section is divided in three parts: In subsection 4.4.1, the fundamentals of PIV are discussed which also includes the important considerations to realize a successful measurement campaign. Following, subsection 4.4.2 focuses more into explaining the different facets and properties of what is required to conduct a PIV measurement and what is considered favourable when executing a measurement. Finally, the processing of the raw images is discussed in subsection 4.4.3.

4.4.1. Fundamental imaging equations

Knowing the mean displacement expressed with the exact number of pixels and knowing all optical properties of the PIV setup, the physical mean displacement can be determined. To make this conversion, a relation must be established between the window size in pixels and the FOV in physical space. The image distance d_i

can be determined by knowing the focal length f of the camera's lens and the object distance d_o of the test section (Equation 4.8):

$$\frac{1}{f} = \frac{1}{d_i} + \frac{1}{d_o} \quad (4.8)$$

Following, the ratio between d_i and d_o can be defined, which is known as the magnification factor M . From a practical viewpoint, the magnification factor can also be formulated in terms of the length scales of both the FOV and the sensor (Equation 4.9):

$$M = \frac{d_i}{d_o} = \frac{l_{pix} \cdot N_{pix}}{l_{FOV}} \quad (4.9)$$

where l_{pix} is the pixel size, N_{pix} is the number of pixels and l_{FOV} is the size of the FOV in physical space. Using the definitions in Equation 4.8 and Equation 4.9, the FOV can be determined in standard units. First, it is required to know the f-stop $f_{\#}$, defined as the ratio of the focal length f to the camera's aperture diaphragm d_{lens} (Equation 4.10):

$$f_{\#} = \frac{f}{d_{lens}} \quad (4.10)$$

Combining Equation 4.8 to Equation 4.10 with the laser's wavelength λ , the focal depth δz of the PIV setup can be calculated (Equation 4.11):

$$\delta z = 4.88 \cdot \lambda \cdot f_{\#}^2 \left(\frac{M+1}{M} \right)^2 \quad (4.11)$$

The focal depth δz defines the out-of-plane span in which the seeding particles are imaged in focus. This parameter can be altered by altering the f-stop of the lens, but one should be cautious when doing so since altering the f-stop directly influences how much light is captured by the lens. The higher the f-stop, the larger the focal depth becomes, but at the cost of less light captured by the camera.

Also, one should be aware of the fact that the f-stop $f_{\#}$ has a number of constraints that are ought to be respected accordingly to secure good quality PIV results. The first constraint revolves around the focal depth δz : this parameter shall be at least equal to the laser sheet thickness Δz , which ensures that all particles are viewed within the correct FOV. If the laser sheet thickness is larger than the focal depth, than some of the particles not imaged in focus will also be illuminated by the light and therefore the measurement becomes inaccurate since out of focus particles should be left out as much as possible to support the cross-correlation analysis. The second constraint states that the camera's aperture shall capture sufficient light to avoid under-exposure of the images. Before introducing the last constraint, which is also the most vital one, some background theory must be discussed first.

Due to the finite resolution in the optical systems, diffraction effects take place and the minimum particle image diameter due to these diffraction effects d_{diff} can be defined as (Equation 4.12):

$$d_{diff} = 2.44\lambda(1+M)f_{\#} \quad (4.12)$$

In addition, using the real particle diameter d_p , the particle image diameter viewed with geometrical optics d_{geom} can be defined as (Equation 4.13):

$$d_{geom} = Md_p \quad (4.13)$$

Combining Equation 4.12 and Equation 4.13, the particle image diameter d_{τ} can be defined as (Equation 4.14):

$$d_{\tau} = \sqrt{d_{diff}^2 + d_{geom}^2} = \sqrt{d_{diff}^2 + (Md_p)^2} \quad (4.14)$$

Since $d_{diff} \gg Md_p$, Equation 4.14 reduces to (Equation 4.15):

$$d_{\tau} \approx d_{diff} \quad (4.15)$$

Now comes the last constraint for selecting the proper f-stop: if the particle image diameter is smaller than the size of a single pixel, or $d_{\tau} < l_{pix}$, then peak locking occurs. In this situation, the particle displacement

is too small within one image plane, which causes the same particle to be captured at the very pixel twice by both images from the same pair. This error can be considered a direct discretization effect caused by the dull motion of the seeding particles, which are registered at the minimal resolvable displacement. To avoid peak locking, the optical system has to be set up such as to ensure that individual particles are captured over several pixels in one image. Ideally, the particle image diameter should equal the size of roughly two to three pixel lengths or $2l_{pix} < d_\tau < 3l_{pix}$. In deliberation with the supervisor, it was decided to have d_τ equal two pixel lengths. Combining all three constraints, it was found that $f_\# \geq 9$. Taking into account the discrete $f_\#$ values available on the CMOS camera's, it was decided to have $f_\# = 11$

The last parameter requiring attention is the pulse separation time Δt , which determines the time interval between the two images of a single pair. When selecting Δt , one should respect the quarter rule which states that Δt shall be selected such that the displacement does not exceed a quarter of the interrogation window size. From discussion with the supervisor and experience with the tunnel configuration, it was decided to select the pulse separation time based on the notion that the particle's average displacement should be about 12 pixels. This means that the pulse separation time can be determined by (Equation 4.16):

$$\Delta t = \frac{s_{pix} l_{pix} \overline{M}}{u_\infty} \quad (4.16)$$

Knowing that the average velocity in the intake is roughly $u_\infty \sim 500 \text{ m/s}$, this leads to $\Delta t = 1.2 \mu\text{s}$

4.4.2. PIV Properties

Since PIV is a sophisticated measurement technique, multiple factors are involved in preserving the acquisition of proper results. The following explanation will therefore be centred on the different facets that need to be considered well before the actual measurements can take place to ensure the desired results are obtained.

Seeding Important criteria that guarantee selecting proper seeding particles include the fact that seeding particles shall meticulously follow the flow and scatter sufficient light to be decently imaged. After all, the motion of the seeding particles should represent the motion of the entire flow as genuine as possible.

For high-speed PIV applications, typical seeding particle options are titanium dioxide (TiO₂) and Di-Ethyl-Hexyl-Sebacat (DEHS). The latter particle type is characterized by its accurate tracking behavior of the flow, owing to its small particle response time τ_p . According to Scarano [95], this parameter indicates what time it takes before the seeding particles achieve 63% of the flow velocity. Another parameter used to inspect the capability of seeding particles to follow the flow well enough is the slip velocity u_s , defined as the difference between the velocities of the flow u_f and the seeding particles u_p (Equation 4.17):

$$u_s = u_p - u_f \quad (4.17)$$

The seeding particles trace the flow well when the slip velocity is close to zero, which implies that the particles move with roughly the same velocity as the flow itself. One needs to consider that for high-speed applications, the presence of shock waves can distort the velocity of seeding particles, which was verified by Ragni et al. [96]. Equation 4.17 can be traced back to a more broad expression, which describes the motion of spherical particles having a low Reynolds number, which renders the flow as a Stokes flow ($Re \rightarrow 0$). The velocity development of such a flow can be then be described by the definition (Equation 4.18):

$$\frac{d\mathbf{V}}{dt} = -\frac{3}{4} C_D Re_p \frac{\mu}{\rho_p d_p^2} (\mathbf{U}_p - \mathbf{U}_f) \quad (4.18)$$

The mathematical solution to the above differential equation shows that the particle's motion decays with a change in flow velocity. This means that there will always be a velocity difference between the seeding particles and the main flow and this delay is quantified by means of τ_p as discussed before. A final parameter used to evaluate the seeding particles ability to trace the flow is the Particle Stokes number S_k , which is defined according to Brennen [97] as the ratio of the product of particle time response and the flow freestream velocity to the particle diameter (Equation 4.19):

$$S_k = \frac{\tau_p \cdot U_\infty}{D} \quad (4.19)$$

This shows that for supersonic flows, where the freestream velocity U_∞ is much higher than for subsonic

flows, the Stokes number is also higher. According to Tropea and Gnirß [98], particles follow the streamlines with decent accuracy when this parameter is much smaller than unity, i.e. $S_k \ll 1$. From prior research conducted in the ST-15 testing facility and from experience with its experimental apparatus, the organic DEHS oil proved to be an excellent choice for obtaining adequate results. When atomized, the particle diameter lies around $1 \mu\text{m}$, which is also shown in Figure 4.8. In this figure, the level of atomization is plotted against the particle diameter. The associated time scale τ_p is roughly equal to $2 \mu\text{s}$, which indicates that upon injection into the flow, these particles adapt pretty quick to the flow's behavior.

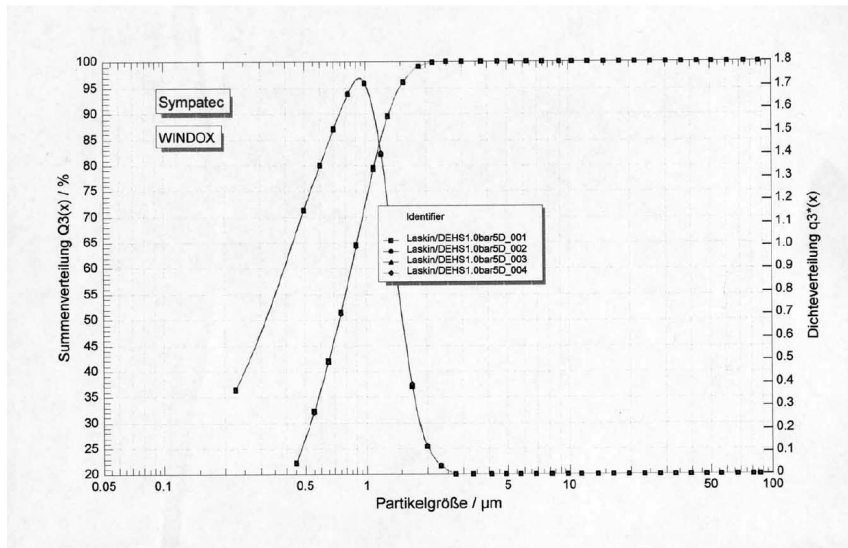


Figure 4.8: Particle atomization level plotted against particle diameter, taken from PivPart45 manual [99].

For this report's experimental campaign, a PivPart45 particle generator, shown in Figure 4.9, was used to inject the DEHS particles through the ST-15 settling chamber, as is shown in Figure 3.1. When all nozzles of the PivPart45 would be activated, approximately 10^8 particles are injected every second [99]. The seeding line was equipped with a seeding rake to allow for a uniform seeding density at the field of view. The seeding equipment operated with 1 bar over-pressure relative to the flow environment in which the particles were injected. As is shown in Figure 4.9, one outlet is reserved for the high pressure hose that provides enough pressure to the seeding particles for proper injection into the test section with the correct overpressure.



Figure 4.9: The PivPart45 particle generator used to inject the seeding particles, taken from the PivPart45 manual [99].

Illumination The main constraint of visibility of the seeding particles depends partially on selecting particles with a mean diameter that is deemed large enough. The DEHS particles used in the testing campaigns were considered sufficient for decent illumination. To capture the motion of the seeding particles, the FOV is illuminated using a laser with a specific pulse separation time to ensure proper illumination of the capture window. Commonly used laser types for PIV research include the Neodymium-doped Yttrium Aluminum Garnet (Nd:YAG) and the Neodymium-doped Yttrium Lithium Fluoride (Nd:YLF) lasers. These types of lasers are very favored for PIV measurements since these systems provide collimated light beams with affordable energy levels per pulse, in addition to their high pulse frequencies. Each experiment though will require a specific laser type: The Nd:YAG system has a low repetition rate of 30 *Hz* or less and a high pulse energy of 400 *mJ* and above. When higher recording rates are demanded, the Nd:YLF laser becomes the most suited laser system since it can achieve high frequencies of up to 10,000 *Hz*, with the penalty of having a low pulse energy of 30 *mJ*.

Generally, it should be noted that the pulse duration of any laser needs to be short to prevent the particle tracks from being blurred on the images. The measurement frequency should be high enough to allow capturing a series of correlated vector fields; in that case the results are said to be time-resolved. However, the higher the measurement frequency, the lower the energy per pulse. This shows that every PIV experiment is confined by two main constraints which are the spatial resolution on one side and the required laser energy on the other. A typical timeframe for PIV consists of a number of elements as is also shown in Figure 4.7: The time-step is what separates one velocity vector field from another and this parameter is usually in the order of 10^{-1} seconds. The pulse separation time Δt is in the order of microseconds and is the fixed time between the two images of a single image pair. Finally, the smallest parameter in PIV measurements is the pulse duration δt , which is in the order of nanoseconds. A rule of thumb for determining the pulse duration is that the particle displacement within the pulse duration is ought to be significantly smaller than the size of the particle image itself, which can be mathematically written as (Equation 4.20):

$$\delta t = \frac{d_p}{VM} \quad (4.20)$$

For the current experiments, the Nd:YAG Quanta Ray Pro Series laser was used. This double-pulsed laser provided around 1 *J* of energy per single pulse and the amount of light emitted was sufficient to make the seeding particles scatter sufficient light. Also, the laser's repetition rate was set at its maximum setting, which corresponded to 10 *Hz*.

The next priority was to determine how the laser sheet should be generated at the desired location of the field of view. For this report's experiments, only one wall-normal plane was considered, parallel to the x-y plane, that runs through the center of the SSI model. In Figure 4.10, a schematic representation is shown of this plane located on the compression plate. It must be mentioned that, in order to avoid getting reflections from the cowl and compression plate pressure holes upon illumination by the laser, the pressure holes of both cowl and compression plates were covered with self-adhesive dc fix foil.

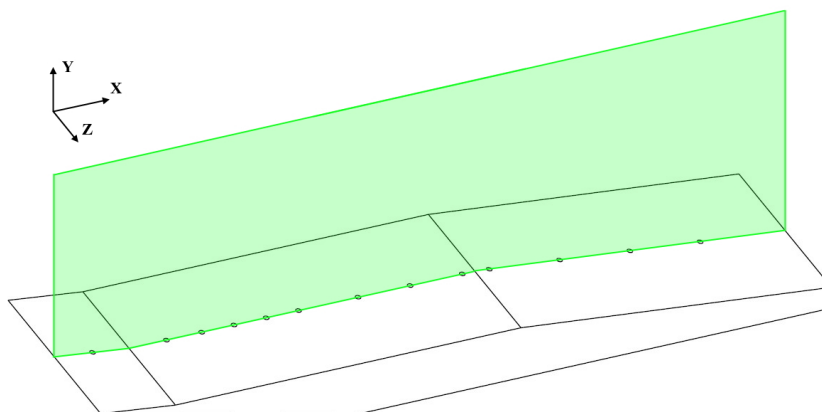


Figure 4.10: Schematic of the wall-normal laser sheet produced on the compression plate.

To generate the aforementioned wall-normal plane, a mirror probe was inserted in the diffuser of the ST-15 to reflect the laser light that enters the diffuser externally. The mirror probe that was used for this report's PIV campaign is shown in Figure 4.11. This probe is clamped using an existing slot on the starboard side of the diffuser. After the laser head shoots the double-pulsed laser beam, two planar mirrors guide the laser beam to the mirror probe to generate the laser sheet in the test section. Figure 4.12 shows the full path traversed by the laser light from the laser head to the test section in a 3D CAD drawing. For clarity, only the compression plate and butterfly valve were shown in the SSI model in this figure. In Figure 4.13, a real image is shown taken of the same laser components and from the same viewpoint next to the wind tunnel.

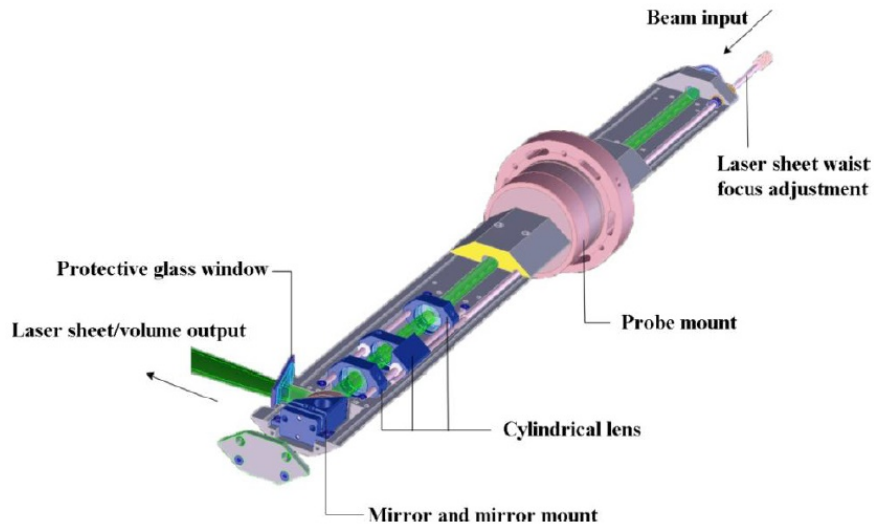


Figure 4.11: Schematic of the mirror probe used during the experiments, taken from Donker Duyvis [100].

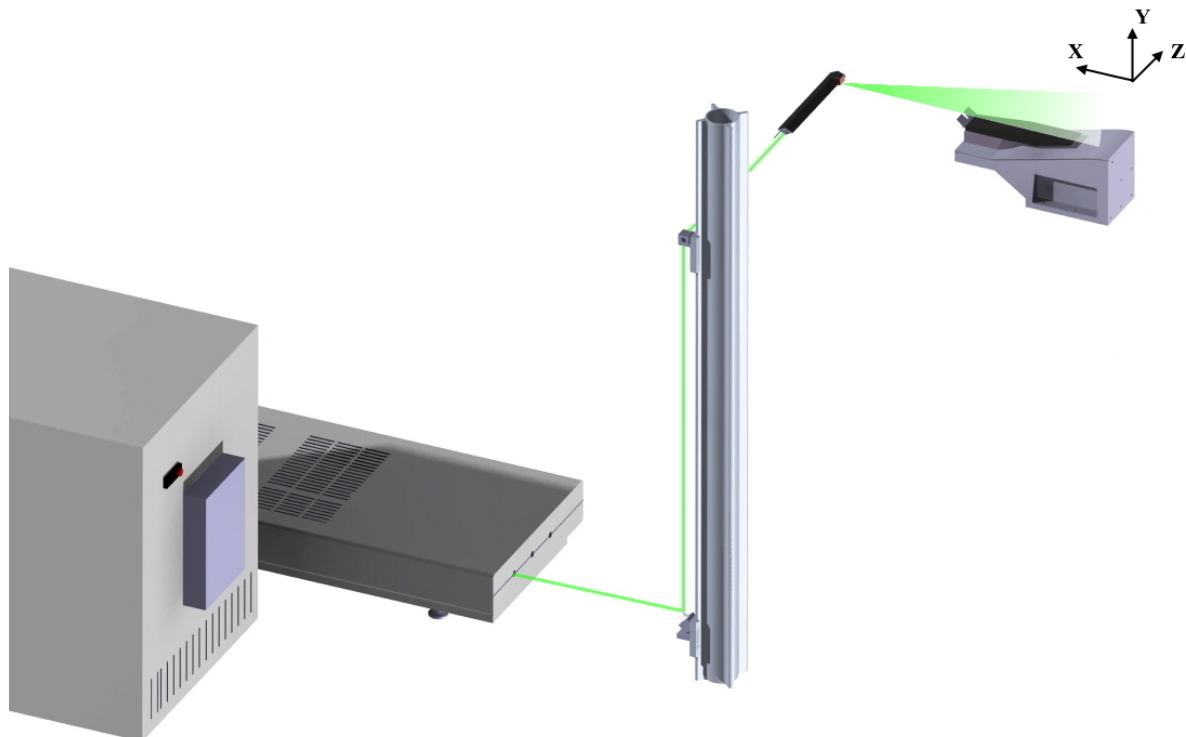


Figure 4.12: Three-dimensional CAD view of the wall-normal laser sheet formation parallel to the x-y plane.

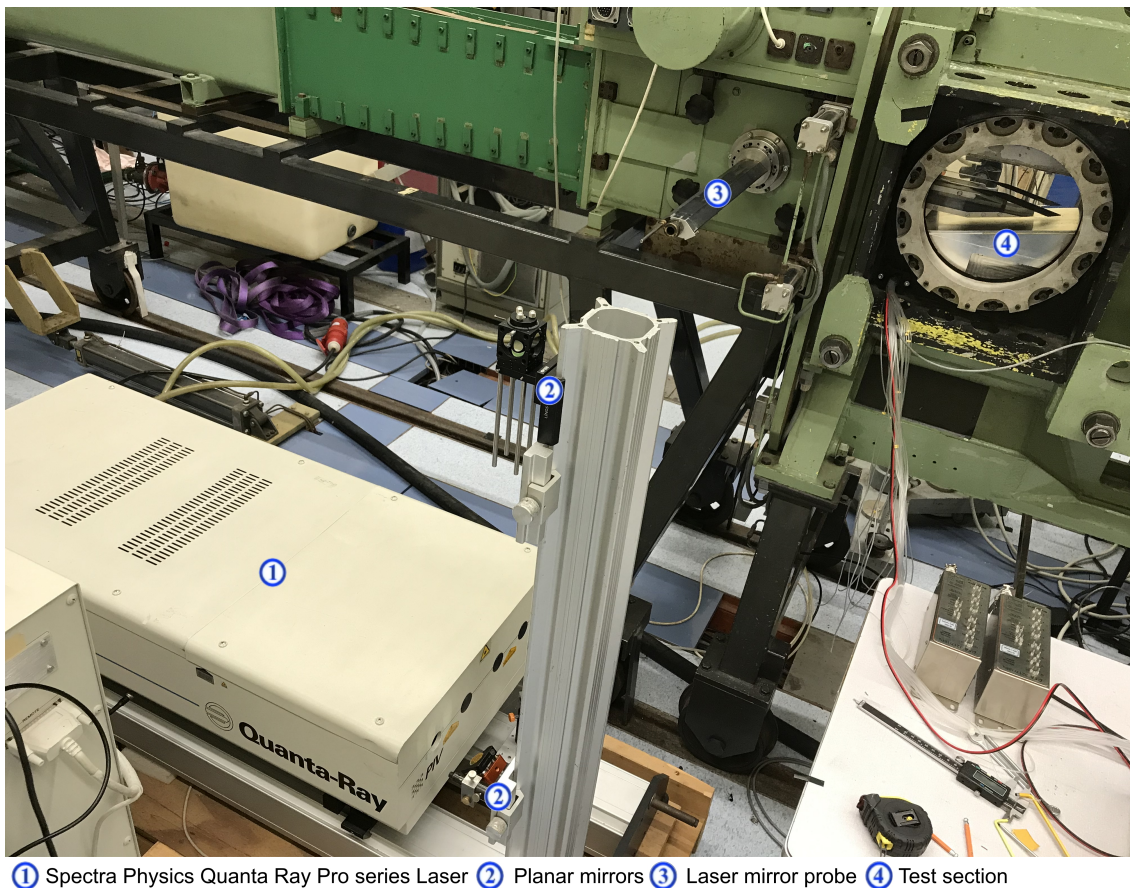


Figure 4.13: Laser components generating and guiding the laser path for the laser sheet formation, from the starboard side of the wind tunnel.

Optical arrangements Upon illumination by the laser, the seeding particles scatter the light in all directions, and by using one or more high-speed digital camera's separated from the test-section by the wind tunnel optical access windows, the motion of the seeding particles and thus of the flow is captured in successive images. The result is given in multiple bitmap-images, showing slight displacements of the seeding particles from one image to the other. To conduct proper PIV analysis, most digital camera's used nowadays are either Charge-Coupled Device (CCD) or Complementary Metal Oxide Semiconductor (CMOS) camera's. Although CCD camera's are used most often in PIV measurements as documented by Raffel et al. [101], CMOS camera's are known to perform better for situations where light intensity levels are so small that CCD camera's return low quality images. Nonetheless, CCD type optical devices remain the best suited option for experiments requiring high-resolution and high-quality imagery, as was confirmed by Hain and Kähler [102].

For this report's PIV experiments, Lavisson Imager sCMOS camera's were used. The optical configuration consisted of two sCMOS camera's placed in series which were located on a X95 beam of 0.5 m length. This X95 beam was then placed on a tripod using a CX95 bracket. This tripod featured caster wheels which made the camera's position adjustable in the streamwise and out-of-plane direction. Using the turning wheel on the tripod, the tripod's center bar could be moved vertically which made the camera's height adjustable. Both camera's were equipped with 105 mm lenses. The two camera's were placed next to each other along the streamwise direction and the reasoning behind this was to get a close view of the intake's sections to analyze in detail the flow dynamics. Both FOVs had a size of 89.7×75.7 mm and the two FOVs were placed next to each other. Making the FOVs overlap over one another was not option since this would require placing the camera's at a bigger distance from the test section optical access window, which would in turn decrease the resolution. The camera setup and the FOVs in this setup are shown in Figure 4.14. After setting up the camera's for the PIV setup, it turned out that to optimally capture the intake domain, the upstream camera's FOV had to be displaced roughly 4 cm to the right, which resulted in the compression plate's leading edge not

being captured by this camera. However, this was sufficient enough though to capture the first OSW created at the compression plate leading edge. In Figure 4.15, an image is shown taken from the real setup in the wind tunnel featuring the two sCMOS camera's placed in series and facing the test section.

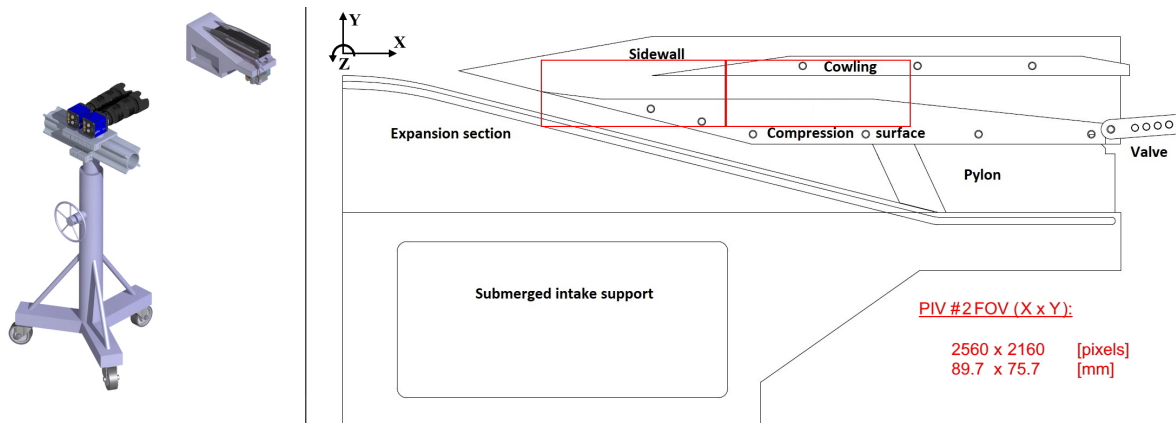


Figure 4.14: Left: 3D CAD view of the double camera configuration. Right: Schematic of the FOV of the two 105mm-camera's.



Figure 4.15: Image of the sCMOS camera setup for the PIV campaign.

4.4.3. Image processing

Processing of this report's PIV data was done using DaVis 10.1. Image processing is required to transform the raw bitmap-images obtained from the experiments to qualitative velocity data. For this to happen, a number of techniques have to be applied to the raw images. During the wind tunnel run, when the seeding particles move along the flow while being illuminated by the laser light, light is scattered in all directions anisotropically, including in the direction of where the optical sensors are located. Due to diffraction effects, caused by the finite resolution of the optical systems, the particles are never imaged as perfect circles but rather as decaying intensity spots with alternating shady and bright regions. In literature, this phenomenon is also referred to as the Airy disk and is named after the scientist who was the first to document this occurrence. Determining the proper $f_{\#}$ of the PIV setup partially depends on the occurrence and size of the Airy disk.

Reconstructing the velocity vector field from raw images is done using a cross-correlation algorithm. Every image is divided into smaller interrogation windows with each window holding approximately 10 particles. For all interrogation windows, the cross-correlation procedure is then carried out between the images of the same pair. Between the images of a single pair, it is desirable to have the same particles contained in the same interrogation windows on both images with the particles only having moved about one fourth of the window size to obtain a clear pattern of their motion. Based on their displacement in the image space, a transformation can be made to the displacement in the physical space. Combining this with the time between two images, which is the pulse separation time Δt , the velocity field can be reconstructed for all interrogation windows, and therefore for the entire FOV. Following a displacement $\mathbf{d} = [x, y]^T$, the correlation coefficient ϕ can be defined as (Equation 4.21):

$$\phi(x, y) = \frac{\sum_{i=1}^X \sum_{j=1}^Y [I_1(i, j) - \bar{I}_1] [I_2(i + x, j + y) - \bar{I}_2]}{\sigma_1 \sigma_2} \quad (4.21)$$

where \bar{I} refers to the intensity peak on the cross-correlation plot, which is an indication to how high the probability is that a certain displacement magnitude and direction correspond to the real displacement traversed by the particles, the overline represents the average quantity and σ is the standard deviation of the algorithm. The subscripts 1 and 2 denote the two images of a single pair. Quantifying the flow velocity at subpixel accuracy requires the use of a sophisticated cross-correlation interpolation algorithm, such as the Gaussian fit, to decently resolve the characteristics of the Airy disk.

On a cross-correlation plot, the mean displacement is then identified by the highest peak in Equation 4.21, which is the peak with the largest magnitude or intensity. An illustration for the cross-correlation analysis of the PIV measurement scheme is schematically shown in Figure 4.16.

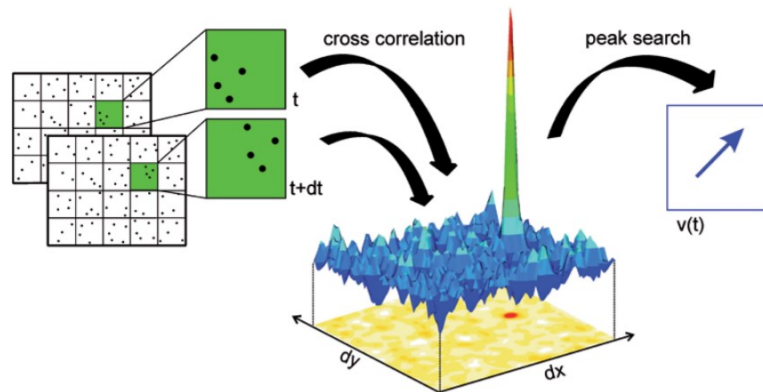


Figure 4.16: Schematic representation of the cross-correlation analysis for PIV, taken from the LaVision Davis product manual [103].

The complete analysis of the data retrieved from the PIV experiments can be divided in three phases: pre-processing, processing and post-processing. In the pre-processing phase, the images are inspected and a time-filter is applied to lessen the effect from the reflections. In the processing phase, the cross-correlation analysis is executed and velocimetry data is obtained from the pre-processed bitmap images. Finally, in the post-processing phase the obtained velocity data is adjusted to plot all parameters of interest in the desired format.

Pre-processing Image pre-processing is considered a general necessity, but it becomes more profound in case the raw particle images contain a high degree of light reflections. The latter problem was encountered in all images of this report's PIV campaign. The reason behind these reflections are mainly the edges and corner parts of the SSI model which automatically cause a lot of light reflections coming from the laser sheet. There were four main regions causing reflections: compression plate leading edge, compression plate lip-to-flat surface junction, cowling leading edge and the subsonic diffuser ramp junction. These are shown in [Figure 4.17](#). Laser reflections can be neutralized by using a time-filter.



Figure 4.17: Side view of the SSI model featuring the locations with the highest degree of light reflections, indicated with red circles, during the PIV campaign.

In [Figure 4.18](#) and [Figure 4.19](#), two raw bitmap images of the same pair are shown for the upstream sCMOS camera. As can be clearly recognized, the cowling leading edge at the top right and the compression plate lip-surface junction at the bottom left are causing reflections with very high intensities.

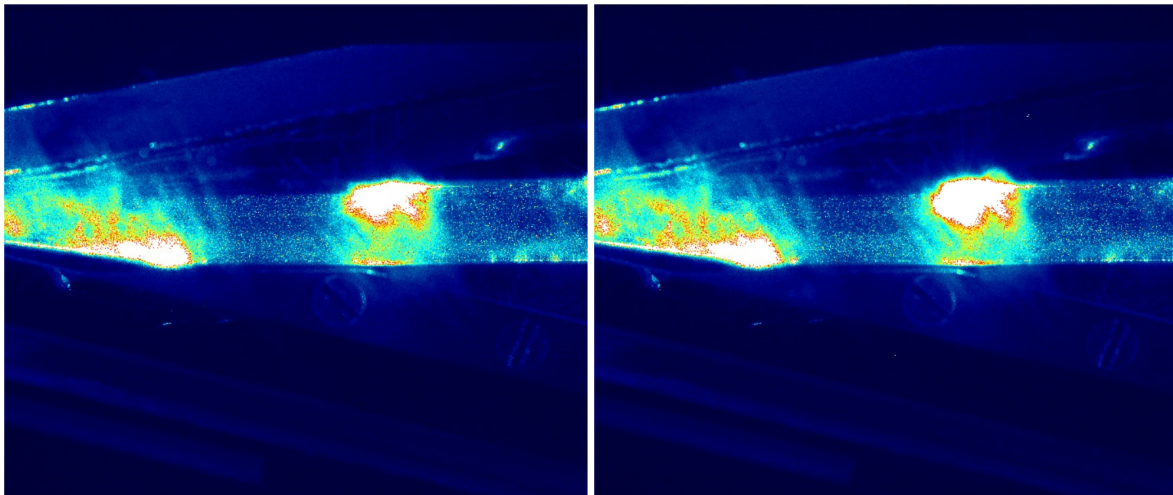


Figure 4.18: Image 1 of a pair, showing the reflections from the laser sheet.

Figure 4.19: Image 2 of a pair, showing the reflections from the laser sheet.

To make sure the reflections do not complicate the cross-correlation analysis, a time-filter is subtracted from the images to remove all forms of background noise from the image, which also includes the reflections caused by the laser sheet. Since these reflections had high intensities and were very dynamic (i.e. the reflection bubble continuously changed in size and shape), it was decided to pre-process all raw particle images using a Butterworth filter, which is a high-pass filter based on a predefined number of images or window length. The chosen window length was 7 images. This filter is specialised in removing unsteady laser reflections for high-speed PIV applications. The use of a minimum or average time-filter would only yield adequate results in case the reflection's size and shape were constant over time. But since the laser light reflections typically move several order of magnitudes slower than the particles, it is possible to separate both the particle and reflection signals in the frequency domain. By applying a suitable high-pass filter, only the low frequencies of the slow moving reflections are attenuated, resulting in an elimination of these reflections while the intensities of the particles remain unaffected. [Figure 4.20](#) and [Figure 4.21](#) show the effect of subtracting the Butterworth high pass filter from [Figure 4.18](#) and [Figure 4.19](#), respectively.

Also, during any PIV campaign, one may expect that the raw images contain more than only the region of interest that is to be processed. As can be clearly seen in the FOV of the PIV setup in [Figure 4.14](#), the intake's duct region, cowling, compression plate and some of the surroundings are all included in the imaged

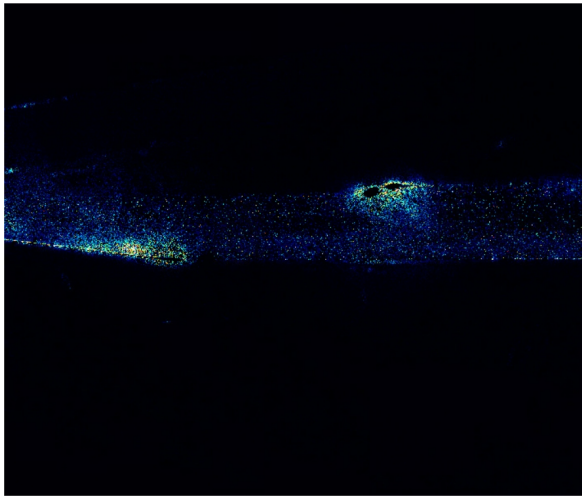


Figure 4.20: Image 1 of a pair, after subtracting the Butterworth high-pass filter.

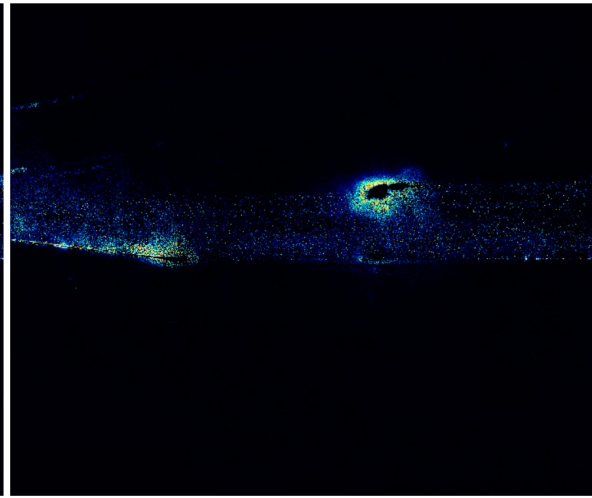


Figure 4.21: Image 2 of a pair, after subtracting the Butterworth high-pass filter.

FOVs. Therefore, to remove these parts a number of geometric masks were created to hide all intake walls and the regions which are not illuminated by the laser sheet. These geometrical masks are indicated by the blue shaded areas in Figure 4.22.

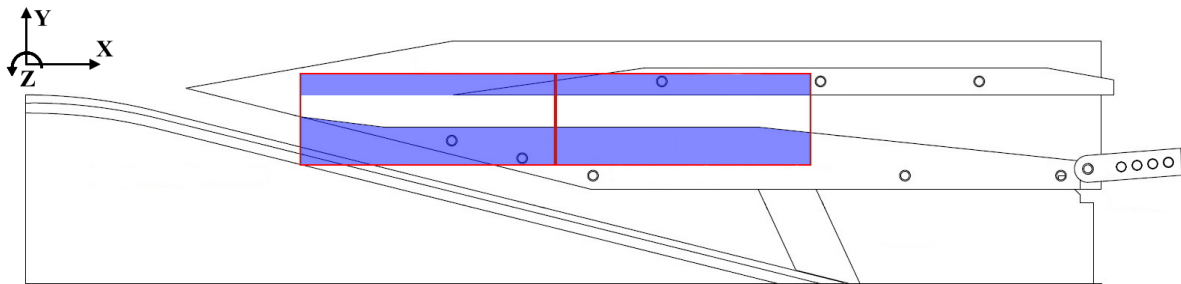


Figure 4.22: Side view of the SSI model featuring the second PIV setup FOVs with the geometric masks indicated by the blue shaded areas.

Processing After successfully subtracting a time-filter from the raw particle images, the images become valid to be used as an input for the cross-correlation analysis. The first step in processing the particle images is to mask the regions of lesser interest as was already explained in subsection 4.4.2. After successfully applying all required geometrical masks to the bitmap images, the next step is to process all images accordingly with the cross-correlation algorithm. The interrogation window size used for the images was 32×32 pixels, since this option yielded the highest resolution for viewing the flow features in the intake. Any smaller window sizes would lead to a lack of proper discretization, which is a direct result of too much in-plane pair losses. This gave rise to illogical and often negative velocities.

Also, a multi-pass approach was used. To understand what this means, one should first understand what a single-pass approach is. In a single-pass approach, the entire image set is analyzed once with the cross-correlation algorithm. Doing so, the maximum displacement of the particles is restricted to half or even less of the window size. In a multi-pass approach, the complete image set is analyzed more than once and the window on the second frame of an image pair is shifted by a value which is determined using the result of the first pass. This means that the result of this first pass functions as a 'pre-shift' or first guess for future passes. Using the multi-pass approach helps the cross-correlation algorithm in keeping more particles inside the interrogation windows. This does not only increase the Signal-to-Noise ratio, but it also prevents the occurrence of in-plane pair losses, and therefore, discretization errors. It was chosen to have a total of four passes per cross-correlation analysis.

When using the multi-pass approach, one usually starts with large window sizes and selects the preferred

resolution as the final window size. The initial and final window sizes chosen were 96×96 and 32×32 pixels, respectively. Another parameter is the weight of the passes, which gives the cross-correlation analysis an indication of how the particles are geometrically divided. Since for the intake domain under consideration the streamwise space is geometrically larger than the vertical space, it was chosen to have an initial weight of 1:1 (square-shaped) and a final weight of 4:1 (horizontally-extended horizontal ellipsis-shaped).

As a final addition to the multi-pass approach, an overlap factor was used. The motivation for using an overlap factor is that the particle pairs near the edges of the images contribute less to the correlation result. Therefore, by letting two adjacent windows overlap over one another, the data yield may be increased. Usually, an optimal choice is to set the overlap factor to 50 %, since higher overlap factors may lead to relatively uncorrelated results due to oversampling. For this PIV analysis, the initial and final overlap factors were chosen to be 50 % and 75 %.

To improve the validity of the velocity vector results, it was chosen to apply a median filter after finishing the cross-correlation analysis. A median filter, sometimes also called a median test, is a widely-used method for outlier detection in post-correlation validation of PIV data. A median filter generally works in the following way: first, a filter region is selected made up of $a \times a$ interrogation windows. The velocity in the center window of this filter region is then regarded as the reference velocity U_0 and this velocity is simply the numerical median of the velocities in the neighbouring windows. Next, the residuals are calculated between this reference velocity and the velocity vectors in the neighbouring windows. If the residuals exceed a certain threshold, the corresponding velocity vectors in the neighbouring windows are discarded. The discarded vectors are then replaced by either the local median or the local secondary correlation peak. The threshold is usually the standard deviation, or a constant that is proportional to the standard deviation, of the neighbouring windows.

However, this classical method for the median filter usually gives rise to a very cumbersome problem: if a PIV measurement contains both high velocity data (e.g. the intake center region) and low velocity data (e.g. the intake wall region), the average value of the median vector residual correlates with the mean velocity. This means that, if only a single threshold would be applied to the entire flow domain, a large part of the valid measurement data tends to be rejected and spurious measurement data will be accepted. To avoid this hazardous approach, a specific type of median filter was used for this report's PIV data which is known as the universal outlier detection method by Westerweel and Scarano [104]. In this median filter, the residual is normalized with an estimate of the expected instantaneous flow fluctuations. The most adopted choice is the root mean square of the velocity fluctuation u' . This works in the following way: Consider a reference velocity U_0 and its $a \times a$ neighbourhood data. If for the sake of this example $a = 3$, the neighbourhood data can be denoted as $\{U_1, \dots, U_8\}$, and U_m as the median of $\{U_1, \dots, U_8\}$. A residual r_i , defined as $r_i = |U_i - U_m|$, is then determined for each vector $\{U_i | i = 1, \dots, 8\}$ and the median r_m of $\{r_1, \dots, r_8\}$ is used to normalize the median residual with the reference velocity U_0 (Equation 4.22):

$$r'_0 = \frac{|U_0 - U_m|}{r_m} \quad (4.22)$$

Westerweel and Scarano [104] showed that this alternative median filter indeed clears the residual from any biased tendencies of accepting one half of the PIV data and discarding the other half. However, a weak correlation between the mean residual and the turbulence level of the flow remains and it was shown by the above authors that r'_0 shows elevated values in flow regions with low turbulence levels. For purely uniform flow, r'_m would tend to zero. To compensate for this oddity, a minimum normalization level ϵ is assumed (Equation 4.23):

$$r'_0 = \frac{|U_0 - U_m|}{r_m + \epsilon} \quad (4.23)$$

where ϵ may be viewed as the acceptable fluctuation level due to the cross-correlation. A comparison between a median test and a normalized median test is shown in Figure 4.23, which affirms how powerful the use of normalized median tests are by showing how correlated the data from different turbulent levels are for this technique.

As a final option, one may opt for the use of a low pass filter to the vector field for smoothing. However, this option was not applied for this report's PIV results since smoothing changes all vectors and modifies the data!

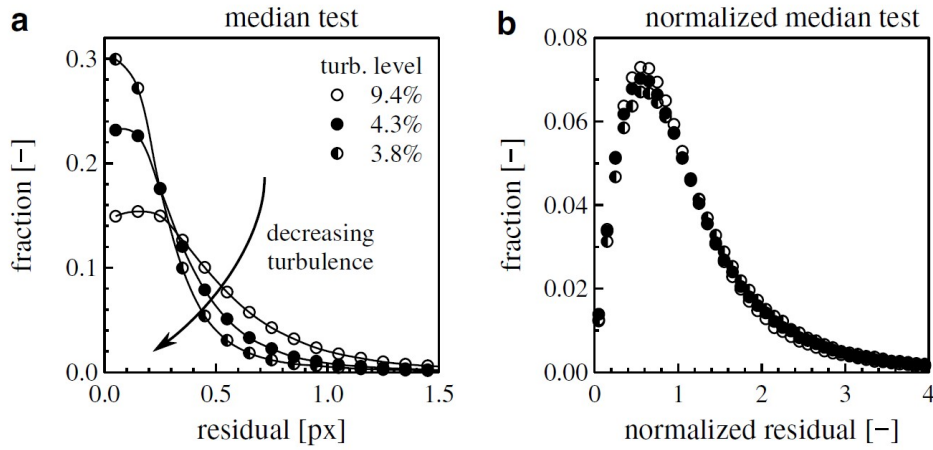


Figure 4.23: The histograms of the residual obtained with the conventional median test (a) and the normalized median test (b) for the grid turbulence data at decreasing turbulence levels. The histograms represent at least 99.7% of the vector data, taken from Westerweel and Scarano [104].

In Figure 4.24, the velocimetry result is shown for the complete processing phase for the image pair of Figure 4.18 and Figure 4.19. As becomes clearly visible from this figure, the degree of uncertainty is still very large in the regions where lots of laser reflections are found.

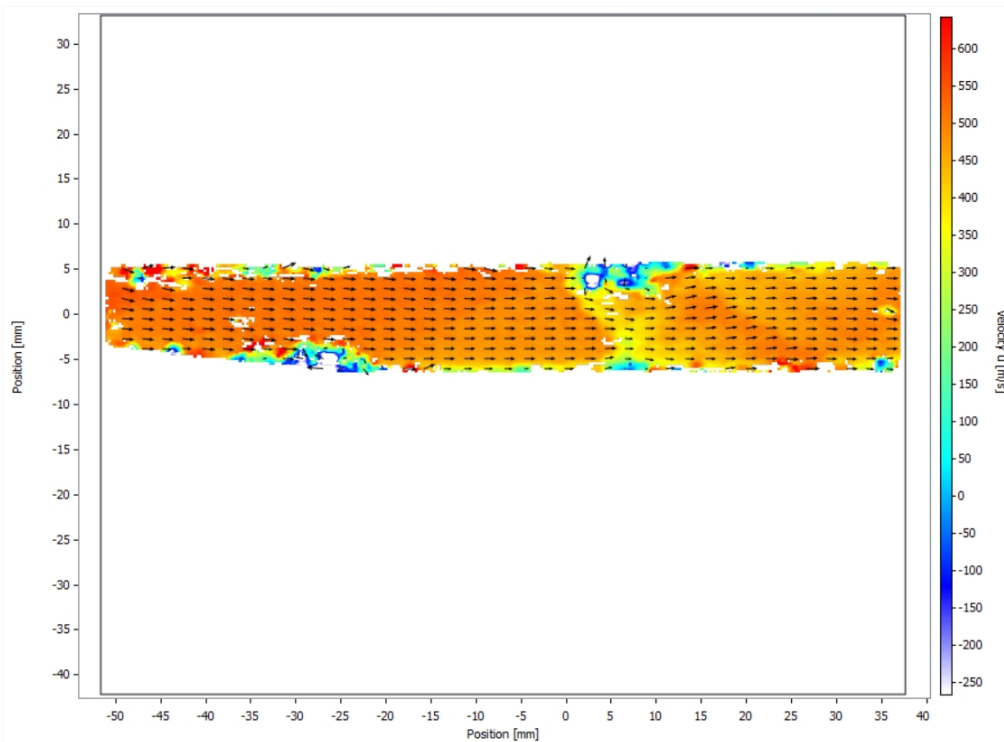


Figure 4.24: Instantaneous velocimetry result of the u-component of the velocity of the image pair of Figure 4.18 and Figure 4.19.

Especially near the wall regions, velocities are not captured well due to either reflections or insufficient seeding. Therefore, to accurately find the result of PIV measurements, all images of a single run are statistically averaged. However, to ensure proper averaging is conducted, a few additional options were adopted. First, it was chosen to re-pass all individual instantaneous vector fields a 3rd and 4th time and only accept those vectors that lied within a confidence level CL , defined as (Equation 4.24):

$$CL = Avg \pm f \cdot \sigma \quad (4.24)$$

where Avg is the average velocity at a specified location, f is a constant factor and σ is the standard deviation. Both Avg and σ are determined from the first two passes when calculating the statistical average. For this report's PIV data, the factor f was chosen to be 2.5. As a final note, it was chosen to only determine velocity vectors on all grid points of the domain when there would be at least 20 valid velocity vectors at the same points. This guarantees a high degree of validity of the statistical results. The statistically averaged result is then shown in Figure 4.25.

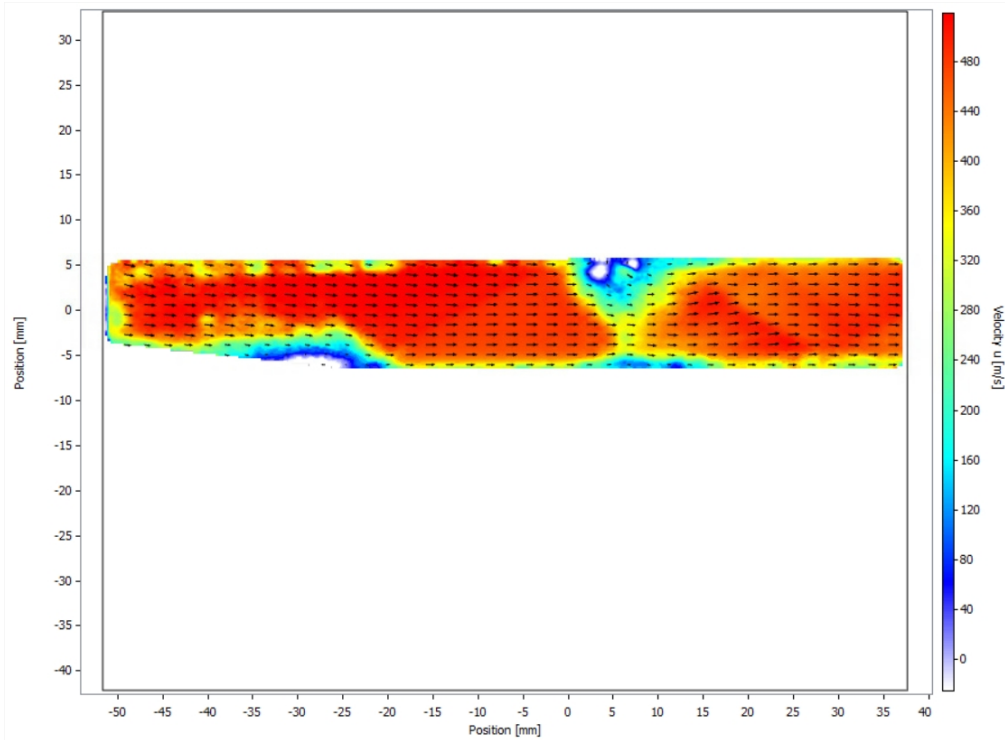


Figure 4.25: Statistically averaged velocimetry result of the u-component of the velocity of the entire image set.

Post-processing After finishing the largest part of the PIV analysis, the only thing left will be to post-process the data. The velocity data from this report's PIV analysis was post-processed to obtain the streamwise and vertical velocity distributions, as well as the local Mach number throughout the intake. The streamwise and vertical velocity components were nondimensionalized. Furthermore, presentation of the final PIV results included viewing the vector fields inside the intake geometry. This was done by drawing the geometry around the vector field. Another crucial point, the scaling was adjusted for the final result since the calibration of Davis 10.1 did not provide the correct coordinate system origin. The final result after finishing the post-processing phase for Figure 4.18 and Figure 4.19 is shown in Figure 4.26. As a last note, since the reflections generated at the sharp edges of the geometry made it hard to determine the velocity at these locations, all reflection-influenced locations were blanked out to avoid confusion while interpreting the results.

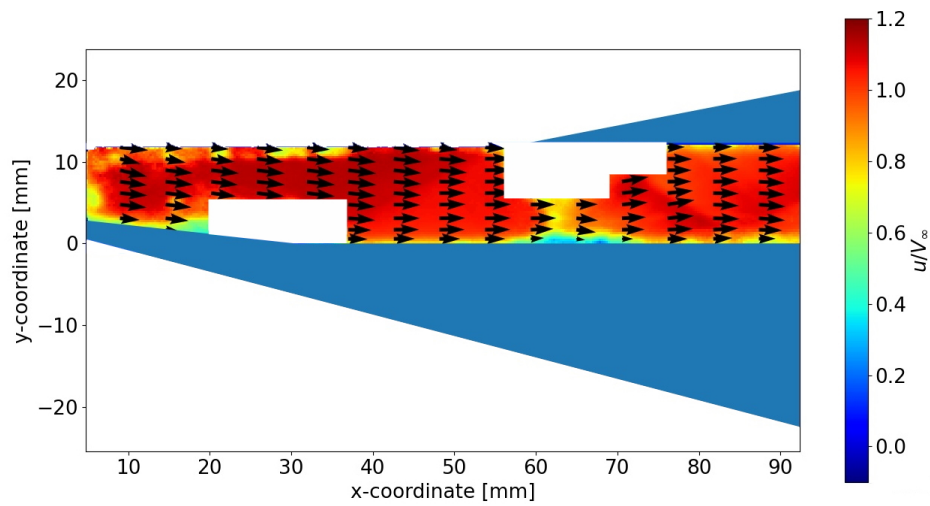


Figure 4.26: Final PIV result following the post-processing phase.

4.4.4. Experimental setup

All items of interest required to execute this report's PIV campaign are listed in [Table 4.4](#)

Item	Quantity	Details
Seeder	1x	PIVtech PivPart45
Optical sensor	2x	Lavision sCMOS camera
Laser	1x	Spectra Physics Quanta Ray Pro series
Synchronizer	1x	Lavision Programmable Timing Unit (PTU), type X
Optical lenses	2x	105 mm
Acquisition machine	1x	Running Davis 10.1

Table 4.4: Detailed list of equipment used for the PIV measurement campaign.

Moreover, [Figure 4.27](#) presents the final experimental setup that was used during the PIV campaign.

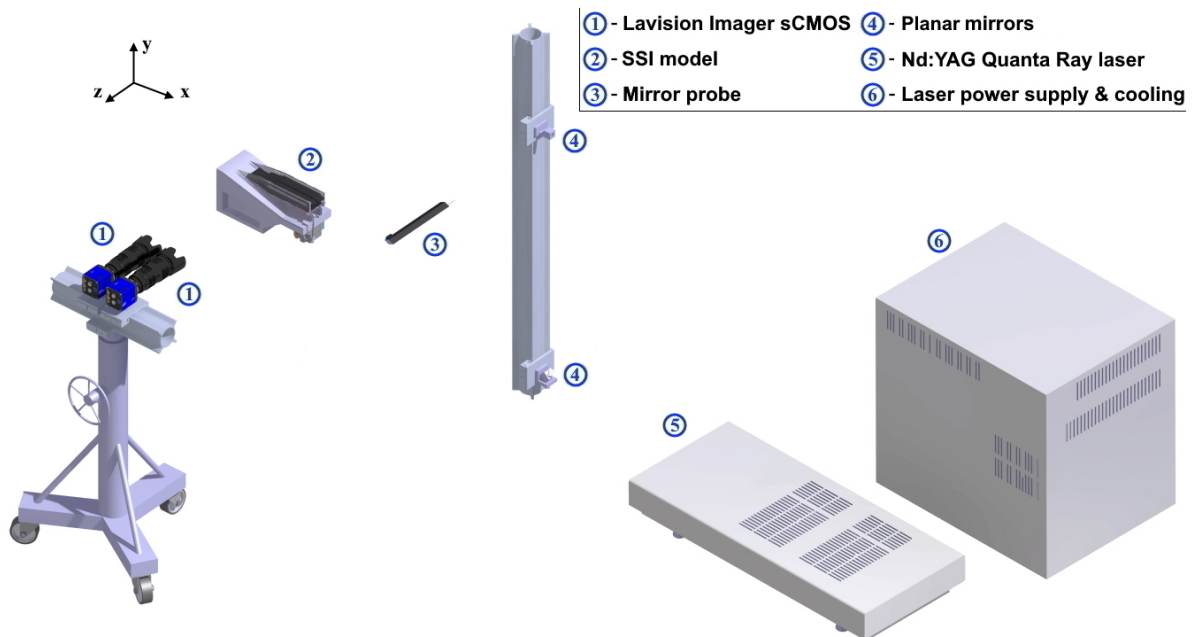


Figure 4.27: Three-dimensional CAD view of the complete PIV test setup, seen from the port side of the wind tunnel.

4.5. Uncertainty analysis

Like in every experimental effort, this report's experimental campaigns have been naturally prone to several errors that must be quantified to assess the experimental accuracy of the results. This provides an estimate as to how much the experimental outcomes would have deviated from the actual values. Hence, the quantification of these errors is done by means of an uncertainty analysis on all probable error sources for the different measurement campaigns. First, the uncertainty analysis for the Schlieren campaign is treated in [subsection 4.5.1](#). Next, the uncertainty analysis for the static pressure campaign is discussed in [subsection 4.5.2](#). At last, the PIV uncertainty analysis is covered in [subsection 4.5.3](#).

4.5.1. Schlieren imagery

The Schlieren experimental setup introduced a number of sources for probable errors, owing to hardware limitations of the optical system. The following contains a number of issues highly likely to have caused inaccuracies in the Schlieren images.

Integration along line-of-sight This is considered the main error from which all other errors originate. Any light ray traveling through the domain of the Schlieren system will experience distortions as a result of the compressible flow features it has encountered. Therefore, the images captured by the camera only provide an averaged result of the real flow phenomena in the test section.

Flow unsteadiness The supersonic flow through the SSI model can be described as quite unsteady, mainly due to the presence of the oscillating pseudo-shock in the intake's duct. The error due to unstable flow features is a direct result of the brightness effects that are being integrated along the line of sight in the Schlieren system. An example of this issue is that the pseudo-shock is imaged larger in some frames and smaller in other frames. This repetitive but unpredictable cycle makes it hard to confirm the real size of the pseudo-shock due to these brightness-related effects.

Optical misalignment's The Schlieren system uses multiple lenses, mirrors and test section windows, and of course the test section. Any misalignment or pollution (commonly dust) on the optical setup parts can lead to significant inaccuracies upon acquisition by the sensor. Even after confirming all equipment was clean and aligned, optical aberrations will remain inevitable and the results will suffer minimal depreciation due to the above flaws.

4.5.2. Static pressure measurements

Experimental static pressure measurements will always be subjected to errors due to a variety of factors. Quantifying these errors is a crucial part of investigating the true pressure distribution through the SSI model to have an idea of how large the discrepancies are.

Wall pressure error propagation The finite size of pressure orifices that can be smoothly manufactured may be sufficiently large to induce an error in the measured pressure, such that

$$p_{wm} = p_w + \Delta p_w \quad (4.25)$$

where p_{wm} is the measured pressure at a wall, p_w is the actual pressure at the wall and Δp_w is the introduced error in the pressure measurement. From dimensional analysis, one may infer that for a pressure tapping of a given geometry in a zero pressure-gradient flow (or where the tapping diameter is small compared with the scale of the pressure variation), Δp non-dimensionalized with the wall shear stress τ_w is a function of the following variables ([Equation 4.26](#)):

$$\Pi = \frac{\Delta p}{\tau_w} = f\left(\frac{d_s u_\tau}{\nu}, \frac{d_s}{D}, M, \frac{l_s}{d_s}, \frac{d_c}{d_s}, \frac{\epsilon}{d_s}\right) \quad (4.26)$$

and the last variable is the boundary layer condition (laminar or turbulent) of the wall-bounded flow. Here, d_s is the pressure orifice diameter, $u_\tau = \sqrt{\tau_w/\rho}$ is the friction velocity, D is the flow lengthscale, M is the Mach number, l_s is the orifice depth, d_c is the diameter of the cavity behind the orifice, ϵ is the root-mean-square height of the burrs on the edge of the pressure orifice, ρ is the fluid density and ν is the kinematic viscosity. A generic pressure orifice with the relevant geometry and features labeled is seen in [Figure 4.28](#).

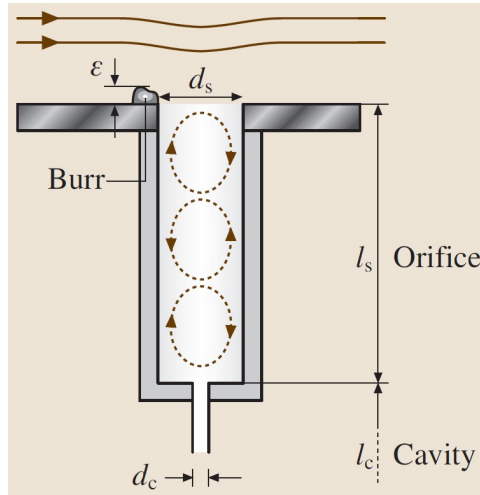


Figure 4.28: Schematic of generic wall tapping with the relevant geometry, taken from Tropea et al. [105].

The true pressure at the wall is (Equation 4.27):

$$p_w = p_{mw} - \Pi \tau_w \quad (4.27)$$

The complexity of the flow local to the orifices shows that analytical or numerical solutions for the pressure error are only present for very low Reynolds numbers and two-dimensional geometries. The following contains the most outspoken error sources in pressure measurements, directly related to the variables introduced above.

1. Finite-area effects Given a deep orifice with smooth edges, the finite size (diameter) of the orifice causes local curvature of the streamlines and a complicated system of vortices within the cavity (and potentially a stagnation point on the downstream wall), which was observed by Ray [106]. The effect of a finite orifice diameter on the measured static pressure is expressed as (Equation 4.28):

$$\Pi = f\left(d_s^+, \frac{d_s}{D}\right) \quad (4.28)$$

where $d_s^+ = d_s u_\tau / \nu$ is the ratio of tapping diameter to viscous scale and d_s/D is the flow lengthscale. The error introduced into the measurement of pressure at the wall by a tapping of finite diameter in turbulent flow is positive for deep holes and increases with the ratio of the hole diameter to the viscous scale, d_s^+ (for a given tapping diameter d_s/D), but decreases as the ratio to the flow lengthscale, d_s/D , increases for a given d_s^+ . Of course the error will be averaged out in the measurement of the pressure gradient in steady internal flows since the flow lengthscale does not change. However, for boundary-layer pressure gradients the effect may be significant.

2. Compressibility effects Experiments at high Mach numbers entail highly compressible flow regimes. For high Reynolds numbers, experimental data shows a general trend of increasing error with decreasing Mach number and increasing d_s/δ^* (at least for the smaller tappings), where δ^* is the displacement thickness. Rainbird [107] proposed that for approximately $d_s/\delta^* > 10$, the compressibility calibration coefficient can be estimated by (Equation 4.29):

$$C_{ps} \approx \frac{0.04}{\sqrt{M_e^2 - 1}} \quad (4.29)$$

According to Ducruet [108], the effect of the Mach number is more important for laminar than for turbulent boundary layers.

3. Finite depth effects The depth of the tapping cavity l_s is defined here as the distance between the plane of the wall and either the cavity behind the orifice or the connection to the transducer, with diameter

d_c and depth l_c . This parameter has shown to affect the magnitude of the pressure error in a complex fashion (that also involves the relative cavity width with respect to the orifice, d_c/d_s). For shallow tappings and moderate values for d_s^+ , Ray [106] formulated the error as (Equation 4.30):

$$\Pi_{fd} = f \left(\frac{l_s}{d_s} \sqrt{d_s^+} \right) \quad (4.30)$$

where the fraction term at the right of the equation represents a function of the minimum deep tapping ratio l_s/d_s , which is defined to mark the point beyond which the error ceases to change. Shaw [109] found that the pressure error was independent of the depth-to-diameter ratio for $l_s/d_s > 1.5$, but that the error steadily decreased for shallower tappings.

4. Condition of orifice edge Two main aspects are known to affect the pressure error by altering the flow field in and around the orifice: the size of any burrs remaining after drilling and the magnitude of the radius on the edge of the hole (either imposed or caused by drilling, sanding or polishing. Shaw [109] discovered that burrs can cause errors that increase linearly with d_s^+ , when considering a constant ϵ/d_s and deep tappings ($l_s/d_s = 4$). The same author found a maximum non-dimensional pressure error of $\Pi \approx 8$ for $d^+ = 275$. One should note that a large speck of dust resting on the edge of a tapping could cause a similar effect, hence there is reason to clean out tappings before making sensitive measurements.

Uncertainty analysis results Concluding the static pressure uncertainty analysis, Table 4.5 shows a table with the calculated uncertainty values resulting from the error sources mentioned above, assuming that the viscous lengthscale d^+ was roughly 1000.

Error source	Symbol	Error
Finite area effects	Π_{fa}	<3.6
Compressibility effects	C_{ps}	<0.023
Finite depth effects	Π_{fd}	<7.9
Condition port edge	Π_{pe}	<29

Table 4.5: Table reporting the static pressure uncertainty values.

4.5.3. PIV

Throughout the PIV campaign, different issues arose from the acquisition phases that deserve a discussion to reflect on the campaign's accuracy and precision of the results.

Seeding particle slip uncertainty As was explained in section 4.4, the seeding particles are supposed to follow the flow with roughly the same velocity. However, due to inertia effects, the seeding particles do not attain the real flow velocity and a velocity difference exists which is known as the particle slip velocity (Equation 4.31):

$$\vec{U}_{slip} \approx \vec{u}_f - \vec{u}_p = \tau_p \cdot \vec{a}_p \quad (4.31)$$

where τ_p is the particle response time and \vec{a}_p is the particle acceleration. Assuming that the particle motion is in the Stokes regime ($Re \ll 1$ and viscous forces dominate the motion) and that the flow is steady, then according to Sun [110], \vec{a}_p can be expressed as the inner product of the velocity with its gradient (Equation 4.32):

$$\vec{a}_p = \vec{V} \cdot \nabla \vec{V} \quad (4.32)$$

Substituting Equation 4.32 back in Equation 4.31 gives, assuming a two-dimensional flowfield (Equation 4.33):

$$\vec{U}_{slip} = \tau_p \cdot (\vec{V} \cdot \nabla \vec{V}) = \tau_p \vec{V} \cdot \left(\frac{\partial u}{\partial x} + \frac{\partial v}{\partial y} \right) \quad (4.33)$$

From Equation 4.33, one may infer that the errors will be larger in the regions where the gradients are larger. For high-speed flowfields, this points to the regions in which shock waves are present. The uncertainty can be quantified by the mathematical norm of the slip velocity vector (Equation 4.34):

$$\epsilon_{slip} \approx \|\vec{U}_{slip}\| \quad (4.34)$$

Window-size uncertainty Since the velocity is obtained through confining the particles by finite interrogation windows, an error is introduced. One may imagine that flow features smaller than the window sizes cannot be resolved due to a strict discretization pattern. The uncertainty due to the spatial resolution, as defined by Schrijer and Scarano [111], is written as (Equation 4.35):

$$\epsilon_{ws} = \text{sinc}\left(\frac{l_{ws}}{\lambda}\right) \quad (4.35)$$

where l_{ws} is the window size and λ is the wavelength of interest.

Cross-correlation uncertainty The cross-correlation algorithm, responsible for converting raw particle images to velocity field plots, has a particular degree of uncertainty. The error propagated from this algorithm, as defined by Raffel et al. [101], is expressed as (Equation 4.36)

$$\epsilon_{cc} = \frac{\epsilon_{corr} l_{px}}{M\Delta t} \quad (4.36)$$

where ϵ_{corr} is the correlation uncertainty. According to Raffel et al. [101], this error is in the order of 0.1 pixels for planar and 0.2 pixels for tomographic PIV.

Statistical uncertainty The PIV campaign consisted of making wind tunnel runs in which 300 image pairs were shot per single run. The final PIV result was then obtained by averaging the velocimetry result from these 300 image pairs. One may imagine that the velocities and fluctuations in one image pair are not quite same as in any other pair. Therefore, the practice of averaging the results of a finite number of vector fields to obtain one mean flow vector field introduces a statistical error that is based on the ensemble size. This error can be quantified for both the mean velocity and the velocity RMS using error propagation theory (Equation 4.37, Equation 4.38):

$$\epsilon_{\bar{u}} = \frac{\sqrt{u'^2}}{\sqrt{N}} = \frac{\sigma}{\sqrt{N}} \quad (4.37)$$

$$\epsilon_{u'} = \frac{\sqrt{u'^2}}{\sqrt{2N}} = \frac{\sigma}{\sqrt{2N}} \quad (4.38)$$

According to Benedict and Gould [112], the flow fluctuations are associated with the standard deviation σ according to the relation $\sigma = \sqrt{u'^2}$.

Uncertainty analysis results Concluding the PIV uncertainty analysis, Table 4.6 shows a table with the calculated uncertainty values resulting from the different error sources mentioned above.

Error source	Symbol	Error
Particle slip	ϵ_{slip}	<1.8 m/s
Window size	ϵ_{ws}	<2.5 mm
Cross-correlation	ϵ_{cc}	<2.9 m/s
u-component	$\epsilon_{\bar{u}}$	<1.6 m/s
v-component	$\epsilon_{\bar{v}}$	<1.1 m/s
RMS-u	$\epsilon_{u'}$	<1.1 m/s

Table 4.6: Table reporting the PIV uncertainty values.

5

Experimental Results

In this chapter, all experimental results are discussed which followed from the flow measurement campaigns treated in [chapter 4](#). In [section 5.1](#), the flow behavior is analyzed using both Schlieren and static pressure data. In [section 5.2](#), the final results following from the Schlieren and static pressure campaign are provided and carefully discussed. Following, in [section 5.3](#) the Particle Image Velocimetry (PIV) results are presented. Ultimately, the intake performance is assessed by determining the total pressure recovery (TPR) in [section 5.4](#).

5.1. Schlieren & static pressure - Flow analysis

The Schlieren and static pressure results are necessary to characterize the flow structure and to make the trade-off between the three butterfly valve designs to determine which valve design assures the most stable flow profile in the intake, profoundly in the critical condition. Before delving into this trade-off, it is important to first get familiar with all the relevant flow phenomena that take place inside the intake. In [subsection 5.1.1](#), all relevant flow features are explained using Schlieren imagery. Following, [subsection 5.1.2](#) takes the reader through the trade-off process which produced the best valve design used for the PIV campaign.

5.1.1. Intake flow characteristics

In [Figure 5.1](#), a Schlieren image is shown of the SSI model while operating in the critical condition. As becomes clear from the labels in this figure, multiple flow features emerge in and around the SSI model during a wind tunnel run.

Around the SSI model, a number of Mach waves are found which emanate from seams and other surface irregularities inside the test section. Since these do not affect the flow through the intake, no further explanation is required on these features. Label '1' indicates the double shock system of the supersonic diffuser that is generated by the compression plate leading edge and lip-surface transition. From [Figure 5.1](#), two aspects become clear: The first OSW is not straight but rather curvy. This is a direct consequence of the compression plate leading edge being slightly blunted. This will make it difficult to obtain a reliable result on the shock wave angle. Also, the second OSW is seen being fairly wide at the shock root and near the cowling it looks very thin. This effect may be caused by the fact that Schlieren integrates along the optical path due to which some 3D features are shown as warped or distorted features in the 2D Schlieren. Nonetheless, this still confirms the concession made in [subsection 3.3.2](#), in which it was predicted that multiple compression waves will be formed at this lip-surface junction of the compression plate. Following, label '2' indicates the two OSW that are generated at the leading edge of the cowling due to the supersonic flow. Since the lower OSW enters the intake duct, this shock wave will keep reflecting downstream. This reflection-pattern disappears upon the appearance of the shock train inside the duct. Coming to label '3', the most important feature of the SSI model is indicated which is the pseudo-shock. What becomes immediately clear is that the pseudo-shock has an asymmetric tendency towards the cowling. This confirms the research conducted by Gawehn et al. [113], which stated that if ducts had small cross-sections and no streamwise gaps at the side-walls, asymmetric pseudo-shocks would be observed. Furthermore, the alternating bright and dark shades in the pseudo-shock confirm its very nature, namely that the shock train decelerates the flow to subsonic speed through the bright shocks, after which the flow accelerates again to supersonic speeds through the darker expansion regions. Label '4' shows the boundary bleed flow that is removed from underneath the SSI model.

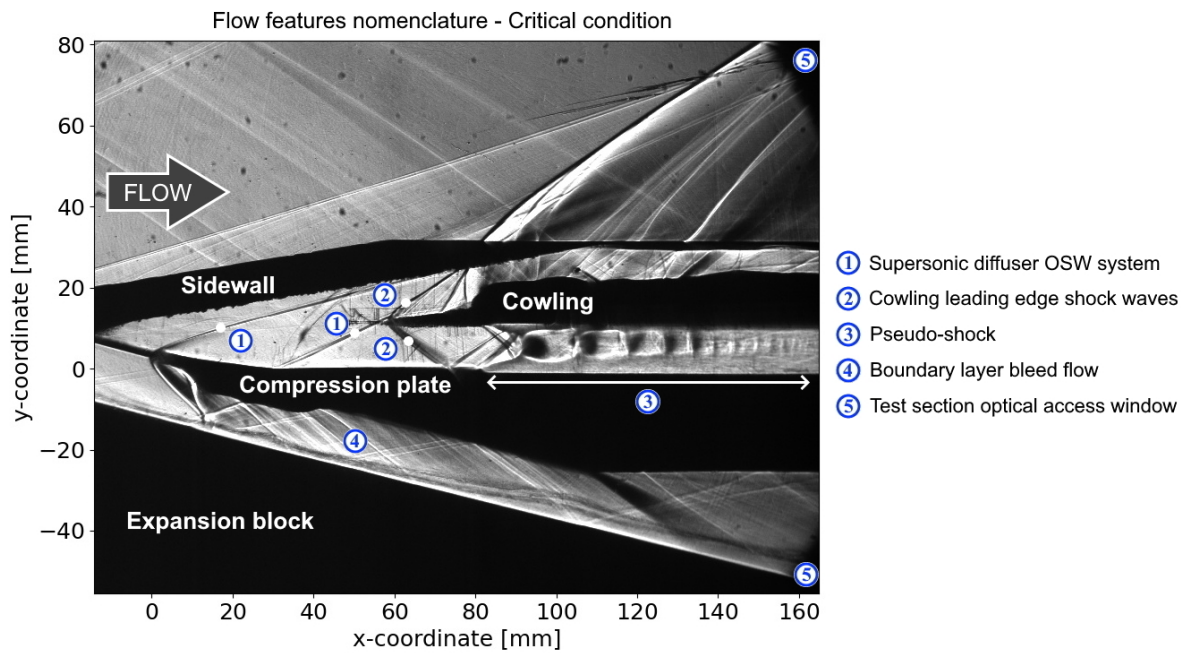


Figure 5.1: Schlieren image of the SSI model in critical condition showing the different flow features.

As was mentioned in [section 4.1](#), the SSI model was placed at the most downstream location of the elongated expansion block holes to create biggest bleed hole possible, with a bleed slot width of 61 mm. Finally, at label '5' in the top and bottom corners on the right side of the image, the shadow is captured of the optical access windows.

5.1.2. Butterfly valve trade-off

The trade-off process based on which the butterfly valve yielding the highest performance was chosen used both: a sub-trade-off based on the Schlieren and static pressure results. Since the critical condition is the only operational condition in which the supersonic flow has tendencies to transition to the subcritical regime and is able to create arbitrary oscillations, this is the only one considered for the trade-off process since this condition will clearly distinguish the most robust from the lesser robust valves. From the results on the supercritical and near-supercritical conditions, there were hardly any differences in performance between the three valve designs regarding both the Schlieren and static pressure results.

Schlieren Trade-off To quantify which butterfly valve design performed best based on the Schlieren results, it was chosen to consider amongst others the streamwise range in which the terminal shock wave oscillates during the critical condition. This was done for all three butterfly valves. Also, the mean Schlieren image and the associated standard deviation image were plotted to clearly distinguish per butterfly valve how the pseudo-shock behaved. The mean image was generated based on the individual frames in which the Schlieren setup captured the intake whilst in the critical condition. This gives an indication as to how stable the pseudo-shock was in the critical condition. The standard deviation was computed by determining the root-mean-square of the Schlieren images in the critical condition. This would return an image of the SSI model in which the locations with a high standard deviation (colored bright) are shown in direct contrast with the locations with a low standard deviation (colored dark). Hence, one could indicate whether the duct terminal shock wave, and therefore the pseudo-shock, was confined to just the intake duct or whether it got expelled frequently outside the intake. This would be visible if the standard deviation near the intake entrance would be high. From this analysis pattern, the following results were found for the different valve designs:

For the airfoil valve, the front and aft limits of the oscillation range are shown in [Figure 5.2](#), respectively. It becomes clear that the front limit of the oscillation range touches the leading edge of the compression plate which indicates that the intake is operating deep in the subcritical regime. This front limit was designated

by the streamwise position 0 mm due to the shock's foot reaching the compression plate leading edge. For designating the position of the shock train inside the intake duct, the x-coordinate (streamwise) position of the terminal shock along the duct's centerline is used to determine the position. Regarding the aft limit of the oscillation range for this butterfly valve, the shock train stem is seen located pretty deep inside the intake's duct. This is not preferred since this means that the pseudo-shock is cut-off early which implies that the pressure recovery will be very low and the flow's deceleration will be insufficient to bring the flow to subsonic speeds before entering subsonic diffuser.

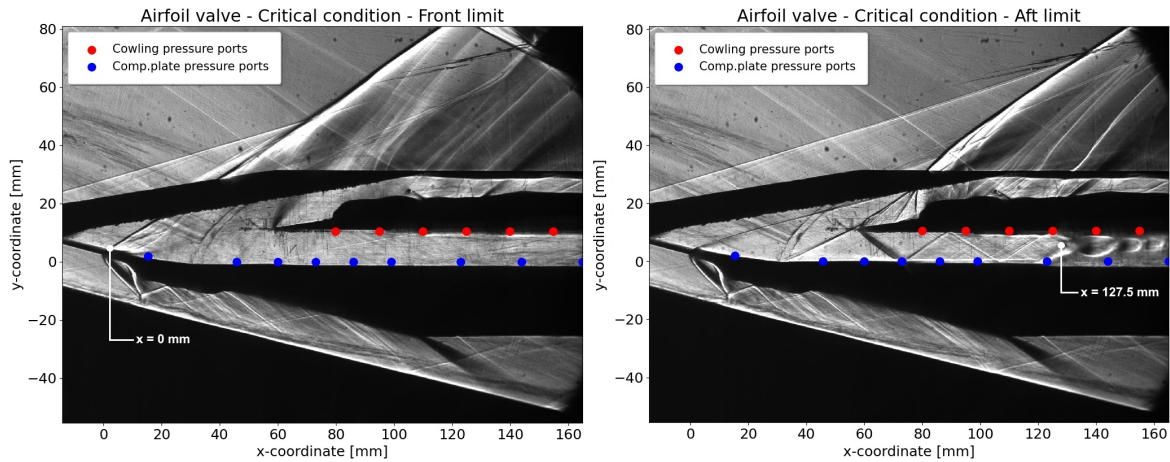


Figure 5.2: Front (left) and aft (right) limits of the oscillation sequence during the critical condition for the airfoil valve.

The mean Schlieren image for the airfoil valve is shown in [Figure 5.3](#). The structure of the pseudo-shock in the intake duct has nearly vanished and is virtually unrecognizable. This is a direct result of what happens when a highly unsteady flowfield is averaged to one image. Due to this, the mean shock location cannot be located with certainty. However, taking the entire Schlieren set during the critical condition and determining the average of the terminal shock location, the mean is found at $x = 47.3 \text{ mm}$. This confirms that the shock train frequently entered the subcritical condition. The fact that the shock train is barely recognizable in [Figure 5.3](#) can also be supported by the fact that the broad oscillation domain of the pseudo-shock for this butterfly valve did not keep the pseudo-shock on a regular basis inside the intake duct.

In [Figure 5.4](#), the Schlieren standard deviation is shown for the airfoil valve in the critical condition. From this image, one may infer that the unsteadiness in the flowfield was significant based on the high standard deviation values, which is visible near the cowling leading edge. Also, high standard deviations are found on the backside of the cowling, which indicates that the shock features outside the duct were not stationary, and this means that the duct terminal shock wave interacted frequently with the shock features outside the duct due to which the standard deviation in this region is very significant. Therefore, when combining the mean shock location with the standard deviation plot, one may conclude that the airfoil valve causes a relatively high flow unsteadiness and fails to properly maintain the pseudo-shock in the critical condition. On a total basis based on all figures above, the net range over which the terminal shock wave oscillates was about 127.5 mm .

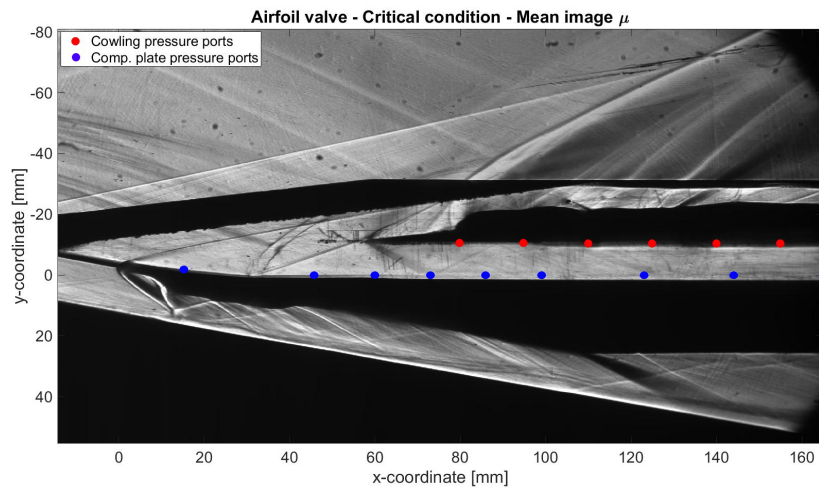


Figure 5.3: Mean Schlieren image of the SSI model in the critical condition for the airfoil valve.

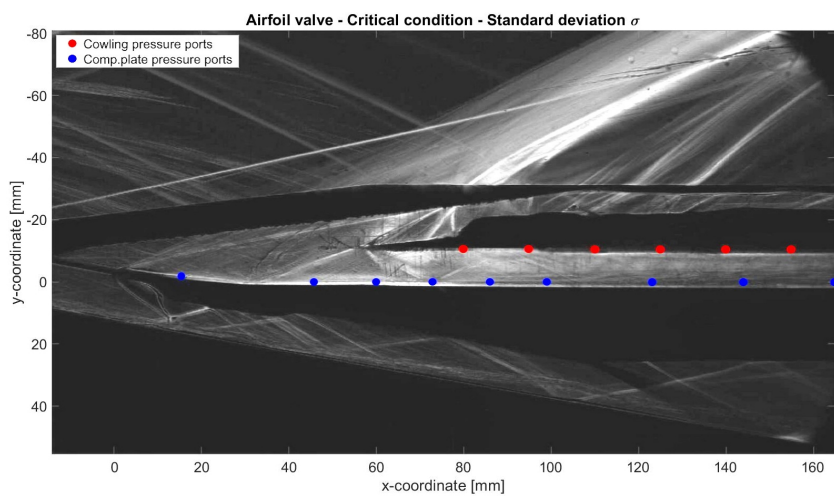


Figure 5.4: Schlieren image featuring the standard deviation of the SSI model in the critical condition for the airfoil valve.

Following, in [Figure 5.5](#) the front and aft oscillation limits are shown for the arc valve. For an intake operating at the critical condition, the aft limit for the arc valve is located not too far downstream from the intake opening. Also, even though the front limit of the arc valve is shown to be located near the entrance of the intake duct, the shock train is seen dangerously close to the intake opening, which is confirmed by the fact that the most upstream shock of the shock train is nearly indiscernible. This limiting case in which the flow is captured at the exact border between the critical and subcritical conditions may be another product of the fact that these shock features are 3D and are being viewed on a 2D image. Anyhow, this is clearly an indication of the pseudo-shock's strong bias towards the subcritical regime. From the complete Schlieren set for the arc valve, it was confirmed that the shock train did not get expelled from the duct at all. The oscillation range covered about 40 mm of space in the streamwise sense, which is less worse than with the airfoil valve but still a considerable distance.

The mean Schlieren image for the arc valve is shown in [Figure 5.6](#). The shock train structure can now be clearly recognized in the duct, which provides a first impression of the low unsteadiness found with the arc valve. Determining the average terminal shock location from the complete Schlieren set results in a streamwise location of $x = 78.2 \text{ mm}$, which means that on average the pseudo-shock resided inside the intake duct. The standard deviation plot, shown in [Figure 5.7](#) verifies the former explanation by showing that the higher standard deviations are exclusively found inside the intake duct area. This confirms that the pseudo-shock did indeed stay in the duct without showing large tendencies towards creating any shock instabilities or trying to exit the duct. Combining the above results for the arc valve, it can be deduced that this valve design

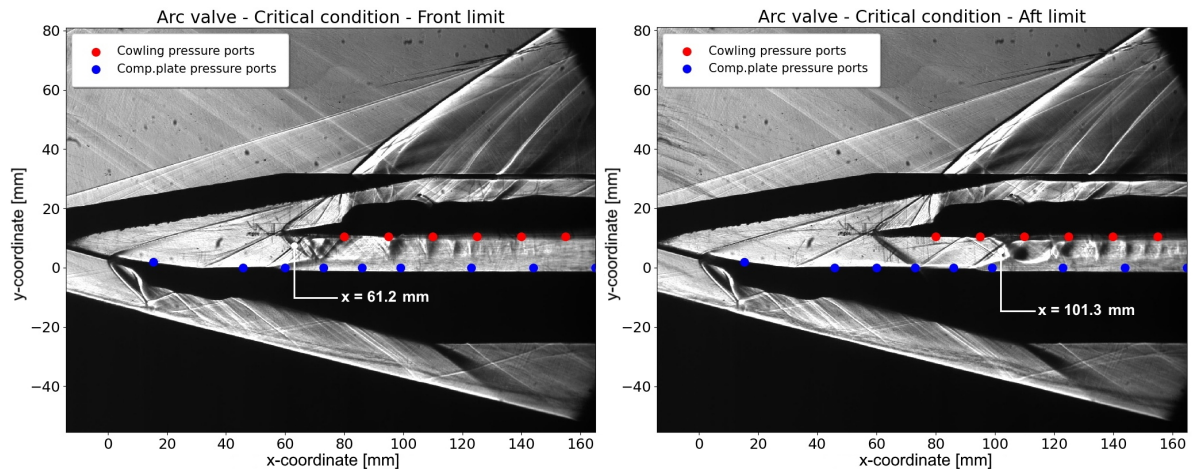


Figure 5.5: Front (left) and aft (right) limits of the oscillation sequence during the critical condition for the arc valve.

ensures a stable operation during the critical condition without any vigorous shock oscillations.

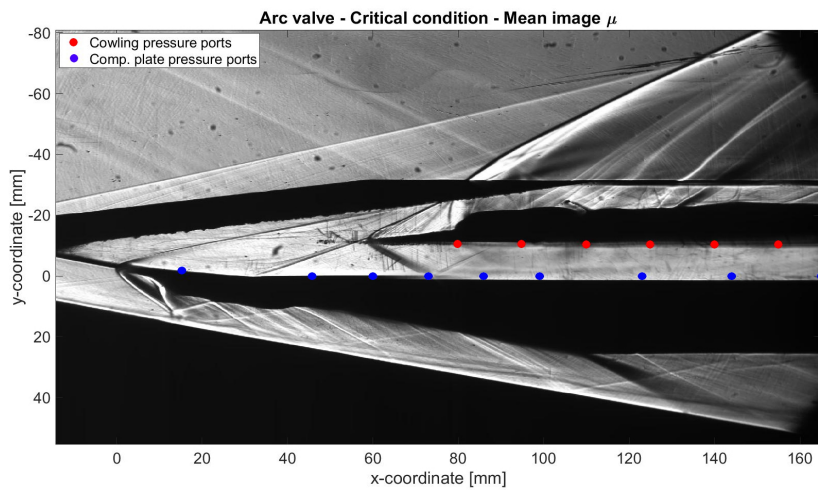


Figure 5.6: Mean Schlieren image of the SSI model in the critical condition for the arc valve.

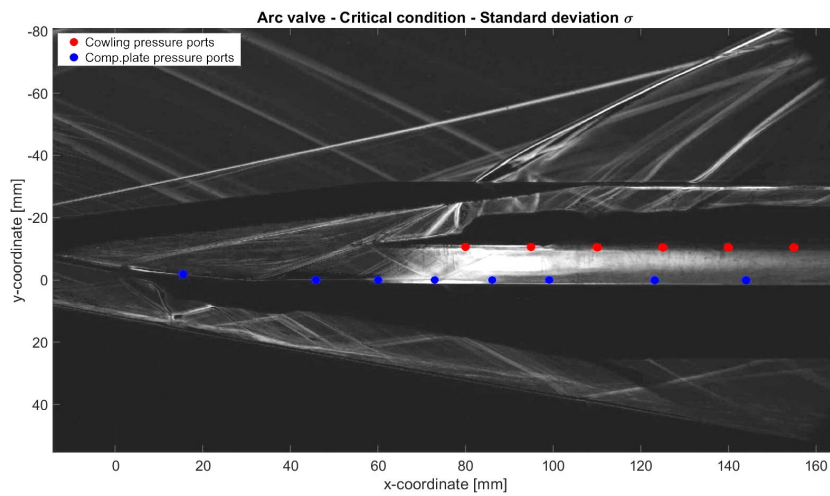


Figure 5.7: Schlieren image featuring the standard deviation of the SSI model in the critical condition for the arc valve.

Finally, the diamond valve front and aft oscillation limits are shown in Figure 5.8. The shock train front limit is seen at approximately the same location as the first cowling pressure orifice at $x = 79 \text{ mm}$. Also, the shock train structure is intact and no distortions are visible in its upstream part, which is a clear difference from the arc valve's results. Regarding the aft limit, also here the shock train structure is clearly recognized and no abnormalities are reported. The range over which the shock train oscillates for this last valve is roughly 16 mm , which is the smallest range found in all three valve designs.

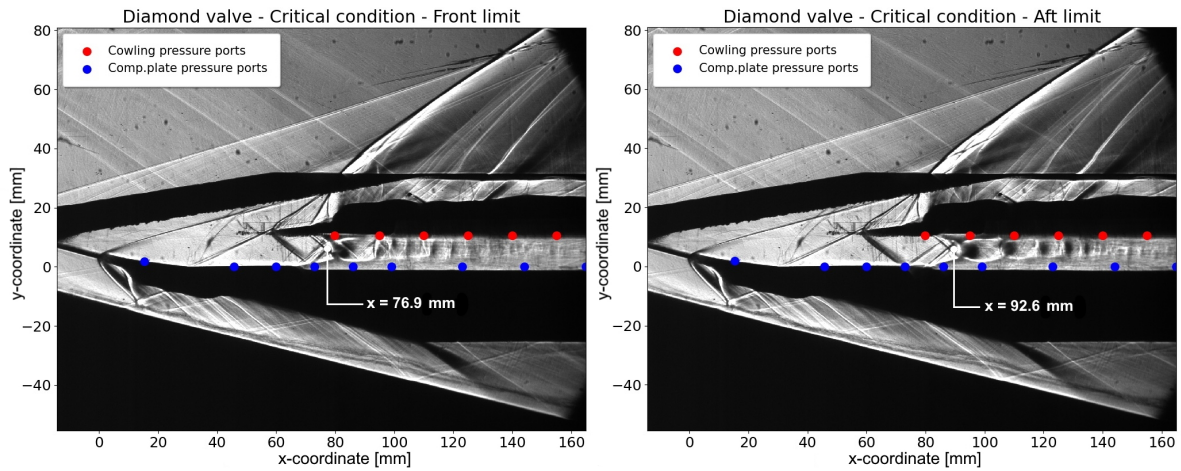


Figure 5.8: Front (left) and aft (right) limits of the oscillation sequence during the critical condition for the diamond valve.

The Schlieren mean image for the diamond valve is shown in Figure 5.9. Hardly any differences are found when comparing this to the result for the arc valve. The mean image verifies also for this valve that the pseudo-shock is contained in the duct and that no large oscillation tendencies appear at all. This adds another point of proof to this valve's robustness. The mean pseudo-shock location for the diamond valve was determined to be $x = 74.8 \text{ mm}$ based on the Schlieren set in the critical condition. The standard deviation image for the diamond valve is shown in Figure 5.10, where it is clearly visible that the higher standard deviations are found solely in the intake duct. Ultimately, this valve has shown the highest degree of robustness by showing the smallest shock oscillation displacements, proven by its standard deviation pattern, and having also the best identifiable shock structure in its mean image.

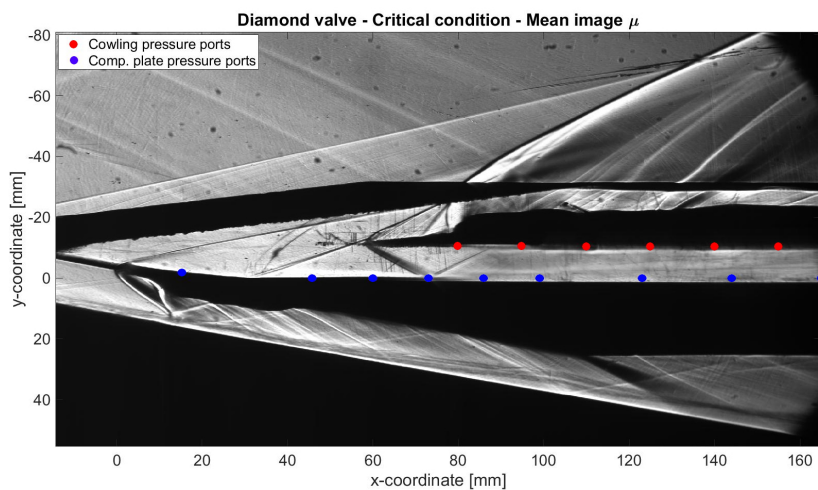


Figure 5.9: Mean Schlieren image of the SSI model in the critical condition for the diamond valve.

Static pressure trade-off To verify the decision taken following the sub-trade-off based on the Schlieren results, another sub-trade-off is performed based on the static pressure results. Unlike the Schlieren-based

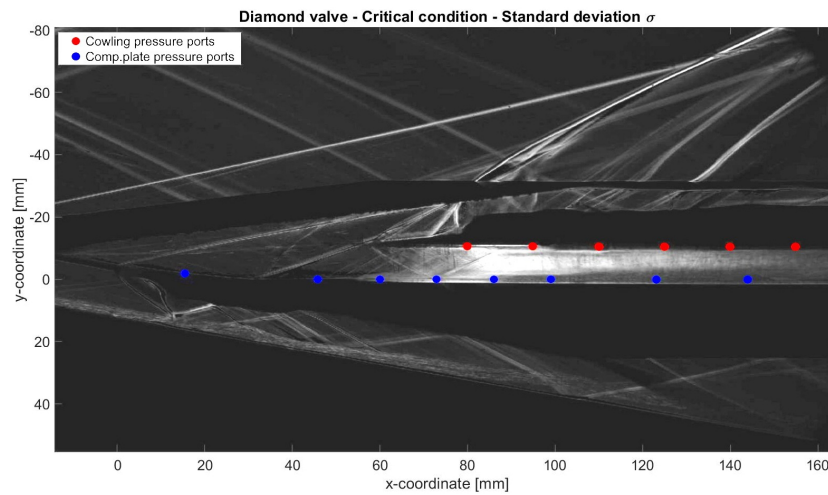


Figure 5.10: Schlieren image featuring the standard deviation of the SSI model in the critical condition for the diamond valve.

trade-off, the current trade-off will consider more than only inspecting the performance based on the pressure of the three valve designs in the critical condition. Since the pressure results are quantitative, there is much more to explore performance-wise regarding the use of the three valve designs in comparison with the predominantly qualitative Schlieren results. Note that the Schlieren results are not purely qualitative since quantitative information can still be retrieved from Schlieren images, such as the shock locations and shock standard deviations. One of the interesting aspects is to compare the static pressure results of the three butterfly valve designs with the analytical solution found with compressible flow theory. Also, the fluctuations in Static Pressure Recovery (SPR) is another result that is deemed interesting based on which one may decide which butterfly valve provides the best performance.

In [Figure 5.11](#), the static pressure normalized to the stagnation pressure is shown plotted as a function of the streamwise position. This figure shows the normalized static pressure results of the intake at all pressure orifices for both cowling and compression plate for the critical condition for all three butterfly valves. From this figure it becomes clear that, since in the critical operation the shock train is located near the duct's entrance, all three pressure curves show a gradual increase in static pressure as expected according to the theory of pseudo-shocks. However, upon further inspection of the results, the airfoil pressure curve is seen to follow a different path than the arc and diamond curves. Even though the airfoil curve initially shows higher static pressure results during the supersonic diffuser and the first half of the duct, the arc and diamond curves outperform the airfoil curve when reaching the last pressure orifice located in the subsonic diffuser just upstream of where the butterfly valve is located. However, to reveal which butterfly valve provides the most robust pressure profile that is as close as possible to the analytical solution, it becomes necessary to examine the pressure curves in comparison with the solution obtained from the two-dimensional shock relations, which is shown in [Figure 5.11](#) for the first four pressure orifices of the compression plate. The reason that the analytical solution was determined for only these four points comes from the fact that downstream of the fourth point the pseudo-shock is present, as shown in [Figure 5.12](#), where the two-dimensional shock relation can no longer be used.

A zoomed in version of [Figure 5.11](#) is shown in [Figure 5.13](#), where the first four normalized static pressure results for all three valve designs including the analytical solution are shown with greater clarity. When inspecting this figure, the airfoil curve is seen to clearly have the biggest discrepancy with the analytical solution. This is again explainable by the fact that, as discussed during the Schlieren trade-off, the pseudo-shock oscillates very vigorously when controlled using the airfoil valve. The arc and diamond valves perform almost identical behavior-wise with regards to the first four pressure orifices of the compression plate, which was expected since the oscillation behavior for both valves was roughly the same. This was confirmed from the Schlieren results. One might wonder why *all* valves overestimate the analytical solution and no pressure curve underestimates this analytical solution. The answer can be found in [subsection 3.3.2](#), where it was mentioned that the compression plate leading edge and the transition corner from the compression plate

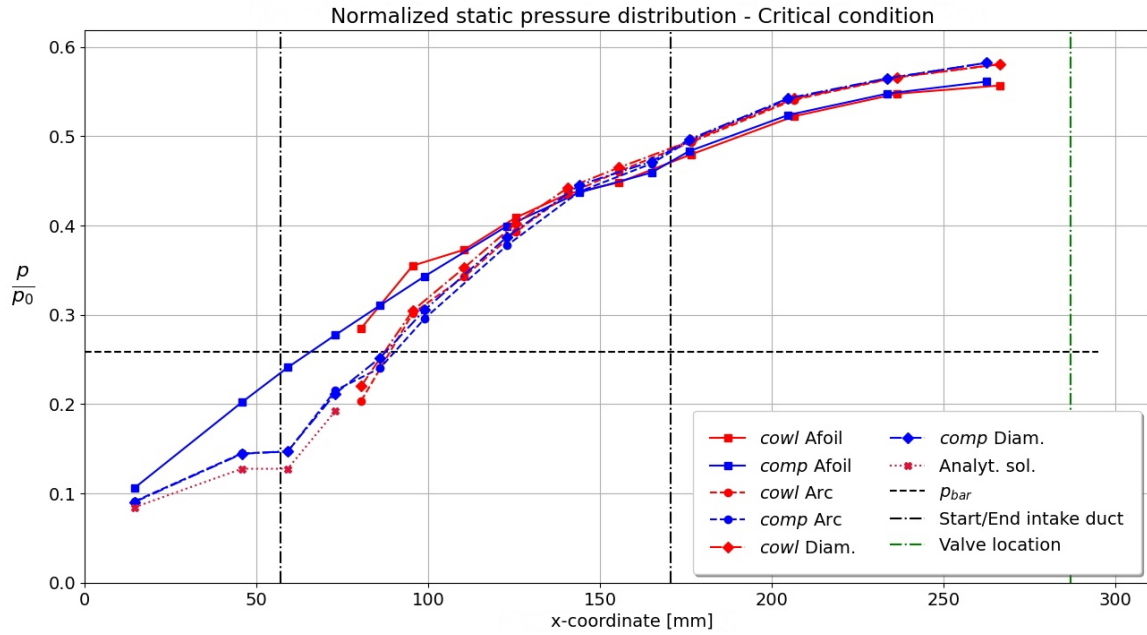


Figure 5.11: Normalized static pressure results vs. streamwise position for all three butterfly valves at the critical condition.

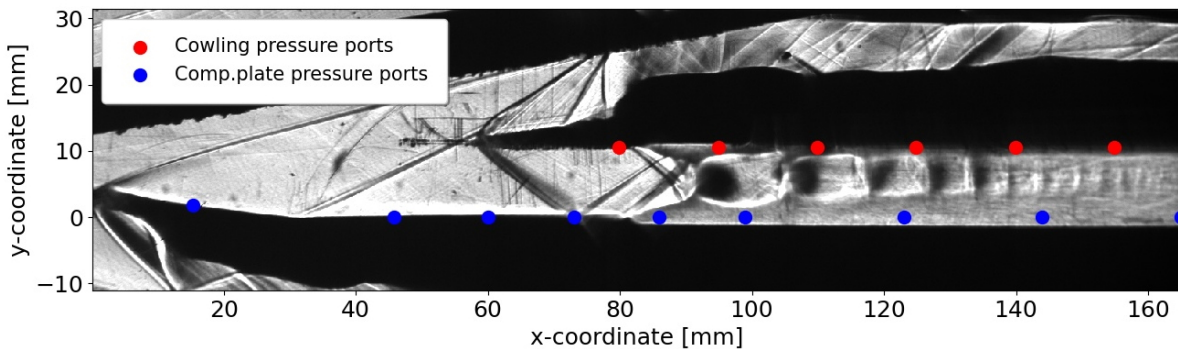


Figure 5.12: Zoomed in Schlieren image of the pressure orifice locations during the critical condition.

lip to the plate’s flat surface are not perfect corners but rather regions with a finite curvature. Theoretically speaking, these do not generate one OSW but rather a couple of grouped together Mach waves. Since a group of Mach waves can form one shock wave, the overestimation in static pressure seen in Figure 5.13 can be explained by the presence of more than just one shock wave which are grouped together over the finite curvatures at the two locations mentioned above. Unfortunately, the higher static pressures cannot be explained through the shock wave angles, since the analytical shock angle is higher than the experimental value (this will also be explained in section 5.3). Hence, the higher static pressure values found from the experiments can only be explained by the presence of a compression mechanism which is stronger than an ordinary analytical OSW which, as explained above, is formed by multiple Mach waves that coalesce into one strong shock-like structure.

Also, in Figure 5.14 the three pressure curves are again shown but this time for the last three pressure orifices of both the cowling and compression plate located in the subsonic diffuser. Again, the arc and diamond valve curves are seen following almost exactly the same path while the airfoil curve shows a lower final SPR than the first two curves. As explained before, this has to do with the airfoil valve’s poor performance in the critical condition since its aft oscillation limit was located pretty deep in the intake, which clearly indicates that the SPR region could not be fully completed due to the pseudo-shock lying deep in the intake.

Another aspect to consider are the fluctuations in SPR for all valves. In Figure 5.15, the SPR for all three

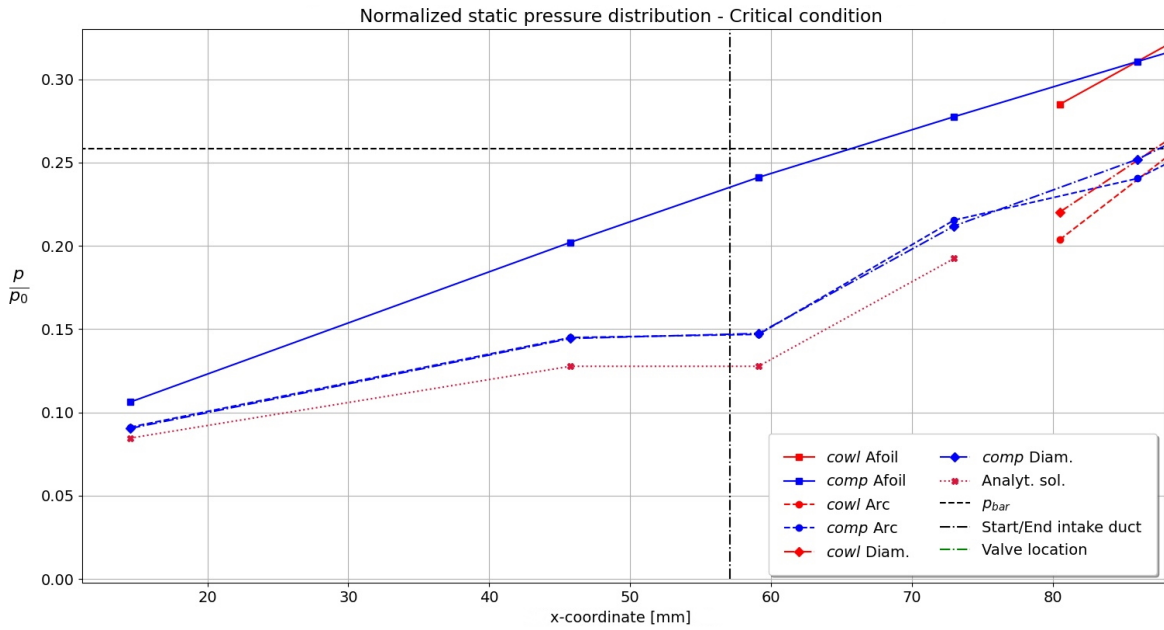


Figure 5.13: Zoomed in plot of the first four normalized static pressure results vs. streamwise position for all three butterfly valves at the critical condition.

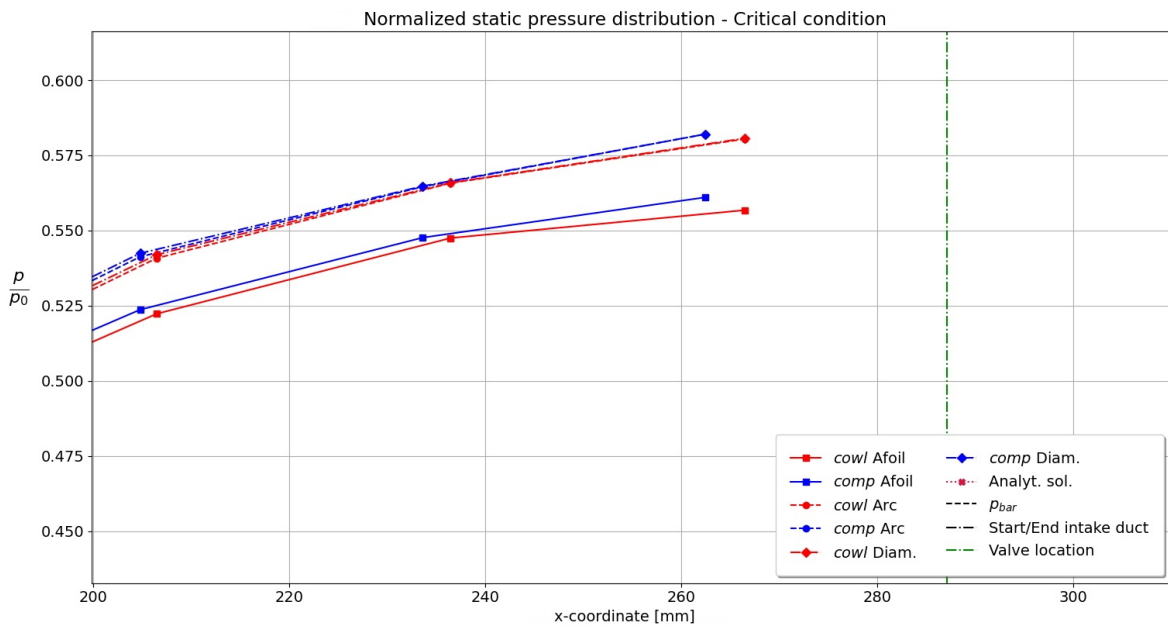


Figure 5.14: Zoomed in plot of the last three normalized static pressure results vs. streamwise position for all three butterfly valves at the critical condition.

butterfly valves is plotted against the time in which the measurements took place. Each of these three plots contains 500 data points and is the average of three sets of each 500 data points. It must be mentioned that these SPR results do not indicate the instantaneous results but rather the mean fluctuations that were found in the static pressure measurements. The reason to this is that the static pressure measurements experience a damping effect from the long path traversed to the Scannivalve pressure transducers, which causes an additional cut in the accuracy since the pressure capillaries act like time filters which average out the instantaneous results. In this figure it becomes clear that the diamond valve prevails in terms of highest mean SPR and that the fluctuations in the arc and diamond valve are similar. The airfoil valve is by far the less robust valve which becomes evident from its relatively lower mean SPR.

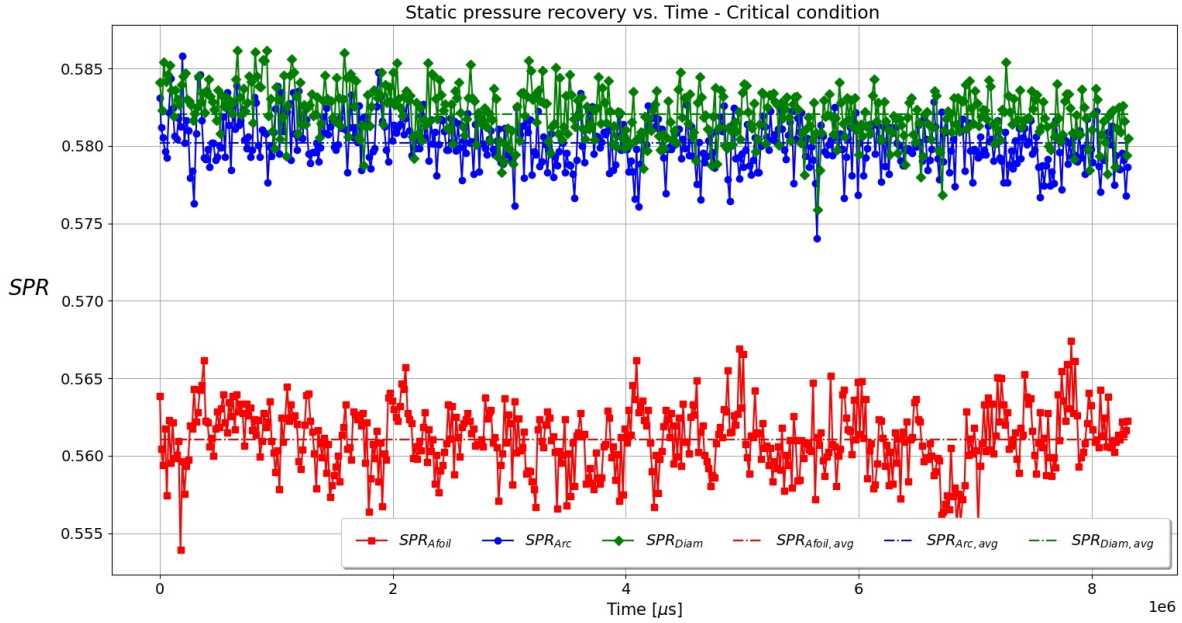


Figure 5.15: Plot of the SPR of the three valve designs in the critical condition.

5.2. Final Results

Based on the above two trade-off outcomes, it turns out that the diamond valve shows the best performance in terms of both qualitative and quantitative results. This part is meant to show the final Schlieren and static pressure results of the diamond valve for all three supersonic operational conditions of interest: supercritical, nearly-supercritical and critical conditions.

In [Figure 5.16](#) to [Figure 5.19](#), the final Schlieren and static pressure results are shown for the SSI model equipped with the diamond valve for the three aforementioned conditions. To make these final results also more comprehensible, it was chosen to place the Schlieren images at each of the operating conditions in the same figure of the static pressure plots to synchronize the streamwise position of both results to make it easier to compare the qualitative viscous flow phenomena in the Schlieren images with the quantitative changes in static pressure.

Supercritical condition In [Figure 5.16](#), the static pressure results and Schlieren image are shown for the SSI model whilst operating in the supercritical condition. The static pressure profile in this condition can be analyzed as follows: After the freestream Mach 2.0 flow has turned 14° over the expansion corner, the static pressure has decreased. Upon approaching the intake compression plate, an OSW is crossed that increases the static pressure. This static pressure is what is measured by the compression plate orifice at $x = 15 \text{ mm}$. This is then followed by the second somewhat weaker OSW that again raises the static pressure. This is the static pressure at the orifice at $x = 46 \text{ mm}$. Since no shocks exist between this orifice and the orifice immediately located downstream at $x = 59 \text{ mm}$, their static pressures are expected to remain constant. The reason why the orifice at $x = 59 \text{ mm}$ shows a slightly lower static pressure is unknown. One may speculate that the local roughness or the presence of any burrs around these orifices may provoke certain compressible flow effects that slightly alter the theoretical expectations. As expected from the presence of the lower cowling leading edge shock, the static pressure experiences a jump which is seen at the orifice at $x = 73 \text{ mm}$. Behind this orifice, the static pressure is seen to decrease, while the presence of a reflection wave at that location would suggest otherwise. The reason for this counter-intuitive behavior is explained by closer inspection of the Schlieren image. In this image, it becomes clear that the lower cowling leading edge shock wave impinges fairly close next to the pressure orifice at $x = 73 \text{ mm}$, causing an overshoot at this location.

This very anomaly was described by Liepmann et al. [114] on the effect of an impinging shock wave close to pressure orifices. One of the theories encompasses the intersection of a shock wave by means of a 'impulse-type' wave, which is classified as a situation in which a shock wave is closely followed by an expansion fan. This happens when the corner, or cowling leading edge in this case, causing this shock wave has a finite curvature. [Figure 5.17](#) shows that depending on the streamwise distance between the pressure orifice and

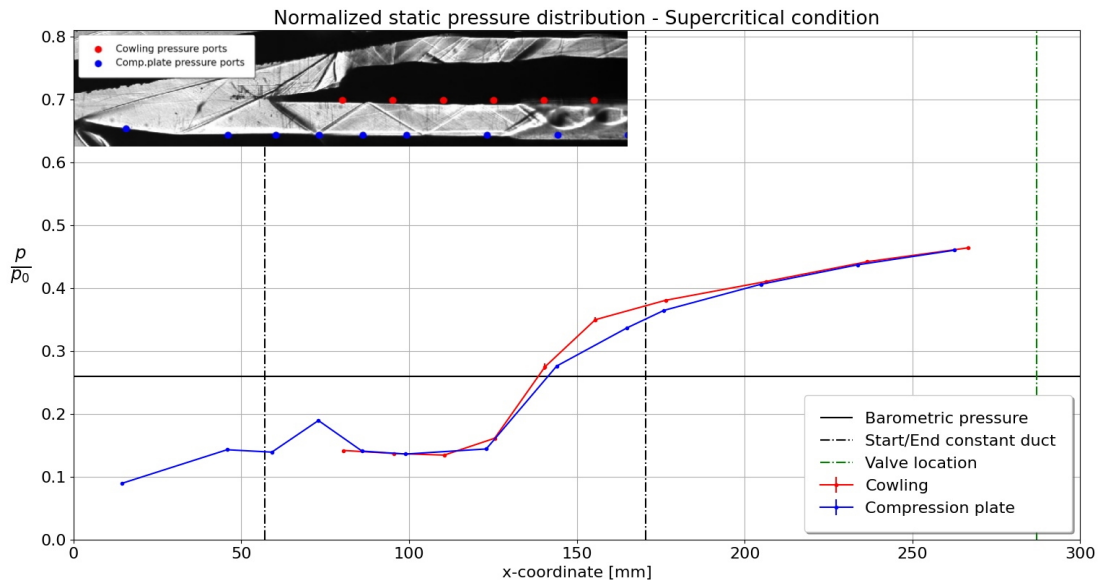


Figure 5.16: Schlieren image and Static pressure plot of the diamond valve in the supercritical condition.

the impinging shock and based on the state of the boundary layer, one may find from the static pressure readings at this very orifice an increase, decrease or no pressure alteration at all. This is exactly what happens in Figure 5.16. Closely inspecting the Schlieren image shows that the lower leading edge shock wave from the cowling has a slim bright signature and a large dark shade following behind it. Based on the explanation of this report's Schlieren measurements in subsection 4.2.3, this means that the slim bright line represents the shock wave and the shaded region behind it shows an expansion wave. Therefore, based on Figure 5.17, the decrease in pressure must be the result of the impulse-type wave that impinges close to the pressure orifice at $x = 73 \text{ mm}$.

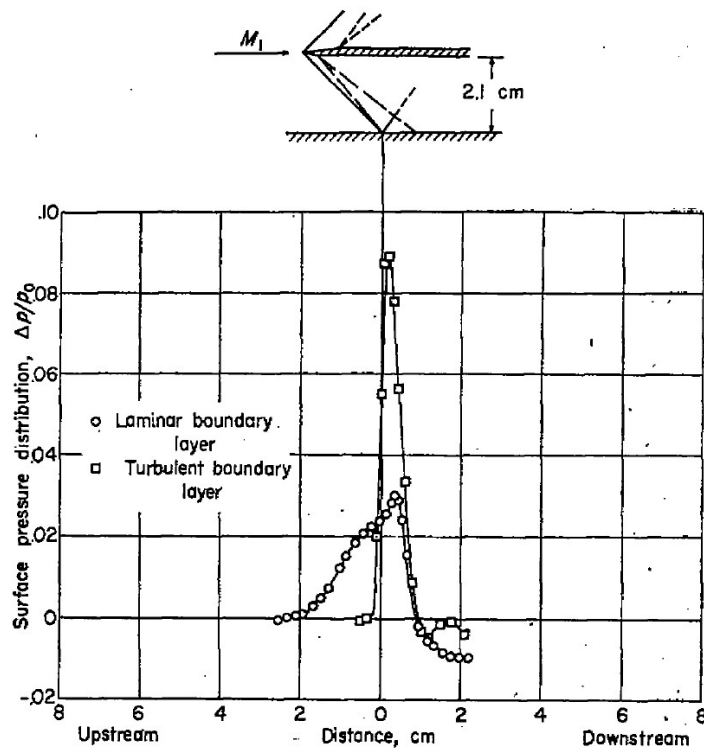


Figure 5.17: Reflection of an impulse-type wave from a flat surface, taken from Liepmann et al. [114].

The compression plate orifice at $x = 99 \text{ mm}$ has roughly the same static pressure as the compression plate orifice at $x = 86 \text{ mm}$ due to the absence of any shocks. The compression plate orifice at $x = 123 \text{ mm}$ reads the same static pressure, despite of the fairly weak reflected shock wave between the compression plate orifices located at $x = 99 \text{ mm}$ and $x = 123 \text{ mm}$.

Between the cowling pressure orifices at $x = 24$ and $x = 39 \text{ mm}$, the static pressure remains constant even though the flow has interacted twice with the reflected shock. However, since this reflected shock is fairly weak, this may be expected. In the absence of a shock wave between the cowling orifices at $x = 39$ and $x = 54 \text{ mm}$, the latter cowling orifice has the same static pressure as found at the orifice at $x = 39 \text{ mm}$. The cowling orifice at $x = 69 \text{ mm}$ has a higher static pressure after the flow negotiated the reflected shock. After the cowling orifice at $x = 69 \text{ mm}$ and the compression plate orifice at $x = 123 \text{ mm}$, the flow encounters the pseudo-shock, which causes the static pressure to gradually increase as is expected from the theory of pseudo-shocks. The reason why the increase in static pressure measured by the cowling orifices is greater in comparison with the compression plate orifices can be traced back to the asymmetry of the pseudo-shock along the duct centerline. When the flow arrives at the pseudo-shock, the cowling boundary layer has not grown as much as the compression plate boundary layer. This asymmetry in boundary layer causes an asymmetry in the pseudo-shock appearance, making the pseudo-shock tilted towards the cowling where the boundary layer is thinner. This also explains why the growth of the lower boundary layer, as a result of the adverse pressure gradient, starts earlier than the upper boundary layer. This thinner boundary layer of the cowling stimulates the static pressure rise on the upper wall due to less friction from the boundary layer. After the velocity has dropped sufficiently in the shock train and the boundary layers of both walls get closer to the pseudo-shock center, both cowling and compression plate static pressure curves are seen to follow the same path.

The statistical uncertainty in the static pressure results was quantified by determining the standard deviation of the static pressure results. The vertical bars at the measurement points in [Figure 5.16](#) show the statistical uncertainty in all measurement points and in this particular figure it is quite small due to the supercritical condition being a fairly stable operating mode. One should note that the standard deviation only serves as means of quantifying the statistical uncertainty in the final static pressure results and has no additional purpose. The largest standard deviations are found at the three pressure orifices on both cowling and compression plate downstream of the shock train stem in the streamwise range of $x = [142, 179] \text{ mm}$.

Nearly supercritical condition In [Figure 5.18](#), a Schlieren image and the static pressure results of the near-supercritical condition are shown. Here it becomes clear that these results follow the same explanation provided for the supercritical condition, only that this time the pseudo-shock has moved slightly more upstream. This is also visible in the final static pressure result, which is higher in comparison with the supercritical condition.

Analogous to the supercritical condition, the highest statistical uncertainty in the near-supercritical condition is found in the immediate vicinity of the shock train stem located in the streamwise range $x = [95, 144] \text{ mm}$. The statistical uncertainty is higher than in the supercritical case, but its order of magnitude remains fairly low due to the near-supercritical condition being a stable condition in the absence of any shock oscillations.

Critical condition In [Figure 5.19](#), a Schlieren image and the static pressure results of the critical condition are shown. In this figure, it becomes clear that the weak impulse-type shock causing a decrease in the static pressure between the compression plate orifices at $x = 73$ and $x = 86 \text{ mm}$ is absent due to the presence of the pseudo-shock. Also, in [Figure 5.16](#) it was mentioned that in the supercritical condition the asymmetry of the pseudo shock caused the cowling pressure orifices to have a higher static pressure due to less friction from the upper boundary layer. In the critical condition this static pressure difference between cowling and compression plate orifices in the pseudo-shock is less. This is very likely the result of the pseudo-shock being less asymmetric than in the previous two operating conditions. This in turn can be seen from the fact that at the pseudo-shock location in the Schlieren image of [Figure 5.19](#) the cowling boundary layer has barely had a streamwise distance over which it could grow and the compression plate boundary layer has not grown much in size either at the pseudo-shock starting location. Another point of interest is that at the end of the constant-area duct region of the intake the static pressure has not yet reached a maximum (plateau) value. This implies that the pseudo-shock length is potentially larger than the 90 mm streamwise distance wherein the pseudo-shock was present during the critical condition inside the constant-area duct region. To fully understand the static pressure rise from the pseudo-shock, in [Figure 5.19](#) the static pressure rise by a single inviscid normal shock wave is included to provide theoretical reference with the experimental result. When

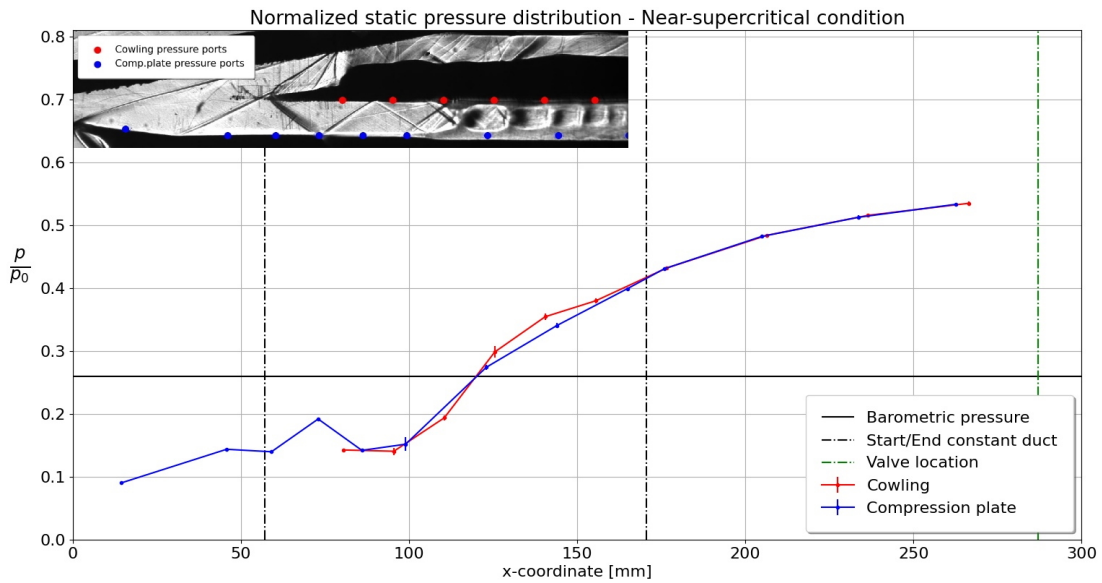


Figure 5.18: Schlieren image and Static pressure plot of the diamond valve in the nearly supercritical condition.

comparing the theoretical and experimental static pressure profiles, the experimental curve is found to lie close to the inviscid normal shock solution, implying that even though no maximum pressure was found in the experiments, the experimental solution was very close in reaching this maximum. Since the critical condition is highly unstable with the presence of aggressive shock oscillations, the statistical uncertainty in the static pressure measurements in Figure 5.19 is large and it spans a big streamwise range of $x = [81, 144] \text{ mm}$. The order of magnitude of the uncertainty lies close to that of the static pressure measurements themselves, indicating how high the degree of randomness is surrounding the pseudo-shock in the critical condition.

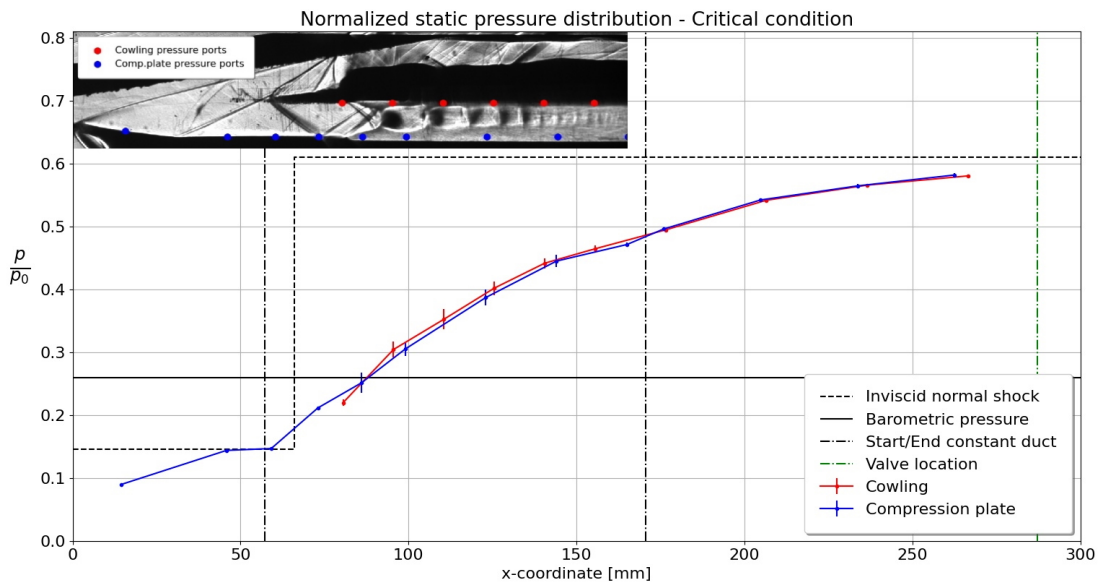


Figure 5.19: Schlieren image and Static pressure plot of the diamond valve in the critical condition.

5.3. PIV results

This section discusses the crucial planar PIV results that are going to aid in answering this report’s research questions and reveal the dynamical flow structure throughout the SSI model. But before discussing the flow behavior per operating condition, it is important to mention that some locations in the domain have been

subjected to laser light reflections, which explains why sometimes clear portions of the domain were blanked out. Also, it is worth mentioning that at $x = 92 \text{ mm}$ the interface is located between the PIV results of the two sCMOS camera's. Hence, for the PIV results discussed below, at this location it may seem as if a slight discontinuity exists between both results, which in fact is merely caused by the edges of Field of Views (FOVs). First, a discussion will take place in which the general flow is fully characterized. Next, the flow structure per operating condition is treated while directly comparing these flow structures to their Schlieren results counterparts. Finally, the PIV data will be used to validate the pseudo-shock to see whether its properties correlate with empirical relations from open literature.

Flow dynamics characterization Figure 5.20 and Figure 5.21 show the entire flow domain in which the PIV results are shown using vectors and colormaps for the streamwise and vertical velocities u and v , respectively, normalized to the freestream velocity V_∞ . The flow configuration used in this example is the near-supercritical condition. The streamwise velocity field u/V_∞ is a handy tool for exploring to what extent the flow, after having turned inwards at the expansion corner, has accelerated beyond the freestream velocity. This plot is also convenient for assessing the change in velocity after the shock waves and throughout the pseudo-shock. As can be seen from Figure 5.20, the maximum velocity attained in the domain, which is upstream of the first OSW of the supersonic diffuser, is slightly larger the freestream velocity. The location of all shock waves in the domain can be clearly identified in the vertical velocity field v/V_∞ in Figure 5.21, while the pseudo-shock is much better viewed in the streamwise velocity field u/V_∞ in Figure 5.20. After passing the first OSW, the velocity decelerates from 1.2 to 1.1 times the freestream velocity. After passing the second OSW, the velocity drops slightly below the freestream velocity. After passing the second OSW and before negotiating the cowl leading edge shock wave, the vectors in Figure 5.20 are clearly seen diving below the blanked region that is present below the cowl leading edge at $x = 58 \text{ mm}$. This is because this region was a reflection area that was not resolved well by the cross-correlation algorithm. In reality, the flow beyond the second OSW in the supersonic diffuser is predicted to continue in a quasi-streamwise sense, just as is shown by the vectors at the streamwise position $x = 53 \text{ mm}$. Following, the flow comes in contact with the cowl leading edge shock. The distinct deep red signature in the v/V_∞ -plot, indicating the presence of strong gradients at this location, confirms the theoretical speculation of this feature of being a impulse-type wave, in which a shock wave and a subsequent brief expansion region appear, as was discussed in section 5.2. After passing the cowl leading edge shock wave, the flow continues to pass through the intake duct until meeting the pseudo-shock, which in this example is located at a streamwise location of $x = 138 \text{ mm}$. From Figure 5.21, it can be seen that starting from the cowl leading edge towards the pseudo-shock location, the reflection shock in the duct gets repeatedly weaker. When the flow starts to negotiate the pseudo-shock, Figure 5.20 illustrates clearly that the boundary layer becomes thicker and that the velocity in the shock train decreases gradually. Also, the shock train is clearly seen having an asymmetric nature, just as was observed with the Schlieren results. The presence of dark-colored core regions surrounded by lighter colors throughout the pseudo-shock confirms the alternating acceleration/deceleration scheme of shock trains. The final piece of the puzzle in characterizing the flow dynamics is found in the Mach number plot of the flow domain as shown in Figure 5.22. From this figure, it becomes clear as explained before that the highest Mach number is found before the supersonic diffuser's first OSW, where the flow has a Mach number of approximately 2.55. Afterwards, the Mach number will generally only decrease. One might think that the only exception to this would be the brief acceleration of the flow due to the impulse-type wave at the cowl leading edge. However, in the Mach-plot in Figure 5.22, this is barely visible, if not absent. Anyhow, the Mach plot is a crucial tool, since it will indicate for the critical condition whether the flow becomes subsonic before it enters the subsonic diffuser. To complete this explanation, the PIV vector plots for all three intake supersonic conditions can be found in Appendix D.

A different way of investigating the quality of the PIV results is by analyzing the Mach number standard deviation. Since the Mach number is the most prominent output of the PIV analysis, the accuracy of this parameter has to be closely assessed. The PIV plot for the Mach number standard deviation in the critical condition is shown in Figure 5.23. From this plot, the standard deviation is found to be fairly low when excluding the wall regions, areas of high reflections and the pseudo-shock envelope. Along the centerline flow, the standard deviations are generally as low as 0.1, while the standard deviation near the wall areas is found to be around 0.2 or 0.3. In the region of the pseudo-shock, the centerline flow shows higher standard deviations, which makes sense since the standard deviation for the pseudo-shock actually represents the flow unsteadiness of this region. One may therefore conclude from Figure 5.23 that pseudo-shocks are indeed unstable since the standard deviation along the centerline region may be as high as 0.2 to 0.3, indicating large

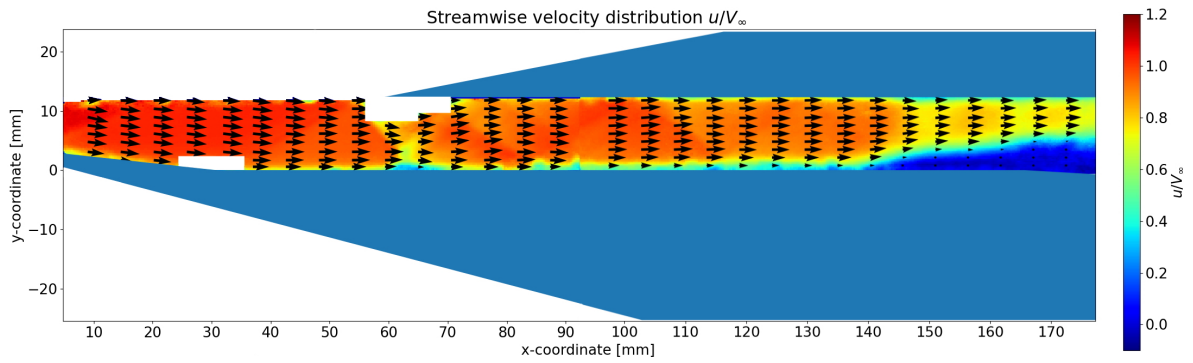
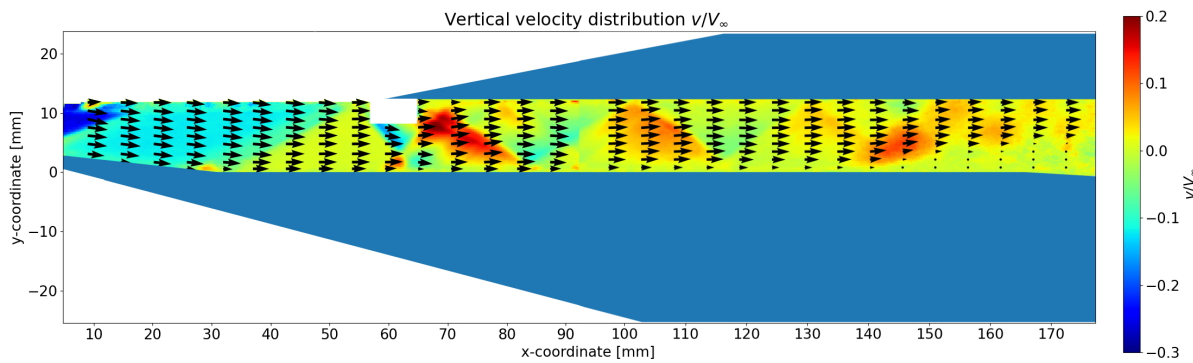
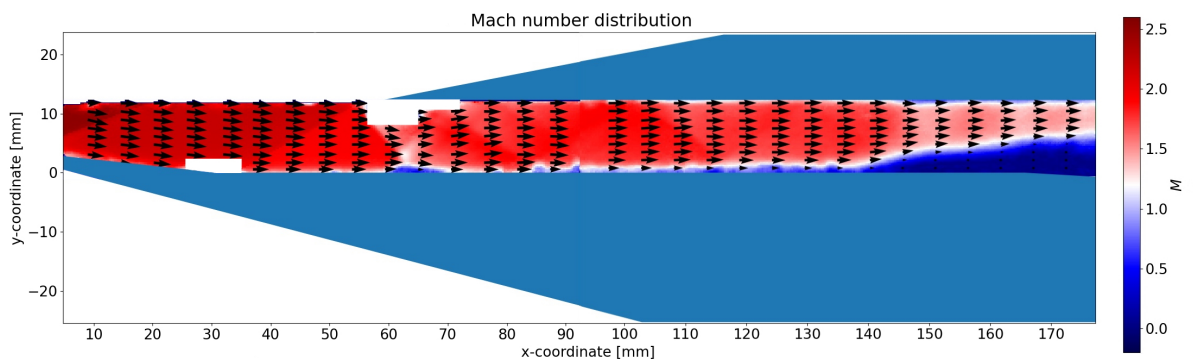
Figure 5.20: Normalized streamwise velocity field of u/V_∞ .Figure 5.21: Normalized vertical velocity field of v/V_∞ .

Figure 5.22: Mach plot.

repetitive shifts in flow Mach number. Nevertheless, these standard deviations are fairly low when compared to the standard deviations in the wall region, i.e. in the thickened boundary layer of the pseudo-shock. This is logical since the amount of flow distortion along the centerline is not as big as near the wall regions of the pseudo-shock. Near the walls, the boundary layers have rapidly grown in size and constitute an area of large flow distortions and reverse flow, which explains why the standard deviations in these regions can surge so quickly.

PIV validation using Schlieren imagery Even though the above explanation treated the dynamical flow behavior of the SSI model by taking the PIV results for granted, the validity of these results has to be discussed to treat the probable error in the PIV results. This is done by using the known flow conditions upstream of the SSI model and combining that with the Schlieren results to determine the Mach number over a trajectory, starting from the freestream station until reaching the pseudo-shock. This is done using two-dimensional shock theory. These results are then compared to the PIV results to see whether the same numerical results are found. This will be compared with both the Mach number distribution and the normalized vertical velocity

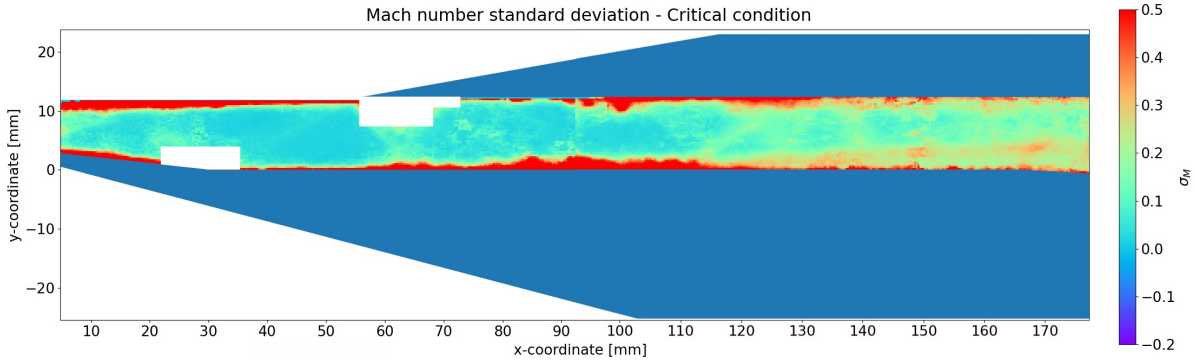


Figure 5.23: Mach number standard deviation in the critical condition.

v/V_∞ distribution, which follow from PIV. The Mach number throughout the intake was determined by the local speed of sound. Since the flow was adiabatic, the total temperature throughout the domain was constant and this could be used to determine the static temperature in the entire domain using the relation:

$$T = T_0 - \frac{V^2}{2C_p} \quad (5.1)$$

where T is the static temperature, T_0 is the stagnation temperature, V is the local flow velocity and C_p is the heat capacity coefficient at constant pressure. For the Mach number results, the C_p corresponding to the total temperature was used which was equal to $1004.18 \text{ J}/(\text{kg} \cdot \text{K})$.

In [Figure 5.24](#), the Schlieren image, Mach number and normalized vertical velocity v/V_∞ plots are shown for the supersonic condition. Consider the freestream flow, ahead of the expansion corner, where the flow is known to have a Mach number of $M_\infty = 2.0$. After passing the expansion corner with an expansion angle of 14° , the flow has analytically accelerated to a Mach number of approximately $M = 2.55$. This is portrayed by the small deep crimson region, located in the upper left of the Mach number plot in [Figure 5.24](#). For the PIV result, this Mach number was found to be $M = 2.51$. The reason for this slight difference is most probably the deformed OSW at the compression plate leading edge. Estimating the wave angle from the Schlieren image and using the fact that the flow turn angle is 7° , the Mach number upstream of the first OSW is found to be roughly $M = 2.53$.

Afterwards, the flow starts to negotiate the shock system of the supersonic diffuser, which contains two OSW, each of these shocks turns the flow by an angle of 7° . The first OSW decelerates the Mach number analytically to $M = 2.26$. Comparing the shock angle of the first OSW for both the PIV plot and the Schlieren image, their shock angles are found to be 28.99° and 28.64° , respectively. When determined analytically however, a shock angle of roughly 28.59° is expected for the first OSW. This explains why the downstream Mach numbers from the PIV and Schlieren results also give different results, namely 2.22 and 2.24, respectively. The reason for this difference between the experimental and analytical values can be once again explained by the nature of the compression plate leading edge, which as explained in [subsection 3.3.2](#) and [subsection 5.1.1](#) is not sharp, but has a finite curvature which tweaks the generated OSW and makes it curvy. This causes the flow to locally experience different shock angles which results in Mach numbers that are different from the analytical prediction.

Next, the flow encounters the second OSW, which decelerates the flow analytically to a Mach number of $M = 1.99$. This is practically the freestream Mach number which proves why the region behind this second OSW in the PIV Mach number plot shows a region coloured by a value of roughly $M = 2.0$. A closer comparison though shows that the Mach number is not 1.99 for the PIV and Schlieren results, but rather 2.06 and 2.08, respectively. Even though the analytically predicted value for the Mach number between the first and second OSW was higher when compared to both the Schlieren and PIV values, the analytical Mach number downstream of the second OSW is lower than both experimental values, indicating a larger net jump in the analytical Mach number! This abnormality can be again explained by knowing that in the practical case no shock wave was present at the compression plate lip-junction, but rather a cluster of Mach waves that coalesced together into one shock-like structure. This explanation can also be verified by analyzing the shock angle of this OSW in the PIV and Schlieren plots, where it is found that the angle is not 32.11° as analytically predicted, but rather 30.18° and 29.42° , respectively. The next feature is the cowling leading edge shock

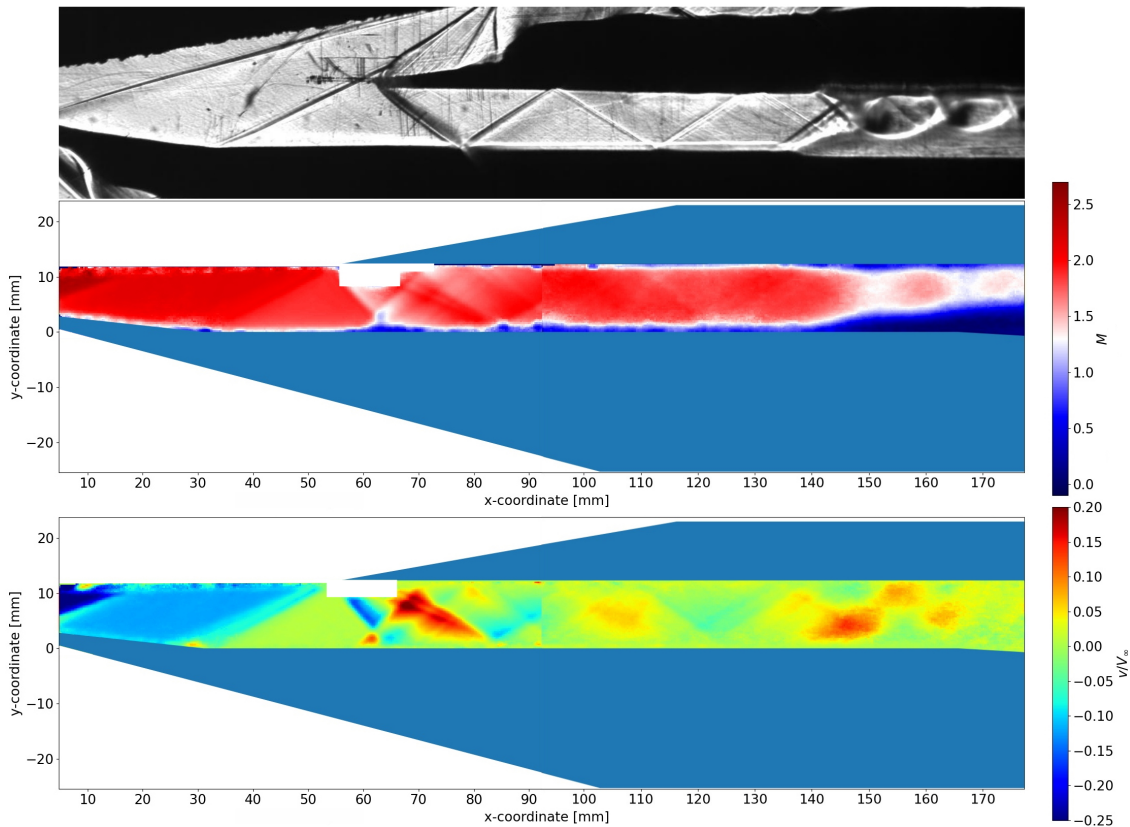


Figure 5.24: Schlieren image, Mach number by PIV and normalized vertical velocity by PIV plots for the supercritical condition.

wave, which in reality is an impulse wave as has been discussed before. Since this impulse wave contains both a shock wave and an expansion fan, one would expect to see a decrease in the Mach number which is afterwards followed by an increase. However, before getting to this cowling impulse wave, the v/V_∞ plot provides additional information on another flow features in the flow domain. When inspecting the duct entrance of the intake in the v/V_∞ plot, one may clearly find that upstream of the cowling impulse wave, characterized by its red signature and surrounded by a sharp red glow, another shock-like feature is found in the v/V_∞ plot, shown as a blue line emanating from the location $x = 57 \text{ mm}$. This blue colour indicates that the local velocity is pointed downwards, which most probably is an effect caused by the accumulation of seeding near the cowling leading edge, which has caused the flow to locally duck downwards. This is also found from the PIV velocity vectors in Figure 5.21. Another possible explanation is that this blue shock is the reflection caused by the second OSW of the compression plate after impinging the cowling leading edge, which is highly impossible since a) in the Schlieren image the second OSW of the supersonic diffuser is seen clearly passing the cowling leading edge without impinging it and b) no reflection shocks are found further downstream of where this initial blue shock impinges the compression plate surface in the v/V_∞ plot. Anyhow, this shock-like feature is clearly seen impinging the compression plate at a location of $x = 63 \text{ mm}$, causing a brief SBLI after which the boundary layer reattaches again. Back to the cowling impulse wave, and since no certainty exists with the value of the cowling leading edge shock, no analytical solutions can be determined beyond this point. The PIV Mach number plot gives a Mach number downstream of this cowling leading edge shock of roughly $M = 1.9$ and a shock angle of 35.78° , and no clear patterns are visible of any expansions. This indicates that this expansion from the cowling impulse wave must have had almost no influence on the Mach number, judging from the fact that the net change in Mach number over this cowling leading edge shock has only been a decrease. From the Schlieren image, the shock wave angle can be roughly determined to be 35.28° . The reason why the flow has not experienced any significant deceleration further inside the duct can be reasoned by the weak behavior of the reflection shocks, which were caused by the initial cowling leading edge shock. The flow along the duct centerline will continue to move downstream with a Mach number roughly equal to $M = 1.9$ until the flow makes contact with the pseudo-shock. Since the change in Mach number

throughout the pseudo-shock cannot be determined using Schlieren imagery, this part of the flow dynamics validation is passed on to the next paragraph.

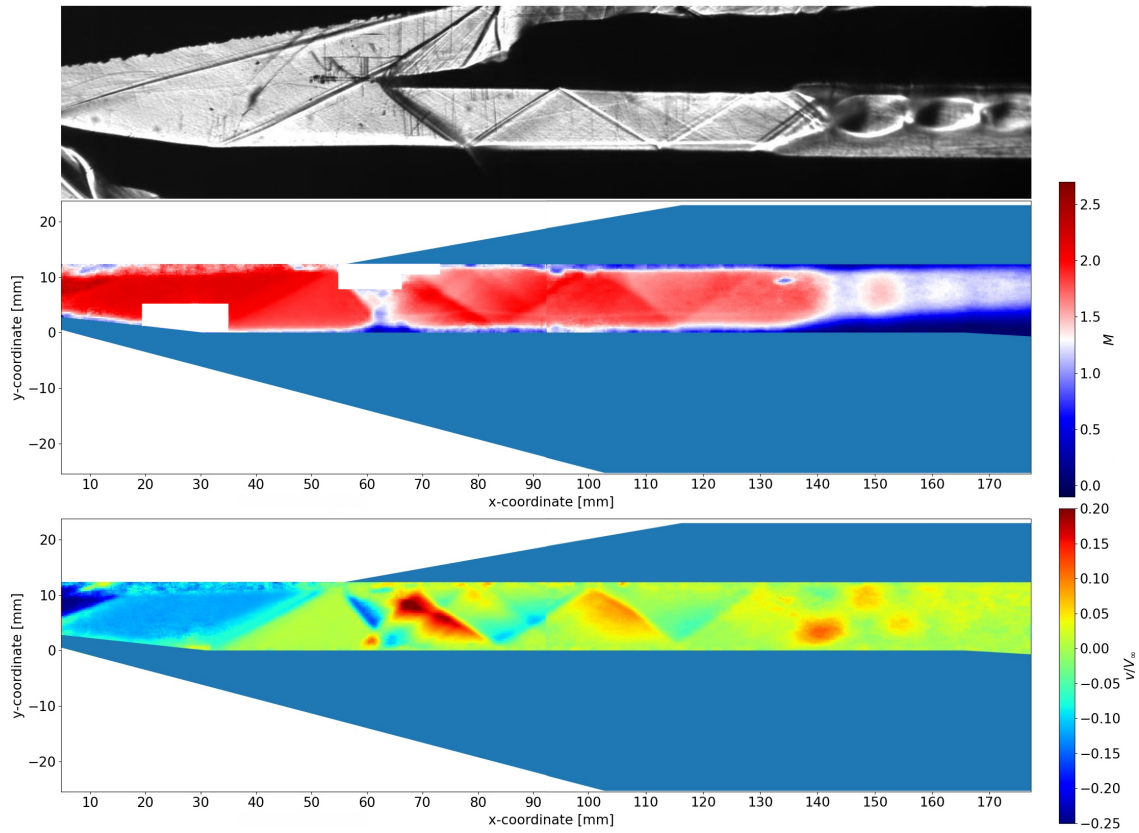


Figure 5.25: Schlieren image, Mach number by PIV and normalized vertical velocity by PIV plots for the near-supercritical condition.

In [Figure 5.25](#), the Schlieren image and the Mach number and v/V_∞ PIV plots are shown for the near-supercritical condition. As becomes clear, the same rationale discussed for the supercritical condition also holds for this condition. The only difference is that the pseudo-shock has moved more upstream and has therefore resulted in a larger net deceleration of the Mach number at the end of the FOV.

Finally, [Figure 5.26](#) features the Schlieren image and PIV plots for the critical condition. Similar to the previous two conditions, no changes were reported regarding the strength and location of the flow features, except that this time the pseudo-shock has moved even more upstream. As an interesting side note, when comparing the Mach number plots of all three conditions from [Figure 5.24](#) to [Figure 5.26](#), one may infer that the Mach number just upstream of the pseudo-shock M_{1e} in all three cases is the same Mach number, corresponding to $M_{1e} = 1.9$.

Finally, in [Appendix E](#), a table is documented in which a close comparison is provided between all experimental results and analytical solutions for the different shock angles, static pressures and Mach numbers.

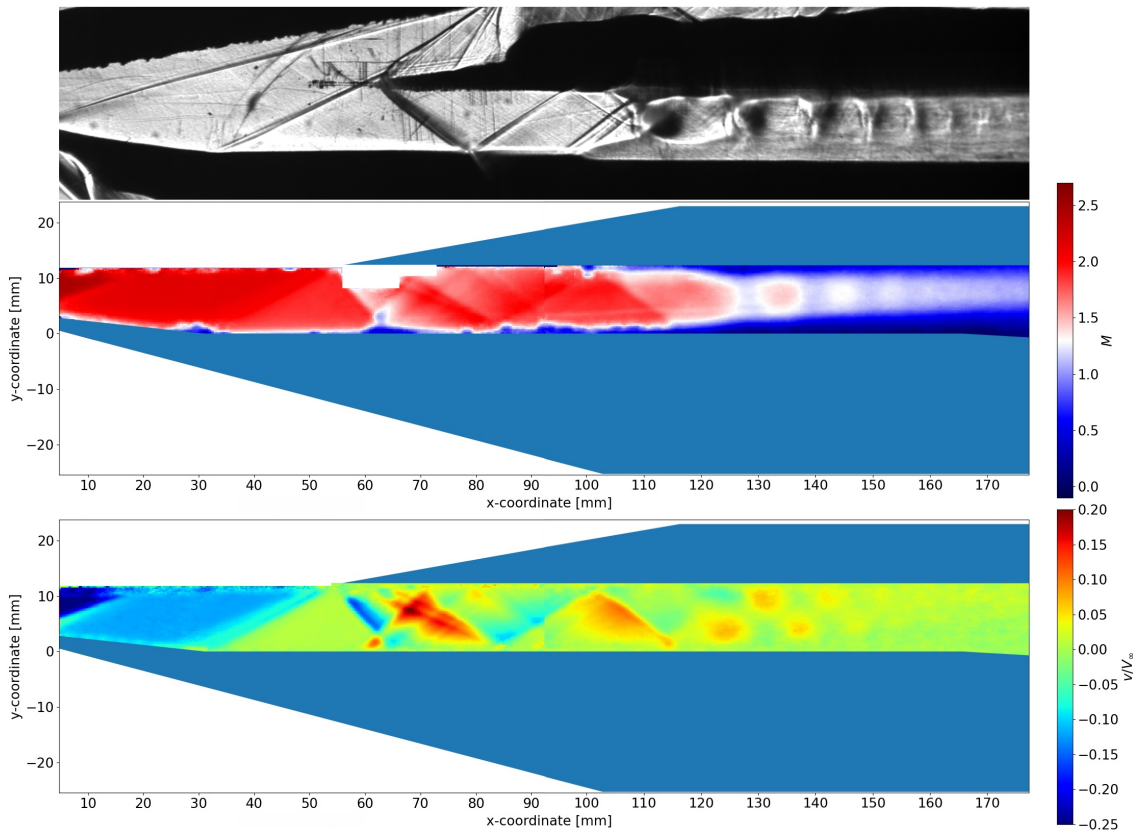


Figure 5.26: Schlieren image, Mach number by PIV and normalized vertical velocity by PIV plots for the critical condition.

PIV validation using analytical models PIV validation by comparison with the Schlieren images is not sufficient to prove that the flow dynamics results actually make sense, let alone provide a representation of pseudo-shocks similar to what is found in open literature. Therefore, the next step is not to validate the Mach number distribution throughout the intake, as was done in the previous paragraph, but to validate the pseudo-shock structure as found in the SSI model and to investigate its properties using the analytical models discussed in subsection 2.3.2. This will help in bridging the gap on how well pseudo-shocks in submerged intakes correlate with well-known analytical models from open literature.

1. Validation of pseudo-shock Mach number The Mach number relationship as a function of the shock train pressure ratio by the Lin et al. [42] will be used to verify to what extent this report's Mach number-pressure ratio results correlate with the above relationship. The Mach number distribution can be retrieved from the PIV data as is shown in Figure 5.27. In this particular Mach number plot, the black contour line, which stretches over the entire flow domain, corresponds to the unity Mach number. This is an important tool to confirm whether the Mach number becomes subsonic before the flow enters the subsonic diffuser in accordance with the basic supersonic intake design criteria. From Figure 5.27 however, it becomes evident that this is not the case since the centerline Mach number at the duct exit in the critical condition equals $M_{CL} = 1.06$, which means that the flow will enter the subsonic diffuser whilst supersonic.

Having determined the Mach number distribution inside the SSI model, the next step is to mention the important assumptions used to construct the analytical relationship of Lin et al. Even though this has been a purely experimental effort, and the relations in Equation 2.28a and Equation 2.28b were constructed based on empirical data, a large portion of the calculation could only be completed by using the following assumption:

- The static pressure distribution across the isolator transverse plane is uniform.

Since the SSI model had an isolator with rectangular cross-section, Equation 2.28a was used together with the experimental results from this report's campaigns. Proper validation is done by recreating Figure 2.16 and Figure 2.17 including the experimental results. This is shown in Figure 5.28 and Figure 5.29.

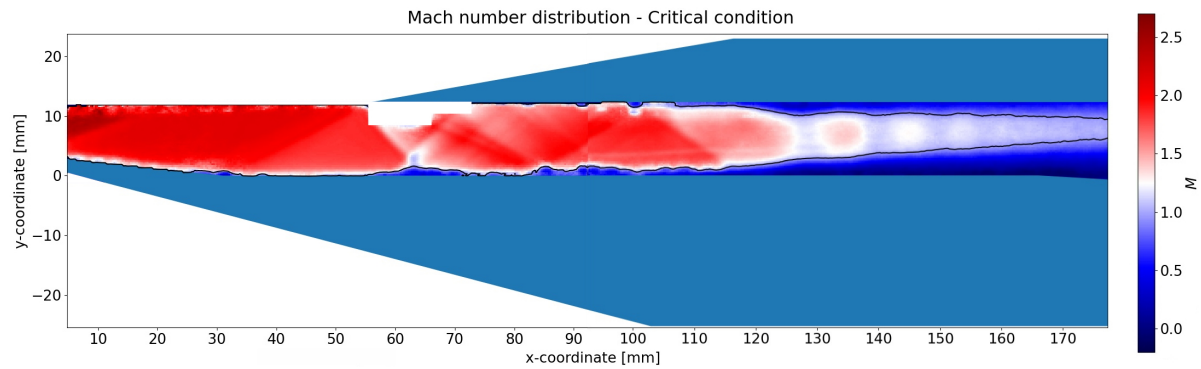


Figure 5.27: Mach number PIV plot for the critical condition with the black contour representing the sonic line of $M = 1$.

In [Figure 5.28](#), two trendlines are shown for rectangular duct intakes at $M = 1.8$ and $M = 2.2$, which is similar to [Figure 2.16](#). In addition, a trendline was generated for $M = 2.0$ to have an additional reference line, and this report's experimental result for the critical condition was added to the plot to analyze how well this result fits in the plot. From inspecting [Figure 5.28](#), the experimental result is found to reside between the trendlines for $M = 2.0$ and $M = 2.2$. Since the pre-pseudo-shock Mach number was $M = 1.9$, the experimental result would ideally be located between the trendlines for $M = 1.8$ and $M = 2.0$. The offset in this case can be explained in the following way: For any particular pressure ratio P_b/P_1 , ideally one centerline Mach number at the isolator exit M_{CL} is expected when assuming no other parameters are changed. This can be understood by knowing that based on how much the butterfly valve closes the intake, the corresponding backpressure will place the pseudo-shock at a particular position in the duct which ultimately results in a certain Mach number at the end of the isolator. However, this only holds when the full pseudo-shock has developed inside the isolator. For partial pseudo-shocks, like the one encountered in this report's experiments, the pseudo-shock has not decelerated the flow completely. This implies that the error found in [Figure 5.28](#) is not a result of a wrong back pressure ratio P_b/P_1 , but rather of a too high centerline isolator exit Mach number M_{CL} . This is also proven by the fact that a proper pseudo-shock would decelerate the flow to subsonic Mach numbers, which was not realized from this report's experimental results in the critical condition.

Coming to [Figure 5.29](#), the experimental result is also seen here differing from the optimal solution as represented by the trendline. This discrepancy is explained in the following way, primarily making use of the same discussion used for explaining the offset in [Figure 5.28](#): On the correlation side, the relation established in [Equation 2.28a](#) assumes a fully developed pseudo-shock, meaning that this correlation relation is independent of any specific details to any experiment and is therefore virtually error-free. The real error comes from the measurement side, since it was already elucidated that the appropriate centerline Mach number at the isolator exit M_{CL} was not reached due to insufficient deceleration from a shorter shock train. This means that the experimental value for M_{CL} was too high, resulting in a too high Mach number ratio M_{CL}/M_0 on the measurement side, which explains in this case why the experimental result was shifted too much to the right.

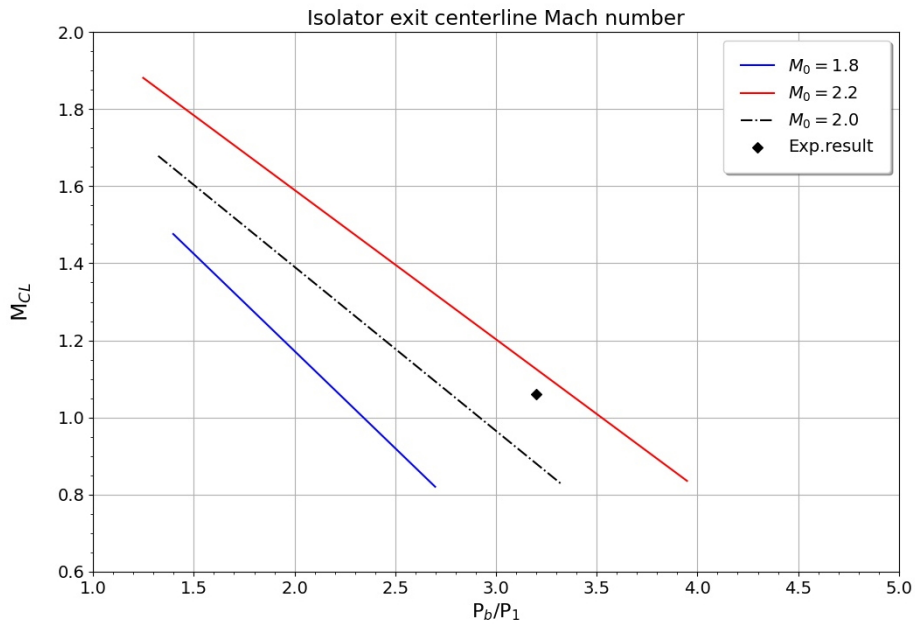


Figure 5.28: Relationship between centerline flow Mach numbers at the exit of the isolator extension piece and pressure ratios along the entire isolator length, including this report's experimental result.

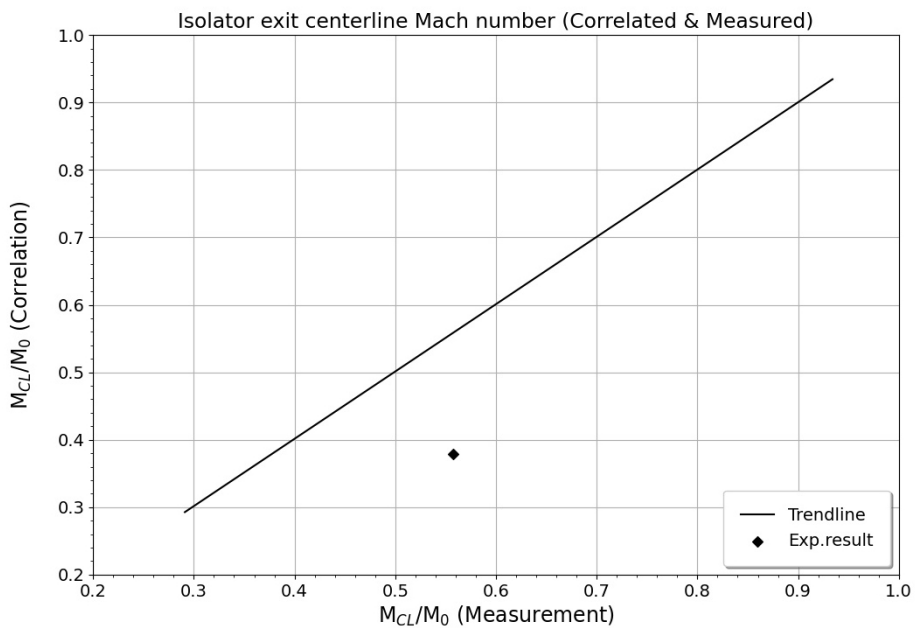


Figure 5.29: Comparison between measured and predicted Mach number ratios from correlations for centerline flow Mach numbers at the exit of the isolator with this report's experimental result.

2. Validation of pseudo-shock pressure ratio The validation of the pseudo-shock pressure ratio is done by making use of the figure compiled by Matsuo et al. [59] shown in Figure 2.22, which features the ratio of pseudo-shock-to-inviscid normal shock wave pressure ratios $(p_2/p_1)_p/(p_2/p_1)_n$ plotted for several Mach numbers upstream of the pseudo-shock M_{1e} . The validation plot is shown in Figure 5.30. For clarity, a mean correlation line or trendline was added together with the experimental solution to the plot to estimate the mean and potentially ideal solution. Closely examining this plot shows that the experimental result is clearly situated within the correlation region and that it is located close to the mean trendline too. The Mach number M_{1e} for the experimental result was the Mach number in the critical condition just before the flow entered the pseudo-shock, which from the PIV Mach number results was found to be $M_{1e} = 1.9$. A probable expla-

nation on the offset of the experimental result can be traced back to the incomplete pseudo-shock, which had a lower pressure ratio than a complete pseudo-shock. A lower pseudo-shock pressure ratio $(p_2/p_1)_p$ will definitely also result in a lower normalized pressure ratio $(p_2/p_1)_p/(p_2/p_1)_n$, which ultimately proves why the experimental result is smaller than the predicted solution along the mean trendline.

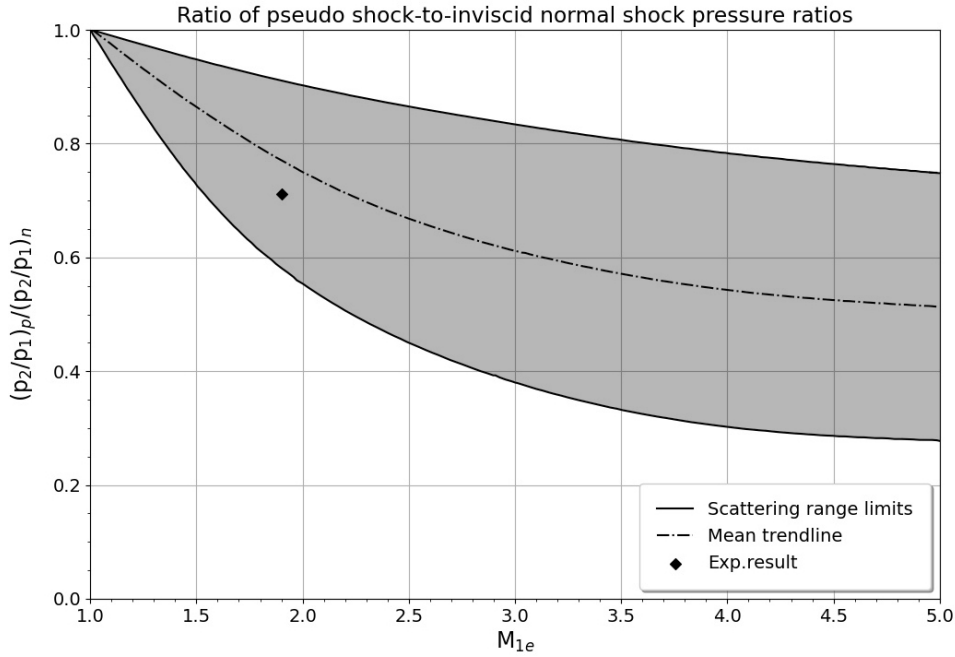


Figure 5.30: Static pressure ratio across pseudo shock normalized by that across a normal shock wave versus the upstream Mach number, including a mean trendline and this report's experimental result.

3. Validation of pseudo-shock length Validating the pseudo-shock length is done using Figure 2.24, which features a correlation plot compiled by Matsuo et al. [59] on the pseudo-shock length normalized by the duct height L_p/D based on prior experiments for various pre-pseudo-shock Mach numbers M_{1e} . Also, instead of using the mean trendline of this correlation region, the diffusion model by Ikui et al. [40] was used (see Equation 2.38). First, the assumptions of the diffusion model must be named to get more insight into the limitations of this model:

- The high-speed uniform flow in the central core region of a duct is not isentropic.
- Inside the pseudo-shock, the high speed flow at the central region and the lower speed flow near the wall surface are diffused together, eventually resulting in the subsonic uniform flow at the final section.
- The streamwise velocity variation in the two regions is expressed by the following relations:

$$\frac{dw'}{dx} = -cw' \quad (5.2)$$

$$\frac{dw'}{dx} + B \frac{dw''}{dx} = 0 \quad (5.3)$$

where the first equation represents the velocity variation in the central core region and c is the coefficient of the velocity decay, and the second equation combines the streamwise velocity variation in the central region with the lower velocity flow close to the wall and the coefficient B is derived from the boundary conditions at the initial and final sections of the pseudo-shock.

The validation outcome is provided in Figure 5.31. The experimental result lies clearly within the scattering range but does still differ from the expected solution at the particular M_{1e} of this report's experiments. The explanation is quite straightforward: since the pseudo-shock did not reach its full length, this resulted in

a smaller pseudo-shock length L_p compared with what it actually was supposed to be based on the diffusion model, ultimately providing a smaller normalized pseudo-shock length L_p/D .

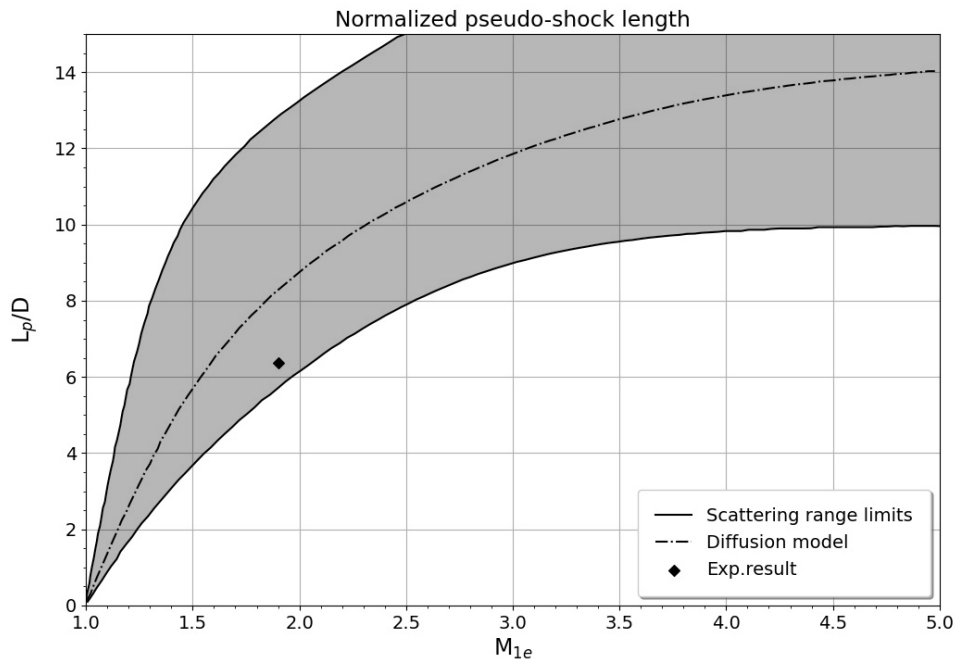


Figure 5.31: Non-dimensional pseudo shock length in constant-area duct versus the Mach number upstream of the shock, including this report's experimental result.

5.4. Intake Total Pressure Recovery

Having discussed all relevant results from the different experimental campaigns, the final step is to determine the TPR in the intake which ultimately will give an indication as to how efficient this intake's operation was for the specific Mach number at which it operated. After processing the PIV results, retrieving the static pressure distribution using the Pressure from PIV technique from van Oudheusden [115] turned out to be incompatible with the flow domain for this report's PIV results. Therefore, it was decided to combine the static pressure results from the Scannivalve transducers with the Mach number results from the PIV campaign instead to roughly determine the TPR. It was decided to determine the TPR of the SSI model by making use of the mass-averaging pseudo-shock model (see Equation 2.36). It was found by Weiss et al. [35] that for the shock train in a narrow rectangular channel at moderate Mach numbers the TPR across the pseudo-shock is well predicted by the mass averaging model by Matsuo et al. [28]. Before diving into the result from this model though, the assumptions of this model have to be named to understand the limitations of this model:

- The pseudo-shock flows are restricted to a constant-area duct.
- The pseudo-shock interacts with a fully developed turbulent boundary layer.
- The working fluid is a single-phase, perfect gas with a ratio of specific heats of 1.4.
- The flow is steady.
- The effects of heat transfer and wall mass transfer are excluded.

Most of these assumptions seem reasonably applicable to the current flow problem in the SSI model, but the first assumption does not hold completely for the current problem since part of the pseudo-shock in the SSI model during the critical condition was located in the subsonic diffuser, which may be deduced from the static pressure rise in this region during the said condition as was shown in Figure 5.19. Even though this first assumption does not fully hold, it was decided to use this model anyways. Also, the second assumption has to be very verified. By using the local flow properties just upstream of the pseudo-shock, it is found that the

Reynolds number has an order of magnitude of $\mathcal{O}(10^5)$. This is sufficient proof to assume that the boundary layer is far above the transition region between laminar and turbulent flows. The TPR as determined with the mass averaging pseudo shock model is shown in Figure 5.32. The total pressure across the pseudo-shock $P_{0,p}$ is plotted normalized to the total pressure in the settling chamber $P_{0,sc}$. Also, it was decided to plot the TPR as a function of the streamwise distance normalized with the duct height x/H . For the sake of having reference data, it was decided to plot the TPR result from an inviscid normal shock wave at the same Mach number upstream of the pseudo-shock in addition to two TPR results from two different sources: the $M_\infty = 1.60$ result from Tamaki et al. [39] and the $M_\infty = 1.99$ result from Tamaki et al. [116].

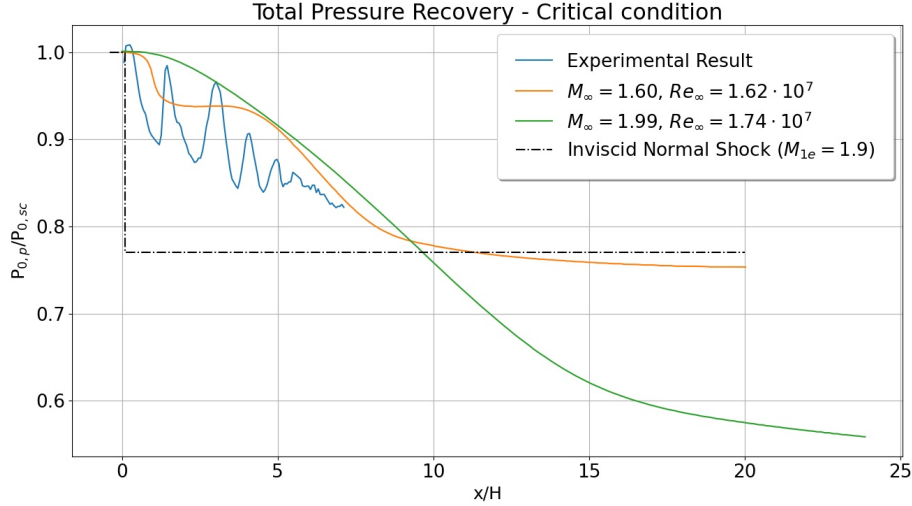


Figure 5.32: TPR across the pseudo-shock.

From close inspection of this plot, it becomes evident that the experimental net TPR does not differ a lot from what is found in open literature. The discrepancy between the experimental solution and the $M = 1.99$ is on average $\Delta P_{0,p}/P_{0,sc} = 0.06$. This is principally assessed by looking at how much the total pressure has decreased over a certain streamwise distance. However, it should be mentioned though that the reference curves from literature mostly used an isolator test section with a much larger streamwise length.

The minima and maxima in the experimental result are explained by knowing that the Mach number throughout the pseudo-shock centerline keeps changing, from an acceleration to a deceleration and back. The maxima indicate the points of a high local Mach number, while the minima indicate the points of a low local Mach number. Since the experimental result did not have the complete pseudo-shock inside the duct, the experimental TPR result in Figure 5.32 is also considered incomplete which explains why against all odds the experimental result seemingly ends up with a higher TPR than the inviscid normal shock solution. The final total pressure reached by the experimental result comes down to 0.82, while the inviscid normal shock predicts a final total pressure of 0.77.

When comparing the experimental result with the reference results, one aspect is found to differentiate between the reference results of Tamaki et al. and the experimental results. The Reynolds number in both reference results was found to be two orders of magnitude larger, even though the freestream Mach number was either not very different from or almost similar to this report's pre-pseudo-shock Mach number. This suggests that the reference length (possibly the duct height) was also larger than this report's reference length. In the experiment for the $M_\infty = 1.60$ result [39], the duct height was 40 mm and for the experiment on the $M_\infty = 1.99$ result, the duct height was 20 mm.

The experimental result shows roughly the same TPR behavior as the reference curves until a streamwise position of $x/H = 7$. This is identified by the gradual decrease in total pressure, found for all curves shown in Figure 5.32. Thereafter, the two reference curves keep on going since their isolator lengths were larger. But how may one address the differences between the different plots? First, since the orange curve had a pre-pseudo-shock Mach number of 1.60, the shock train for this curve has been a normal shock train, in accordance with the works of Tamaki et al. [39] and Ikui et al. [40]. Also, judging from the Mach number of the $M_\infty = 1.99$ reference curve, this shock train was likely an oblique one. Since the highest SPR and TPR are

achieved ideally with a single normal shock, this explains why the TPR of the $M_\infty = 1.60$ curve is superior to the $M_\infty = 1.99$ one. This reasoning would therefore also suggest that had the isolator streamwise length been larger in the experimental effort, the TPR envelope would have looked quite similar to the $M_\infty = 1.99$ curve. Another interesting difference between both reference plots in Figure 5.32 is the streamwise distance over which the TPR trajectory was measured. This is not a coincidence, since normal shock trains are known to have λ -type shocks and oblique shock trains are known to have χ -type shocks. According to Heiser and Pratt [31], χ -type shock trains have a higher number of shocks in the shock train and the complete shock region is longer. This is another proof as to why the $M_\infty = 1.99$ TPR plot moves farther and why the final total pressure is lower. Although the $M_\infty = 1.99$ plot shares the same approximate behavior as the experimental result, including the fact that both pre-pseudo-shock Mach numbers are almost the same, it still ends up with a higher TPR at $x/H = 7$. One may suggest that a difference in the flow confinement parameter between both curves may explain the difference in TPR. As Lustwerk [36] observed, the higher the flow confinement parameter δ/h , the larger the distance gets between two subsequent shocks in the shock train. However, oblique shock trains barely show any sensitivity to the flow confinement parameter. This explains why the difference between the experimental plot and the $M_\infty = 1.99$ plot is a mere translation discrepancy and not a difference in TPR gradient. The difference between both curves most likely has to do with the loss of total pressure before the flow arrived at the pseudo-shock. In the reference result from Tamaki et al., no upstream shock system or additional geometry (like this report's expansion corner) was introduced to the test section. Although the expansion corner in this report's test setup did not change the total pressure, judging from the fact that a Prandtl-Meyer expansion is isentropic and maintains a constant total pressure, the supersonic diffuser together with the cowl leading edge shock and reflection shocks all contributed to a number of slight losses in the total pressure which proves why the experimental TPR did not start at a normalized total pressure of unity but rather at roughly 0.98.

6

Conclusion

The aim of this work was to document the experimental efforts and outcomes of a research project which had the objective of investigating the role of the viscous flow effects, and most notably the pseudo-shock, on the performance of submerged supersonic intakes. The experiment was carried out by using a submerged supersonic intake model in a Mach 2.0 freestream flow in which the operational condition of the intake was regulated by changing the backpressure by means of a butterfly valve. Using Schlieren imagery, static pressure measurements and Particle Image Velocimetry, the complete flow behavior was quantified and evaluated in comparison with existing analytical models from open literature.

To thoroughly examine this research topic, a number of research questions were posed to confirm whether the main research objective had been accomplished. This chapter will answer these research questions and will summarize the important findings of this report.

First, the research questions will be answered based on the findings of this report:

1. What information can be gained about the qualitative understanding of pseudo-shock waves in submerged supersonic intakes at Mach 2.0?

This report's Schlieren and static pressure results have validated that the general behavior of the pseudo-shock in the constant-area duct of a submerged supersonic intake did adhere to the theory of pseudo-shocks as described in open literature. This includes showing repetitive shock oscillations, demonstrating the main shock train structure inside the duct and clearly showing a static pressure rise over a trajectory spanning from the constant-area duct to the subsonic diffuser. Also, the maximum static pressure attained was close to the inviscid normal shock solution, indicating that the experiments achieved near-ideal conditions from the respect of the static pressure results. The PIV results have shown that the Mach number upstream of the pseudo-shock is pretty close to the freestream Mach number. This clearly emphasizes the role of the expansion corner and supersonic diffuser designs in determining the Mach number just upstream of the intake's main deceleration mechanism, i.e. the pseudo-shock. Also, discrepancies between the experimental and reference Total Pressure Recovery (TPR) results illustrated the difference between λ -type normal shock trains and χ -type oblique shock trains, which explains the difference in shock-train size and final TPR.

2. What is the most optimal butterfly valve design to obtain proper pseudo-shock occurrences in SSI's at Mach 2.0?

From the trade-off on the different butterfly valve designs, the diamond valve provided the intake with the most ideal operational behavior. This was verified using the Schlieren results, which clearly explicated the diamond valve's robustness by showing the most minimal shock oscillations. In addition, its Schlieren standard deviation image showed the least tendencies of expelling the duct's terminal shock wave. The static pressure results reaffirmed this butterfly valve choice, showing the most natural envelope of the static pressure rise through the flow domain as well as attaining the highest static pressure recovery with the least pressure fluctuations.

3. **How does the performance of a submerged intake correlate with the results from analytical models?**

The submerged supersonic intake used in the experimental efforts, with its current geometrical design, was close in being able to properly accommodate for the complete pseudo-shock in its constant-area duct, which was confirmed using different analytical models. First, the Mach number did not decelerate below unity upon entering the subsonic diffuser, which constituted an immediate breach of the base supersonic intake design criteria. Second, all analytical models agreed on the same type of anomaly for the current submerged supersonic intake design, namely that its isolator lacked sufficient length which lead to a marginal decrease in its performance. Also, the lack of proper isolator space lead to the TPR result to be presented as unreal, owing to its superior performance in comparison with an inviscid normal shock wave, while basic pseudo-shock theory and fundamental flow theory would predict the opposite to be true. All in all, this report's submerged intake showed a significant degree of similarity with the analytical models documented in this report. Still, the validation results on the submerged supersonic intake model in comparison with models from open literature made it possible to acquire new knowledge on how to alter the geometry of submerged supersonic intakes, to fully harbour the pseudo-shock in a better fashion and to ultimately optimize the performance of the complete intake.

The main outcome of this report was the preliminary indication that submerged supersonic intakes show great potential in being able to perform at the same levels of generic lateral intakes and that the role played by pseudo-shocks in these submerged designs is a very crucial one. One could possibly state that the extent to which one is able to control the pseudo-shock matches the extent to which one can control the intake's performance. The Schlieren and static pressure results have proofed how important the choice for a proper butterfly valve or throttle system really is to avoid jeopardizing the intake by expelling the terminal shock. Most importantly, the PIV results have shown how the dynamical profile of submerged supersonic intakes is structured and how particularly the Mach number distribution looks like in all segments of the intake, including throughout the pseudo-shock.

7

Future Recommendations

Following the results and conclusions from this experimental research, the author seeks to notify the reader that improvements can still be made, both in terms of research methodologies and submerged intake design parameters and conditions. These recommendations follow from the lessons learned during the experimental testing of this report's setup. Therefore, this chapter presents a number of crucial aspects which were not considered in this research but which may aid in finding the optimal submerged supersonic intake design.

7.1. Using alternative flow measurement techniques

After successfully completing the different experimental campaigns of this research, the author discovered that the use of PIV introduced a number of anomalies which made it difficult to capture images of good quality and therefore process adequate results. This was mainly caused by the fact that viewing the inside of the submerged intake required plexiglass sidewalls and these sidewalls were partially influenced by the Particle Image Velocimetry (PIV) laser sheet. This caused significant reflections that require advanced solutions to get attenuated. Therefore, the use of Background Oriented Schlieren (BOS) is a good alternative to PIV since this technique roughly works along the same lines as PIV. The use of BOS involves placing a background image behind the desired FOV and capturing a number of images using a high-speed camera. This completely eliminates the use of seeding particles and lasers to conduct the measurements. Using a cross-correlation analysis, just as with PIV, the velocity field can be fully determined. For analysing submerged supersonic intakes, BOS can thus be regarded as a worthwhile alternative to PIV to determine the velocity field and more quantities of interest by means of post-processing. For more information on the use of BOS for supersonic intakes, the reader is referred to the works of Wang et al. [117] and Geerts and Yu [118].

7.2. Performing measurements using Stereoscopic PIV

Although the PIV results of this report have shed light on the particular structure and effects of pseudo-shocks in supersonic intakes, there is more to meet than meets the eye. The research performed by Edelman and Gamba [119] has shown that at the sidewalls of an enclosed duct in which a pseudo-shock is present, local separation bubbles are formed since the flow separates in the out-of-plane direction from the sidewalls. This implies therefore that the two-dimensional problem is transformed into a three-dimensional problem. Quantifying the performance of any supersonic intake requires also thorough analysis of anything detrimental to this performance, including any separation regions. This is why stereoscopic PIV is essential in analyzing pseudo-shocks, since this technique serves as a means of capturing the velocity component in the out-of-plane direction. Next to the research by Edelman and Gamba, the reader is also referred to the research by Hunt and Gamba [120] which also discusses the three-dimensional structure of shock-trains and how that is related to the shock train's unsteadiness.

7.3. Performing measurements with different isolator lengths

Since only one cowl and one compression plate were used, the effect of the isolator length on the intake's performance was not clarified enough. Experiments with different isolator lengths may throw light on whether the full length of the pseudo-shock is contained inside the isolator or whether the pseudo-shock is

either cut off early or maybe even extended with a mixing region. Therefore, the author recommends investigating the behavior in submerged intakes with different isolator lengths to obtain a clear view on how the pseudo-shock behavior in submerged supersonic intakes changes with different isolator lengths.

7.4. Applying flow control techniques regarding SBLI

Following the theoretical explanation of this report, Shock-Boundary Layer Interactions (SBLI) are very detrimental to the performance of supersonic intakes in general and it's due to one SBLI occurrence that a pseudo shock is formed at high Mach numbers. To slacken the effect of SBLI, it is advised to conduct experiments in which several flow control techniques may be applied inside the intake to test their capabilities in dampening the SBLI's harmful influence on the intake performance. One way of doing so is to install shock bumps inside the intake. According to Huang et al. [121], this particular method proved very successful in reducing the harmful influences of the cowling SBLI.

7.5. Applying boundary-layer bleed inside the intake isolator

Following the first research slot, it was concluded that external flush boundary bleed did not aid in improving the performance of the submerged intake. Therefore, to discover the potential of boundary layer bleed, it is advised to investigate the use of internal boundary layer bleed. This involves inserting a bleed slot or cavity through either the cowling or the compression plate to remove a large portion of the boundary-layer. However, the reader must understand that the placement of these boundary-layer bleed solutions should not be installed at the cost of ruining the pseudo-shocks behavior inside the intake. The installment of bleed slots or cavities is also interesting for investigating the extent to which flow separation inside the intake is suppressed. Since the latter is not easily controllable inside the intake at all, it is worthwhile to inspect this possibility to assess whether the problem of intake flow separation can be mitigated.

7.6. Designing optimal intake geometry

The geometry used in this report's experiments was designed as to provide a first impression of the potential behind the use of submerged supersonic intakes. In [chapter 3](#), it was mentioned that due to the fact that sharp edges are quickly damaged in experimental efforts, the leading edge of both cowling and compression plate was not perfect from an aerodynamic point of view since these were slightly blunted. Therefore, since the intake components of this report can be considered as prototype level parts, it is highly recommended to first invent and design a more optimized geometry before conducting future experiments. For a detailed road map on how to achieve an optimized intake design, the reader is referred to the works of Zha et al. [122] and Gaidon et al. [123].

A

Technical drawings of submerged supersonic intake model

This appendix contains the technical drawings of the different parts of the submerged supersonic intake wind tunnel model. Except for the support block and expansion section, all parts in this appendix were designed by Kwakman [91].

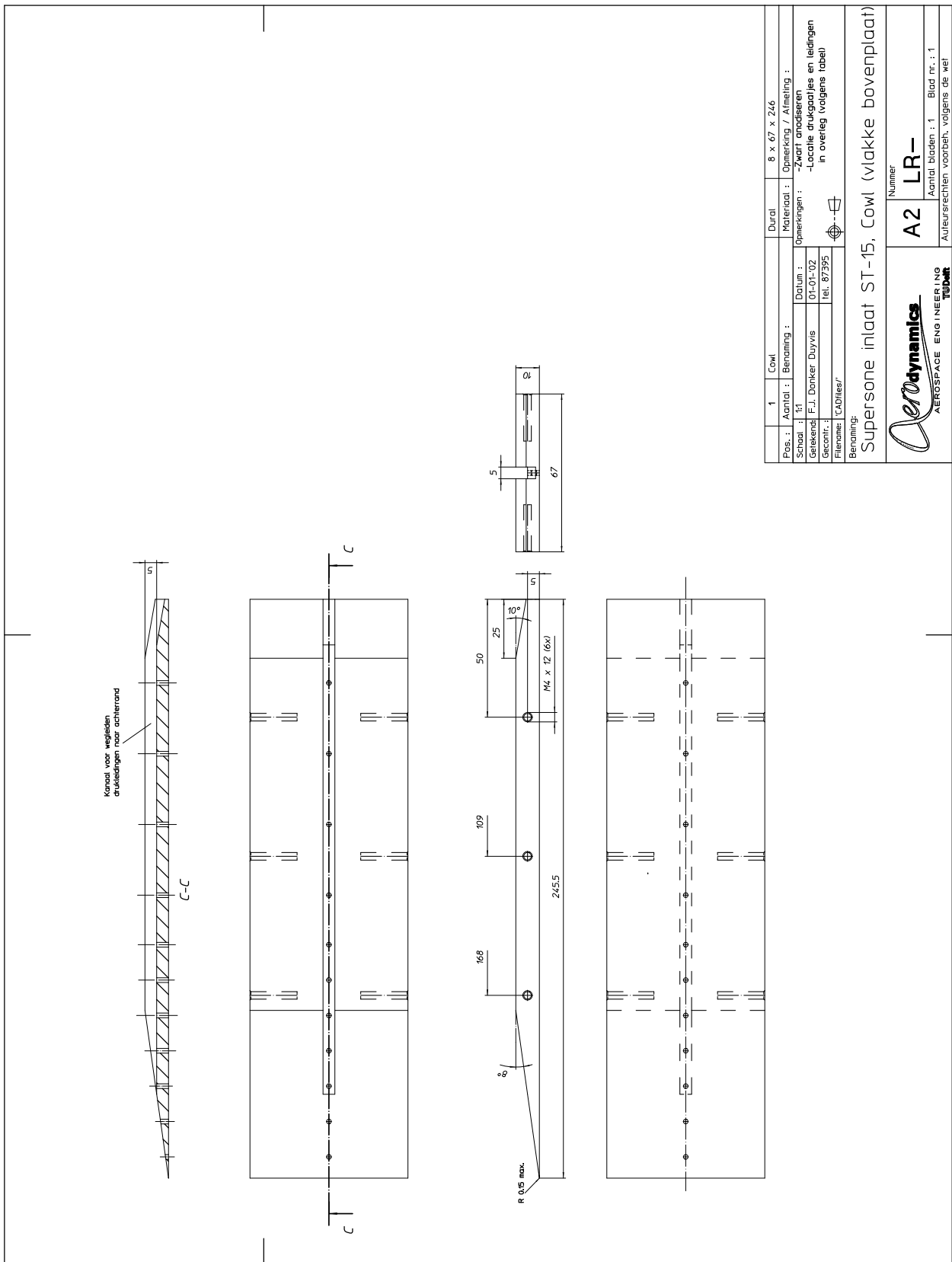


Figure A.3: Intake cowl.

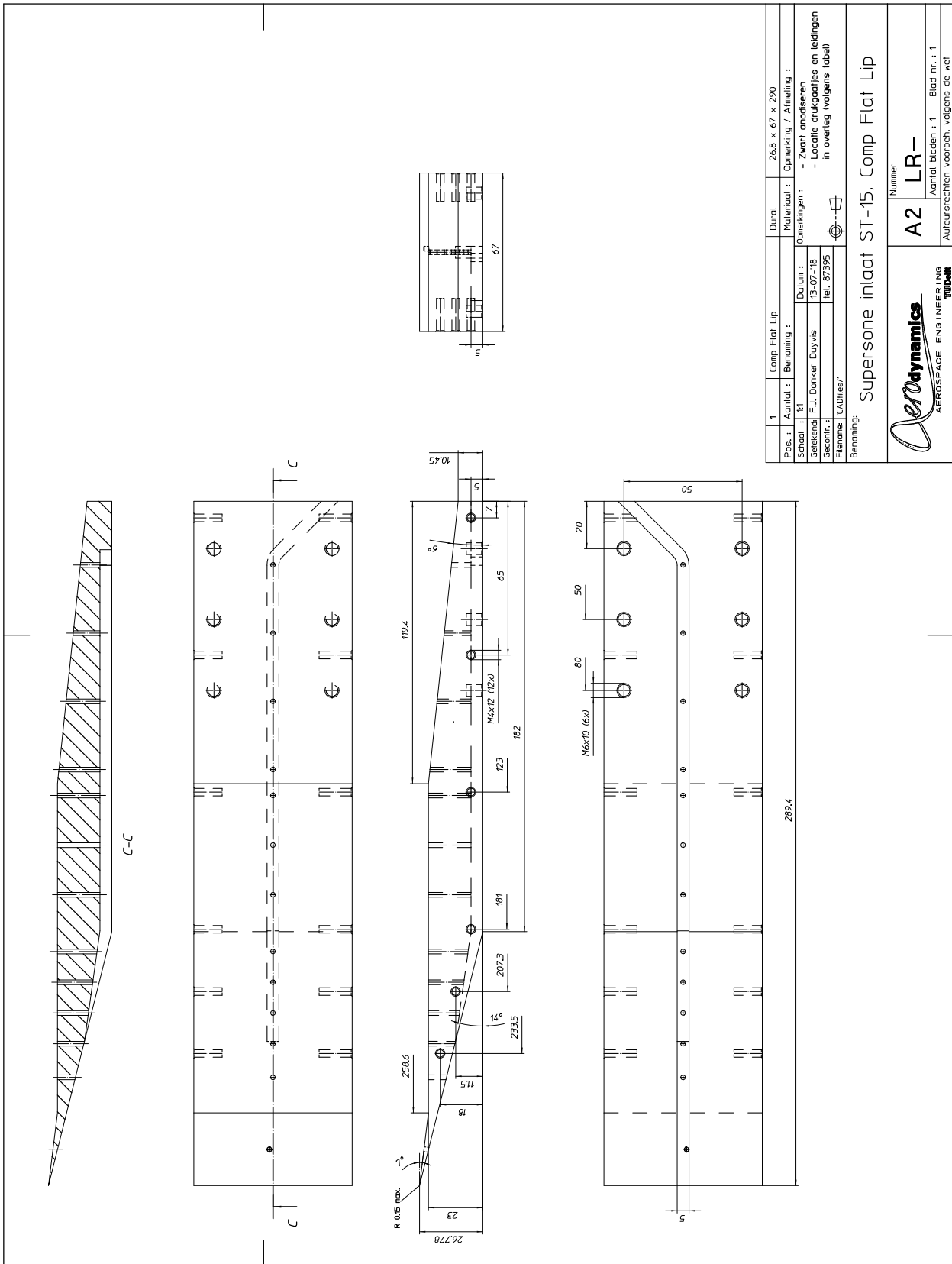


Figure A.4: Double-shock compression surface.

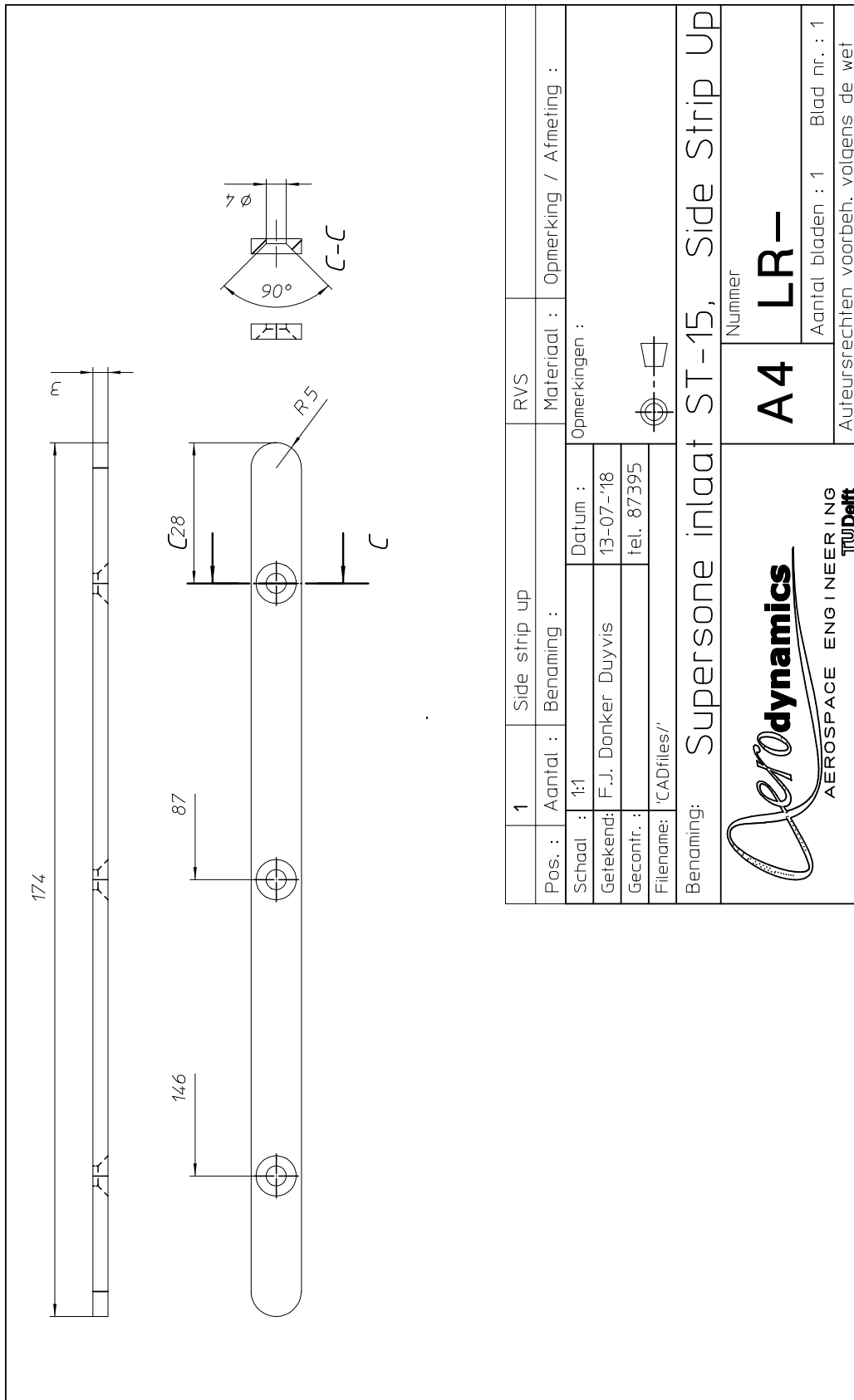


Figure A.6: Upper sidewall strip.

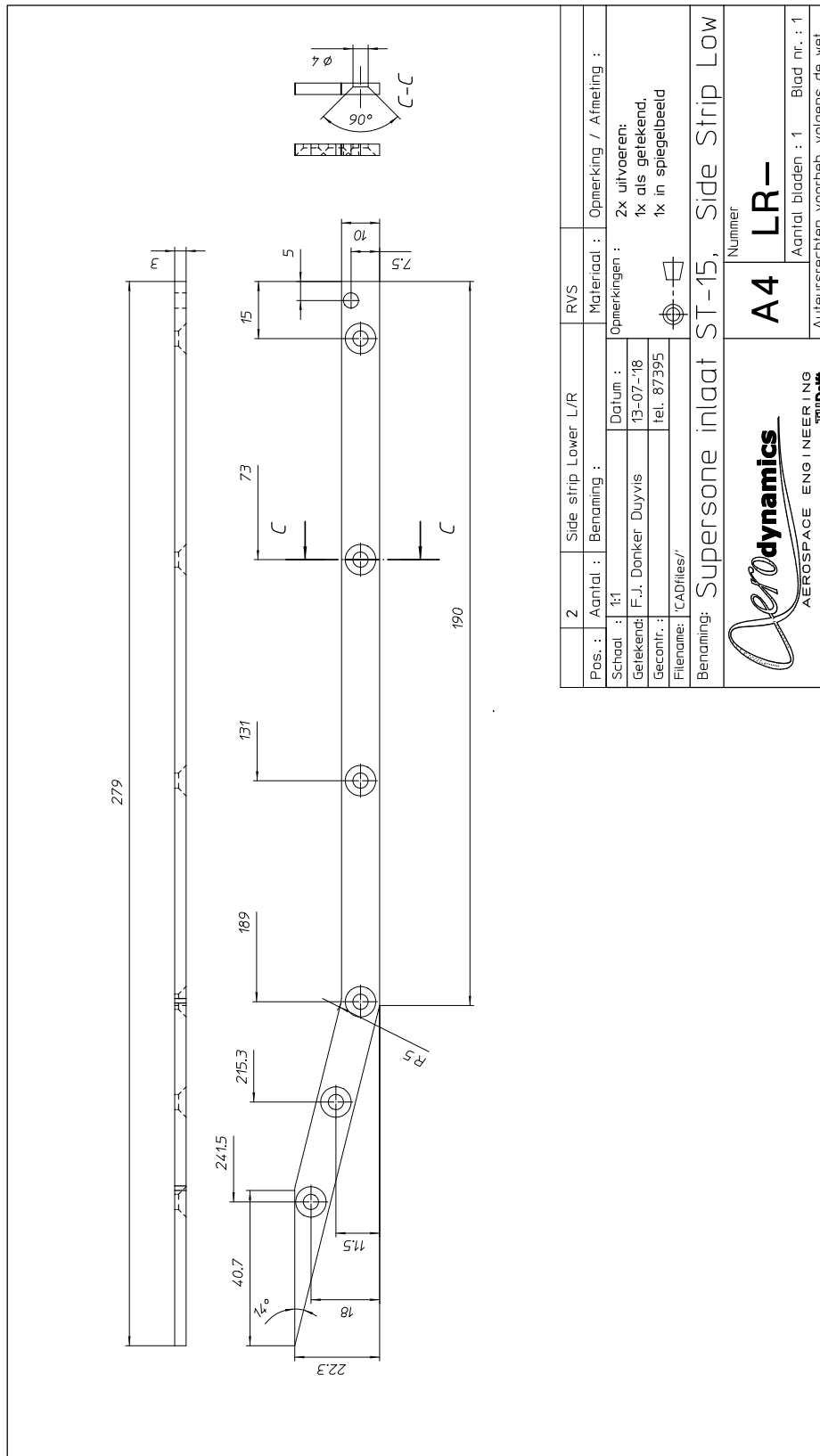


Figure A.7: Lower sidewall strip.

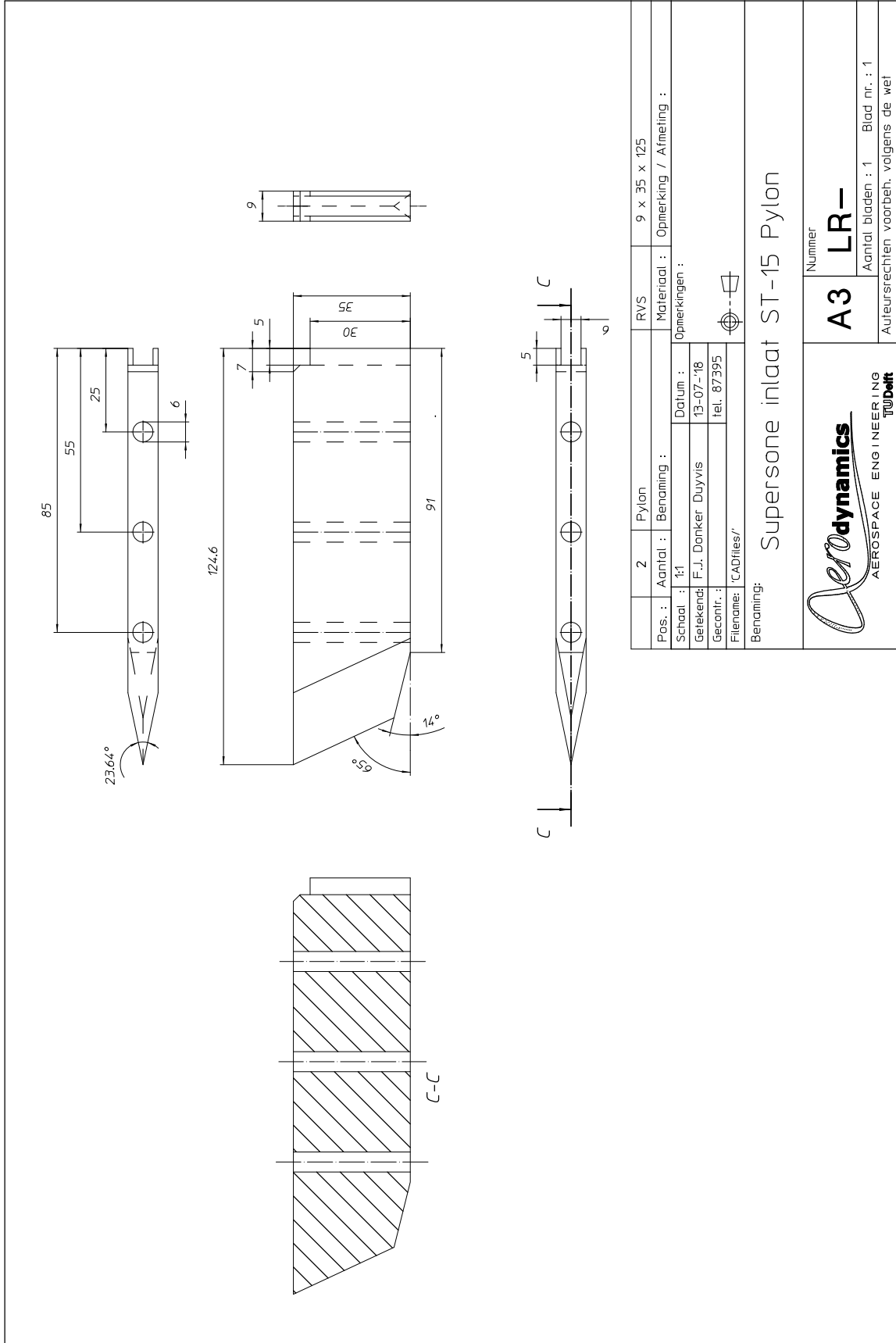


Figure A.8: Intake support pylon.

B

Technical drawings of the throttle system

This appendix contains the technical drawings of the different parts of the control system, designed by the author of this report, used to regulate the massflow in the intake.

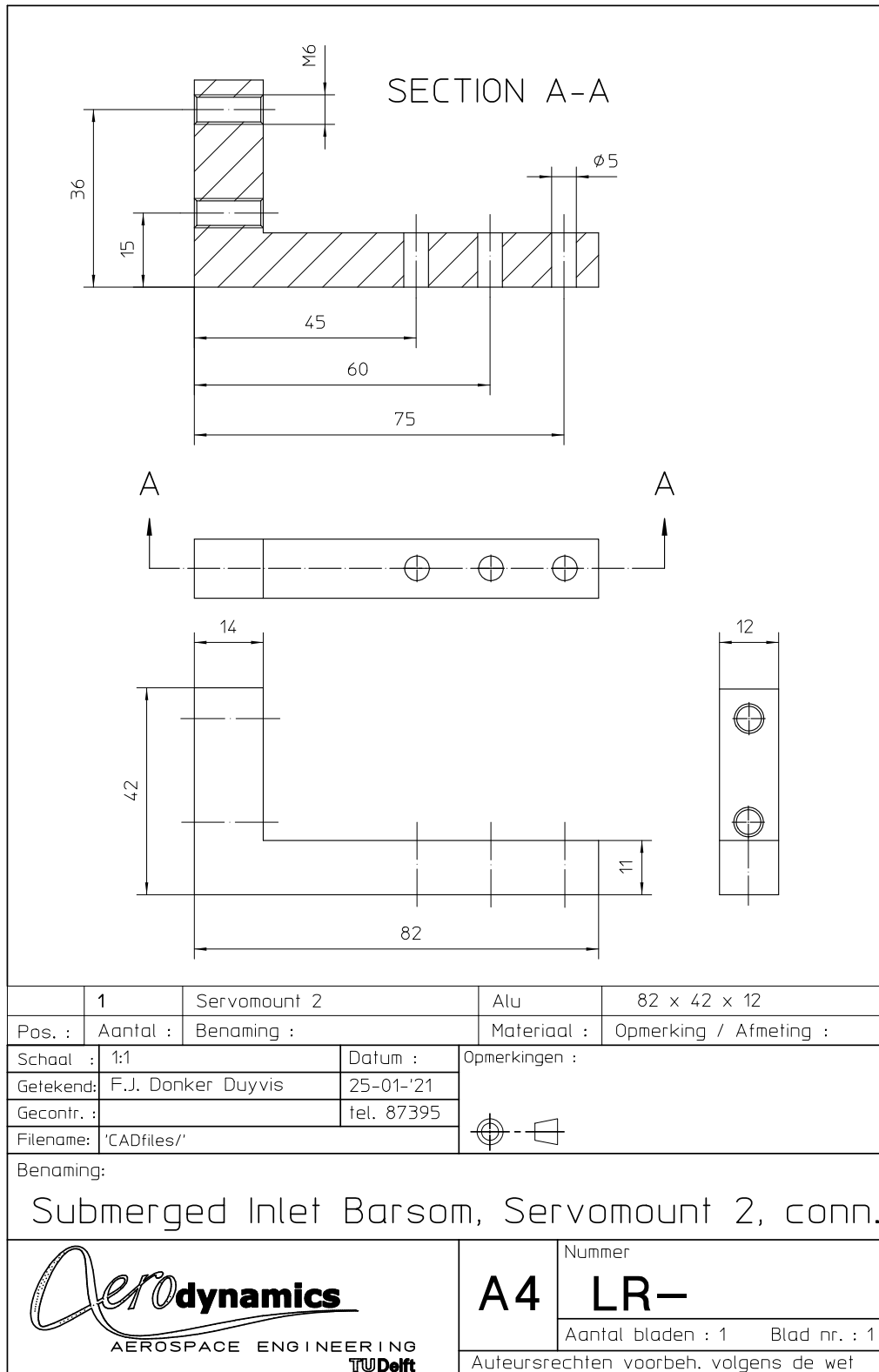


Figure B.1: Servo bracket (cable side).

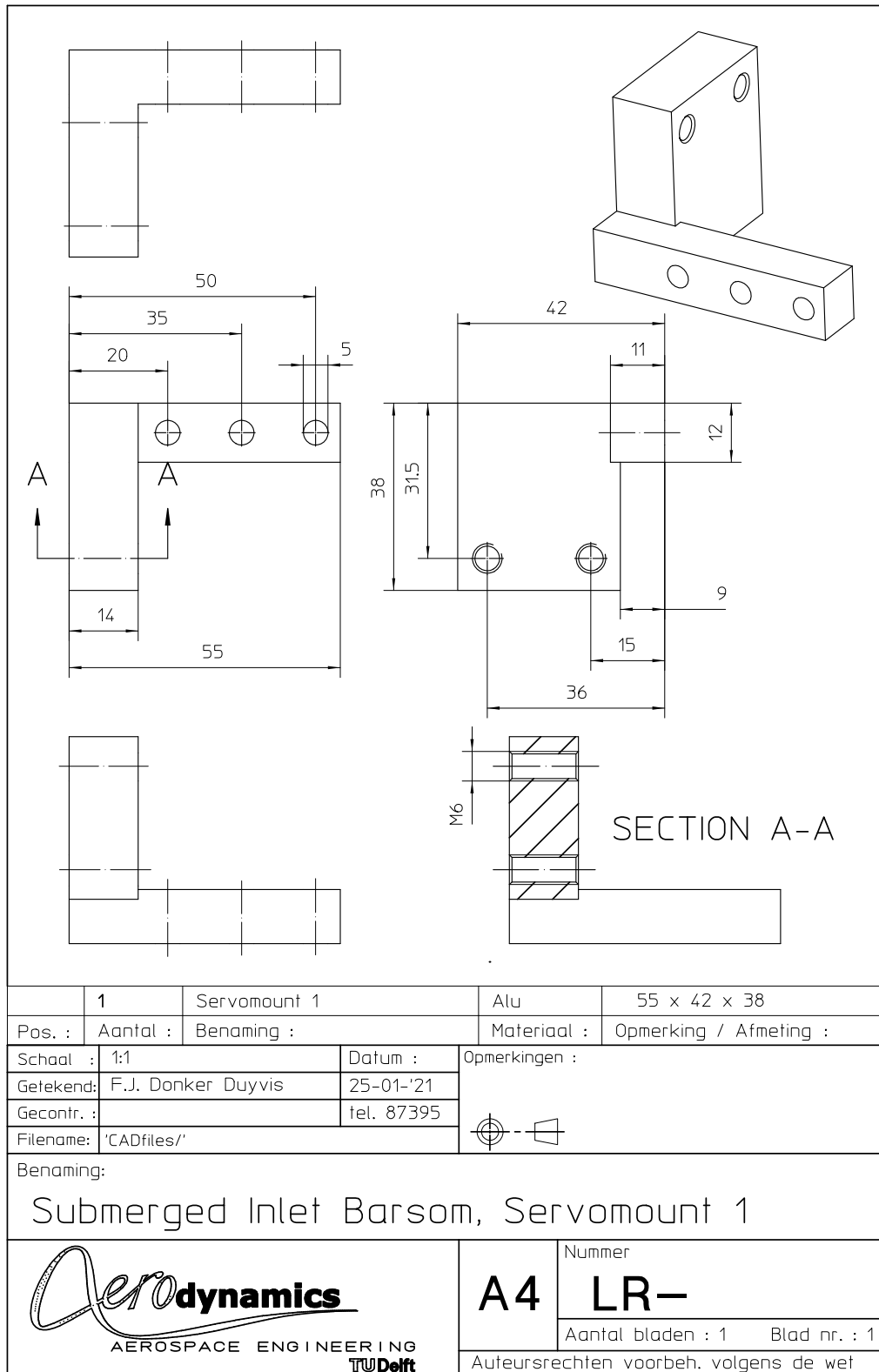


Figure B.2: Servo bracket (free side).

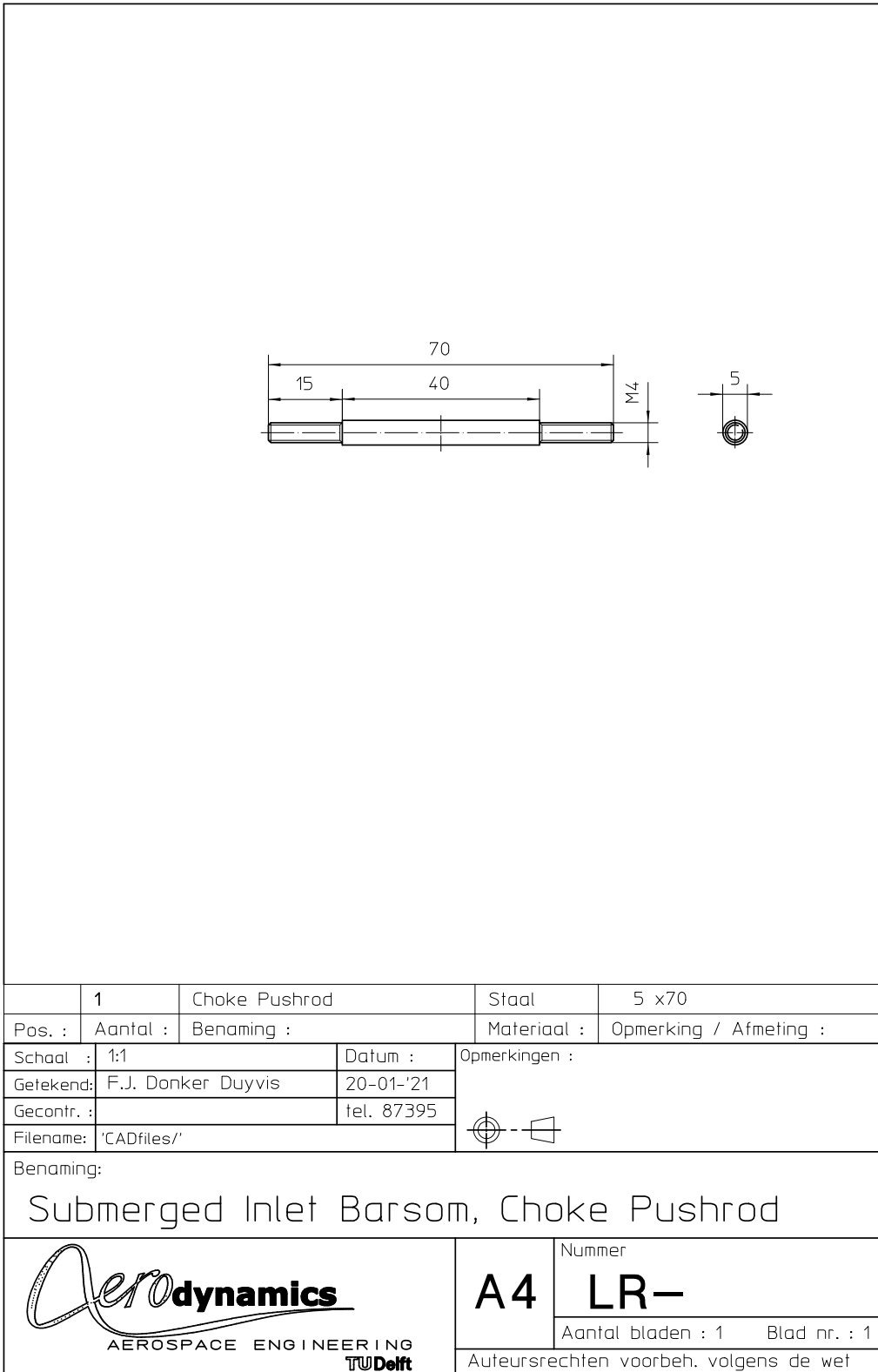


Figure B.3: Pushrod.

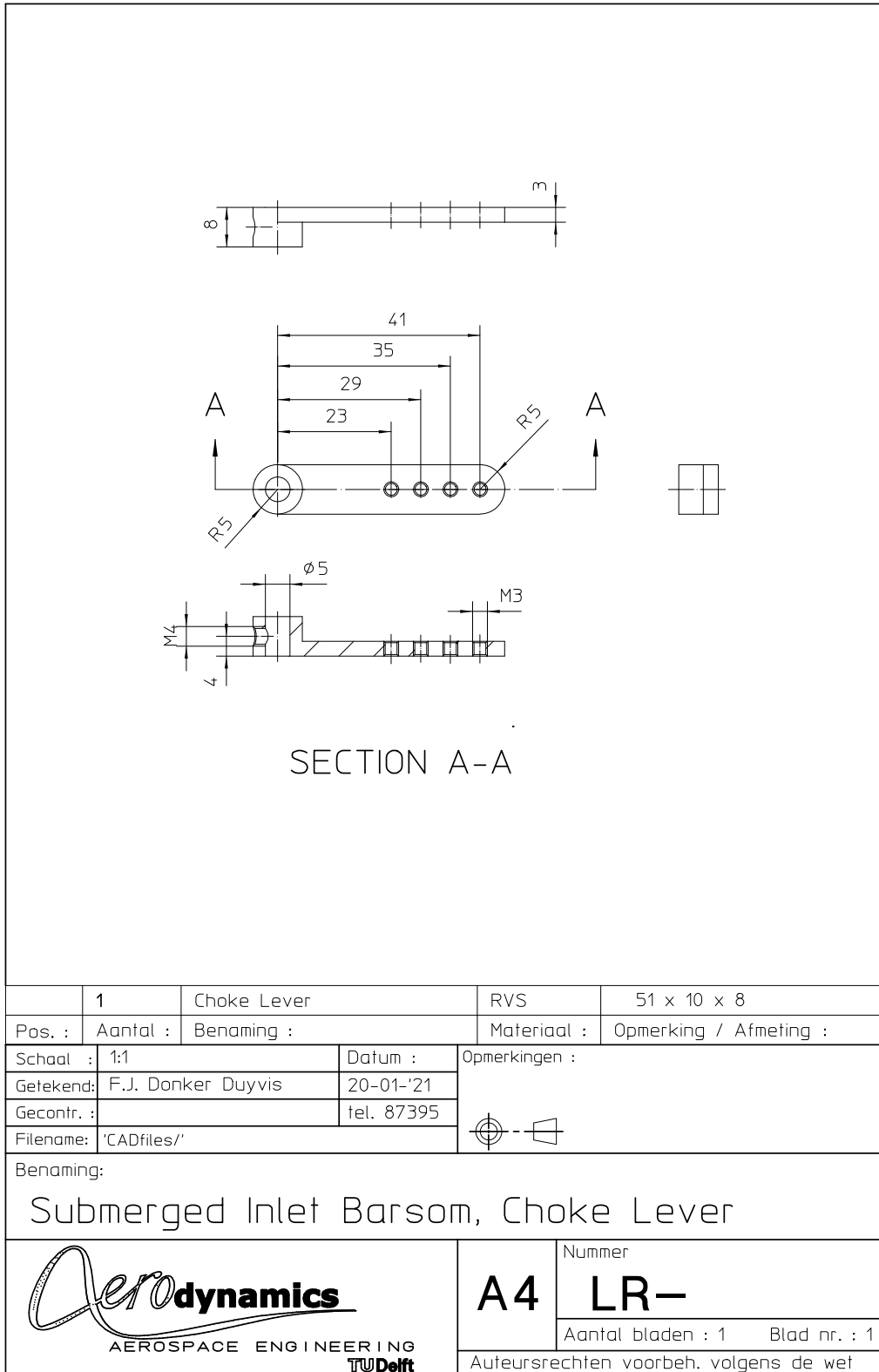


Figure B.4: Butterfly valve lever.

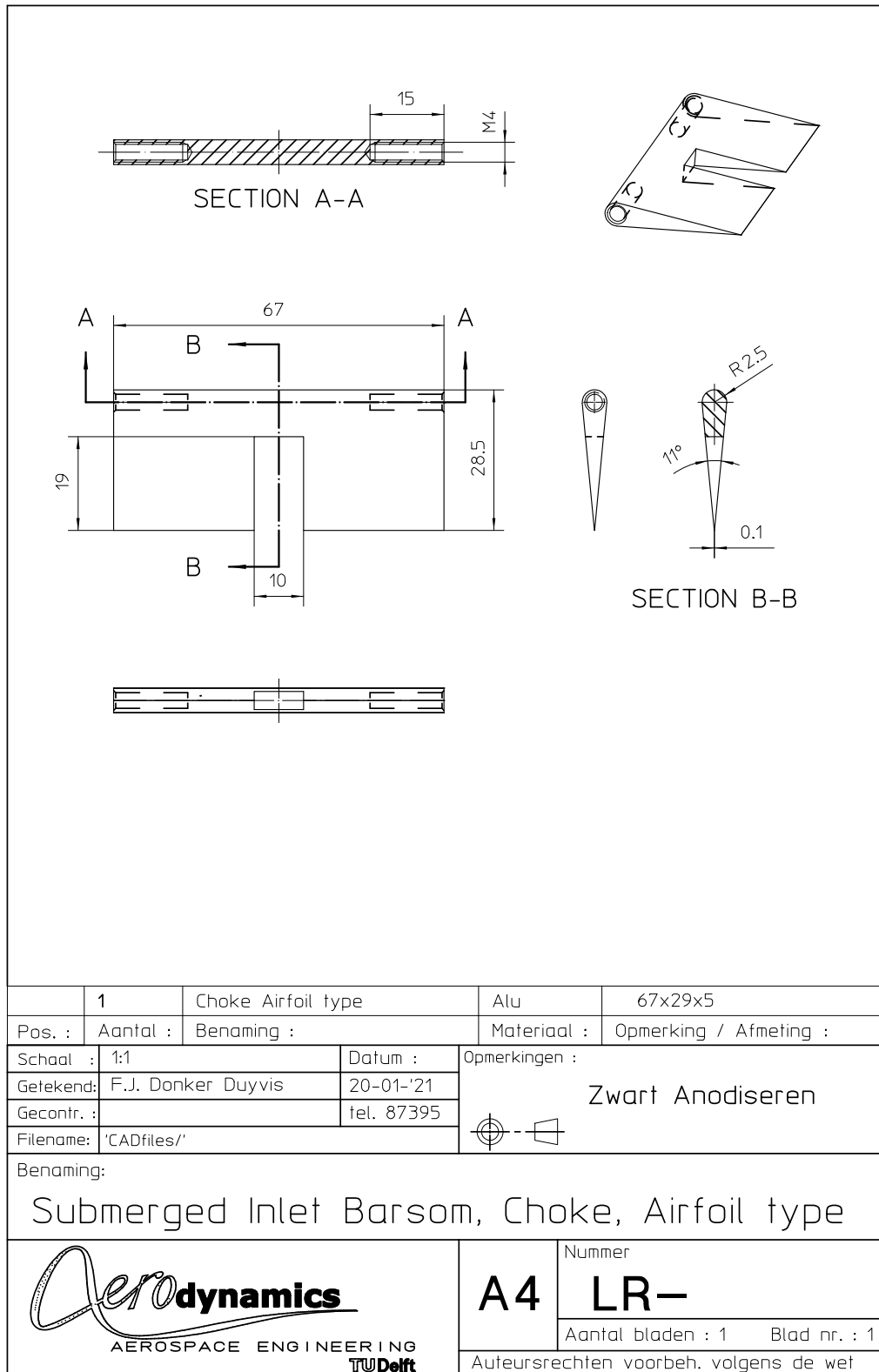


Figure B.5: Butterfly valve (airfoil shape).

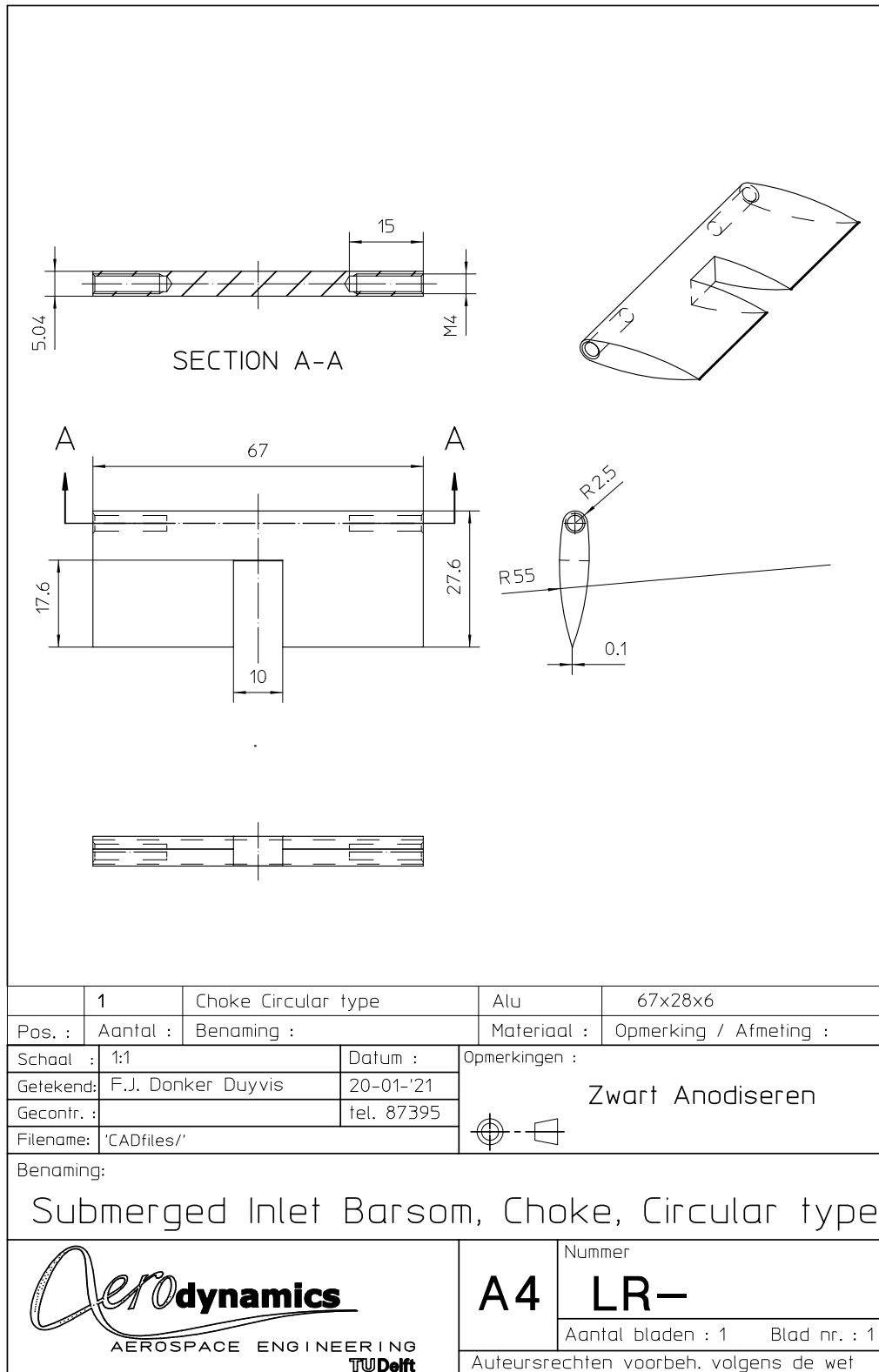


Figure B.6: Butterfly valve (arc shape).

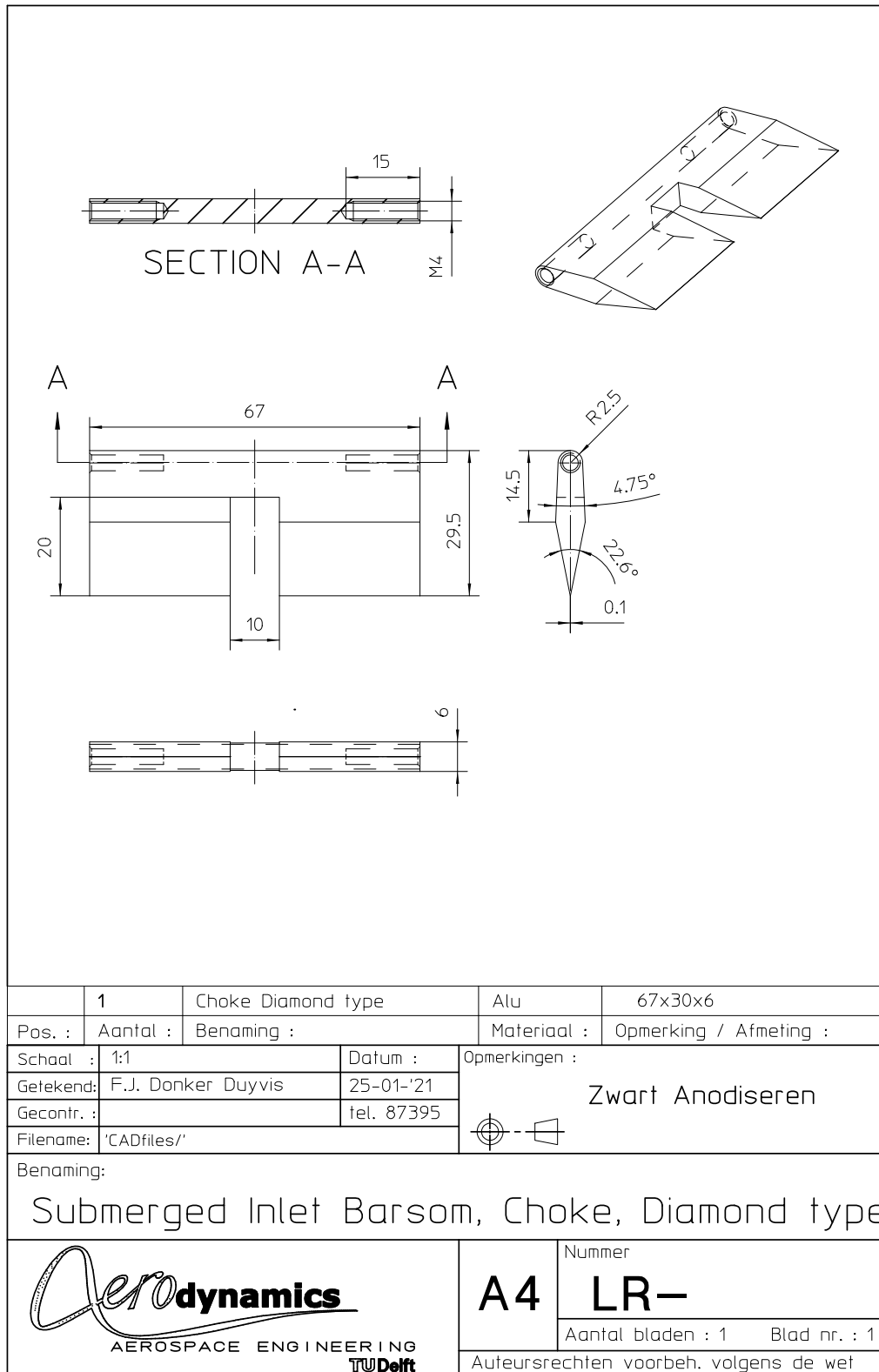


Figure B.7: Butterfly valve (diamond shape).

C

Test Matrices

This appendix contains the two test matrices used for this report’s experimental campaigns. As an additional remark, two different butterfly valve angles corresponded to both the near-supercritical and critical conditions. These cases were labeled as the ‘high’ and ‘low’ angle cases.

#	Condition	Butterfly valve	Measurement Technique
1	Supercritical	Airfoil	Schlieren imagery & Static pressure
2	Supercritical	Airfoil	
3	Supercritical	Airfoil	
4	Near-supercritical	Airfoil	
5	Near-supercritical	Airfoil	
6	Near-supercritical	Airfoil	
7	Critical	Airfoil	
8	Critical	Airfoil	
9	Critical	Airfoil	
10	Supercritical	Arc	
11	Supercritical	Arc	
12	Supercritical	Arc	
13	Near-supercritical	Arc	
14	Near-supercritical	Arc	
15	Near-supercritical	Arc	
16	Critical	Arc	
17	Critical	Arc	
18	Critical	Arc	
19	Supercritical	Diamond	
20	Supercritical	Diamond	
21	Supercritical	Diamond	
22	Near-supercritical	Diamond	
23	Near-supercritical	Diamond	
24	Near-supercritical	Diamond	
25	Critical	Diamond	
26	Critical	Diamond	
27	Critical	Diamond	

Table C.1: Test matrix for the Schlieren imagery and static pressure campaigns

#	Condition	Butterfly valve	Measurement Technique
1	Supercritical	Diamond	Planar PIV
2	Supercritical	Diamond	
3	Supercritical	Diamond	
4	Near-supercritical (lower angle)	Diamond	
5	Near-supercritical (lower angle)	Diamond	
6	Near-supercritical (lower angle)	Diamond	
7	Near-supercritical (higher angle)	Diamond	
8	Near-supercritical (higher angle)	Diamond	
9	Near-supercritical (higher angle)	Diamond	
10	Critical (lower angle)	Diamond	
11	Critical (lower angle)	Diamond	
12	Critical (lower angle)	Diamond	
13	Critical (higher angle)	Diamond	
14	Critical (higher angle)	Diamond	
15	Critical (higher angle)	Diamond	

Table C.2: Test matrix for the PIV campaign

D

PIV Results

This appendix features the complete PIV vector results for the supercritical, near-supercritical and critical conditions. These PIV results contain the normalized streamwise velocity distribution u/V_∞ , normalized vertical velocity distribution v/V_∞ and the Mach number distribution M .

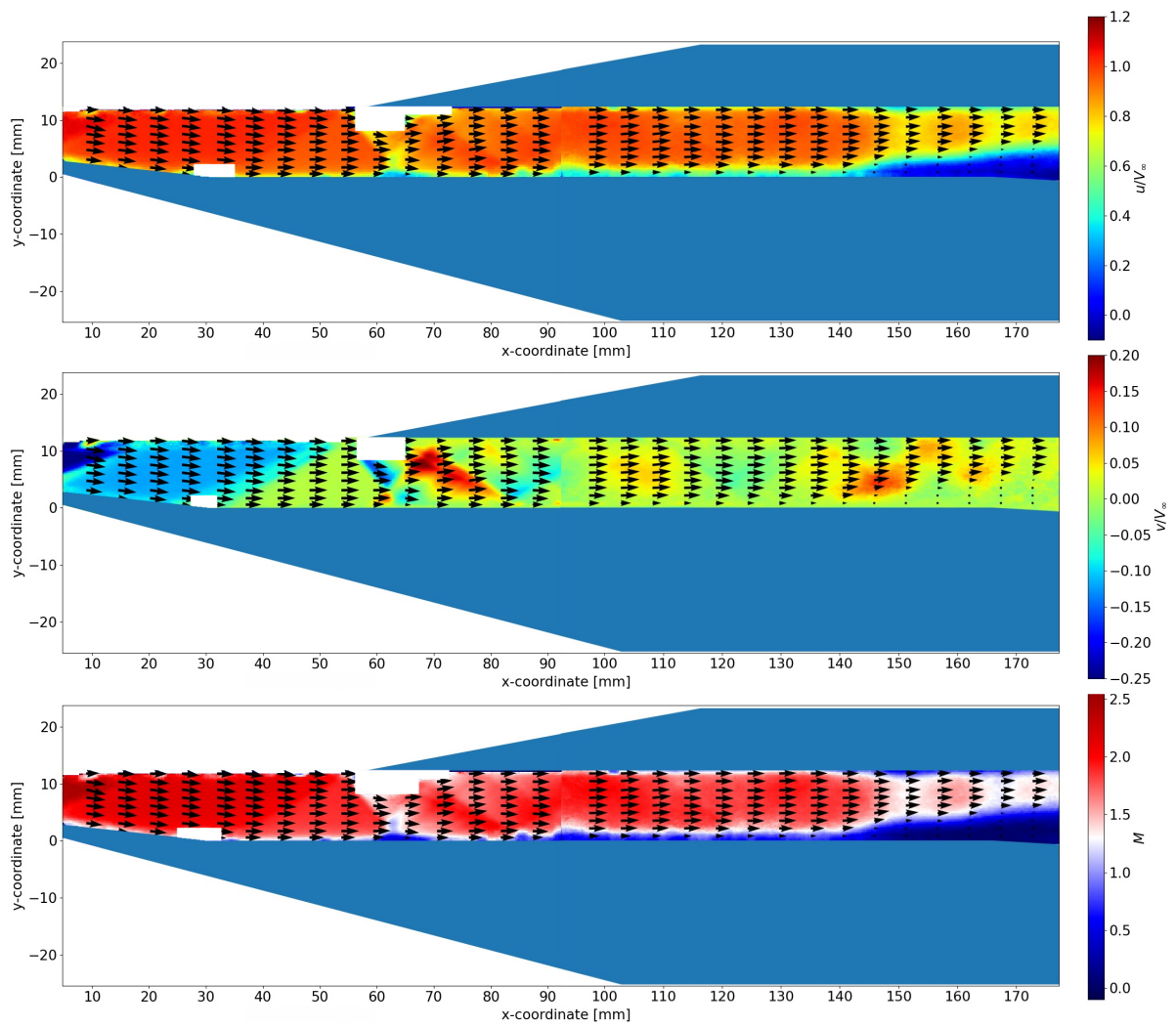


Figure D.1: PIV vector results for the normalized streamwise velocity, normalized vertical velocity and the Mach number for the supercritical condition.

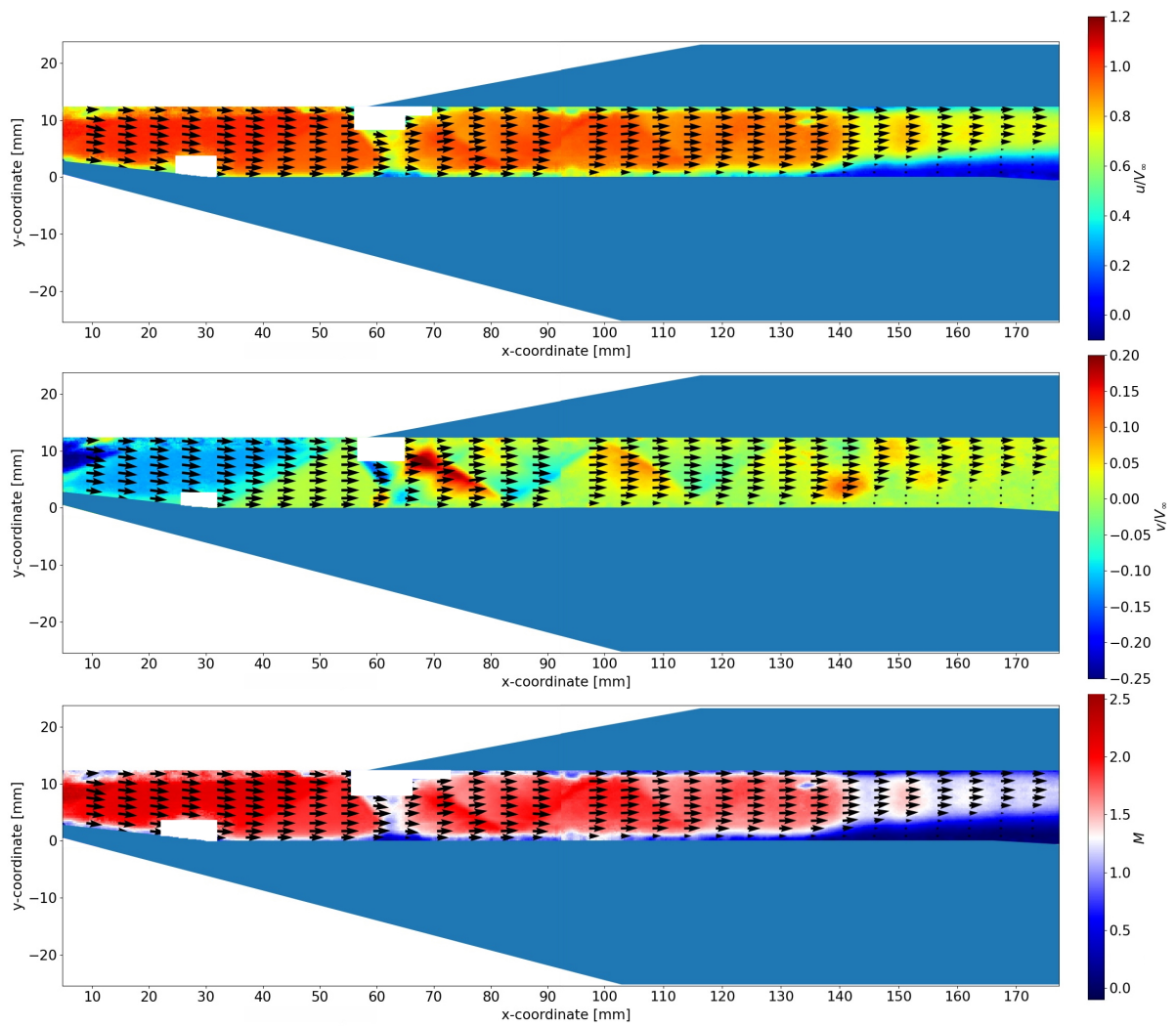


Figure D.2: PIV vector results for the normalized streamwise velocity, normalized vertical velocity and the Mach number for the near-supercritical condition.

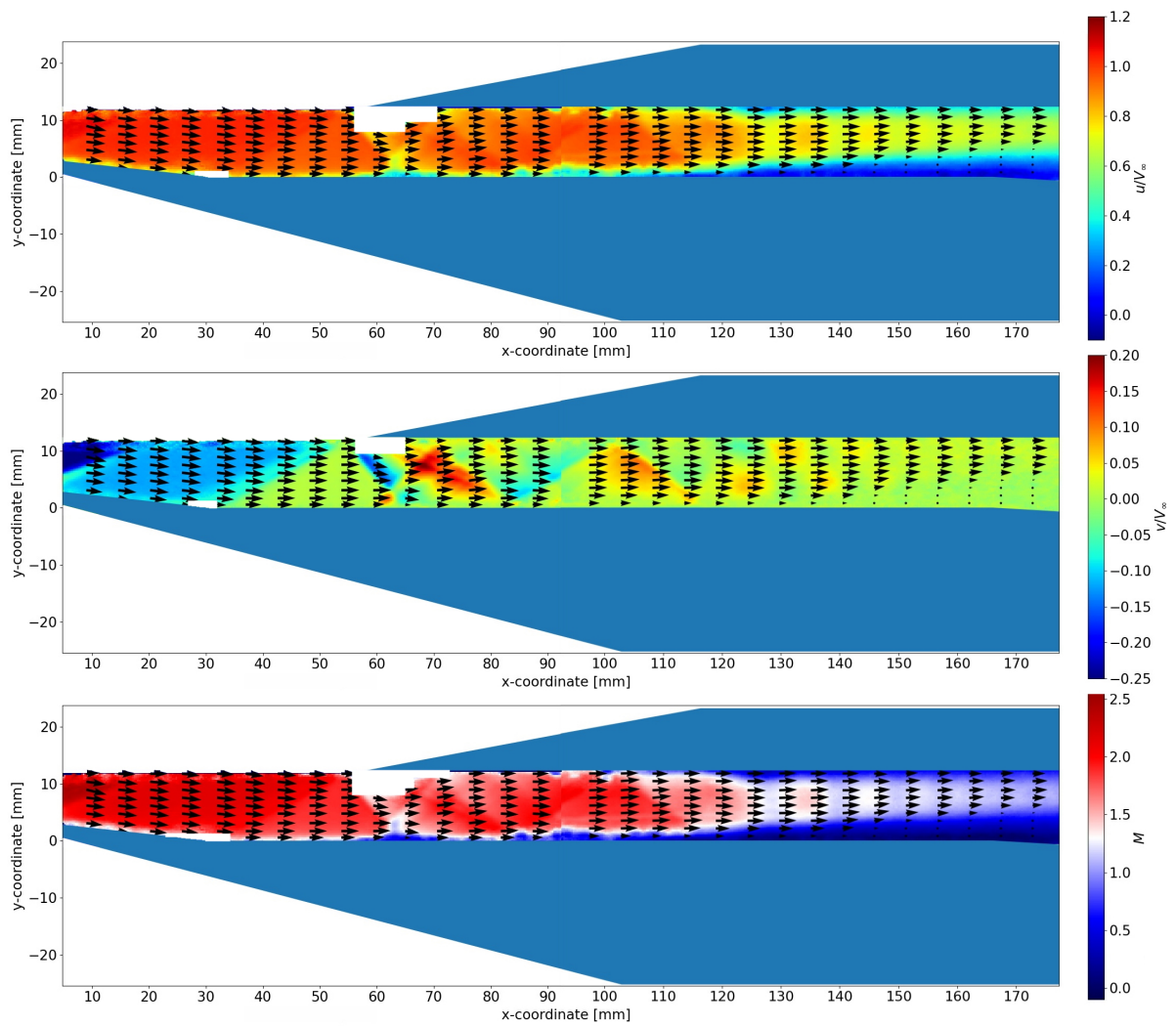


Figure D.3: PIV vector results for the normalized streamwise velocity, normalized vertical velocity and the Mach number for the critical condition.

E

Performance study

This appendix features a performance analysis table, which draws a comparison between the analytical solutions and experimental results of several parameters of interest in the SSI model. Please note that no analytical solution on the cowling leading edge shock wave angle exists, since the flow's turn angle at that location was theoretically zero.

Parameter [unit]	Location	Analytical solution	Experimental result
Mach number M [-]	Post-expansion	2.55	2.51 (PIV) 2.53 (Schlieren)
	Post-first OSW	2.25	2.22 (PIV) 2.24 (Schlieren)
	Post-second OSW	1.98	2.06 (PIV) 2.08 (Schlieren)
Shock angle β [°]	First OSW	28.59	28.99 (PIV) 28.64 (Schlieren)
	Second OSW	32.11	30.18 (PIV) 29.42 (Schlieren)
	Cowling LE Shock	N/A	35.78 (PIV) 35.28 (Schlieren)
Normalized static pressure p/p_0 [-]	$x = 15$ [mm]	0.084	0.090
	$x = 46$ [mm]	0.1277	0.1444
	$x = 59$ [mm]	0.1277	0.1474
	$x = 73$ [mm]	0.1924	0.2119

Table E.1: Analytical and experimental performance study of the SSI model

Bibliography

- [1] D. Barrie. *Trends in missile technologies*. <https://www.iiss.org/blogs/analysis/2019/03/trends-in-missile-technologies>. [Online; accessed 23-March-2021]. Mar. 2019.
- [2] *Global Cruise Missile Market (2020 to 2025) - Growth, Trends and Forecasts*. <https://www.globenewswire.com/news-release/2020/05/06/2028552/0/en/Global-Cruise-Missile-Market-2020-to-2025-Growth-Trends-and-Forecasts.html>. [Online; accessed 23-March-2021]. May 2020.
- [3] T. Cain. *Ramjet Intakes*. Technical report. DTIC Document. 2010.
- [4] F. Falempin. *Ramjet and Dual Mode Operation*. RTO. by MDBA France. 2007.
- [5] A. Sóbester. “Tradeoffs in Jet Inlet Design: A Historical Perspective”. In: *Journal of Aircraft* 44.3 (May 2007), pp. 705–717. DOI: [10.2514/1.26830](https://doi.org/10.2514/1.26830).
- [6] G. Laurelle. “Air Intakes: Role, Constraints and Design”. In: *ICAS 2002 Congress*. EADS Launch Vehicles. Les Mureaux, France: International Council of the Aeronautical Sciences, 2002.
- [7] E. van Wijk. “Submerged Ramjet Intake Modeling”. MSc. Thesis. Delft University of Technology, Nov. 2017.
- [8] D.J. Peake, W.J. Rainbird, and E.G. Atraghji. “Three-Dimensional Flow Separations on Aircraft and Missiles”. In: *AIAA 10.5* (May 1972), pp. 567–580. DOI: [10.2514/3.50159](https://doi.org/10.2514/3.50159).
- [9] T. Osborne. *Airpower Demands Drive Air-Launched Cruise Missile Evolution*. <https://aviationweek.com/defense-space/missile-defense-weapons/airpower-demands-drive-air-launched-cruise-missile-evolution>. [Online; accessed 24-March-2021]. Feb. 2021.
- [10] Raytheon Missiles & Defence. *Arming the F-35: Adding firepower to the world's most advanced fighter jet*. <https://www.raytheonmissilesanddefense.com/news/feature/arming-the-f-35>. [Online; accessed 24-March-2021]. Dec. 2019.
- [11] Reportlinker. *Global Air Defense System Industry*. <https://www.globenewswire.com/news-release/2020/04/14/2015422/0/en/Global-Air-Defense-System-Industry.html>. [Online; accessed 24-March-2021]. Apr. 2020.
- [12] K. Oswatitsch. *Pressure recovery for missiles with reaction propulsion at high supersonic speeds (the efficiency of shock diffusers)*. Technical Memorandum 1140. NACA, 1947.
- [13] J. Seddon and E.L. Goldsmith. *Intake Aerodynamics*. ISBN 9780930403034. Collins Professional and Technical Books, 1985.
- [14] L.L. Cronvich and I.D.V. Faro. “Ducts, Nozzles and Diffusers.” In: *Handbook of supersonic aerodynamics*. Vol. 4. 1964.
- [15] H. Wittenberg. “Some Fundamentals on the Performance of Ramjets with Subsonic and Supersonic Combustion”. In: *The Aeronautical Journal* 105.1044 (2000), pp. 96–99.
- [16] M.A. Faget. *A proposed ramjet control system operated by use of diffuser pressure recovery*. Research Memorandum RM L52EO5b. Langley Aeronautical Laboratory Langley Field, Virginia: NACA, Sept. 1952.
- [17] D.S. Dolling. “Fifty Years of Shock-Wave/Boundary-Layer Interaction Research: What Next?” In: *AIAA Journal* 39.8 (Aug. 2001), pp. 1517–1530. DOI: [10.2514/2.1476](https://doi.org/10.2514/2.1476).
- [18] J. Delery and R. Blur. “The Physics of Shock Wave / Boundary Layer Interaction Control: Last Lessons Learned”. In: *European Congress on Computational Methods in Applied Sciences and Engineering - ECCOMAS 2000*. Barcelona, Spain, Sept. 2000. DOI: [10.13140/2.1.4478.8169](https://doi.org/10.13140/2.1.4478.8169).
- [19] J. Sepahi-Younsi et al. “Boundary layer suction for high-speed air intakes: A review”. In: *Journal of Aerospace Engineering* 233.9 (Aug. 2018). DOI: [10.1177/0954410018793262](https://doi.org/10.1177/0954410018793262).
- [20] S.B. Verma, C. Manisankar, and P. Akshara. “Control of shock-wave boundary layer interaction using steady micro-jets”. In: *Shock Waves* 25.5 (May 2014). DOI: [10.1007/s00193-014-0508-5](https://doi.org/10.1007/s00193-014-0508-5).

- [21] H. Babinsky and J.K. Harvey. *Shock Wave-Boundary-Layer Interactions*. ISBN 9780521848527. Cambridge University Press, 2011.
- [22] D.R. Chapman, D.M. Kuehn, and H.K. Larson. *Investigation of separated flows in supersonic and subsonic streams with emphasis on the effect of transition*. NACA Technical Report. report 1356. Jan. 1958.
- [23] J. Delery and J.G. Marvin. *Turbulent shock-wave/boundary-layer interaction*. Report. AGARD, 1986.
- [24] F. Feldmann, J. Ackeret, and N. Rott. *Investigations of compression shocks and boundary layers in gases moving at high speed*. NACA Technical report. no. 1113. Jan. 1947.
- [25] H. Babinsky, J. Oorebeek, and T.G. Cottingham. "Corner effects in reflecting oblique shock-wave/boundary layer interactions". In: *51st AIAA Aerospace Sciences Meeting including the New Horizons Forum and Aerospace Exposition*. 2013-0859. Grapevine (Dallas/Ft. Worth Region), TX, USA, Jan. 2013, pp. 1–10. DOI: [10.2514/6.2013-859](https://doi.org/10.2514/6.2013-859).
- [26] L. Kral. "Active flow control technology". In: *ASME FED, Technical Brief* (Jan. 2000).
- [27] N. Titchener, H. Babinsky, and E. Loth. "Can Fundamental Shock-Wave/Boundary-Layer Interaction Research be Relevant to Inlet Aerodynamics?" In: *50th AIAA Aerospace Sciences Meeting including the New Horizons Forum and Aerospace Exposition*. 2012-0017. Nashville, TN, USA, Jan. 2012. DOI: [10.2514/6.2012-17](https://doi.org/10.2514/6.2012-17).
- [28] K. Matsuo, Y. Miyazato, and H.D. Kim. "Shock train and pseudo-shock phenomena in internal gas flows". In: *Progress in Aerospace Sciences* 35.1 (Jan. 1999), pp. 33–100. DOI: [10.1016/S0376-0421\(98\)00011-6](https://doi.org/10.1016/S0376-0421(98)00011-6).
- [29] L. Crocco. *High Speed Aerodynamics and Jet Propulsion*. Vol. 3. ISBN 9780691626499. Princeton: Princeton University Press, 1958.
- [30] F. Gnani, H. Zare-Behtash, and K. Kontis. "Pseudo-shock waves and their interactions in high-speed intakes". In: *Progress in Aerospace Sciences* 82 (Feb. 2016), pp. 36–56. DOI: [10.1016/j.paerosci.2016.02.001](https://doi.org/10.1016/j.paerosci.2016.02.001).
- [31] W.H. Heiser and D.T. Pratt. *Hypersonic airbreathing propulsion*. ISBN 9781563470356. AIAA, 1994.
- [32] Y. He, H. Huang, and D. Yu. "Investigation of corner separation and suction control in constant area duct". In: *Aerospace Science and Technology* 66 (July 2017), pp. 70–82. DOI: [10.1016/j.ast.2017.01.029](https://doi.org/10.1016/j.ast.2017.01.029).
- [33] V.N. Ostras and V.I. Penzin. "Experimental Study of Friction in a Channel with a Pseudo shock". In: *Fluid Mechanics-Soviet Research* 4 (1975), pp. 32–38.
- [34] D. Om, J.R. Viegas, and M.E. Childs. "Transonic shock-wave/turbulent boundary-layer interactions in a circular duct". In: *AIAA* 23.10 (May 1985), pp. 707–714. DOI: [10.2514/3.8974](https://doi.org/10.2514/3.8974).
- [35] A. Weiss, A. Grzona, and H. Olivier. "Behavior of shock trains in a diverging duct". In: *Experiments in Fluids* 49 (Jan. 2010), pp. 355–365. DOI: [10.1007/s00348-009-0764-9](https://doi.org/10.1007/s00348-009-0764-9).
- [36] F. Lustwerk. *The Influence of Boundary Layer on the 'normal' Shock Configuration*. Meteor report. ASIN B0007FUY8Q. Massachusetts Institute of Technology, Guided Missiles Program, 1950.
- [37] B.F. Carroll and J.C. Dutton. "Characteristics of multiple shock wave/turbulent boundary-layer interactions in rectangular ducts". In: *Journal of Propulsion and Power* 6.2 (Mar. 1990), pp. 186–193. DOI: [10.2514/3.23243](https://doi.org/10.2514/3.23243).
- [38] P. Lin, G.V.R. Rao, and G.M. O'Connor. "Numerical analysis of normal shock train in a constant area isolator". In: *27th Joint Propulsion Conference*. 1991-2162. Sacramento, CA, USA, June 1991. DOI: [10.2514/6.1991-2162](https://doi.org/10.2514/6.1991-2162).
- [39] T. Tamaki, Tomita Y., and Yamane R. "A study of pseudo-shock, 1st Report, λ -type pseudo-shock". In: *Bull JSME* 13.55 (1970), pp. 51–58. DOI: [10.1299/jsme1958.13.51](https://doi.org/10.1299/jsme1958.13.51).
- [40] T. Ikui, K. Matsuo, and M. Nagai. "The mechanism of pseudo-shock waves". In: *Bull JSME* 17.108 (1974), pp. 731–739. DOI: [10.1299/jsme1958.17.731](https://doi.org/10.1299/jsme1958.17.731).
- [41] B.F. Carroll, P.A. Lopez-Fernandez, and J.C. Dutton. "Computations and experiments for a multiple normal shock/boundary-layer interaction". In: *Journal of Propulsion and Power* 9.3 (May 1993), pp. 405–411. DOI: [10.2514/3.23636](https://doi.org/10.2514/3.23636).

- [42] K.C. Lin et al. "Characterization of Shock Train Structures Inside Constant-Area Isolators of Model Scramjet Combustors". In: *44th AIAA Aerospace Sciences Meeting and Exhibit*. 2006-816. Reno, NV, USA, Jan. 2006, pp. 1442–1452. DOI: [10.2514/6.2006-816](https://doi.org/10.2514/6.2006-816).
- [43] D. Om and M.E. Childs. "Multiple transonic shock-wave/turbulent boundary-layer interaction in a circular duct". In: *AIAA J.* 23.10 (Oct. 1985), pp. 1506–1511. DOI: [10.2514/3.9117](https://doi.org/10.2514/3.9117).
- [44] T. Gawehn et al. "Experimental and numerical analysis of the structure of pseudo-shock systems in laval nozzles with parallel side walls". In: *Shock Waves* 20 (July 2010), pp. 297–306. DOI: [10.1007/s00193-010-0263-1](https://doi.org/10.1007/s00193-010-0263-1).
- [45] P.J. Waltrup and F.S. Billig. "Structure of shock waves in cylindrical ducts". In: *AIAA Journal* 11.10 (Oct. 1973), pp. 1404–1408. DOI: [10.2514/3.50600](https://doi.org/10.2514/3.50600).
- [46] P.J. Waltrup and F.S. Billig. "Prediction of precombustion wall pressure distributions in scramjet engines". In: *Journal of Spacecraft Rockets* 10.9 (Sept. 1973), pp. 620–622. DOI: [10.2514/3.27782](https://doi.org/10.2514/3.27782).
- [47] L.D. Nill and A.T. Mattick. "An experimental study of shock structure in a normal shock train". In: *34th Aerospace Sciences Meeting and Exhibit*. 1996-0799. Reno, NV, USA, Jan. 1996. DOI: [10.2514/6.1996-799](https://doi.org/10.2514/6.1996-799).
- [48] D.A. Bement, J.R. Stevens, and M.W. Thompson. "Measured operating characteristics of a rectangular combustor/inlet isolator". In: *26th Joint Propulsion Conference*. 1990-2221. Orlando, FL, USA, July 1990. DOI: [10.2514/6.1990-2221](https://doi.org/10.2514/6.1990-2221).
- [49] F.S. Billig. "Prediction of Precombustion Wall Pressure Distributions in Scramjet Engines". In: *AIAA Journal of Spacecraft and Rockets* 10.9 (Sept. 1973), pp. 620–622. DOI: [10.2514/3.27782](https://doi.org/10.2514/3.27782).
- [50] C.P. Wang, K.Y. Zhang, and K.M. Cheng. "Pressure Distribution Measurements in Scramjet Isolators under Asymmetric Supersonic Flow". In: *44th AIAA Aerospace Science Meeting and Exhibit*. 2006-818. Reno, NV, Jan. 2006. DOI: [10.2514/6.2006-818](https://doi.org/10.2514/6.2006-818).
- [51] T. Sridhar, G. Chandrabose, and S. Thanigaiarasu. "Numerical Investigation of Geometrical Influence On Isolator Performance". In: *IJTARME 2* (Oct. 2013), pp. 7–12.
- [52] M. Nagai. "Mechanism of Pseudo-shock Wave in Supersonic Jet". In: *Bulletin of JSME* 26.212 (1983), pp. 207–214. DOI: [10.1299/jsme1958.26.207](https://doi.org/10.1299/jsme1958.26.207).
- [53] L.Q. Sun et al. "Numerical and experimental investigations on the mach 2 pseudo-shock wave in a square duct". In: *Shock Waves* 6.4 (May 2003), pp. 363–370. DOI: [10.1007/BF03181743](https://doi.org/10.1007/BF03181743).
- [54] M. Nagai and M. Yaga. "On the pseudo-shock wave relations". In: *Transitional and turbulent compressible flows*. Vol. 224. ISBN 9780791809594. The American Society of Mechanical Engineers, 1995, pp. 103–108.
- [55] K. Matsuo, Y. Miyazato, and H.D. Kim. "Mass averaging pseudo-shock model in a straight flow passage". In: *Proceedings of the Institution of Mechanical Engineers* 213.6 (June 1999), pp. 365–375. DOI: [10.1243/0954410991533089](https://doi.org/10.1243/0954410991533089).
- [56] P.J. Ortwerth. "Scramjet Vehicle Integration". In: *Scramjet Propulsion*. ISBN 9781563473227. Progress in Astronautics and Aeronautics, 2001.
- [57] Q. Tu and C. Segal. "Isolator/Combustion Chamber Interactions During Supersonic Combustion". In: *Journal of Propulsion and Power* 26.1 (Jan. 2010), pp. 182–186. DOI: [10.2514/1.46156](https://doi.org/10.2514/1.46156).
- [58] T. Ikui, K. Matsuo, and K. Sasaguchi. "Modified Diffusion Model of Pseudo-Shock Waves Considering Upstream Boundary Layers". In: *Bull JSME* 24.197 (1981), pp. 1920–1927. DOI: [10.1299/jsme1958.24.1920](https://doi.org/10.1299/jsme1958.24.1920).
- [59] K. Matsuo. "Shock train and pseudo-shock phenomena in supersonic internal flows". In: *Journal of Thermal Science* 12.3 (Aug. 2003), pp. 204–208. DOI: [10.1007/s11630-003-0068-y](https://doi.org/10.1007/s11630-003-0068-y).
- [60] C.L. Dailey. "Supersonic Diffuser Instability". In: *Journal of Aeronautical Sciences* 22.11 (Nov. 1955), pp. 733–49. DOI: [10.2514/8.3452](https://doi.org/10.2514/8.3452).
- [61] A. Kantrowitz and C. Doanldson. *Preliminary investigation of supersonic diffusers*. Advance Confidential Report L5D20, Wartime report. NACA, May 1945.
- [62] S. Das and J.K. Prasad. "Cowl Deflection Angle in a Supersonic Air Intake". In: *Defence Science Journal* 59.2 (Mar. 2009), pp. 99–105. DOI: [10.14429/dsj.59.1496](https://doi.org/10.14429/dsj.59.1496).

- [63] R.B. Pearce. "Causes and Control of Power Plant Surge". In: *Aviation Week* (Jan. 1950).
- [64] A. Ferri and L.M. Nucci. *Theoretical and Experimental Analysis of Low-Drag Supersonic Inlet having a Circular Cross-Section and a Central Body at Mach number 3.30, 2.75 and 2.45*. NACA Research Memorandum. no. RM L8H13. Nov. 1948.
- [65] I.M. Davidson and L.E. Ummey. *Concerning the Annular Air Intake in Supersonic Flight*. No. 2651. ACR. and M., Aug. 1947.
- [66] J. Sepahi-Younsi and B.F. Feshalami. "Performance Evaluation of External and Mixed Compression Supersonic Air Intakes: Parametric Study". In: *Journal of Aerospace Engineering* 32.5 (Nov. 2019), p. 14. DOI: [10.1061/\(ASCE\)AS.1943-5525.0001048](https://doi.org/10.1061/(ASCE)AS.1943-5525.0001048).
- [67] Sybil P. Parker. *Dictionary of Scientific & Technical Terms*. sixth. ISBN 9780070423138. 1325 Avenue of the Americas, New York, NY 10019: McGraw-Hill Education, 2003.
- [68] F.B. Gessner, S.D. Ferguson, and C.H. Lot. "Experiments on Supersonic Turbulent Flow Development in a Square Duct". In: *AIAA Journal* 25.5 (May 1987), pp. 690–697. DOI: [10.2514/3.9684](https://doi.org/10.2514/3.9684).
- [69] J. Mahoney. *Inlets for Supersonic Missiles*. AIAA Education Series. ISBN 9780930403799. AIAA, Jan. 1991.
- [70] E.S. Billig, S. Corda, and P.P. Pandolfini. "Design Techniques for Dual Mode Ram-Scramjet Combustors". In: *AGARD 75th Symposium of Hypersonic Combined Cycle Propulsion*. Madrid, Spain, 1990, p. 20.
- [71] E.P. Neumann and F. Lustwerk. "High-Efficiency Supersonic Diffusers". In: *AIAA Journal* 18.6 (June 1951), pp. 369–374. DOI: [10.2514/8.1975](https://doi.org/10.2514/8.1975).
- [72] G. Sullins and G. McLafferty. "Experimental results of shock trains in rectangular ducts". In: *AIAA 4th International Aerospace Planes Conference*. 1992-5103. Orlando, FL, USA, Dec. 1992, pp. 1–20. DOI: [10.2514/6.1992-5103](https://doi.org/10.2514/6.1992-5103).
- [73] S. Emami et al. *Experimental Investigation of Inlet-Combustor Isolators for a Dual-Mode Scramjet at a Mach Number of 4*. NASA Technical Report. report 3502. May 1995.
- [74] L.A. Povinelli and C.E. Towne. *Viscous analyses for flow through subsonic and supersonic intakes*. Technical Memorandum NASA TM-88831. Lewis Research Center, Cleveland, Ohio 44135 U.S.A.: NASA, Sept. 1986.
- [75] T. Cain. *Design and Evaluation of High Speed Intakes*. NATO lecture. 2004.
- [76] H. Ran and D. Mavris. "Preliminary Design of a 2D Supersonic Inlet to Maximize Total Pressure Recovery". In: *AIAA 5th Aviation, Technology, Integration, and Operations Conference*. Ed. by AIAA. Arlington, Virginia, Sept. 2005. DOI: [10.2514/6.2005-7357](https://doi.org/10.2514/6.2005-7357).
- [77] C. Bauer and G. Kurth. "Importance of the Bleed System on the Overall Air Intake Performance". In: *47th AIAA/ASME/SAE/ASEE Joint Propulsion Conference & Exhibit*. 2011-5759. San Diego, CA, USA, July 2011. DOI: [10.2514/6.2011-5759](https://doi.org/10.2514/6.2011-5759).
- [78] M.R. Soltani, J.S. Younsi, and M. Farahani. "Effects of Boundary-Layer Bleed Parameters on Supersonic Intake Performance". In: *Journal of Propulsion and Power* 31.3 (June 2015), pp. 826–836. DOI: [10.2514/1.B35461](https://doi.org/10.2514/1.B35461).
- [79] M.R. Soltani, J. Sepahi-Younsi, and M. Farahani. "Effects of Boundary-Layer Bleed Parameters on Supersonic Intake Performance". In: *Journal of Propulsion and Power* 31.3 (May 2015), pp. 826–836. DOI: [10.2514/1.B35461](https://doi.org/10.2514/1.B35461).
- [80] D. O. Davis, B. P. Willis, and W. R. Hingst. "Flowfield measurements in a normal-hole-bled oblique shock-wave and turbulent boundary-layer interaction". In: *31st Joint Propulsion Conference and Exhibit*. 1995-2885. San Diego, CA, USA, July 1995, pp. 1–13. DOI: [10.2514/6.1995-2885](https://doi.org/10.2514/6.1995-2885).
- [81] G. J. Harloff and G. E. Smith. "Supersonic-Inlet Boundary-Layer Bleed Flow". In: *AIAA Journal* 34.4 (Apr. 1996), pp. 778–785. DOI: [10.2514/3.13140](https://doi.org/10.2514/3.13140).
- [82] L. J. Obery and R. W. Cubbison. *Effectiveness of boundary-layer removal near throat of ramp-type side inlet at free-stream Mach number of 2.0*. NACA Research Memorandum. no. RM E54I14. Nov. 1954.

- [83] M.R. Soltani, J. Sepahi Younsi, and A. Daliri. "Performance investigation of a supersonic air intake in the presence of the boundary layer suction". In: *Journal of Aerospace Engineering* 229.8 (Mar. 2014), pp. 1495–1509. DOI: [10.1177/0954410014554815](https://doi.org/10.1177/0954410014554815).
- [84] A.K. Flock and A. Gülhan. "Modified Kantrowitz Starting Criteria for Mixed Compression Supersonic Intakes". In: *AIAA Journal* 57.5 (May 2019), pp. 2011–2016. DOI: [10.2514/1.J057283](https://doi.org/10.2514/1.J057283).
- [85] E. V. Timofeev, R. B. Tahir, and S. Mölder. "On Recent Developments Related to Flow Starting in Hypersonic Air Intakes". In: *15th AIAA International Space Planes and Hypersonic Systems and Technologies Conference*. 2008-2512. Apr. 2008, pp. 1–9. DOI: [10.2514/6.2008-2512](https://doi.org/10.2514/6.2008-2512).
- [86] R.T. Biedron and C. Adamson Jr. "Unsteady Flow in a Supercritical Supersonic Diffuser". In: *AIAA Journal* 26.11 (Nov. 1988), pp. 1336–45. DOI: [10.2514/3.10045](https://doi.org/10.2514/3.10045).
- [87] A. Ferri and L.M. Nucci. *The origin of aerodynamic instability of supersonic inlets at subcritical conditions*. Research Memorandum RM L50K30. NACA, Jan. 1951.
- [88] N.R. Kingsbury. *Aerospace technology : Technical data and information on foreign test facilities : Fact sheet for the chairman*. Tech. rep. General Accounting Office, Washington, D.C.: committee on science, space, and technology, house of representatives, June 1990.
- [89] A. Flinkerbusch. "Oblique shock wave boundary layer interactions over porous plates". MSc. Thesis. Delft University of Technology, 2018.
- [90] M.E.N. Wisse. "An Asymptotic Analysis of Compressible Base Flow and the Implementation into Linear Plug Nozzles". PhD thesis. Delft University of Technology, June 2005.
- [91] K.J.W. Kwakman. "Submerged supersonic air intakes: An experimental investigation and inviscid study into their performance". MA thesis. Delft University of Technology, 2019.
- [92] Scannivalve. *DSA3217/3218 Series Pressure Scanner Digital Sensor Array Operation and Service Manual*. 1.18. Scannivalve. 1722 N. Madson Street, Liberty Lake, WA 99019.
- [93] Jerry Westerweel. "Fundamentals of digital particle image velocimetry". In: *Measurement science and technology* 8.12 (Dec. 1997), pp. 1379–1392. DOI: [10.1088/0957-0233/8/12/002](https://doi.org/10.1088/0957-0233/8/12/002).
- [94] W.A.S. Kumara, B.M. Halvorsen, and M.C. Melaaen. "Particle image velocimetry for characterizing the flow structure of oil–water flow in horizontal and slightly inclined pipes". In: *Chemical Engineering Science* 65.15 (Aug. 2010), pp. 4332–4349. DOI: [10.1016/j.ces.2010.03.045](https://doi.org/10.1016/j.ces.2010.03.045).
- [95] F. Scarano. "AE 4180: Experimental Aerodynamics". Delft, 2013b. Feb. 2013.
- [96] D. Ragni et al. "Particle tracer response across shocks measured by PIV". In: *Experiments in Fluids* 50 (May 2011), pp. 53–64. DOI: [10.1007/s00348-010-0892-2](https://doi.org/10.1007/s00348-010-0892-2).
- [97] C.E. Brennen. *Fundamentals of Multiphase Flow*. ISBN: 9780511807169. Cambridge University Press, 2005.
- [98] C. Tropea and M. Gnirß. "Simultaneous PIV and concentration measurements in a gas-turbine combustor model". In: *Experiments in Fluids* 45 (June 2008), pp. 643–656. DOI: [10.1007/s00348-008-0518-0](https://doi.org/10.1007/s00348-008-0518-0).
- [99] *User Manual Aerosol Generator PivPart45 series*. PIVTEC. Stauffenberggring 21, D-37075 Göttingen, Germany.
- [100] E.J. Donker Duyvis. "Laser sheet probe design for piv in high-speed wind tunnels". In: *PIVNET II International Workshop on the Application of PIV in Compressible Flows*. 2005.
- [101] M. Raffel et al. *Particle Image Velocimetry: A Practical Guide*. ISBN 9783319688510. Springer, 2018.
- [102] R. Hain and C.J. Kähler. "Fundamentals of multiframe particle image velocimetry (PIV)". In: *Experiments in Fluids* 42 (Feb. 2007), pp. 575–587. DOI: [10.1007/s00348-007-0266-6](https://doi.org/10.1007/s00348-007-0266-6).
- [103] *LaVision DaVis 8.3 Product Manual*. LaVision GmbH. 2015.
- [104] J. Westerweel and F. Scarano. "Universal outlier detection for PIV data". In: *Experiments in Fluids* 39 (Aug. 2005), pp. 1096–1100. DOI: [10.1007/s00348-005-0016-6](https://doi.org/10.1007/s00348-005-0016-6).
- [105] C. Tropea, A.L. Yarin, and J.F. Foss. *Handbook of Experimental Fluid Mechanics*. ISBN: 978-3-540-25141-5. Springer, 2007.

- [106] A.K. Ray. "On the effect of orifice size on static pressure reading at different Reynolds numbers". In: *Ing.-Arch* 24.3 (1956). Engl. transl. Aero. Res. Council. unclassified 'A3' report 18829, FM 2479, EA 527, TP 498.
- [107] W.J. Rainbird. "Errors in measurement of mean static pressure of a moving fluid due to pressure holes". In: *Quart. Bull. Div. Mech. Eng. Nat. Aero. Est. DME/NAE #3* (1967). National Research Council, Ottawa.
- [108] C. Ducruet. "A method for correcting wall pressure measurements in subsonic compressible flow". In: *Journal of Fluid Engineering* 113.2 (1991), pp. 256–260. DOI: [10.1115/1.2909489](https://doi.org/10.1115/1.2909489).
- [109] R. Shaw. "The influence of hole dimensions on static pressure measurements". In: *Journal of Fluid Mechanics* 7 (1960), pp. 550–564.
- [110] Z. Sun. "Micro Ramps in Supersonic Turbulent Boundary Layers: An experimental and numerical study". PhD Thesis. Delft University of Technology, 2014.
- [111] F.E.J. Schrijer and F. Scarano. "Effect of predictor–corrector filtering on the stability and spatial resolution of iterative PIV interrogation". In: *Experiments in Fluids* 45.5 (2008), pp. 927–941. DOI: [10.1007/s00348-008-0511-7](https://doi.org/10.1007/s00348-008-0511-7).
- [112] L.H. Benedict and R.D. Gould. "Towards better uncertainty estimates for turbulence statistics". In: *Experiments in Fluids* 22 (1996), pp. 129–136.
- [113] T. Gawehn et al. "Analysis of gap influence on pseudo-shock system asymmetry in rectangular Laval nozzles". In: *20th International Shock Interaction Symposium*. Aug. 2012.
- [114] H.W. Liepmann, A. Roshko, and S. Dhawan. *On reflection of shock waves from boundary layers*. Technical report 2334. National Advisory Committee for Aeronautics, 1951.
- [115] B.W. van Ousheusden. "PIV-based pressure measurement". In: *Measurement Science and Technology* 24 (Jan. 2013), pp. 1–32. DOI: <https://doi.org/10.1088/0957-0233/24/3/032001>.
- [116] T. Tamaki, Y. Tomita, and R. Yamane. "A study of pseudo-shock, 2nd Report, X-type pseudo-shock". In: *Bull JSME* 14.74 (1971), pp. 807–817. DOI: [10.1299/jisme1958.14.807](https://doi.org/10.1299/jisme1958.14.807).
- [117] C. Wang, P.X. Longsheng, and X.Y. Jiao. "Three-dimensional reconstruction of incident shock/boundary layer interaction using background-oriented schlieren". In: *Acta Astronautica* 157 (Apr. 2019), pp. 314–349. DOI: [10.1016/j.actaastro.2019.01.002](https://doi.org/10.1016/j.actaastro.2019.01.002).
- [118] J.S. Geerts and K.H. Yu. "Systematic Application of Background-Oriented Schlieren for Isolator Shock Train Visualization". In: *AIAA Journal* 55.4 (Apr. 2017), pp. 1105–1117. DOI: [10.2514/1.J054991](https://doi.org/10.2514/1.J054991).
- [119] L.M. Edelman and M. Gamba. "Structure of a Mach 2 Shock Train from Experimental Measurements". In: *AIAA Scitech 2020 Forum*. 2020-1609. Orlando, FL, USA, Jan. 2020, pp. 1–18. DOI: [10.2514/6.2020-1609](https://doi.org/10.2514/6.2020-1609).
- [120] R.L. Hunt and M. Gamba. "Shock Train Unsteadiness Characteristics, Oblique-to-Normal Transition, and Three-Dimensional Leading Shock Structure". In: *AIAA Journal* 56.4 (Apr. 2018). DOI: [10.2514/1.J056344](https://doi.org/10.2514/1.J056344).
- [121] W. Huang et al. "Recent advances in the shock wave/boundary layer interaction and its control in internal and external flows". In: *Acta Astronautica* 174 (Sept. 2020), pp. 103–122. DOI: [10.1016/j.actaastro.2020.05.001](https://doi.org/10.1016/j.actaastro.2020.05.001).
- [122] G.-C. Zha et al. "High-Performance Supersonic Missile Inlet Design Using Automated Optimization". In: *Journal of Aircraft* 34.6 (Nov. 1997), pp. 697–705. DOI: [10.2514/6.1996-4142](https://doi.org/10.2514/6.1996-4142).
- [123] A. Gaiddon, D. D. Knight, and C. Poloni. "Multicriteria Design Optimization of a Supersonic Inlet Based upon Global Missile Performance". In: *Journal of Propulsion and Power* 20.3 (May 2004), pp. 542–558. DOI: [10.2514/1.2390](https://doi.org/10.2514/1.2390).